Simultaneous Three-Dimensional Shape Estimation and Tracking in Maritime Environments

Zur Erlangung des akademischen Grades eines

Doktors der Ingenieurwissenschaften

von der KIT-Fakultät für Informatik
des Karlsruher Instituts für Technologie (KIT)

genehmigte

Dissertation

von

Tim Baur

Tag der mündlichen Prüfung:	14.11.2025
Erster Gutachter:	Prof. Dr.-Ing. Uwe D. Hanebeck
Zweiter Gutachter:	Prof. Dr.-Ing. Johannes Reuter
Dritter Gutachter:	Prof. Dr.-Ing. Marcus Baum

Acknowledgments

This thesis represents the results of my research over the last few years at the Institute of System Dynamics (ISD) at HTWG Konstanz and the Intelligent Sensor-Actuator-Systems (ISAS) laboratory at the Karlsruhe Institute of Technology (KIT). As this work would not have been possible without the help and support of many people who have accompanied me over this time, I would like to take this opportunity to express my sincere thanks. First of all, I would like to thank Prof. Dr. Johannes Reuter for giving me the opportunity to write my dissertation in Konstanz, such an inspiring workplace. His tireless efforts to guide me professionally and secure my funding, but also his willingness to support me personally, made this work possible in the first place. I would also like to thank Prof. Dr. Uwe D. Hanebeck for agreeing to be my official first supervisor for my doctoral studies at KIT. His valuable professional guidance and involvement in his working group have enriched this work through many discussions and contributed significantly to its development in its current form. Furthermore, I would like to thank Prof. Dr. Marcus Baum for his willingness to act as an independent reviewer for this thesis. Finally, many thanks go to Prof. Dr. Gunnar Schubert, who also provided me with financial support and considerable freedom in my project work during my time at HTWG, without which this work would not have been possible.

This work would never have been possible without the enriching and friendly working environment at HTWG and KIT, which I have enjoyed over the past few years. Many thanks to Patrick, Hannes, Stefan, Dennis, Ruven, Oliver, Matthias, Christian, Florian, Tristan, Michael, Manuela, Marcel, Lea, Johannes, and Roman at the HTWG for the coffee breaks, walks, hiking trips, bowling and barbecue evenings, and for making my time at the HTWG so enjoyable. I would also like to thank Michael, Marcel, Daniel, Dominik, Markus, Benjamin, Sascha, Antonio, and Florian from KIT. You enriched my visits to the department and the group retreats in Karlsruhe, as well as several conference visits with many conversations.

I am lucky to have many wonderful friends who are always there and have time when you need them, who always distract me when I need it, and who have helped me not to lose sight of the important things in life. Many thanks to Kebron, Dimitri, and Paul in Stuttgart. Many thanks to Julian, Rico, and Peter in Konstanz. Many thanks to Christoph in Berlin. Many thanks to Javier in München. Many thanks to Matthias in Taipei. Many thanks to Martin in Ingolstadt. Many thanks to Anna, Dennis, Lisa, Maximilian, Sven, Tobias, and Yannick in Mössingen and the surrounding area. But above all, I would like to thank Felix, Johannes, Julian, and Simon in Mössingen, my oldest and most loyal friends. I am very grateful to all of you.

Finally, I would like to thank the people closest to me. I am deeply grateful for my wonderful family, my parents, Valeria and Uwe, and my siblings, Clarissa and Nikolai, with their partners Marvin and Mona. I know that I can always rely on you. Thank you for always being by my side and, above all, for always lending me an ear, especially when times are tough. Lastly, I would like to thank my partner Wera and her family for making the final phase of my doctoral studies so special and beautiful. I consider myself very lucky to have met such a wonderful person, and I look forward to every day we get to spend together.

Thanks to all of you!

Konstanz, April 2025 Tim Baur

Contents

Glossary and Notation **iv**

Zusammenfassung **vi**

Abstract **viii**

1 Introduction **1**

1.1 Context 1

1.2 Extended Object Tracking in Maritime Applications 2

1.3 Related Work 3

1.4 Challenges 5

1.5 Contributions and Outline of the Thesis 6

1.6 Publications 8

2 Bayesian Extended Object Tracking **9**

2.1 Motivation and Contributions 9

2.2 Problem Formulation 11

2.3 Recursive Bayesian Extended Object Tracking 11

2.4 Measurement-to-Source Association 17

2.5 Interval Constraints in Extended Object Tracking 27

2.6 Recursive Artificial Measurement Noise Estimation 29

2.7 Conclusions 34

3 Parametric Shapes: Object-Specific Shapes **36**

3.1 Motivation and Contributions 36

3.2 Related Work 37

3.3 Elliptic Cylinders for Motor Boats 38

3.4 Elliptic Cones for Sailing Boats 42

3.5 Implementation Details 45

3.6 Experiments 49

3.7 Conclusions 55

4 Non-Parametric Shapes: Series Expansions **56**

4.1 Motivation and Contributions 56

4.2 Related Work 57

4.3 Shape Estimation and Tracking in Cylindrical Coordinates 58

4.4 Implementation Details 67

4.5 Experiments 73

4.6 Conclusions 78

5 Flexible Parametric Shapes: Superellipses **81**

5.1 Motivation and Contributions 81

5.2 Related Work 82

5.3 Superellipses as Shape Representation 83

5.4 Superellipse measurement models 84

5.5 Implementation Details 89

5.6 Experiments 91

5.7 Conclusions 94

6 Evaluation **95**

6.1 Evaluation in a Maritime Environment 95

6.2 Generalization to an Automotive Environment 109

6.3 Discussion 113

6.4 Conclusions 114

7 Final Conclusions and Future Work **116**

7.1 Summary 116

7.2 Future Work 117

Directories **119**

Bibliography **123**

Own Publications **136**

Own Published Code Repositories **137**

Co-authored Publications **138**

Glossary and Notation

General Conventions

a	scalar
$\underline{a}$	vector
$\mathbf{A}$	matrix
$\mathscr{A}$	set
$\mathbb{R}$	set of real numbers
$\mathbb{N}$	set of natural numbers
$\mathbf{A}^\top$	transpose of a matrix
$\mathbf{A}^{-1}$	inverse of a matrix
$\lvert a \rvert$	absolute value of a scalar
$\lVert \underline{a} \rVert$	Euclidean norm of a vector
$a^{(\eta)}$	coordinate η of vector $\underline{a}$
$\underline{a}^{(\eta\xi)}$	coordinates η, ξ of vector $\underline{a}$
$\underline{0}_n$	vector of n zeros
$\mathbf{I}_n$	identity matrix of size n
$\lfloor a \rfloor$	rounding off a
$\frac{\partial f}{\partial a}$	partial derivative of f with respect to a
$\mathrm{diag}(\underline{a})$	diagonal matrix of vector $\underline{a}$
$\mathrm{sign}(a)$	sign of scalar a
$\mathrm{atan2}(y, x)$	4-quadrant extension of inverse tangent for scalars x, y
$\mathrm{erf}(a)$	Gauss error function at scalar a
$\Phi(a)$	standard normal distribution cumulative distribution function at scalar a
$\mathcal{N}(\mu, \sigma^2)$	Gaussian distribution with mean μ and standard deviation σ
$\mathcal{U}(a, b)$	uniform distribution in interval $[a, b]$
$\mathcal{T}(a, b, c)$	triangular distribution with lower limit a, upper limit b, and mode c

State Estimation

$\underline{x}_k$	system state at time step k
$\hat{\underline{x}}_{k\lvert k-1}$	predicted state mean at time step k
$\hat{\underline{x}}_k$	updated state mean at time step k
$\mathbf{P}_{k\lvert k-1}$	predicted state covariance matrix at time step k
$\mathbf{P}_k$	updated state covariance matrix at time step k
$\underline{y}_{k,l}$	l-th measurement at time step k
$\hat{\underline{y}}_{k,l}$	l-th predicted measurement at time step k
$\tilde{\underline{y}}_{k,l}$	l-th measurement in local coordinates at time step k
$\underline{z}_{k,l}$	l-th measurement source at time step k
$\underline{\boldsymbol{x}}_{k,i}$	i-th sample of state x at time step k
${}^s\underline{a}_k$	stacked vectors $\underline{a}_{k,1}, \ldots, \underline{a}_{k,n}$ at time step k

${}^{s}\mathbf{A}_k$	stacked matrices $\mathbf{A}_{k,1}, \ldots, \mathbf{A}_{k,n}$ at time step k
n_s	number of samples in the linear regression Kalman filter (LRKF)
n_u	number of processed measurements in a single sequential batch update
n_k	number of measurements gathered at time step k
n_a	dimensionality of vector $\underline{a}$

Abbreviations

EOT	extended object tracking
Lidar	light detection and ranging
Radar	radio detection and ranging
EKF	extended Kalman filter
LRKF	linear regression Kalman filter
UKF	unscented Kalman filter
S2KF	smart sampling Kalman filter
SDM	spatial distribution model
RM	random matrix
GAM	greedy association model
RHM	random hypersurface model
ERHM	extrusion random hypersurface model
RAMN	recursive artificial measurement noise
PDF	probability density function
RMSE	root mean square error
MC	Monte Carlo
CDF	cumulative distribution function
IoU	intersection over union
SDFS	spherical double Fourier series
FCDS	Fourier-Chebyshev double series
SH	spherical harmonics
GP	Gaussian process
DFS	double Fourier series
CAD	computer-aided design
CT	coordinated turn
RTK	real-time kinematic
GPS	global positioning system
IMU	inertial measurement unit

Zusammenfassung

Bei der Verwendung von modernen und hochauflösenden Sensoren wie Lidar oder Radar, welche zunehmend auch in der Umfelderkennung der automatisierten bis autonomen Schifffahrt eingesetzt werden, wird eine Vielzahl von Messungen pro Zeitschritt und Objekt aufgezeichnet. Die Anzahl der Messdaten hängt dabei von der Auflösung des Sensors und dem Abstand des Sensors zum aufgezeichneten Objekt ab und kann bei modernsten Sensoren mehrere tausend Messungen pro Zeitschritt und Objekt betragen. Durch die Fusion dieser Messungen in zeitlicher Reihenfolge und die Annahme eines Bewegungsmodells, welches dem dynamischen zu verfolgenden Objekt unterstellt wird, kann die kinematische Zustandsverteilung des Objekts innerhalb eines Zustandsfilters geschätzt werden.

Da die Fülle an Messdaten, welche die Sensoren generieren, im Normalfall über die Oberfläche des gesamten Objekts verteilt sind, beinhalten diese zusätzlich zu den Informationen über den kinematischen Zustand Informationen über die Ausdehnung und Form der zu verfolgenden Objekte. Die Schätzung dieser Ausdehnungs- und Forminformationen innerhalb des Messmodells eines Zustandsfilters zur Verfolgung von Objekten wird in der einschlägigen Literatur als Extended Object Tracking (EOT) bezeichnet. Diese Dissertation beschäftigt sich mit der Erstellung und Untersuchung von entsprechenden Messmodellen für Messdaten im dreidimensionalen Raum, welche speziell für Anwendungen im maritimen Bereich geeignet sind. Der Inhalt der Arbeit lässt sich dabei in drei Teile untergliedern.

Im ersten Teil der Arbeit werden die theoretischen Grundlagen erarbeitet, welche für die Erstellung eines EOT-Filters benötigt werden. Dazu gehören zunächst die Herleitung gängiger nichtlinearer Filterverfahren wie des Extended- und des Linear-Regression-Kalman-Filter anhand der allgemeinen Bayes-Filter-Gleichungen und die Verarbeitung mehrerer Messdaten pro Zeitschritt innerhalb dieser Verfahren. Innerhalb der Messmodelle dieser Verfahren können nun die Systemzustände, welche aus einem kinematischen und einem Ausdehnungs- bzw. Formanteil bestehen, auf die vorhergesagte Messung abgebildet werden, welche für die Berechnung eines Residuums im Korrekturschritt des Filters benötigt wird. Da die vorhergesagte Messung sich aus einem Messrauschen mit angenommener bekannter Verteilung und einem im Allgemeinen unbekannten Punkt auf der Oberfläche des Objekts, der sogenannten Messquelle, zusammensetzt, werden im Anschluss unterschiedliche Methoden aus der Literatur zur Messquellenzuordnung hergeleitet und diskutiert. Speziell werden, ausgehend von Spatial Distribution Modellen (SDM), das sogenannte Greedy Association Modell (GAM), welches eine greedy Zuordnung der Messquelle verwendet, und das Random Hypersurface Modell (RHM) und Extrusion RHM (ERHM) als Kombination eines SDM und GAM zur Lösung des Zuordnungsproblems vorgestellt.

Im Anschluss werden in zwei weiteren Abschnitten praktische Probleme beim Einsatz von EOT-Verfahren mit Realdaten behandelt. Zunächst wird ein effektiver und einfach zu implementierender Ansatz vorgestellt, um Intervallbeschränkungen anhand von beschränkten Transformationsfunktionen bei der Zustandsschätzung einzuhalten. Speziell im EOT können Intervallbeschränkungen, welche eingehalten werden sollten, auftreten, sodass beispielsweise keine negativen Längen, Breiten oder Höhen als Ausdehnungsparameter möglich sind. Ein weiteres praktisches Problem besteht darin, dass dreidimensionale reale Messdaten oftmals aufgrund der physischen Struktur der zu verfolgenden Objekte sowohl von der äußeren Hülle als auch vom

Innenbereich aufgezeichnet werden. Wird in den Messmodellen allerdings davon ausgegangen, dass die Messdaten lediglich von der äußeren Hülle der Objekte generiert werden, so kann das Schätzergebnis verzerrt werden. Für die Lösung dieses Problems wird am Ende des ersten Teils ein künstliches rekursiv geschätztes Messrauschen für Messdaten aus dem Innenbereich eingeführt, welches diese Verzerrungen reduziert und dabei auf kein Vorwissen angewiesen ist, da die Korrekturgrößen anhand der aufgezeichneten Messdaten geschätzt werden. Diese beiden Verfahren werden im Laufe der Arbeit auf alle neu vorgestellten Messmodelle angewendet.

Aufbauend auf diesen theoretischen Grundlagen werden im zweiten Teil der Arbeit drei unterschiedliche Kategorien von Messmodellen für 3D-EOT von maritimen Objekten vorgestellt, diskutiert und zunächst in statischen simulierten Szenarien untersucht. Dabei wird bei der Definition dieser Messmodelle die charakteristische Eigenschaft von Messdaten im maritimen Bereich berücksichtigt, bei der davon auszugehen ist, dass in den meisten Szenarien hauptsächlich Messungen der Mantelfläche der Objekte aufgezeichnet werden. Messdaten der Ober- und Unterseite sind oftmals aufgrund von Verdeckungen durch das Wasser und die Montageposition der Sensoren spärlich. Formrepräsentationen in zylindrischen Koordinaten berücksichtigen diese charakteristische Eigenschaft durch die Definition der Form anhand der Mantelfläche.

Ausgehend von einer vorherigen Klassifizierung der Objekte werden daher in einem ersten Kapitel zwei Messmodelle in zylindrischen Koordinaten, welche parametrische Formrepräsentationen verwenden, vorgestellt. Dabei werden unterschiedliche Messmodelle, welche die Form eines Motorboots mit einem elliptischen Zylinder und die Form eines Segelboots mit einem elliptischen Kegel approximieren, vorgestellt und untereinander verglichen. Um die Objektverfolgung ohne vorgelagerte Klassifizierung verbessern zu können, werden in einem weiteren Kapitel unterschiedliche Varianten an Messmodellen vorgestellt und untersucht, welche eine flexible Reihenentwicklung, zusammengesetzt aus einer Fourier- und einer Chebyshevreihe, als Formrepräsentation in zylindrischen Koordinaten verwenden. Die Schätzung der Reihenkoeffizienten innerhalb eines EOT-Filters ermöglicht dann die Anpassung der Form an die vorliegenden Messdaten. Aufgrund der nur schwer vorhersagbaren Anzahl an Formkoeffizienten, die für diesen Ansatz benötigt werden, werden in einem letzten Kapitel unterschiedliche Varianten eines Messmodells, welches eine flexible parametrische Formrepräsentation basierend auf Superellipsen verwendet, vorgestellt und untereinander verglichen. Diese ermöglichen beispielsweise die Unterscheidung zwischen einer elliptischen und einer rechteckigen Grundform innerhalb eines einzelnen Modells, welches nur wenige Formparameter benötigt, was für viele Anwendungen bereits ausreichend sein kann.

Der dritte Teil der Arbeit beschäftigt sich mit einer vergleichenden Untersuchung der vorgestellten Messmodelle in unterschiedlichsten dynamischen Szenarien. Im maritimen Bereich werden die Modelle, welche für Motorboote geeignet sind, mithilfe der *Solgenia*, eines Forschungsboots der HTWG Konstanz, als Referenzobjekt getestet. In dieser Untersuchung wird ein CAD Modell der *Solgenia* innerhalb einer Simulation für die Messdatengenerierung und in der Simulation, sowie einem Realdatenexperiment als Formreferenz eingesetzt. Eine solche Untersuchung ist einzigartig in der bisherigen Literatur. Die Messmodelle, welche speziell für Segelboote erstellt wurden, werden in diesem Kapitel anhand von Realdaten eines Segelboots aus einer Regatta validiert. Um die Generalisierbarkeit der Messmodelle zu untersuchen, werden diese in einem letzten Schritt unter Verwendung des berühmten KITTI-Datensatzes untersucht. Dabei werden etwa 1200 Szenarien mit unterschiedlichen Objektklassen für die erarbeiteten Messmodelle sowie Vergleichsmodelle der Literatur ausgewertet und verglichen. Die Ergebnisse aller Untersuchungen untermauern die Effektivität und gleichzeitige Effizienz der in dieser Dissertation erarbeiteten Modelle. Offene Fragen, die in dieser Arbeit nicht beantwortet werden konnten, werden am Ende der Arbeit vorgestellt und diskutiert.

Abstract

When using modern, high-resolution sensors such as Lidar or Radar, which are increasingly being used in environment perception for automated and autonomous shipping, a large number of measurements are recorded per time step and object. The number of measurements then depends on the resolution of the sensor and the distance between the sensor and the recorded object, and can amount to several thousand measurements per time step and object with state-of-the-art sensors. By fusing these measurements in chronological order and assuming a motion model that is applied to the dynamic object being tracked, the kinematic state distribution of the object can be estimated within a state filter.

Since the wealth of measurement data generated by the sensors is typically distributed over the surface of the entire object, this data contains information about the kinematic state and the extent and shape of the objects to be tracked. Estimating this extent and shape information within the measurement model of a state filter for object tracking is referred to in the relevant literature as extended object tracking (EOT). This dissertation deals with the creation and investigation of corresponding measurement models for measurement data in three-dimensional space, which are particularly suitable for applications in the maritime sector. The content of the thesis can be divided into three parts.

The first part of the thesis develops the theoretical foundations required for the creation of an EOT filter. This includes the derivation of common nonlinear filtering methods, such as the extended and linear regression Kalman filters, based on the general Bayes filter equations, and the processing of multiple measurement data per time step within these methods. Within the measurement models of these methods, the system states, which consist of a kinematic and an extent or shape component, can now be mapped to the predicted measurement, which is required for calculating a residual in the correction step of the filter. Since the predicted measurement consists of measurement noise with an assumed known distribution and a generally unknown point on the surface of the object, known as the measurement source, various methods from the literature for the so-called measurement-to-source association problem are derived and discussed. Specifically, based on spatial distribution models (SDM), the so-called greedy association model (GAM), which uses a greedy assignment of the measurement source, and the random hypersurface model (RHM) and extrusion RHM (ERHM), as a combination of an SDM and a GAM, are presented as solutions to the association problem.

Two further sections then deal with practical problems when applying EOT methods to real-world data. First, an effective and easy-to-implement approach is presented for maintaining interval constraints using bounded transformation functions in state estimation. In EOT in particular, interval constraints that must be maintained can occur, so that, for example, negative lengths, widths, or heights are not possible as extent parameters. Another practical problem is that three-dimensional real-world measurements are often recorded both from the outer hull and the interior of the objects being tracked due to their physical structure. However, if the measurement models assume that the measurements are generated solely by the outer hull of the objects, the estimation result may be biased. To solve this problem, an artificial, recursively estimated measurement noise for measurements from the interior is introduced at the end of the first part, which reduces these distortions and does not require any prior knowledge, as

the correction variables are estimated based on the recorded measurement data. These two methods are applied to all newly presented measurement models in the further course of the thesis.

Building on these theoretical foundations, the second part of the thesis presents and discusses three different categories of measurement models for 3D EOT of maritime objects, which are initially investigated in static simulated scenarios. The definition of these measurement models takes into account the characteristic property of measurements in the maritime sector, where it can be assumed that, in most scenarios, measurements of the lateral surface of the objects are mainly recorded. Measurements from the top and bottom surfaces are often sparse due to occlusions by water and the mounting position of the sensors. Shape representations in cylindrical coordinates consider this characteristic property by defining the shape based on the lateral surface.

Based on a previous classification of the objects, two measurement models in cylindrical coordinates that use parametric shape representations are then presented in the first chapter. Different measurement models that approximate the shape of a motor boat with an elliptical cylinder and the shape of a sailing boat with an elliptical cone are presented and compared. To improve object tracking without upstream classification, a further chapter presents and examines different variants of measurement models that use a flexible series expansion, composed of a Fourier series and a Chebyshev series, as shape representation in cylindrical coordinates. Estimating the series coefficients within an EOT filter then allows the shape to be adapted to the available measurement data. Due to the difficulty of predicting the number of shape coefficients required for this approach, a final chapter presents and compares different variants of a measurement model that uses a flexible parametric shape representation based on superellipses. These enable, for example, the distinction between an elliptical and a rectangular basic shape within a single model that requires only a few shape parameters, which may already be sufficient for many applications.

The third part of the thesis deals with a comparative investigation of the presented measurement models in a wide variety of dynamic scenarios. In the maritime sector, the models suitable for motor boats are tested using the *Solgenia*, a research boat belonging to the HTWG Konstanz, as a reference object. In this study, a CAD model of the *Solgenia* is used within a simulation for measurement data generation and in the simulation, as well as in a real-data experiment as a shape reference. Such an investigation is unique in the literature to date. The measurement models, which were created specifically for sailing boats, are validated in this chapter using real data from a sailing boat from a regatta. To investigate the generalizability of the measurement models, they are examined in a final step using the famous KITTI data set. Approximately 1200 scenarios with different object classes are evaluated and compared for the developed measurement models and comparison models from the literature. The results of all investigations confirm the effectiveness and efficiency of the models developed in this dissertation. Open questions that could not be answered in this work are presented and discussed at the end of the thesis.

CHAPTER 1

Introduction

Contents

1.1 Context 1
1.2 Extended Object Tracking in Maritime Applications 2
1.3 Related Work 3
1.4 Challenges 5
1.5 Contributions and Outline of the Thesis 6
1.6 Publications 8

1.1 Context

Surface vessels represent an essential means of transportation, currently employed in transporting goods and people, in the leisure sector, in fishing, in warfare, and in research. The main advantage of shipping is that existing geographical conditions, such as rivers, lakes, seas, or oceans, can be used directly for transportation, leisure activities, or fishing without the need to build large-scale artificial infrastructure. Mankind has relied on shipping for many millennia and utilized it to establish the globalized and interconnected world order that prevails today. Due to this profound importance, the development of assistance systems for the fully or partially automated operation of surface vessels has become increasingly important in recent years. Such systems provide multiple benefits, including:

- **Increased safety:** Between 2014 and 2023, 26595 marine casualties and incidents were reported. Contributing factors related to the human element were involved in 80.1% of these casualties and incidents [4]. The deployment of sensor technology and assistance systems based on sensor data can significantly reduce this human factor influence.
- **Improved operational efficiency:** Optimized route planning can reduce energy consumption and travel time, thereby improving overall shipping efficiency [12]. Increased safety can also reduce crew requirements, enhancing cost-effectiveness [65].
- **Enhanced availability:** Highly automated and efficient transportation can increase the availability of public transport in remote areas. In addition, automated public transportation can be safeguarded via remote access to the control system of the corresponding vehicle [65, 89].

Further positive effects of automated shipping are summarized in [C6]. The main focus of this thesis within automated shipping is environmental perception, which constitutes a key component in the development of automated driver assistance systems.

In recent years, a considerable number of projects have been carried out to develop automated or autonomous surface vessels across a wide range of shipping categories. In the field of autonomous

water cabs, the *RoBoat* project [131–133] and the *Seabubble* project [99] were developed to enable individualized passenger transport, automated waste disposal, and goods delivery. At HTWG Konstanz, the *Solgenia* research vessel [C6] is being developed for the investigation of multi-sensor environment perception and energy-efficient, collision-free, and time-optimal path-planning and control applications in maritime environments [73, 135]. A picture of the *Solgenia* and its computer-aided design (CAD) model with a graphical representation of the installed sensors and actuators can be seen in Fig. 1.1. In this thesis, the *Solgenia* and its sensor

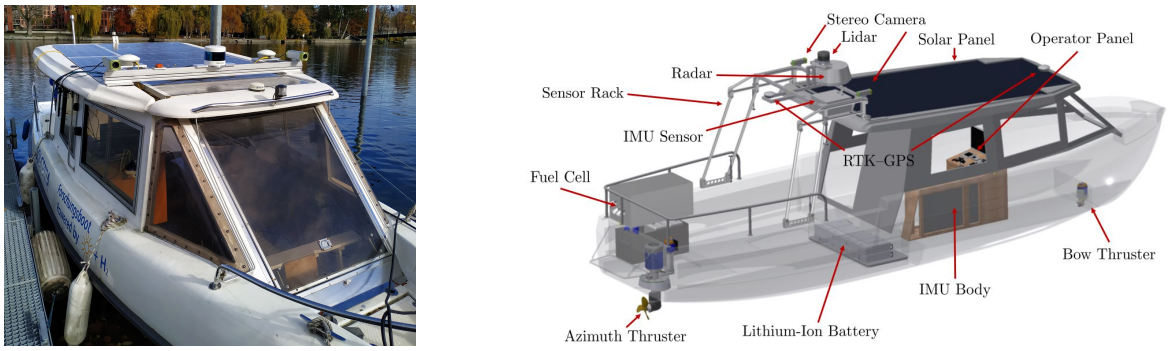

(a) *Solgenia* with old sensor mounting.

(b) *Solgenia* CAD with new sensor mounting [C6].

Figure 1.1: *Solgenia* picture and CAD model with the old and new sensor mounting. The description of sensors and actuators is given in the CAD model.

mounting are utilized for data acquisition [64], and the vessel is also used as an object to be tracked for testing. As a further shipping category, autonomous ferries are, for example, being developed in the *Zeabuz* [71], *MS WaveLab* [39], and *milliAmpere* [23] and *milliAmpere2* [3] projects. Further examples of recent developments and investigations in autonomous maritime systems can be found in [C6].

1.2 Extended Object Tracking in Maritime Applications

One module in environment perception is object tracking, which is required to estimate the dynamic state of the environment. In classical applications of object tracking [10, 11, 19], the algorithms focused on tracking objects that generate at most a single measurement per time step, leading to object models representing them as mathematical points with no physical extent. Using state-of-the-art sensors such as high-resolution light detection and ranging (Lidar) or radio detection and ranging (Radar), a vast amount of measurements per time step distributed over the object's surface is generated, which can be employed to extract extent or shape information over time. These algorithms are summarized under the term extended object tracking (EOT) [58, 59, 98].

In automated maritime applications, tracking extended objects instead of point objects is crucial for several reasons. First, in reality, every object has a physical extent, which must be taken into account when navigating autonomously. Especially in closely spaced scenarios, the extent and pose of an object must be known precisely for collision-free control of the vessel. In addition, extent or precise shape information can be applied for classification in higher-level algorithms [123, 124].

In the past decade, studies have mainly focused on processing Radar data for environment perception in maritime systems. Radar has the advantage that even adverse weather conditions do not affect its performance [151]. In addition, the measurement range can be expected to be

much greater compared to modern Lidar sensors. When tracking extended objects using Radar data, the shape of a vessel is often approximated using ellipses [42, 43, 127, 128] since these have proven to approximate the shape of the ship sufficiently accurately. In these approaches, tracking of the objects is performed in 2D space. Tracking maritime objects in 3D space using modern Radar sensors, which are often developed for the automotive sector [101, 150], remains future work in the maritime domain.

In recent years, Lidar sensors, which are already applied extensively in automotive environments [48], have also been deployed in the maritime sector. The *RoBoat* [131–133], *milliAmpere* [3, 23], and *Solgenia* [C6] test vessels, for example, are all equipped with high-resolution Lidar sensors. An advantage of Lidar over Radar is its high resolution and low measurement noise, which means that it can be used for localization and mapping in coastal areas where static objects are within the range of the sensors [23, C6, 110]. In addition to localization tasks, Lidar data is also applied for tracking dynamic and extended objects in maritime surroundings. Compared to assuming mathematical points in the measurement models, it has been shown that EOT can provide better performance using Lidar [7]. Due to the high resolution of modern Lidar sensors, not only can ellipses be fitted to the measurements [22, 109], but detailed shape information can also be extracted in 2D [8, 94] and 3D space [95].

1.3 Related Work

In EOT, two important aspects must be considered before developing the measurement model. First, the shape class to be estimated must be defined. This shape class can consist of parametric or non-parametric shapes that are to be adapted to the object to be tracked.

Definition 1.1 (Parametric Shape)**.** *A parametric shape is defined as a shape that can be described by a specific geometric logic, where the parameters directly determine the size of the object. Examples include rectangles or ellipses.*

Definition 1.2 (Non-Parametric Shape)**.** *A non-parametric shape is defined as a shape for which no direct geometric logic is encoded by the shape coefficients. Examples include splines or radial function expansions.*

Furthermore, it must be defined whether the object is to be tracked in 2D or 3D Euclidean space. When tracking extended objects in 2D space modeled using parametric shapes, the first choice is often to use ellipses as the shape representation. Ellipses have proven to be flexible and low-dimensional shape representations, which provide a sufficiently accurate shape approximation for a large number of objects. Numerous elliptical EOT measurement models have therefore been introduced over the years.

The best known of these models is the famous random matrix (RM) method [40, 83]. The RM method assumes that the measurements are scattered according to a normal distribution around the center of the object. This assumption is based on the theory of spatial distribution models (SDMs) [51, 52], defined in Sec. 2.4.1, and leads to a robust, efficient, and easy-to-implement algorithm. The RM approach has been applied in many scenarios and refined in various studies [62, C5, 112, 125]. Another method for estimating an elliptical extent is the random hypersurface model (RHM) approach, which is proposed in [15, 16] and discussed in detail in Sec. 2.4.3. The RHM approach assumes that the measurements are generated from a scaled version of the object's boundary, where the scaling factor is modeled as a user-definable random variable, ultimately providing a more flexible approach than the RM method. Further

measurement models assuming an elliptical extent can be found in [141, 142], which are based on modeling the measurement sources using a multiplicative noise model [14], and [25, 57]. A comparison of the most common measurement models assuming an elliptical extent can be found in [121].

Further common parametric shapes in 2D space, often used to represent the extent of vehicles in automotive applications, are rectangles. Popular rectangular EOT measurement models can be found in [26, 61, 79, 82]. These measurement models rely on different measurement source association techniques, spanning from an SDM, described in Sec. 2.4.1, to a greedy association model (GAM), described in Sec. 2.4.2. Furthermore, learning-based rectangular approaches have recently been proposed that attempt to learn the spatial distribution of measurements from real data [74, 81, 111, 139]. In doing so, assumptions often made for the measurement source association are left to the learning process based on real-world data.

If the object's shape class is unknown, and measurement sources are to be modeled precisely, non-parametric shape descriptions for simultaneous shape estimation and tracking can be utilized. In 2D space, a non-parametric shape description can be achieved by estimating a radial function $\ell : \mathbb{R} \to \mathbb{R}$, $\theta \mapsto r$ that maps each angle $\theta \in [0, 2\pi)$ to a radius $r \in [0, \infty)$ describing the shape of the object. Such non-parametric shapes then have the only restriction of being star-convex. In the RHM framework, a shape estimation and tracking approach can be defined using Fourier series [17, 94], a Gaussian process (GP) [9, 129], or lengths of radial segments [2] for describing the radial function using a series expansion or directly estimating a discretized function. Besides estimating radial functions, which are restricted to star-convex shapes, non-convex and arbitrarily shaped objects can be tracked using either polygonal chains [147], or a potential function represented as a GP [86].

In recent years, measurement models for shape estimation and tracking in 3D Euclidean space have also been proposed. With parametric shape descriptions in 3D space, there are considerably more options for different shapes compared to 2D space. The most common parametric shape in 2D space is an ellipse, which can be extended to ellipsoids in 3D space. The models proposed in [15, 16, 40, 83] can easily be extended to tracking ellipsoids instead of ellipses. Further parametric shape measurement models in cylindrical coordinates for cylinders, cones, and tori have been proposed in [33, 38]. These measurement models are based on the theory of extrusion random hypersurface models (ERHMs) [148] where the scaling parameter in the RHM approach is redefined to an extrusion parameter for unbiased height estimates. Details on the ERHM can be found in Sec. 2.4.3.

In addition, there are also non-parametric measurement models in 3D space that can be used if the shape class of the object to be tracked is unknown or if measurement sources are to be modeled precisely. For example, an extension to the B-spline shape representation in [79] has been proposed in [100]. In this approach, non-uniform rational B-spline surfaces are used for both extent and shape estimation by estimating either the scaling parameters of a fixed shape or the weights of the control points of the surface. Another method applying B-splines in 3D space can be found in [67]. In this model, the positions for the control points of the B-spline, which represent the profile of the side view, are estimated. The estimated 2D shape is then extruded to form the 3D shape. Furthermore, radial functions $\ell : \mathbb{R}^2 \to \mathbb{R}$, $[\theta, \varphi]^\top \mapsto r$, that map each angle pair $[\theta, \varphi]^\top \in [0, \pi] \times [0, 2\pi)$ to a radius $r \in [0, \infty)$, are another way of representing flexible non-parametric shapes in 3D space. Comparable to 2D radial functions, these shape representations have the restriction of only being able to represent star-convex shapes. The shape function in spherical coordinates can then be represented using spherical harmonicss (SHs) [87], or a GP [30, 84, 85]. An algorithm for shape estimation and tracking can then be developed using the RHM approach.

In contrast to the work mentioned so far, in real-world applications, it must be assumed that an unknown number of dynamic objects are present in the environment of the ego vehicle. This problem is then referred to as multiple EOT [58]. Although this thesis does not deal with the tracking of multiple extended objects, the relationship of the contributions made herein to the multiple EOT problem is briefly explained. In multiple EOT, the main focus is on associating the measurements gathered in a single time step to newborn or existing objects or categorizing them as clutter [96]. However, due to the unknown number of measurements that each object generates at a specific time step, a highly complex data association problem arises where, in theory, each partitioning of the measurement set must be taken into account [C1, 63]. Once the measurement data have been associated, the models presented before, such as the RM [62] or GP [70] approach, can be used to estimate the extent or shape of the individual objects. Finally, so-called sets of trajectories can be used to generate an assignment of the individual objects throughout the scenario in addition to the current estimates of the kinematic and extent state [136].

1.4 Challenges

When dealing with 3D high-resolution Lidar measurements for EOT in maritime applications, which are mainly employed in this thesis, several challenges arise that are summarized and discussed in this section. Since complex challenges of this type naturally give rise to a large number of problems, the three main issues addressed in this thesis are described below.

- **Challenge 1: Missing Measurements** When recording 3D point measurements in maritime environments, dynamic objects to be tracked are partly underwater. Therefore, no measurements are usually gathered from the bottom parts of objects on the water surface. In addition, depending on the sensor mounting position and viewing angle, measurements from the top part of the objects can also be rare. When tracking maritime objects, it must therefore be assumed that measurements will mainly be available from the lateral surface of the objects. This circumstance must be taken into account when designing the measurement models. If the measurements are projected onto the 2D horizontal plane and subsequently tracked, the missing measurements do not play a significant role. However, when tracking in 3D Euclidean space, the missing measurements must be considered. If the measurement models expect measurements in these areas, the results may be subject to errors. This problem occurs primarily with measurement models that are defined in spherical coordinates, such as [15, 16, 40, 83] for parametric and [30, 84, 85, 87] for non-parametric shape descriptions in 3D space. However, representations in spherical coordinates are often the standard in 3D EOT, especially for non-parametric shape descriptions in 3D space.
- **Challenge 2: Unknown Object Class** When designing an automated or autonomous surface vessel, it must be assumed that a wide variety of objects, such as motorboats, sailing boats, swimmers, or various leisure sports equipment, but also dredgers or other construction vessels, can enter the surveillance area of the sensor system. If a camera system is installed to classify the objects, as is the case with [C6], for example, the classifications can be used to apply specialized measurement models for individual object classes. However, these camera systems often pose a further challenge when designing a surveillance system, as additional data has to be processed, a complex calibration of the individual sensors to one another has to be carried out, and they are often unusable at night or in poor weather conditions. If no classification of the objects is available, the measurement models should have the necessary flexibility to compensate for this lack of

knowledge. The information gained through this flexibility can subsequently be used for an enhanced analysis of the scene. In addition, it can be assumed that a more precise modeling of the measurement sources on a flexible surface can lead to better tracking results [32, 145]. Although several approaches with flexible shape descriptions in 3D space, such as [30, 84, 85, 87, 100], have already been proposed in the literature, these have not been evaluated in the maritime domain. Moreover, in the following, it will become clear that these approaches have weaknesses, as the characteristic measurement data distributions that prevail when recording 3D measurements in the maritime domain have not been taken into account in the modeling process.

- **Challenge 3: Unknown Spatial Measurement Distribution** Another problem with tracking objects using 3D measurements is that measurements are not recorded exclusively from the object's boundary. Due to openings such as windows or loading areas in the object's hull, measurements can also be recorded from the interior. In addition, the measurement data distribution in the vertical direction can also change if the shape and perimeter of the object vary in this direction. However, measurement models such as [33, 38], in which the object's shape is modeled as a cylinder, for parametric and [30, 84, 85, 87] for non-parametric 3D shape descriptions, only specify the measurement source association on the boundary of the shape. When using such measurement models for high-resolution 3D measurements, a bias of the extent estimate towards the object's center can occur.

1.5 Contributions and Outline of the Thesis

The challenges previously outlined are systematically addressed in this thesis. In this section, the individual contributions are summarized and assigned to the respective chapters to provide the reader with an overview.

- **Proposal for Challenge 1: Measurement Models in Cylindrical Coordinates** A natural solution to the problem of missing measurements at the top and bottom parts of objects in maritime applications is the utilization of 3D shape descriptions in cylindrical coordinates in the measurement model. This means that the missing measurements at the top and bottom are no longer a problem, as the contour of the cylindrical shape representation only describes the lateral surface of the object. A formal derivation of the measurement-to-source association for 3D measurement models in cylindrical coordinates can be found in Ch. 2. Especially when associating the height parameter, considerable differences exist in the two approaches presented, as an unbiased height estimate is subject to several challenges. Based on this, the 3D measurement models in Ch. 3, 4, and 5 are all defined in cylindrical coordinates, and different strategies for the measurement-to-source association are presented. A comparison of these 3D measurement models in cylindrical coordinates to measurement models in spherical coordinates in various scenarios can be found in Ch. 6.
- **Proposal for Challenge 2: Several Shape Descriptions of Varying Complexity** To address the problem of unknown object classes, several 3D measurement models with different complexities of shape descriptions in cylindrical coordinates are presented in this thesis. Ch. 3 presents various parametric measurement models for the most common object classes in maritime applications. These can be used to track motor and sailing boats, and to estimate their 3D extent. When using these measurement models, the object class must be known from higher-level algorithms such as classification using a camera system [C6]. However, if the object's class is unknown, more flexible measurement

models should be applied to be able to achieve more accurate estimation results. Ch. 4 therefore introduces a non-parametric shape description using a Fourier-Chebyshev series expansion for representing flexible radial functions in cylindrical coordinates. This approach is comparable to series expansions in spherical coordinates as presented in [O7, 87]. Since the system state to be estimated can be very high-dimensional with this shape representation, and the application of the previously mentioned measurement-to-source association procedures is not directly applicable in parts, a further measurement model is presented in Ch. 5, which uses extruded superellipses [29, 105] as a flexible parametric shape representation. Each measurement model presented is examined in the respective chapters and compared in Ch. 6.

- **Proposal for Challenge 3: Recursive Artificial Measurement Noise Estimation** The challenge of the unknown spatial measurement distribution is handled by a recursively estimated artificial measurement noise in this thesis. With this artificial measurement noise, it is assumed that measurements near the boundary and outside the object can be associated with the boundary, while measurements inside the object must be associated with the interior. For these measurements associated with the interior, the parameters of a Gaussian distributed artificial measurement noise are calculated using a recursive maximum likelihood estimator and the distances of the measurements to the associated measurement sources, which are located on the boundary of the object. The formal derivation of the recursive artificial measurement noise (RAMN) estimation procedure is presented in Ch. 2. The RAMN is then applied to every measurement model in Ch. 3, 4, and 5 to be able to process measurement sets consisting of mixed boundary and interior measurements with each presented measurement model. A comparison of the measurement models with and without applying the RAMN estimation procedure can be found in the respective chapters where the measurement models are derived and in Ch. 6.
- **Extensive Examination in Simulated and Real-World Scenarios** The previously developed measurement models with different approaches for the measurement-to-source association and the RAMN estimation procedure are examined in Ch. 6 in simulative and real-world scenarios and additionally compared with each other. For the measurement models that can be used to track motor boats, a simulated and real-world scenario is presented with the *Solgenia* as the tracking object. Using a CAD model that is available for the *Solgenia*, a precise shape reference can be used to evaluate the tracking, extent, and shape estimation performances of the individual approaches. The measurement model for tracking a sailing boat is only evaluated using a real-world scenario in Ch. 6. In addition to evaluating the measurement models in a maritime domain, an extensive evaluation in an automotive environment is presented using the KITTI raw data set [48]. In this evaluation, 1237 scenarios with different object classes are examined. As a final contribution made in this thesis, pseudo-code for every presented measurement model is provided, and implementations in Matlab are published in [R1–R3, R5].

Further details on the contributions made in this thesis are given at the beginning of the respective chapters.

Remark 1.1. *This thesis assumes that the measurement-to-object association problem is handled by a higher-level track management algorithm. Only measurements belonging to the object to be tracked are processed. The treatment of the multiple EOT problem and clutter measurements is beyond the scope of this work.*

1.6 Publications

The approaches, investigations, and results presented in this thesis are essentially based on the following publications, which have been developed in recent years.

- Publication [O4]: In this paper, the idea of the elliptic cylinder 3D measurement model for tracking motor boats is published. In Ch. 3, this measurement model is derived in more detail and developed further. In addition to [O4], several measurement-to-source association procedures and the RAMN estimation procedure are investigated for the elliptic cylinder shape representation.
- Publication [O5]: In this paper, the idea of the elliptic cone 3D measurement model for tracking sailing boats is published. In Ch. 3, this measurement model is also derived in more detail and developed further. For the elliptic conical shape representation, the same extensions are made as for the elliptic cylinder.
- Publication [O8]: This paper presents the idea of expanding a radial function in cylindrical coordinates using a Fourier-Chebyshev double series (FCDS) as a 3D shape representation. In Ch. 4, this idea is described in detail, and an additional measurement-to-source association procedure is presented for the FCDS shape representation.
- Publications [O2, O3]: In these papers, the idea of representing the shape of an extended object using extruded superellipses is presented. In addition, the RAMN estimation procedure, which is also applied to every other previously mentioned measurement model, is developed in this work.

The publications [O1, O6, O7] are only applied as references, and the approach presented in [O7] is additionally used as a comparison method in the investigation in Ch. 4 and 6. In [O6], the initial idea that shape representations for tracking objects in maritime applications should be defined in cylindrical coordinates is published. The publications [C1–C6] are also only used as references in this thesis.

CHAPTER 2

Bayesian Extended Object Tracking

Contents

2.1 Motivation and Contributions . . . 9
2.2 Problem Formulation . . . 11
2.3 Recursive Bayesian Extended Object Tracking . . . 11
2.3.1 Extended Kalman Filter . . . 13
2.3.2 Linear Regression Kalman Filters . . . 14
2.3.3 Extended Object Measurement Update . . . 15
2.4 Measurement-to-Source Association . . . 17
2.4.1 Spatial Distribution Model . . . 18
2.4.2 Greedy Association Model . . . 19
2.4.3 Random Hypersurface Model . . . 23
2.5 Interval Constraints in Extended Object Tracking . . . 27
2.6 Recursive Artificial Measurement Noise Estimation . . . 29
2.6.1 Derivation . . . 30
2.6.2 Experiments . . . 31
2.7 Conclusions . . . 34

2.1 Motivation and Contributions

This chapter aims to develop a general Bayesian framework for tracking extended objects using 3D range data captured from dynamic objects. In contrast to classical object tracking [10, 19, 27], where objects are assumed to generate at most a single measurement per time step, modern sensors such as light detection and ranging (Lidar) or radio detection and ranging (Radar), as well as depth cameras, potentially generate a vast amount of measurements per object and time step. The number of measurements depends on the sensor resolution and the distance between the sensor and the detected object. Out of this measurement set, the goal of extended object tracking (EOT) [58, 59, 98] is to estimate the extent or shape of the object jointly with the kinematic state, potentially comprising the pose and velocity.

Definition 2.1 (Extent)**.** *In this thesis, the extent is defined as the measurements of the spatial dimensions of an object. In 3D space, these are defined by the length, width, and height of an object. Within this definition, different bodies with different shapes can still have the same extent. For example, a cuboid and an elliptical cylinder can have the same extent but still have a different shape.*

Definition 2.2 (Shape)**.** *The shape of an object defines the visual appearance of a body. For example, clear visual differences can be seen between a cuboid and an elliptical cylinder, as the*

two bodies have different shapes with possibly identical extents. In EOT, the shape information can be implicitly contained in the measurement model, for example, if the extent parameters of a cuboid are to be estimated, or explicitly represented by corresponding shape coefficients.

When recording 3D range measurements, the processing in an EOT filter can be carried out in two ways. First, the measurements can be projected to the 2D horizontal plane and processed in a 2D EOT measurement model. On the other hand, the 3D measurements can be processed directly in a 3D EOT measurement model. Both approaches can be advantageous in specific applications:

- Processing measurements in a 2D measurement model is often sufficient for collision avoidance applications when objects are moving on the water surface [24, 31]. In maritime planning and control approaches, for example, 2D processing is also suitable for carrying out automated maneuvers on the water [73, 135]. Furthermore, the computation time of 2D processing algorithms can be significantly lower due to the fewer system states that need to be estimated and the lower modeling complexity.
- On the other hand, processing measurements directly in a 3D measurement model can be advantageous for several reasons. First of all, extracting as much information as possible from the provided measurements can be beneficial in handling unexpected situations, such as accidents or situations with closely spaced objects. Furthermore, there can also be situations in the maritime domain where 3D information is indispensable, for example, if aerial vehicles are added or when ships need to pass under a bridge. Finally, 3D extent or shape information can be of great use when classifying objects from 3D point cloud data.

However, further research is required in the future regarding the processing of 3D measurements directly in a 3D measurement model and the resulting advantages over processing these measurements in a 2D measurement model.

Contributions The first main contribution of this chapter is the derivation of a formal procedure for tracking extended objects using 3D measurements in a recursive Bayesian fashion in Sec. 2.3. Although this is mainly based on studies from the literature, individual aspects have not yet been examined in detail. This includes a discussion on

- processing measurements from a single time step in a batch update, a sequential update, or a mixture of both procedures,
- and a detailed discussion on solving the so-called measurement-to-source association problem for 3D measurements.

The following two further contributions are also presented in this chapter. First, an efficient and easy-to-use procedure for considering interval constraints in the filtering procedure is presented in Sec. 2.5. Especially in EOT, the extent parameters to be estimated are often subject to interval constraints due to physical reasons that need to be considered. The approach is based on applying monotonically increasing transformation functions with an unbounded domain and a bounded codomain to the state variables subject to interval constraints. In doing so, the filter remains untouched while being able to incorporate interval constraints into the estimation procedure.

The final contribution of this chapter deals with the spatial distribution of measurements often present when recording 3D data. In the 2D case, depending on the applied sensor, measurements from either the boundary or the interior of the object are mostly gathered. In the 3D case, a mixture of boundary and interior measurements is often present. However, many

state-of-the-art EOT methods, such as [16, 40, 79], assume either that measurements originate from the boundary or are uniformly distributed over the extent of the object. In this chapter, an approach is presented in which all measurements are generally associated with a point on the object's boundary initially. However, for measurements inside the predicted boundary, a recursive artificial measurement noise (RAMN) distribution, based on results published [80], is estimated to represent and estimate the distribution of the offset of interior measurements to the boundary. The approach is presented and investigated in Sec. 2.6.

Remark 2.1. *The state constraining procedure and the derivation of the RAMN distribution are presented in [O2, O3].*

2.2 Problem Formulation

With EOT, the task is to estimate the extent or shape of the object jointly with the kinematic state at each time step k using the measurement set

$$\mathcal{Y}_k = \left\{ \underline{y}_{k,l} \right\}_{l=1}^{n_k} . \tag{2.1}$$

The measurements $\underline{y}_{k,l} \in \mathbb{R}^{n_y}$ with $n_y \in \{2, 3\}$ are spatially distributed and provide information about the location, extent, and shape of the object. The number of measurements $n_k \geq 1$ potentially varies over time. If 3D measurements are to be processed in 2D measurement models, they can be projected to the 2D horizontal plane.

Using these measurements, the goal of EOT is to estimate the system state $\underline{x}_k \in \mathbb{R}^{n_x}$ with n_x being the dimension of the system state. In general, the system state can be given as

$$\underline{x}_k = \left[\underline{x}_{\mathrm{kin}_k}^\top, \underline{x}_{\mathrm{ext}_k}^\top \right]^\top \tag{2.2}$$

with $\underline{x}_{\mathrm{kin}_k}$ being the kinematic state and $\underline{x}_{\mathrm{ext}_k}$ being the extent state at time step k. The kinematic state typically comprises the position, orientation, and dynamics of the object, while the extent state comprises the parameters defining the extent or shape of the object. This thesis mainly focuses on estimating and defining proper extent states for tracking extended maritime objects using 3D measurements.

Since measurements and object dynamics are generally uncertain, the goal is to estimate a probability distribution of the system state $p(\underline{x}_k)$ rather than a discrete vector. Given the observable measurements $\mathcal{Y}_k$ in each time step k, the hidden variables $\underline{x}_k$ can be estimated recursively by assuming a hidden Markov process for the state evolution over time and the modeled measurement generation process.

2.3 Recursive Bayesian Extended Object Tracking

Assuming a hidden Markov process for the state evolution over time, a recursive procedure for predicting the system state and updating it given a set of measurements in each time step, known as the Bayes filter, can be derived. Typically, the Bayes filter is derived assuming a single measurement in each time step. For EOT, however, a set of measurements, as described before, is assumed. A clear derivation of the Bayes filter formulas can be found in [27]. Besides [58, 59, 98], a good introduction and clear overview of EOT can also be found in [32, 145].

Prediction Step The prediction step describes how the distribution $p(\underline{x}_k)$ evolves over time, given that the object's behavior can be described as a hidden Markov process. Therefore, an initial distribution $p(\underline{x}_0)$ has to be specified in an initialization step. The general Bayesian prediction step can then be given as the Chapman-Kolmogorov [11] equation

$$p(\underline{x}_{k|k-1}) = \int p(\underline{x}_{k|k-1}|\underline{x}_{k-1}) \cdot p(\underline{x}_{k-1}) \, \mathrm{d}\underline{x}_{k-1} \tag{2.3}$$

where $p(\underline{x}_{k|k-1})$ denotes the predicted state distribution. Moreover, $p(\underline{x}_{k|k-1}|\underline{x}_{k-1})$ is known as the transition density, which describes the dynamic behavior of the object. For tracking algorithms, several motion models for describing the dynamics of the tracked object, such as the constant velocity or constant acceleration models, are known [66]. The extent state is modeled as constant over time in this thesis, as rigid objects are assumed to be tracked. To prevent local minima in the extent or shape estimate and to cope with random and unpredictable disturbances, a random walk model is always applied for the evolution of the extent state over time [32, 145].

Update Step In the update step, the information from the gathered measurements $\mathscr{Y}_k$ is integrated into the hidden system state $\underline{x}_k$. According to the recursive Bayes filter formulation, the new system state at time step k can be given as

$$p\left(\underline{x}_k\right) = \nu \cdot p\left(\mathscr{Y}_k|\underline{x}_{k|k-1}\right) \cdot p(\underline{x}_{k|k-1}) \tag{2.4}$$

using the normalization factor ν. In this equation, the distribution $p\left(\mathscr{Y}_k|\underline{x}_{k|k-1}\right)$ is denoted as the likelihood that describes how well the predicted system state fits the measurements. In time step $k+1$, the updated system state $p(\underline{x}_{k+1})$ can then again be used to calculate the predicted system state $p(\underline{x}_{k+2|k+1})$ to close the recursion.

For the likelihood, independent and identically distributed measurements are assumed, meaning that the likelihood can be rewritten as

$$p\left(\mathscr{Y}_k|\underline{x}_{k|k-1}\right) = \prod_{l=1}^{n_k} p\left(\underline{y}_{k,l}|\underline{x}_{k|k-1}\right). \tag{2.5}$$

In the derivation of the measurement models presented in the following chapters, it is, therefore, sufficient to define the models for a single measurement and to incorporate the information of each measurement according to this model individually.

Nonlinear Kalman Filter Preliminaries When assuming linear models for the state transition and measurement model, both corrupted by additive Gaussian noise and a Gaussian distributed system state within the recursive Bayes filter, the famous and well-known linear Kalman filter [10, 27, 78] is obtained. However, in this thesis, only nonlinear measurement models are derived and investigated, where state inference needs to be carried out using nonlinear filters, for which nonlinear Kalman filters are applied. In general, the state transition can be given as

$$\underline{x}_{k|k-1} = \mathscr{f}(\underline{x}_{k-1}, \underline{w}_k) \tag{2.6}$$

using the nonlinear transition function $\mathscr{f}$ that propagates the system state $\underline{x}_{k-1}$ from time step $k-1$ to time step k using the process noise term $\underline{w}_k$. In Kalman filtering, the process noise is often assumed to be additive, zero-mean, and Gaussian distributed, which can be expressed by $\underline{w}_k \sim \mathcal{N}\left(\underline{0}_{n_x}, \mathbf{\Sigma}_{\underline{w}}\right)$ using the process noise covariance matrix $\mathbf{\Sigma}_{\underline{w}}$. In this case, the transition density $p(\underline{x}_{k|k-1}|\underline{x}_{k-1})$ reduces to a Gaussian distribution since the process noise is the only

remaining probabilistic part besides the deterministic transition function. Similar to the state transition, the measurement model can, in general, be given as

$$\underline{y}_{k,l} = \hbar(\underline{x}_{k|k-1}, \underline{v}_{k,l}) \tag{2.7}$$

using the nonlinear measurement function $\hbar$ that calculates the measurement $\underline{y}_{k,l}$ using the system state $\underline{x}_{k|k-1}$ and the measurement noise term $\underline{v}_{k,l}$. Again, in Kalman filtering, the measurement noise is often assumed to be additive, zero-mean, and Gaussian distributed, which can be expressed by $\underline{v}_{k,l} \sim \mathcal{N}(\underline{0}_{n_y}, \mathbf{\Sigma}_{\underline{v}})$ using the measurement noise covariance matrix $\mathbf{\Sigma}_{\underline{v}}$. However, for the likelihood, several approaches exist where the distribution does not reduce to a simple Gaussian distribution, as will be seen later in Sec. 2.4. The final ingredient for nonlinear Kalman filters is that the initial state density is given as a Gaussian distribution

$$p(\underline{x}_0) = \mathcal{N}\left(\hat{\underline{x}}_0, \mathbf{P}_0\right) \tag{2.8}$$

with $\mathbf{P}_0$ being the initial state covariance matrix. In general, the state distribution to be estimated in each time step k can be given as $p(\underline{x}_k) = \mathcal{N}\left(\hat{\underline{x}}_k, \mathbf{P}_k\right)$. In the following section, two approaches for nonlinear Kalman filters are presented.

2.3.1 Extended Kalman Filter

The first approach developed for estimating a Gaussian distributed hidden system state under nonlinear transition and measurement models corrupted by additive Gaussian noise is the extended Kalman filter (EKF). The main idea of this algorithm is to approximate the nonlinear models using a first-order Taylor approximation [27].

Algorithm 2.1 Extended Kalman Filter

1: Predicted mean and covariance matrix of the system state distribution:

$$\hat{\underline{x}}_{k|k-1} = \ell(\hat{\underline{x}}_{k-1}) \tag{2.9a}$$

$$\mathbf{F}_k = \left.\frac{\partial \ell(\underline{x})}{\partial \underline{x}}\right|_{\underline{x}=\hat{\underline{x}}_{k-1}} \tag{2.9b}$$

$$\mathbf{P}_{k|k-1} = \mathbf{F}_k \cdot \mathbf{P}_{k-1} \cdot \mathbf{F}_k^\top + \mathbf{\Sigma}_{\underline{w}} \tag{2.9c}$$

2: Predicted measurement, measurement matrix, and innovation covariance matrix:

$$\hat{\underline{y}}_k = \hbar(\hat{\underline{x}}_{k|k-1}) \tag{2.10a}$$

$$\mathbf{H}_k = \left.\frac{\partial \hbar(\underline{x})}{\partial \underline{x}}\right|_{\underline{x}=\hat{\underline{x}}_{k|k-1}} \tag{2.10b}$$

$$\mathbf{S}_k = \mathbf{H}_k \cdot \mathbf{P}_{k|k-1} \cdot \mathbf{H}_k^\top + \mathbf{\Sigma}_{\underline{v}} \tag{2.10c}$$

3: Updated mean and covariance matrix of the system state distribution:

$$\mathbf{K}_k = \mathbf{P}_{k|k-1} \cdot \mathbf{H}_k^\top \cdot \mathbf{S}_k^{-1} \tag{2.11a}$$

$$\hat{\underline{x}}_k = \hat{\underline{x}}_{k|k-1} + \mathbf{K}_k \cdot (\underline{y}_k - \hat{\underline{y}}_k) \tag{2.11b}$$

$$\mathbf{P}_k = \mathbf{P}_{k|k-1} - \mathbf{K}_k \cdot \mathbf{H}_k \cdot \mathbf{P}_{k|k-1} \tag{2.11c}$$

Assuming the preliminaries presented before, the equations of the EKF are given in Alg. 2.1. This algorithm describes the processing of a single measurement in each time step. Extensions for multiple measurements in each time step are presented in Sec. 2.3.3. In the state prediction step, $\mathbf{F}_k$ is the Jacobian matrix of the transition function evaluated at the previous system state, termed the transition matrix. In the measurement prediction step, $\mathbf{H}_k$ is the Jacobian matrix of the measurement function evaluated at the predicted system state, termed the measurement matrix, and $\mathbf{S}_k$ is the innovation covariance matrix. Finally, the matrix $\mathbf{K}_k$ is the Kalman gain that reflects the confidence in the recorded measurement and how much the state distribution is corrected according to the measurement.

Due to the first-order linearization in the EKF, the filter can diverge for highly nonlinear systems or poor initializations. Therefore, several improvements, such as a second-order model approximation [5, 107] or an iterated implementation [69, 114], have been proposed. However, the second-order implementation is highly complex due to the Hessian matrix that needs to be derived, and the iterated implementation does not guarantee the convergence of the algorithm. Therefore, linear regression Kalman filters (LRKFs), presented in the next section, have been developed to solve these problems.

2.3.2 Linear Regression Kalman Filters

A main disadvantage of the EKF is the need for linearizations and the derivation of Jacobian matrices, which can be very demanding for complex models. In addition, the EKF can diverge. As an alternative, LRKFs [118] have been developed to overcome these drawbacks. The basic idea of these filters is to approximate the Gaussian distribution using deterministic samples of the distribution, often called sigma points, rather than linearizing the nonlinear models. These samples can then be propagated through the nonlinear models to calculate the moments of the transformed Gaussian using the transformed samples. The various LRKFs often differ mainly in how the sigma points are calculated, also referred to as the Dirac mixture approximation of Gaussian distributions [53]. An overview of different approaches for Dirac mixture approximations of Gaussian distributions can be found in [44, 45]. In this thesis, the famous unscented Kalman filter (UKF) [76, 77, 130] and the smart sampling Kalman filter (S2KF) [118, 119] are used for state inference using LRKFs.

In Alg. 2.2, the equations for processing a single measurement in each time step are given. Most importantly, this algorithm does not need the process and measurement noise to be additive. By exploiting the fact that the system state and the process or measurement noise are statistically independent, the joint densities in (2.12) and (2.14) can be sampled to process non-additive Gaussian noise distributions using the sampled noise distributions. This can be achieved by extending the system state by the respective noise parameters and sampling the extended system state distribution rather than sampling only the system state distribution. Proper derivations of the respective sampling techniques can be found in [118, 130]. A toolbox for the S2KF can be found at [116]. As will be seen later, especially for advanced EOT likelihoods, an efficient state inference implementation can be given using sampling-based LRKFs.

In the LRKF algorithm Alg. 2.2, the probability distribution $\alpha_i \cdot \delta(x - \boldsymbol{x}_i)$ represents the weighted Dirac delta distribution with weight α_i which peaks at the point $\boldsymbol{x}_i$. The peaks $\boldsymbol{x}_i$ are called samples throughout this thesis and represented using calligraphic variables. The weights α_i sum up to one for each Dirac mixture approximation. The number of samples n_s calculated in each filter cycle depends on the chosen LRKF. By transforming the sampled probability distributions through the nonlinear transition and measurement functions, the transformed state distribution parameters can be calculated in the prediction and update steps of the LRKF.

Compared to the EKF, LRKFs tend to be more accurate in the state estimate with a lower risk of divergence. For example, for the UKF, it is known that the filter provides a second-order approximation of the propagated Gaussian state distribution [77]. Since the S2KF can be implemented with a variable number of samples, which are optimally placed according to an optimization based on a local distance measure between the true density and the Dirac mixture approximation, its accuracy can be assumed to be even higher. However, the higher accuracy generally comes with a higher computational cost.

Algorithm 2.2 Linear Regression Kalman Filter

1: Dirac mixture approximation of extended system state distribution:

$$p\left(\underline{x}_{k-1}, \underline{w}_k\right) \approx \sum_{i=1}^{n_s} \alpha_{k,i} \cdot \delta\left(\begin{bmatrix} \hat{\underline{x}}_{k-1} \\ \underline{w}_k \end{bmatrix} - \begin{bmatrix} \underline{\boldsymbol{x}}_{k-1,i} \\ \underline{\boldsymbol{w}}_{k,i} \end{bmatrix}\right) \tag{2.12}$$

2: Predicted mean and covariance matrix of system state:

$$\underline{\boldsymbol{x}}_{k|k-1,i} = \boldsymbol{\ell}\left(\underline{\boldsymbol{x}}_{k-1,i}, \underline{\boldsymbol{w}}_{k,i}\right),\ i = 1 \ldots n_s \tag{2.13a}$$

$$\hat{\underline{x}}_{k|k-1} = \sum_{i=1}^{n_s} \alpha_{k,i} \cdot \underline{\boldsymbol{x}}_{k|k-1,i} \tag{2.13b}$$

$$\mathbf{P}_{k|k-1} = \sum_{i=1}^{n_s} \alpha_{k,i} \cdot \left(\underline{\boldsymbol{x}}_{k|k-1,i} - \hat{\underline{x}}_{k|k-1}\right) \cdot \left(\underline{\boldsymbol{x}}_{k|k-1,i} - \hat{\underline{x}}_{k|k-1}\right)^{\top} \tag{2.13c}$$

3: Dirac mixture approximation of the extended predicted system state distribution:

$$p\left(\underline{x}_{k|k-1}, \underline{v}_k\right) \approx \sum_{i=1}^{n_s} \alpha_{k,i} \cdot \delta\left(\begin{bmatrix} \hat{\underline{x}}_{k|k-1} \\ \underline{v}_k \end{bmatrix} - \begin{bmatrix} \underline{\boldsymbol{x}}_{k|k-1,i} \\ \underline{\boldsymbol{v}}_{k,i} \end{bmatrix}\right) \tag{2.14}$$

4: Predicted measurement and innovation covariance matrix:

$$\underline{\boldsymbol{y}}_{k,i} = \boldsymbol{h}\left(\underline{\boldsymbol{x}}_{k|k-1,i}, \underline{\boldsymbol{v}}_{k,i}\right),\ i = 1 \ldots n_s \tag{2.15a}$$

$$\hat{\underline{y}}_k = \sum_{i=1}^{n_s} \alpha_{k,i} \cdot \underline{\boldsymbol{y}}_{k,i} \tag{2.15b}$$

$$\mathbf{S}_k = \sum_{i=1}^{n_s} \alpha_{k,i} \cdot \left(\underline{\boldsymbol{y}}_{k,i} - \hat{\underline{y}}_k\right) \cdot \left(\underline{\boldsymbol{y}}_{k,i} - \hat{\underline{y}}_k\right)^{\top} \tag{2.15c}$$

5: Updated mean and covariance matrix of system state:

$$\mathbf{\Psi}_k = \sum_{i=1}^{n_s} \alpha_{k,i} \cdot \left(\underline{\boldsymbol{x}}_{k|k-1,i} - \hat{\underline{x}}_{k|k-1}\right) \cdot \left(\underline{\boldsymbol{y}}_{k,i} - \hat{\underline{y}}_k\right)^{\top} \tag{2.16a}$$

$$\hat{\underline{x}}_k = \hat{\underline{x}}_{k|k-1} + \mathbf{\Psi}_k \cdot \mathbf{S}_k^{-1} \cdot \left(\underline{y}_k - \hat{\underline{y}}_k\right) \tag{2.16b}$$

$$\mathbf{P}_k = \mathbf{P}_{k|k-1} - \mathbf{\Psi}_k \cdot \mathbf{S}_k^{-1} \cdot \mathbf{\Psi}_k^{\top} \tag{2.16c}$$

2.3.3 Extended Object Measurement Update

In the EKF and LRKF presented before, a single measurement is processed. However, a key feature in EOT is that n_k measurements are to be processed in each time step k. So, the

question that directly arises is how to process a set of measurements within the nonlinear Kalman filter. In the literature, two approaches can be found to solve this problem:

- Batch update: In batch measurement processing, as applied in [33], a single measurement update is performed for all measurements at once. The main advantage of this method is that the final state estimate is reproducible and does not depend on the order of the measurements. A disadvantage is that the size of the innovation covariance matrix and the resulting computation time depend on the number of measurements recorded in a single time step. In general, the inversion of a $n \times n$ matrix is of complexity $\mathcal{O}(n^3)$ [55].
- Sequential update: In sequential measurement processing, as applied in [142], an individual measurement update is performed for each measurement until all measurements have been processed. Of course, a single prediction step is executed before. The main advantage of this method is the lower computational cost resulting from the inversion of a small innovation covariance matrix in the nonlinear Kalman filter update. A disadvantage is that the final state estimate is highly dependent on the order in which the measurements are processed due to the inherent approximations in the nonlinear Kalman filter update.

To combine the merits and mitigate the drawbacks of both approaches, measurements are processed in a sequential batch update in this thesis. Thus, a fixed number of measurements n_u is processed in each cycle until all measurements are handled. If fewer measurements are available in a final cycle, the remaining measurements are processed, and n_u needs to be lowered for that cycle. In doing so, the computation time can be reduced drastically, and the reproducibility of the estimate is increased.

Extended Object EKF Measurement Update In the EKF, the state prediction step is kept unchanged according to (2.9). In the measurement prediction step (2.10), the predicted measurement and the measurement matrix need to be calculated for each of the n_u measurements and stacked according to

$$ {}^{s}\hat{\underline{y}}_k = \left[\hat{\underline{y}}_{k,1}^{\top}, \ldots, \hat{\underline{y}}_{k,n_u}^{\top}\right]^{\top} \tag{2.17} $$

$$ {}^{s}\mathbf{H}_k = \begin{bmatrix} \mathbf{H}_{k,1} \\ \vdots \\ \mathbf{H}_{k,n_u} \end{bmatrix}. \tag{2.18} $$

Since multiple measurements are processed in a single measurement update, a stacked measurement noise covariance matrix, which can be given as

$$ {}^{s}\mathbf{\Sigma}_{\underline{v}} = \begin{bmatrix} \mathbf{\Sigma}_{\underline{v}} & \mathbf{0} & \mathbf{0} \\ \mathbf{0} & \ddots & \mathbf{0} \\ \mathbf{0} & \mathbf{0} & \mathbf{\Sigma}_{\underline{v}} \end{bmatrix}, \tag{2.19} $$

with n_u measurement noise covariance matrices, arranged in a block diagonal matrix, also needs to be generated. The innovation covariance matrix in (2.10) and the measurement update equations in (2.11) can then be calculated using the stacked variables described before. The single steps are then repeated until all measurements are processed. The pseudo-code and further insights for the extended object EKF sequential batch measurement update can be found in Alg. 4.1 and Sec. 4.4.

Remark 2.2. *In (2.10), the predicted measurement and the measurement matrix only depend on the predicted system state $\hat{\underline{x}}_{k|k-1}$. For different measurements, these variables would, therefore,*

not change in the same time step based on this calculation. However, in EOT, the likelihood and measurement equation depend on additional inputs that vary for each measurement in a single time step. Details are given in Sec. 2.4.

Extended Object LRKF Measurement Update In the Dirac mixture approximation step (2.14) of the extended object LRKF for a sequential batch update, the noise samples need to be drawn for each of the n_u measurements individually according to

$$p\left(\underline{x}_{k|k-1}, \underline{v}_{k,1}, \ldots, \underline{v}_{k,n_u}\right) \approx \sum_{i=1}^{n_s} \alpha_{k,i} \cdot \delta\left(\begin{bmatrix} \underline{\hat{x}}_{k|k-1} \\ \underline{v}_{k,1} \\ \vdots \\ \underline{v}_{k,n_u} \end{bmatrix} - \begin{bmatrix} \underline{\boldsymbol{x}}_{k|k-1,i} \\ \underline{\boldsymbol{v}}_{k,i,1} \\ \vdots \\ \underline{\boldsymbol{v}}_{k,i,n_u} \end{bmatrix}\right). \tag{2.20}$$

In the measurement prediction step, the predicted measurement samples and predicted measurements need to be calculated individually for each measurement and sample. For the update step, the stacked predicted measurements are given according to (2.17), and the stacked predicted measurement samples can be given as

$${}^{s}\underline{\boldsymbol{y}}_{k,i} = \left[\underline{\boldsymbol{y}}_{k,i,1}^{\top}, \ldots, \underline{\boldsymbol{y}}_{k,i,n_u}^{\top}\right]^{\top}, \; i = 1 \ldots n_s. \tag{2.21}$$

The innovation covariance matrix and the equations for the update step can then be calculated using these stacked variables. The Dirac mixture approximation (2.14), the measurement prediction (2.15), and the update step (2.16) are then also repeated until all measurements are processed. The pseudo-code and further insights for the extended object LRKF sequential batch measurement update can be found in Alg. 3.1 and Sec. 3.5.

Remark 2.3. *In (2.15), the predicted measurement depends on the predicted system state and the measurement noise. Again, in EOT, the likelihood and also the measurement function depend on additional inputs that vary for each measurement in a single time step. These can then also be subject to sampling in the LRKF. Please refer to [118] and Sec. 2.4 for details.*

Remark 2.4. *In both the extended object EKF and LRKF, after each batch update, the updated state distribution is set as the new predicted state distribution for the next sequential update cycle. This procedure completes the sequential batch update recursion for EOT.*

2.4 Measurement-to-Source Association

In classical tracking applications, the objects are modeled as mathematical points. Thus, the origin of the measurement is clear, as it was generated from the point that represents the object. However, when dealing with extended objects that give rise to n_k measurements each time step, the origin of the measurement is no longer clear, as it can potentially stem from any point on the object. This unknown point is denoted as the measurement source $\underline{z}_{k,l}$ of the measurement $\underline{y}_{k,l}$. Consequently, the association problem of a measurement to the unknown measurement source is denoted as the measurement-to-source association problem, which is well-known in the literature [32, 58, 59, 145].

Once the association problem is solved, a measurement function that can be applied in the update step of the Kalman filter must be defined. In EOT, often the so-called measurement source model

$$\underline{y}_{k,l} = \underline{z}_{k,l} + \underline{v}_{k,l} \tag{2.22}$$

is applied as soon as a measurement source is specified. In this model, the measurement is a noisy record of the measurement source. Since the measurement source is naturally unknown, particular attention must be paid to the measurement-to-source association problem based on the sensors used, their resolution, and measurement noise. This section gives an overview of established approaches found in the literature for solving this association problem. In particular, the application of the association procedures not only to measurements in 2D space but also in 3D space is discussed.

2.4.1 Spatial Distribution Model

One of the first approaches developed for solving the measurement-to-source association problem is the spatial distribution model (SDM) [51, 52]. In the SDM, the likelihood can be given as

$$p\left(\underline{y}_{k,l}|\underline{x}_{k|k-1}\right) = \int \underbrace{p\left(\underline{y}_{k,l}|\underline{z}_{k,l}\right)}_{\text{sensor model}} \cdot \underbrace{p\left(\underline{z}_{k,l}|\underline{x}_{k|k-1}\right)}_{\text{source model}} \mathrm{d}\underline{z}_{k,l} \tag{2.23}$$

comprising a sensor and a source model that must be defined a priori [58, 59]. The sensor model can typically be specified using the sensor data sheet describing the noise distribution of a measurement. The source model needs to be specified, describing a probability for each point located on the object being a measurement source, given the extent or shape of the object. Then, by integrating over all possible measurement sources $\underline{z}_{k,l}$, no direct measurement-to-source association is needed in the SDM. In reality, the source model is typically unknown, which makes using an SDM challenging. In addition, the source model can change drastically in the case of partial occlusions or varying object types. In case of wrong assumptions for the source model, an estimation bias can be introduced [35].

The most popular SDM, assuming a Gaussian spatial distribution for the measurement sources, is the random matrix (RM) model [83]. It has been extended in [40] to also assume uniform distributions for the measurement sources and is directly capable of processing 2D and 3D measurements. In the case of source distributions that do not match a Gaussian or uniform distribution, a virtual measurement model can be applied that can compensate for the mismatch between the filtered extent and the present measurement distribution [C4, 72, C5]. Recent extensions of the RM approach can be found in [90, 91, 149]. Further popular spatial distribution models can, for example, be found in [61, 142].

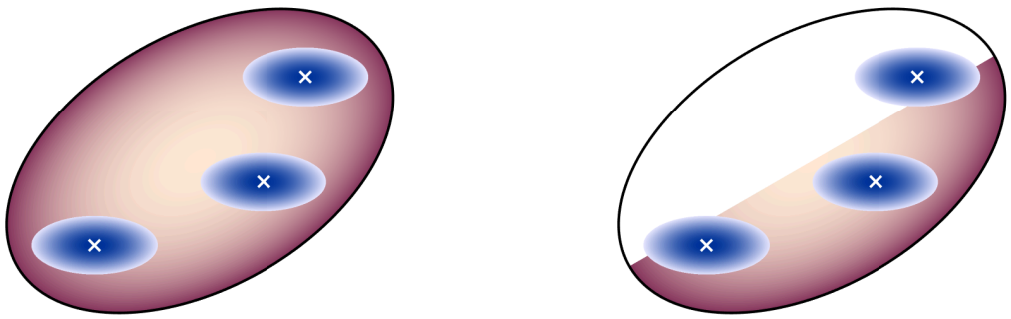

(a) Source distribution covering the full ellipse. **(b)** Source distribution covering half the ellipse.

Figure 2.1: Visualization of the spatial distribution model. Measurement noise distribution in blue and measurement source distribution in red. Measurements as white crosses.

An illustration of the SDM in 2D space can be seen in Fig. 2.1. In the figure, an ellipse is assumed as the reference shape, and three measurements are gathered from the ellipse. The noise and source distributions are color-coded with darker colors representing a higher probability density. It is assumed that the measurements mostly originate from the area close to the boundary of the ellipse in this illustration, which is often the case with sensors such as Lidar. In Fig. 2.1a, it is assumed that the object can be detected from each side. Thus, the source distribution covers the full ellipse. However, in reality, typically only the side of the object facing the sensor can be detected, which must be taken into account in the design of the source distribution, illustrated in Fig. 2.1b. In the case of partial occlusions caused by other static or dynamic objects, the source distribution would then also have to be adjusted.

Remark 2.5. *In this thesis, the SDM is not applied as a measurement-to-source association procedure. However, the likelihood (2.23) serves as a basis for the following approaches to solve the association problem.*

2.4.2 Greedy Association Model

In the greedy association model (GAM), the measurement source is greedily associated based on a predefined rule to lower the computational and modeling burden compared to the SDM. Given a predicted state, a measurement source $\underline{z}_{k,l}$ is calculated as the point on the object that most likely generated the measurement [32, 145]. A key component of this calculation is that the measurement $\underline{y}_{k,l}$ itself, in addition to the predicted system state $\hat{\underline{x}}_{k|k-1}$, is used to calculate a predicted measurement source. Starting with the likelihood (2.23) of the SDM, the likelihood of the GAM can be given as

$$p\left(\underline{y}_{k,l}|\underline{x}_{k|k-1}\right) = \int p\left(\underline{y}_{k,l}|\underline{z}_{k,l}\right) \cdot p\left(\underline{z}_{k,l}|\underline{x}_{k|k-1}\right) \mathrm{d}\underline{z}_{k,l} \tag{2.24a}$$

$$= \int p\left(\underline{y}_{k,l}|\underline{z}_{k,l}\right) \cdot \delta\left(\underline{z} - \underline{z}\left(\hat{\underline{x}}_{k|k-1}, \underline{y}_{k,l}\right)\right) \mathrm{d}\underline{z}_{k,l} \tag{2.24b}$$

$$= p\left(\underline{y}_{k,l}|\underline{z}\left(\hat{\underline{x}}_{k|k-1}, \underline{y}_{k,l}\right)\right) \tag{2.24c}$$

with $\delta\left(\underline{z} - \underline{z}\left(\hat{\underline{x}}_{k|k-1}, \underline{y}_{k,l}\right)\right)$ being the Dirac δ-distribution that peaks at the predicted measurement source $\underline{z}\left(\hat{\underline{x}}_{k|k-1}, \underline{y}_{k,l}\right)$. Given the predicted measurement source, a measurement equation can be defined as

$$\hat{\underline{y}}_{k,l} = \underline{z}\left(\hat{\underline{x}}_{k|k-1}, \underline{y}_{k,l}\right) + \underline{v}_{k,l} \tag{2.25}$$

using the measurement source model (2.22). In this model, measurements are then often assumed to be generated exclusively from the object's boundary. Two approaches are known in the literature for calculating the predicted measurement source, which are visualized in Fig. 2.2. In the following examples, these approaches are discussed in 2D space. A generalization for measurements in 3D space is discussed later in this section.

In general, the point on the object's boundary closest to the measurement can be assumed as the most probable point that generated the measurement [37]. This procedure is visualized in Fig. 2.2a. The measurement noise that can be seen in the illustration is assumed to be an additive disturbance in the measurement equation (2.25). This association procedure is referred to in this thesis as the projected association. Although the projected association yields the optimal prediction of a measurement source, an explicit closed-form calculation is often not possible. When using implicit measurement equations such as [18, 147], the estimator implicitly assumes the projected point as the measurement source.

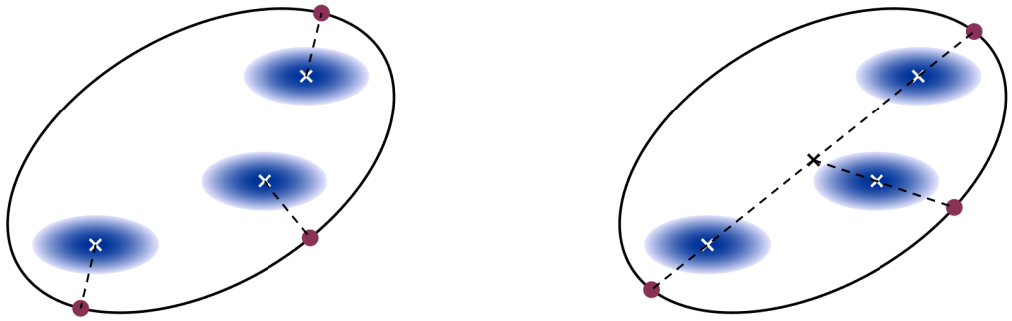

(a) Projected association. **(b)** Radial association.

Figure 2.2: Visualization of the greedy association model. Measurement noise distribution in blue and measurement sources as red balls. Measurements as white crosses.

Another possibility for approximating the unknown measurement source is to use a radial association, visualized in Fig. 2.2b. In this procedure, the intersection of the connection line between the center and the measurement with the boundary is chosen as the predicted measurement source. An advantage of the radial association is that, in most cases, a closed-form analytical expression can be found for calculating the approximated measurement source [O1, 79]. In this thesis, both association procedures are applied in the models presented in the following sections.

Example 2.1 (Circular greedy association)**.** *Given a predicted state of a circular extended object* $\hat{x}_{k|k-1} = r_{k|k-1}$ *comprising the radius, centered at the origin, and a measurement, given as* $\underline{y}_{k,l} = \left[y_{k,l}^{(x)}, y_{k,l}^{(y)}\right]^\top$*, a greedy association can be calculated using the angular parameter* $\hat{\theta}_{k,l} = \operatorname{atan2}\left(y_{k,l}^{(y)}, y_{k,l}^{(x)}\right)$*. The predicted measurement source can then be calculated as*

$$\underline{z}\left(\hat{x}_{k|k-1}, \hat{\theta}_{k,l}\right) = \left[r_{k|k-1} \cdot \cos(\hat{\theta}_{k,l}), r_{k|k-1} \cdot \sin(\hat{\theta}_{k,l})\right]^\top$$

using the parametric representation of the circle. For the circle, this association simultaneously represents the projected and the radial associated measurement source.

Approximated Projected Association In the case where no closed-form expression of the projected association in the GAM exists, a solution to calculate the closest point on the boundary can be found by approximating the boundary as a closed polygonal chain, as was proposed in [146, 147]. Given the closed polygonal chain as an approximation of the boundary, the closest point to the measurement on that boundary can then be calculated in closed form.

Definition 2.3 (Closed polygonal chain)**.** *Given a set of* n_p *points* $\{\underline{p}_1, \ldots, \underline{p}_{n_p}\}$*, a polygonal chain is formed by connecting consecutive points* $\underline{p}_j$ *and* $\underline{p}_{j+1}$ *with* $j \in \{1, \ldots, n_p\}$*. For a closed polygonal chain, the last point* $\underline{p}_{n_p}$ *and the first one* $\underline{p}_1$ *are connected as well, closing the curve.*

Example 2.2 (Ellipse polygonal chain)**.** *When approximating an ellipse as a closed polygonal chain, the parametric shape representation* $\underline{p}(\theta) = [a \cdot \cos(\theta), b \cdot \sin(\theta)]^\top$ *with* $a, b \geq 0$ *being the major and minor semi-axes, can be applied for calculating the shape points on the boundary. The parameters* $\{\theta_1, \ldots \theta_{n_p}\}$ *can be chosen equidistantly in the interval* $[0, 2\pi)$ *to finally calculate the set of points* $\{\underline{p}(\theta_1), \ldots \underline{p}(\theta_{n_p})\}$ *to form the closed polygonal chain.*

To calculate the closest point $\underline{z}_{k,l}$ on a closed polygonal chain to a measurement $\underline{y}_{k,l}$, the closest point on each line segment connecting consecutive points is calculated. Afterwards, the closest point overall is selected as the one with the smallest distance to the measurement. First, the n_p shape points $\{\underline{p}_{k,1}, \dots, \underline{p}_{k,n_p}\}$ need to be generated using the predicted system state $\hat{\underline{x}}_{k|k-1}$. The line segment connecting consecutive points can be given as

$$\underline{p}_k(u) = \underline{p}_{k,j} + u \cdot \left(\underline{p}_{k,j+1} - \underline{p}_{k,j}\right) \tag{2.26}$$

in parametric form using the parameter $u \in \mathbb{R}$. Using the dot product, the parameter u_j of the closest point on the infinite line containing the segment j to the measurement $\underline{y}_{k,l}$ can be calculated as

$$0 = \left(\underline{y}_{k,l} - \underline{p}_k(u_j)\right)^\top \cdot \left(\underline{p}_{k,j+1} - \underline{p}_{k,j}\right) \tag{2.27a}$$

$$0 = \left(\underline{y}_{k,l} - \underline{p}_{k,j} - u_j \cdot \left(\underline{p}_{k,j+1} - \underline{p}_{k,j}\right)\right)^\top \cdot \left(\underline{p}_{k,j+1} - \underline{p}_{k,j}\right) \tag{2.27b}$$

$$u_j = \frac{\left(\underline{y}_{k,l} - \underline{p}_{k,j}\right)^\top \cdot \left(\underline{p}_{k,j+1} - \underline{p}_{k,j}\right)}{\left(\underline{p}_{k,j+1} - \underline{p}_{k,j}\right)^\top \cdot \left(\underline{p}_{k,j+1} - \underline{p}_{k,j}\right)} = \frac{\left(\underline{y}_{k,l} - \underline{p}_{k,j}\right)^\top \cdot \left(\underline{p}_{k,j+1} - \underline{p}_{k,j}\right)}{\left\|\underline{p}_{k,j+1} - \underline{p}_{k,j}\right\|^2}. \tag{2.27c}$$

However, to ensure that the closest point is on the line segment itself within the closed polygonal chain and not on the extension of the line connecting two consecutive points, the parameter u_j is constrained to the interval $[0, 1]$ by applying the transformation $\tilde{u}_j = \max(\min(u_j, 1), 0)$. In doing so, the point $\underline{p}_{k,j}$ or $\underline{p}_{k,j+1}$ itself is chosen as the closest point on the segment instead of a point on the extension of the segment. Using the parameter $\tilde{u}_j$, the closest point on each segment to the measurement $\underline{y}_{k,l}$ can then be calculated as

$$\underline{z}_j = \underline{p}_{k,j} + \tilde{u}_j \left(\underline{p}_{k,j+1} - \underline{p}_{k,j}\right). \tag{2.28}$$

Given the closest points $\underline{z}_j$ for each segment, the approximated projected measurement source association can finally be calculated as

$$\underline{z}\left(\underline{x}_{k|k-1}, \underline{y}_{k,l}\right) = \underset{j \in \{1,\dots,n_p\}}{\arg\min} \left\|\underline{y}_{k,l} - \underline{z}_j\right\|. \tag{2.29}$$

The closest point on the closed polygonal chain is then the point on the segment that has the smallest distance to the measurement.

3D Greedy Association Models In this paragraph, GAMs for shape representations in 3D space are discussed. These can be described with the same likelihood derived in (2.24). Thus, a procedure for calculating a predicted measurement source must be defined in 3D space as well. Theoretically, both association procedures, the projected and the radial approach, can be applied. However, in 3D space, the projected association (i.e., finding the closest point on the boundary to the measurement) can be even harder to calculate analytically than in 2D space. Furthermore, an approximation of the boundary similar to the closed polygonal chain approximation can be highly computationally demanding in 3D space.

Therefore, radial associations are primarily presented in this paragraph for calculating a predicted measurement source. A specialized projected association can be given for shape representations in cylindrical coordinates. The procedures for calculating a radial association can differ depending on the shape representation. For shape representations in spherical coordinates, the radial association can be computed as the intersection of the line connecting the center and the measurement with the shape. This procedure is visualized in Fig. 2.3a.

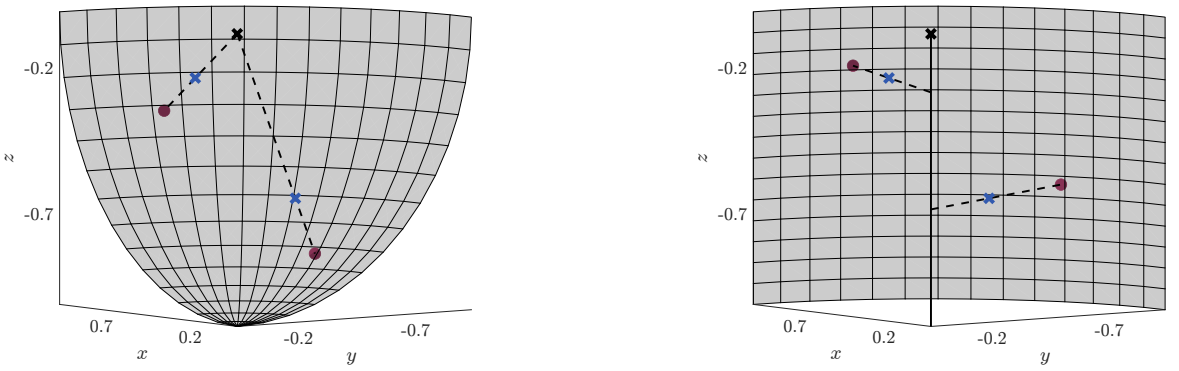

(a) Spherical 3D GAM.

(b) Cylindrical 3D GAM.

Figure 2.3: Visualization of 3D greedy association models for shape representations in spherical and cylindrical coordinates. Measurements as blue crosses, and measurement sources as red balls. Center as black cross, and shape as grey surface. Measurement sources are located on the surface.

Due to difficulties with the visualization, the measurement uncertainty is not shown in either illustration of Fig. 2.3. In the likelihood of the 3D GAM, however, the measurement uncertainty is still included. Let's consider the following example for a spherical 3D GAM.

Example 2.3 (Spherical greedy association)**.** *Given a predicted state of a spherical extended object* $\hat{x}_{k|k-1} = r_{k|k-1}$ *comprising the radius, centered at the origin, and a measurement* $\underline{y}_{k,l} = \left[y_{k,l}^{(x)}, y_{k,l}^{(y)}, y_{k,l}^{(z)}\right]^\top$*, a greedy association can be calculated using the angular parameters* $\hat{\theta}_{k,l} = \arccos\left(\frac{y_{k,l}^{(z)}}{\|\underline{y}_{k,l}\|}\right)$*, and* $\hat{\varphi}_{k,l} = \operatorname{atan2}\left(y_{k,l}^{(y)}, y_{k,l}^{(x)}\right)$*. The predicted measurement source can then be calculated as*

$$\underline{z}\left(\hat{x}_{k|k-1}, \hat{\theta}_{k,l}, \hat{\varphi}_{k,l}\right) = \begin{bmatrix} r_{k|k-1} \cdot \sin(\hat{\theta}_{k,l}) \cdot \cos(\hat{\varphi}_{k,l}) \\ r_{k|k-1} \cdot \sin(\hat{\theta}_{k,l}) \cdot \sin(\hat{\varphi}_{k,l}) \\ r_{k|k-1} \cdot \cos(\hat{\theta}_{k,l}) \end{bmatrix}$$

using the parametric representation of the sphere. Also, for the sphere, this association simultaneously represents the projected and the radial association.

For shape representations in cylindrical coordinates, the radial association that is applied in spherical coordinates cannot be used directly, as the measurement sources would then all appear on the same height section. Therefore, the radial association of a measurement source for shape representations in cylindrical coordinates is chosen as the intersection of the line connecting the center point and the measurement with the 2D shape at the same height section as the measurement. This procedure is visualized in Fig. 2.3b. For cylindrical shape representations, a projected association can also be performed using a polygonal chain approximation at a specific height section and the procedure described before, instead of a radial association. Let's consider the following example for a cylindrical 3D GAM.

Example 2.4 (Cylindrical greedy association)**.** *Given a predicted state of a cylindrical extended object* $\hat{\underline{x}}_{k|k-1} = \left[r_{k|k-1}, h_{k|k-1}\right]^\top$ *comprising the radius* $r_{k|k-1}$ *and the height* $h_{k|k-1}$*, centered at the origin at the bottom of the cylinder, and a measurement* $\underline{y}_{k,l} = \left[y_{k,l}^{(x)}, y_{k,l}^{(y)}, y_{k,l}^{(z)}\right]^\top$*, a greedy association can be calculated using the angular parameter* $\hat{\theta}_{k,l} = \arccos\left(\frac{y_{k,l}^{(z)}}{\|\underline{y}_{k,l}\|}\right)$ *and* $y_{k,l}^{(z)}$*. The predicted measurement source can then be given as*

$$\underline{z}\left(\hat{\underline{x}}_{k|k-1}, \hat{\theta}_{k,l}, y_{k,l}^{(z)}\right) = \left[r_{k|k-1} \cdot \cos(\hat{\theta}_{k,l}), r_{k|k-1} \cdot \sin(\hat{\theta}_{k,l}), \tilde{y}_{k,l}^{(z)}\right]^\top$$

using the parametric representation of the cylinder and $\tilde{y}_{k,l}^{(z)} = \min\big(\max(y_{k,l}^{(z)}, 0), h_{k|k-1}\big)$*, which guarantees that the measurement source is on the cylinder's surface. Also, for the cylinder, this association simultaneously represents the projected as well as the radial association at a specific height section.*

Both the 2D and 3D GAMs can easily be implemented using an extended object EKF or LRKF measurement update as presented before in Sec. 2.3.3. Although shape descriptions in spherical coordinates are not employed in the measurement models presented in this thesis, the comparison methods in the evaluation rely on spherical 3D GAMs, which is why the spherical case is also presented in this paragraph.

2.4.3 Random Hypersurface Model

A measurement-to-source association model that combines the advantages of the SDM and the GAM is the random hypersurface model (RHM) [13, 15, 16, 18]. In the first half of this section, the RHM is generally derived in 2D space. Following this, extensions for processing measurements in 3D space for EOT and further details are discussed. In the 2D RHM, measurements are assumed to be drawn from a scaled version of the object's boundary. In doing so, measurement sources from the object's full surface can be modeled. This can be important both for Radar [137–139, 143] and Lidar [O3, 80] data, as for both sensor devices, measurements distributed over the full surface can occur. For the derivation of the RHM, it is assumed that every point on the boundary and the interior of a specific shape can be represented using two parameters. Let's consider the following example as an illustration of such a representation.

Example 2.5 (Parametric circle representation)**.** *Given the parameters* $\theta \in [0, 2\pi)$ *and* $s \in [0, 1]$*, each point on a unit circle disk can be represented using the parametric equation*

$$\underline{z}(\theta, s) = s \cdot [\cos(\theta), \sin(\theta)]^\top.$$

Given that a point on the full surface of a specific shape can be represented using two parameters, the likelihood of the SDM (2.23) can be adjusted as [32]

$$p\left(\underline{y}_{k,l}|\underline{x}_{k|k-1}\right) = \int p\left(\underline{y}_{k,l}|\underline{z}_{k,l}\right) \cdot p\left(\underline{z}_{k,l}|\underline{x}_{k|k-1}\right) \mathrm{d}\underline{z}_{k,l} \tag{2.30a}$$

$$= \int\int p\left(\underline{y}_{k,l}|\underline{z}\left(\theta_{k,l}, s_{k,l}\right)\right) \cdot p\left(\theta_{k,l}, s_{k,l}|\underline{x}_{k|k-1}\right) \mathrm{d}\theta_{k,l}\, \mathrm{d}s_{k,l} \tag{2.30b}$$

using the joint distribution of $\theta_{k,l}$, and $s_{k,l}$. Subsequently, the parameters are modeled differently. To achieve this, it is assumed that the parameters are independent of each other. Then the association of the parameter $\theta_{k,l}$ is modeled as a GAM and the association of the parameter $s_{k,l}$ as an SDM. The final likelihood of the RHM can then be given as

$$p\left(\underline{y}_{k,l}|\underline{x}_{k|k-1}\right) = \int\int p\left(\underline{y}_{k,l}|\underline{z}\left(\theta_{k,l}, s_{k,l}\right)\right) \cdot p\left(\theta_{k,l}|\underline{x}_{k|k-1}, s_{k,l}\right) \cdot p\left(s_{k,l}|\underline{x}_{k|k-1}\right) \mathrm{d}\theta_{k,l}\, \mathrm{d}s_{k,l} \tag{2.31a}$$

$$= \int\int p\left(\underline{y}_{k,l}|\underline{z}\left(\theta_{k,l}, s_{k,l}\right)\right) \cdot \delta\left(\theta - \hat{\theta}_{k,l}(\hat{\underline{x}}_{k|k-1}, \underline{y}_{k,l})\right) \cdot p\left(s_{k,l}|\underline{x}_{k|k-1}\right) \mathrm{d}\theta_{k,l}\, \mathrm{d}s_{k,l} \tag{2.31b}$$

$$= \int p\left(\underline{y}_{k,l}|\underline{z}\left(\hat{\theta}_{k,l}(\hat{\underline{x}}_{k|k-1}, \underline{y}_{k,l}), s_{k,l}\right)\right) \cdot p\left(s_{k,l}|\underline{x}_{k|k-1}\right) \mathrm{d}s_{k,l} \tag{2.31c}$$

with $\hat{\theta}_{k,l}(\hat{\underline{x}}_{k|k-1}, \underline{y}_{k,l})$ being the greedy association for the parameter $\theta_{k,l}$ depending on the predicted system state $\hat{\underline{x}}_{k|k-1}$, and the measurement $\underline{y}_{k,l}$ [32, 145]. Given the predicted measurement source parametrization, a measurement equation can be defined as

$$\hat{\underline{y}}_{k,l} = \underline{z}\left(\hat{\theta}_{k,l}(\hat{\underline{x}}_{k|k-1}, \underline{y}_{k,l}), s_{k,l}\right) + \underline{v}_{k,l} \tag{2.32}$$

using the measurement source model (2.22). The principle of the RHM that was derived in the likelihood (2.31) is also visualized in the following figure. In Fig. 2.4a, the measurement-to-

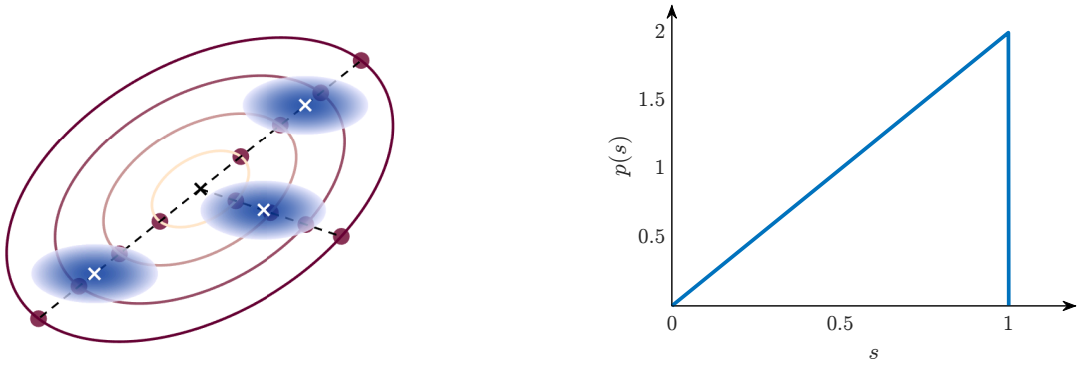

(a) Random hypersurface model illustration. **(b)** Scaling factor distribution.

Figure 2.4: Visualization of the random hypersurface model and the scaling factor distribution. Measurement noise distribution in blue, measurement sources as red balls, and scaled ellipse boundaries as elliptic curves. Measurements as white crosses.

source association as a combination of a GAM and an SDM is visualized. The measurements are greedily associated with scaled versions of the object's boundary. The scaled versions of the object's boundary are color-coded, representing the probability distribution of the scaling factor with higher probabilities for darker colors. The distribution of the scaling factor is visualized in Fig. 2.4b. In the figure, explicit measurement-to-source associations using a radial association for the angle are visualized. The scaling factors for the boundary are drawn with a predefined probability. If no prior knowledge about the distribution of the scaling factor is available, it can be chosen to resemble a uniform distribution of the measurement sources over the whole extent. In this case, the probability density function of the scaling factor linearly scales with the perimeter of the object and can be chosen as a triangular distribution [15], which is visualized in Fig. 2.4b.

Inference using LRKFs In comparison to the GAM, an integral must be solved for the likelihood of the RHM in the update step of the filter. In most cases, this integral cannot be solved analytically. An efficient solution to the inference problem when implementing an RHM is to apply LRKFs and sample the scaling factor in the update step [117]. In the Dirac mixture step (2.14) of the extended object LRKF for a sequential batch update, the noise samples and the scaling samples need to be drawn for every measurement individually according to

$$p\left(\underline{x}_{k|k-1}, \underline{v}_{k,1}, \ldots, \underline{v}_{k,n_u}, s_{k,1}, \ldots, s_{k,n_u}\right) \approx \sum_{i=1}^{n_s} \alpha_{k,i} \cdot \delta\left(\begin{bmatrix} \underline{x}_{k|k-1} \\ \underline{v}_{k,1} \\ \vdots \\ \underline{v}_{k,n_u} \\ s_{k,1} \\ \vdots \\ s_{k,n_u} \end{bmatrix} - \begin{bmatrix} \underline{\boldsymbol{x}}_{k|k-1,i} \\ \underline{\boldsymbol{v}}_{k,i,1} \\ \vdots \\ \underline{\boldsymbol{v}}_{k,i,n_u} \\ \boldsymbol{s}_{k,i,1} \\ \vdots \\ \boldsymbol{s}_{k,i,n_u} \end{bmatrix}\right). \tag{2.33}$$

In the measurement prediction step, the predicted samples and the predicted measurements again need to be calculated individually for each measurement and sample. Afterwards, stacked predicted measurements and stacked predicted measurement samples can be generated to perform the measurement update.

Remark 2.6. *For measurements in 2D space, RHMs are not applied in this thesis since measurements from the interior are modeled using the RAMN estimation discussed in Sec. 2.6. However, a redefinition of the RHM to apply the approach to 3D measurements, described in the following section, is used.*

3D Random Hypersurface Models When processing measurements in 3D space, a shape in cylindrical coordinates can be defined by applying extrusions [33, 145]. Thus, the 3D shape is constructed by extruding a base shape to a specific height. These extrusions can be defined using fixed or varying base shapes in the vertical direction [38, 148]. Let's consider the following example for a shape definition with a fixed base shape.

Example 2.6 (Parametric cylinder representation)**.** *Given the parameters $\theta \in [0, 2\pi)$ and $s \in [0, 1]$, each point on the boundary of a unit cylinder with height h can be represented using the parametric equation*

$$\underline{z}(\theta, s) = [\cos(\theta), \sin(\theta), s \cdot h]^\top.$$

The center is then located at the bottom of the cylinder.

A measurement-to-source association can then be defined using a 3D GAM for cylindrical shapes as described in Sec. 2.4.2. However, it has been shown that a GAM can produce biased height estimates due to a missing penalization mechanism for overestimated heights [32, 34]. To solve this issue, the RHM method can be used to estimate the extrusion in an extrusion random hypersurface model (ERHM). For the ERHM, the likelihood is identical to the 2D RHM likelihood (2.31). In the measurement equation of the ERHM, the measurement source on a plane curve at a fixed height is associated using a GAM. The extrusion is modeled using the multiplicative extrusion factor s. The measurement equation is then given as

$$\begin{bmatrix} \hat{\underline{y}}_{k,l}^{(xy)} \\ \hat{y}_{k,l}^{(z)} \end{bmatrix} = \begin{bmatrix} \underline{z}^{(xy)}\left(\hat{\theta}_{k,l}(\hat{\underline{x}}_{k|k-1}, \underline{y}_{k,l}^{(xy)})\right) + \underline{v}_{k,l}^{(xy)} \\ s_{k,l} \cdot h_{k|k-1} + v_{k,l}^{(z)} \end{bmatrix} \tag{2.34}$$

with (xy) representing xy coordinates of the measurement, the measurement source, and the measurement noise, and (z) the z coordinates respectively. The variable $h_{k|k-1}$ represents the predicted height at time step k. The measurement-to-source association on a 2D height section can be solved using a 2D GAM presented in Sec. 2.4.2. However, it was shown in [14] that the nonlinear Kalman filter is not able to estimate the position in the z direction and the height simultaneously when the height section is modeled using a multiplicative factor [49] as in Ex. 2.6. In this case, the height is not observable by the nonlinear Kalman filter. As a solution, a quadratic extension of the measurement equation, given as

$$\begin{bmatrix} \hat{\underline{y}}_{k,l}^{(xy)} \\ \hat{y}_{k,l}^{(z)} \\ \hat{y}_{k,l}^{(z)^2} \end{bmatrix} = \begin{bmatrix} \underline{z}^{(xy)}\left(\hat{\theta}_{k,l}(\hat{\underline{x}}_{k|k-1}, \underline{y}_{k,l})\right) + \underline{v}_{k,l}^{(xy)} \\ s_{k,l} \cdot h_{k|k-1} + v_{k,l}^{(z)} \\ \left(s_{k,l} \cdot h_{k|k-1} + v_{k,l}^{(z)}\right)^2 \end{bmatrix}. \tag{2.35}$$

can be introduced [14]. Using this extension, the height is again observable in the Kalman filter. However, due to the low sampling rate coverage of the UKF, an S2KF must be applied

for inference using the quadratic extension. Besides that, the same procedure for sampling the multiplicative extrusion factor in the LRKF compared to the RHM in the 2D case can be applied.

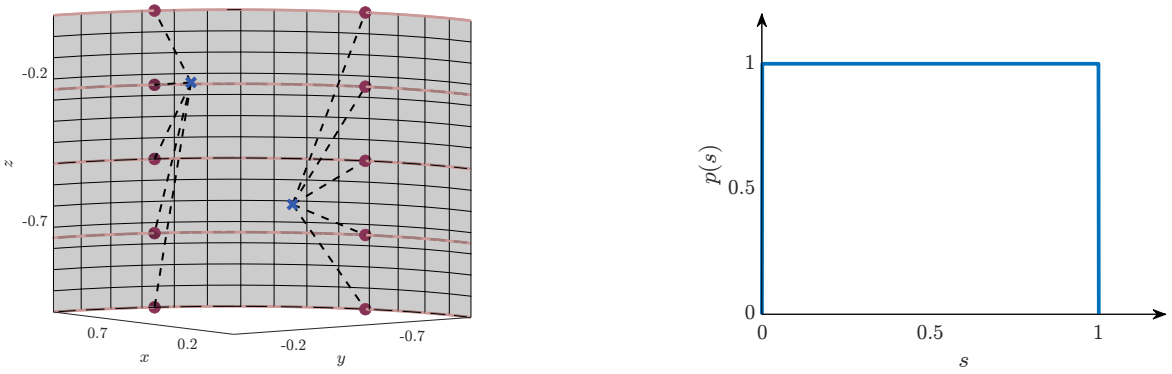

(a) 3D random hypersurface model illustration.

(b) Scaling factor distribution.

Figure 2.5: Visualization of the 3D random hypersurface model and the scaling factor distribution. Measurements as blue crosses, measurement sources as red balls, height sections as red curves, and cylinder surface in grey.

The principle of the ERHM is visualized in Fig. 2.5a. The measurements are associated with sampled height sections instead of scaled versions of the boundary of a 2D shape. If no prior knowledge of the distribution of the extrusion factor is available, a uniform distribution can be applied, which is visualized in Fig. 2.5b. Due to the applied uniform distribution of the extrusion factor, sampled height sections are represented using the same color. In the LRKF, this uniform distribution can then be approximated by a Gaussian distribution.

Symmetric 3D Random Hypersurface Models When assuming a uniformly distributed multiplicative extrusion factor in the ERHM and thus a planar symmetry to the xy plane in the z direction, these symmetry features can be included in the shape estimation procedure. In [32, 36], the likelihoods of the RHM and the ERHM are generally derived for rotoreflections, with planar symmetry as a special case. Using planar symmetry in the z direction, a symmetrical 3D shape in cylindrical coordinates can be defined using a non-redundant part and a redundant part constructed by reflection. Let's consider the following example for a shape definition with planar symmetry.

Example 2.7 (Parametric symmetric cylinder representation)**.** *Given the parameters $\theta \in [0, 2\pi)$, and $s \in [0, 1]$, each point on the boundary of a unit cylinder with height h can be represented using the parametric equation*

$$\underline{z}(\theta, s) = \left[z^{(xy)}(\theta), |z^{(z)}(s)|\right]^\top = \left[\cos(\theta), \sin(\theta), s \cdot \frac{h}{2}\right]^\top. \tag{2.36}$$

The center is then located in the middle of the cylinder.

The integration of symmetry assumptions in the estimation procedure has several advantages. First of all, the complexity of the estimator can be reduced since measurements are only associated with a portion of the shape. However, much more importantly, the height and the position in the z direction are again observable by the Kalman filter [32]. Thus, the quadratic extension that was introduced before in the estimation procedure of the ERHM can be dropped when introducing a planar symmetry in the shape definition.

The likelihood of the symmetrical ERHM is identical to the 2D RHM (2.31) when defining the likelihood only in the non-redundant part of the shape [36]. Overestimated heights are still penalized in the symmetrical ERHM. The height estimate will be unbiased when assuming a distribution for the extrusion factor s that is actually present in the measurements. In the measurement equation, measurement sources on a 2D height section are still associated using a GAM. The extrusion is modeled using the extrusion factor s in the non-redundant part. The measurement equation is then given as

$$\begin{bmatrix} \hat{\underline{y}}_{k,l}^{(xy)} \\ |\hat{y}_{k,l}^{(z)}| \end{bmatrix} = \begin{bmatrix} \underline{z}^{(xy)} \left(\hat{\theta}_{k,l}(\hat{\underline{x}}_{k|k-1}, \underline{y}_{k,l}) \right) + \underline{v}_{k,l}^{(xy)} \\ s_{k,l} \cdot \frac{h_{k|k-1}}{2} + v_{k,l}^{(z)} \end{bmatrix} \tag{2.37}$$

with the absolute value in the z direction, transforming the measurements to the non-redundant part in the positive direction. In this equation, the origin of the local coordinate system is positioned at the shape's center. Due to the planar symmetry assumption, the effective sample resolution is increased when sampling the extrusion factors in the LRKF. Samples are only drawn within the non-redundant part of the object, so the entire shape can be represented by sampling the extrusion factor for only half of the shape, effectively doubling the resolution of the samples for the given computational effort. As a result, an UKF can be applied for inference instead of requiring an S2KF.

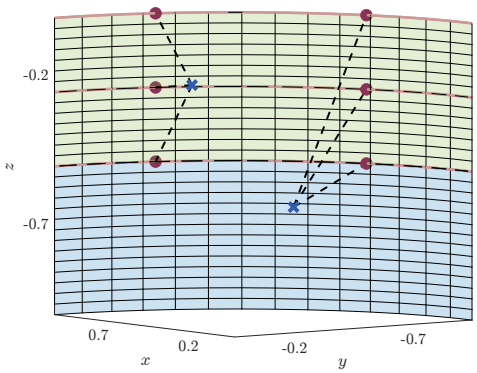

Figure 2.6: Visualization of the 3D symmetrical random hypersurface model. Measurements as blue crosses, measurement sources as red balls, and height sections as red curves. The non-redundant part is the green surface, and the redundant part is the blue surface.

The principle of the symmetrical ERHM is visualized in Fig. 2.6. The measurements are only associated with sampled height sections on the non-redundant part. The distribution of the extrusion factor must be symmetrical as well. If no prior knowledge of the distribution of the extrusion factor is available, again, a uniform distribution can be applied.

2.5 Interval Constraints in Extended Object Tracking

In EOT, one issue is often the fact that extent or shape parameters are subject to interval constraints. When estimating extent parameters such as length, width, and height, for example, the estimates should always be positive. In standard nonlinear Kalman filtering, interval constraints cannot be considered, since a Gaussian distribution, used to represent the state distribution, has an unbounded domain. In the literature, several approaches can be found to modify nonlinear Kalman filtering to handle state interval constraints. In [113] and [140], general procedures for applying linear and nonlinear constraints, respectively, to the Kalman filter are presented. In [120], several algorithms to incorporate interval constraints in the UKF

can be found. In this thesis, a simple approach that allows the nonlinear Kalman filter to estimate mixed constrained and unconstrained variables is used.

The key idea is to define monotonically increasing state transformation functions that have an unbounded domain and a bounded codomain. The filter then operates on the unconstrained state variables, which are transformed back through these functions before using the parameters in the physical model or before using the filter estimate in an evaluation. Thus, within the Kalman filter, unconstrained variables are estimated, while they are embedded in a constrained environment outside the filter. By applying monotonically increasing transformation functions, a unique assignment between constrained and unconstrained variables is ensured. This approach leads to a very efficient and effective method for handling state interval constraints without changing the Kalman filtering procedure. Moreover, the approach is independent of the chosen nonlinear Kalman filter, such as the EKF, LRKFs, or others that can be found in the literature.

To extract the uncertainties of the constrained state variables after the update step of the nonlinear Kalman filter, sampling methods such as the unscented transform can be applied [130]. The samples can be drawn from the estimated state distribution and propagated through the corresponding transformation functions. The constrained mean vector can be determined directly using the transformation functions. The covariance matrix of the constrained state estimate can then be calculated using (2.13c). Since the transformation functions are smooth, the accuracy of these propagated covariance estimates is expected to be consistent with the general accuracy achieved by the UKF [77] when using the unscented transform.

As transformation functions, activation functions that are often used in classical neural network design can be applied [92]. In this thesis, two different interval constraints are considered, for which two different transformation functions c_1 and c_2 are needed to transform the respective parameters to a bounded codomain.

One-sided Constraints The first class of interval constraints that can occur in state estimation are constraints that have only a lower or an upper bound. Thus, the state estimates $\hat{x}_k$ are intended to be within the interval $\hat{x}_k \in [a, \infty]$ for constraints with a lower bound or within the interval $\hat{x}_k \in [-\infty, a]$ for constraints with an upper bound. A transformation function that can map to these bounds is the *softplus* function [28], often applied as an activation function in neural networks. The transformation function that can be defined using the *softplus* function for these constraints is termed the *one-sided* transformation function in the further course of this thesis. It can be given as

$$\tilde{x}_k = c_1(\hat{x}_k, a) = \begin{cases} \log(1 + \exp(\hat{x}_k)) + a & \text{if } a \text{ is lower bound} \\ -\log(1 + \exp(\hat{x}_k)) + a & \text{if } a \text{ is upper bound} \end{cases} \tag{2.38}$$

with the distinction of whether a is an upper or lower bound. This transformation function generates constrained values $\tilde{x}_k$ from unconstrained values $\hat{x}_k$ with either a lower or an upper bound.

Two-sided Constraints The second class of interval constraints that can occur in state estimation are constraints that have a lower and an upper bound. Thus, the state estimates $\hat{x}_k$ are intended to be within the interval $\hat{x}_k \in [a, b]$. A transformation function that can map to these bounds is the *logistic* function [92], also often applied as an activation function in neural networks. The transformation function that can be defined using the *logistic* function for these constraints is termed the *two-sided* transformation function in the further course of this thesis. It can be given as

$$\tilde{x}_k = c_2(\hat{x}_k, a, b) = \frac{b - a}{1 + \exp(-\hat{x}_k)} + a \tag{2.39}$$

with a being the lower bound and b the upper bound. The transformation function generates constrained values $\tilde{x}_k$ from unconstrained values $\hat{x}_k$ with both a lower and an upper bound.

2.6 Recursive Artificial Measurement Noise Estimation

In the previous sections, techniques were presented to process measurements from the boundary of an object. In real-world applications, however, measurements often occur as a mixture of boundary and interior points. In [80], the spatial distribution of LiDAR measurements is investigated by calculating the distribution of an RHM scaling parameter under an assumed radial measurement source association for multiple instances of real-world objects. It is seen that many measurements stem from the boundary of the object, but also that the assumption of a uniformly distributed squared scaling factor, which is frequently made in RHMs, is often not valid for real-world measurements. In the literature, a mixture of boundary and interior measurement source distributions is often not considered explicitly. For comparison, in studies such as [40, 142] and also in the RHM approach [17, 18], measurement sources are assumed to be distributed uniformly over the object's extent. Furthermore, in models such as [O1, 79], it is assumed that measurements originate exclusively from the object's boundary. In [137, 138], the measurement source distribution is modeled as a truncated Gaussian, processing measurements either gathered from the boundary or the interior of the object. In [72], measurements are assumed to be generated either from the boundary or uniformly distributed over the whole extent. The RM estimate is then corrected using an adaptation loop and virtual measurements generated from both the boundary and the interior.

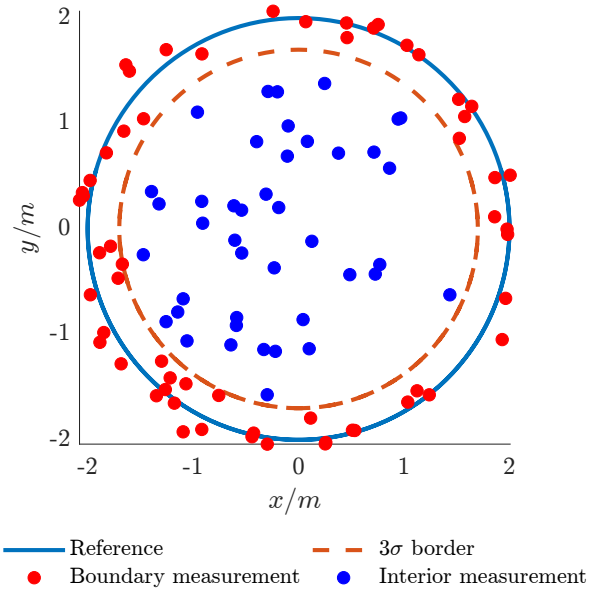

Figure 2.7: Visualization of the measurement separation for the RAMN estimation.

The solution proposed in [80] is to use a measurement equation for boundary measurements and heuristically calculate an asymmetric measurement noise variance for measurements inside the predicted object boundary. In this thesis, the approach presented in [80] is adopted, but the distribution of an artificial measurement noise for measurements that lie within the boundary is recursively estimated, rather than heuristically setting a specific value only for the variance. Furthermore, the association of measurements to the boundary is extended by assigning measurements in a $3\sigma_{\underline{v}}$ surrounding of the boundary to the set of boundary measurements, which takes into account the additive measurement noise with standard deviation $\sigma_{\underline{v}}$. An

illustration of the separation of the measurement set for a circular extended object can be seen in Fig. 2.7. In this simulation, measurements are either drawn from the boundary or uniformly distributed from the interior of the circle. The artificial measurement noise estimation approach can be applied to measurement models in 2D and 3D space, as will be seen in this thesis. Determining whether a measurement lies within a predicted boundary can often be calculated efficiently using implicit shape functions. Let's consider the following example as an illustration.

Example 2.8 ("Inside-outside" circle function)**.** *Given a predicted extent state describing a circle centered at the origin and $\hat{x}_{k|k-1} = r_{k|k-1}$ with radius $r_{k|k-1}$, a measurement $\underline{y}_{k,l}$, and the measurement noise standard deviation $\sigma_{\underline{v}}$, the function*

$$\mathcal{I}(\underline{y}_{k,l}, \hat{x}_{k|k-1}, \sigma_{\underline{v}}) = \|\underline{y}_{k,l}\| - (r_{k|k-1} - 3 \cdot \sigma_{\underline{v}}) = \begin{cases} > 0: & \textit{outside} \\ = 0: & 3\sigma_{\underline{v}} \textit{ boundary} \\ < 0: & \textit{inside} \end{cases} \tag{2.40}$$

determines whether the measurement $\underline{y}_{k,l}$ lies inside the predicted circle but outside the $3\sigma_{\underline{v}}$ border, on the $3\sigma_{\underline{v}}$ border, or outside the boundary.

For measurements inside the boundary and outside the $3\sigma_{\underline{v}}$ border, the artificial measurement noise parameters are then calculated. The "inside-outside" information can be calculated using each shape description applied in this thesis and is added to each measurement model after presenting a measurement equation for measurement sources located on the boundary of the shape.

2.6.1 Derivation

For the calculation of the RAMN, an anisotropic behavior is expected, and measurements in each coordinate axis are assumed to be generated from the same measurement-generating process rather than using a heuristic variance for each measurement. Therefore, the full Gaussian distribution for each coordinate direction is calculated below. The RAMN is calculated using the Euclidean distance between each predicted measurement source $\hat{\underline{z}}_{k,l}^{(i)}$ and the respective measurement $\underline{y}_{k,l}^{(i)}$ for each time step up to k. In this notation, the superscript i represents measurements and measurement sources inside the shape and outside the $3\sigma_{\underline{v}}$ surrounding. Due to the expected anisotropic behavior of the artificial measurement noise, its parameters are calculated for each coordinate direction separately. Therefore, the shortcut $d_{k,l}^{(i,\eta)}$ is used for the Euclidean distance in coordinate direction η between measurement source $\hat{\underline{z}}_{k,l}^{(i)}$ and measurement $\underline{y}_{k,l}^{(i)}$. Using the standard maximum likelihood estimator, the estimated mean of the artificial measurement noise can be given as

$$\hat{\mu}_k^{(i,\eta)} = \frac{1}{\Sigma_k^{(i)}} \sum_{m=1}^{k} \sum_{l=1}^{n_k^{(i)}} d_{m,l}^{(i,\eta)} \tag{2.41}$$

using measurements up to time step k. The notation $\Sigma_k^{(i)} := \sum_{l=1}^{k} n_l^{(i)}$ indicates the number of measurements inside the boundary and outside the $3\sigma_{\underline{v}}$ surrounding from time step 1 to k summed up. In each time step k, $n_k^{(i)}$ measurements are assumed to be inside the shape and outside the $3\sigma_{\underline{v}}$ surrounding. Following this, the respective variance can be calculated as

$$\hat{\mathrm{v}}_k^{(i,\eta)} = \frac{1}{\Sigma_k^{(i)}} \sum_{m=1}^{k} \sum_{l=1}^{n_k^{(i)}} \left(d_{m,l}^{(i,\eta)} - \hat{\mu}_k^{(i,\eta)} \right)^2 \tag{2.42}$$

also using the standard maximum likelihood estimator. In this calculation, however, distances from time step 1 up to k need to be saved. As a solution, recursive estimators for the mean and the variance can be calculated as

$$\hat{\mu}_k^{(i,\eta)} = \frac{\Sigma_{k-1}^{(i)}}{\Sigma_{k-1}^{(i)} + n_k^{(i)}} \hat{\mu}_{k-1}^{(i,\eta)} + \frac{1}{\Sigma_k^{(i)}} \sum_{l=1}^{n_k^{(i)}} d_{k,l}^{(i,\eta)}, \tag{2.43a}$$

$$\hat{\mathrm{v}}_k^{(i,\eta)} = \frac{\Sigma_{k-1}^{(i)}}{\Sigma_{k-1}^{(i)} + n_k^{(i)}} \hat{\mathrm{v}}_{k-1}^{(i,\eta)} + \frac{1}{\Sigma_k^{(i)}} \sum_{l=1}^{n_k^{(i)}} \left(d_{k,l}^{(i,\eta)} - \hat{\mu}_k^{(i,\eta)} \right)^2. \tag{2.43b}$$

In these recursive estimators, measurements from the first and the last time step equally contribute to the noise estimation. This is, however, not preferable as the distribution can vary over time, e.g., when the viewing angle of the object changes. Therefore, a forgetting factor τ similar to [C2, C3] is introduced that can be interpreted as the effective memory length in terms of the number of measurements from the past that still contribute to the recursive noise distribution estimation. The final recursive estimators of the artificial measurement noise distribution are then given as

$$\hat{\mu}_k^{(i,\eta)} = \frac{\tau}{\tau + n_k^{(i)}} \hat{\mu}_{k-1}^{(i,\eta)} + \frac{1}{\tau + n_k^{(i)}} \sum_{l=1}^{n_k^{(i)}} d_{k,l}^{(i,\eta)}, \tag{2.44a}$$

$$\hat{\mathrm{v}}_k^{(i,\eta)} = \frac{\tau}{\tau + n_k^{(i)}} \hat{\mathrm{v}}_{k-1}^{(i,\eta)} + \frac{1}{\tau + n_k^{(i)}} \sum_{l=1}^{n_k^{(i)}} \left(d_{k,l}^{(i,\eta)} - \hat{\mu}_k^{(i,\eta)} \right)^2. \tag{2.44b}$$

The following sections and chapters provide details on the application of the recursively estimated artificial measurement noise.

2.6.2 Experiments

This section investigates the RAMN estimation in more detail before applying it to the measurement models for maritime object tracking. First, the approach is applied to a circular extended object where measurements are generated from the boundary and the interior. Then, the forgetting factor τ is examined in a simulation study to spot a trade-off value that balances the adaptability of the RAMN over time and the consistency of the estimate.

Circular Extended Object In this paragraph, the estimation of the state of a static circular extended object is investigated. Therefore, a set of $n_k = 50$ measurements of the circle with a standard deviation of $\sigma_{\underline{v}} = 0.1\text{m}$ for the additive measurement noise is simulated over 100 time steps. In this simulation, measurements are drawn from the boundary of the circle with a probability of 0.7 and uniformly distributed over the whole extent with a probability of 0.3. The system state to be estimated comprises the 2D position $\underline{m}_k$ and the radius r_k, which together completely define the state of the static circle.

In the investigation, three different filters are compared to get an overview of the performance of the RAMN estimation. The target circle has a reference position of $\underline{m}_{\text{ref}} = [2, 1]^\top\text{m}$ and a reference radius of $r_{\text{ref}} = 2\text{m}$. The system state is initialized using the mean of the first measurement set for the position, while the radius is initialized to be 1m. The filters to be compared are the following:

Circular GAM with RAMN estimation: For this filter, the measurement equation presented in Ex. 2.1 together with an UKF presented in Sec. 2.3 with $n_u = n_k$ is applied. The "inside-outside"

information for circle measurements can be calculated using the implicit equation presented in Ex. 2.8. Therefore, the measurements must be transformed to a local coordinate system. After calculating the RAMN parameters using a forgetting factor of $\tau = 200$, the measurement noise mean and covariance matrix can be generated as

$$\hat{\underline{\mu}}_{\underline{v}_{k,l}} = \begin{cases} \left[\hat{\mu}_k^{(i,x)}, \hat{\mu}_k^{(i,y)}\right]^\top & \text{if inside} \\ [0,0]^\top & \text{else} \end{cases}, \tag{2.45a}$$

$$\mathbf{\Sigma}_{\underline{v}_{k,l}} = \begin{cases} \operatorname{diag}\left(\hat{\mathrm{v}}_k^{(i,x)}, \hat{\mathrm{v}}_k^{(i,y)}\right) & \text{if inside} \\ \operatorname{diag}(\sigma_{\underline{v}}^2, \sigma_{\underline{v}}^2) & \text{else} \end{cases} \tag{2.45b}$$

for each measurement individually. The stacked measurement noise covariance matrix for the sequential batch update is given by (2.19). The artificial measurement noise mean is added to the predicted measurement. In this implementation, the measurement noise is not sampled but rather directly processed as an additive noise in the LRKF.

Circular RHM: For comparison, a circular RHM is implemented where the scaling factor resembles a uniform distribution over the circular extent. The parameters of the approximated Gaussian distribution for the scaling factor are then given as $\mu_s = \frac{2}{3}$ for the mean value and $\sigma_s^2 = \frac{1}{18}$ for the variance. As a measurement equation, the implicit equation of Ex. 2.8 can be modified as

$$\begin{aligned} 0 &= \|\underline{z}_{k,l} - \underline{m}_{k|k-1}\| - s \cdot r_{k|k-1} \\ &= \|\underline{y}_{k,l} - \underline{v}_{k,l} - \underline{m}_{k|k-1}\| - s \cdot r_{k|k-1} \end{aligned} \tag{2.46}$$

using the measurement source model (2.22). The measurement model can also be implemented using an extended object LRKF presented in Sec. 2.3. In this implementation, the measurement noise $\underline{v}_{k,l}$ and the scaling parameter s must be sampled.

Circular GAM using only boundary measurements: For this filter, the "inside-outside" information and the distance to the circle are used to discard measurements that are not associated with the boundary of the circle. The remaining measurements are assumed to fit the circular GAM presented in Ex. 2.1. The filter is also implemented using an UKF. For comparison, two versions of the filter are implemented. The first implementation applies the same initialization that is used for the other two filters. The second implementation assumes that a perfect initialization (PI) is given as prior knowledge using the reference values of the circle.

The results of the simulation study can be seen in Fig. 2.8 with the root mean square errors (RMSEs) of a Monte Carlo (MC) simulation with 100 runs in Fig. 2.8a and a qualitative estimation result at the end of the first MC run in Fig. 2.8b. In both figures, it can be seen that the RHM fails to estimate the correct radius of the circle due to the mismatch of the assumed distribution of the scaling factor with the actual spatial distribution of the measurements. The GAM only using boundary measurements fails to estimate the correct position and the radius of the circle. The incorrect initialization of the filter leads to discarding the wrong measurements, and the filter converges to the wrong values. On the other hand, with a perfect initialization using the reference, the GAM only using boundary measurements converges to the true circular values. However, it is very unlikely that the reference values are given when initializing the filter.

In this simulation, only the GAM with RAMN estimation converges to the true value without prior knowledge of the initialization of the filter. This result is remarkable since it must be assumed that measurements can potentially be associated wrongly with either the boundary

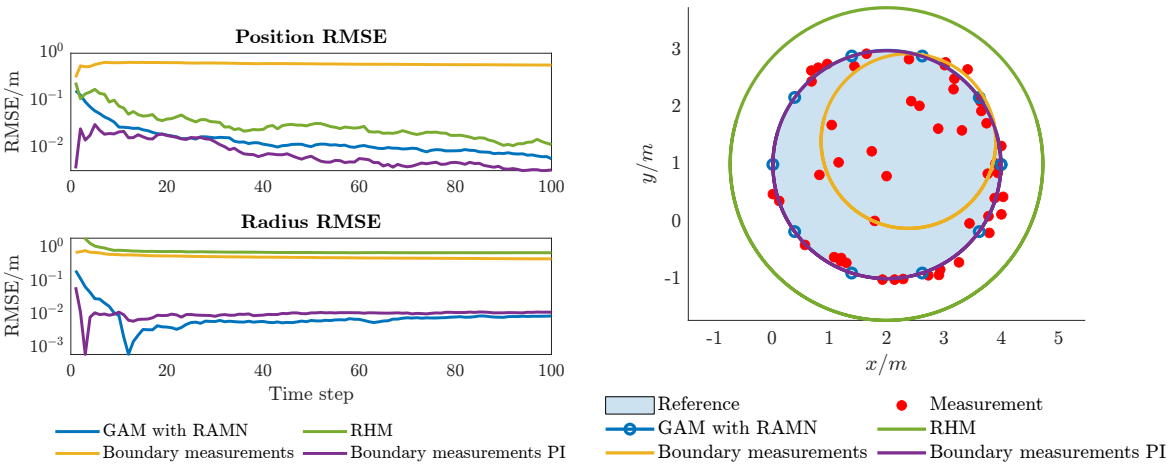

(a) Estimation RMSEs.

(b) Qualitative results.

Figure 2.8: Qualitative and quantitative results of circular EOT investigating the RAMN estimation procedure.

or the interior of the object. In [80], it is stated that if measurements are wrongly associated with the boundary, they must be outside the too-small estimated predicted object state, and the lower measurement noise due to the boundary association results in a stronger correction of the boundary towards the measurement. On the other hand, if measurements are wrongly associated with the interior, they must be inside the too-large estimated predicted object state. The measurement noise is then set too high due to the interior association, and the state converges more slowly to the true state. However, the state can converge to the true state, which is not the case for an RHM when assuming the wrong distribution of the scaling factor. In contrast to [80], measurements in a $3\sigma_{\underline{v}}$ surrounding of the boundary are also associated with the boundary in this thesis, which further expedites the convergence to the true state.

Forgetting Factor Investigation In this paragraph, the forgetting factor τ that is applied in the derivation of the RAMN is investigated in more detail. Especially, the impact of the forgetting factor on the adaptability of the measurement noise is investigated. Therefore, a simulation study is performed where Gaussian-distributed random samples are generated from a distribution that suddenly alters in a single time step. Therefore, 500 measurements per time step are generated. In the first 150 time steps, the samples are generated from a Gaussian distribution with mean $\mu_1 = 0.1$ and standard deviation $\sigma_1 = 0.1$. After 150 time steps, the distribution suddenly changes to a Gaussian distribution with mean $\mu_2 = 0.2$ and $\sigma_2 = 0.2$. This drastic change is an unrealistic event in real-world scenarios since the distribution would likely change more smoothly with a certain type of transition. However, this example illustrates the behavior of the RAMN estimation for altering distributions.

The mean values of a MC simulation with 100 runs are shown in Fig. 2.9. The same scenario is investigated for different forgetting factors $\tau \in \{10, 50, 100, 200, 500, 100, 2000\}$ using the estimator of (2.44) and for the recursive estimator of (2.43) that does not apply any forgetting factor. The figure shows that the estimator that does not apply a forgetting factor very slowly adapts to the new distribution. When introducing a forgetting factor, the mean value almost immediately adapts to the new value for lower values of τ. The adaptability slightly decreases for higher values of τ but is still present. When estimating the standard deviation of an altered Gaussian distribution, the estimator that does not apply any forgetting factor shows a similar behavior compared to the estimator for the mean value. When introducing a forgetting factor, the standard deviation only adapts directly for very low values such as $\tau \in \{10, 50\}$. For higher

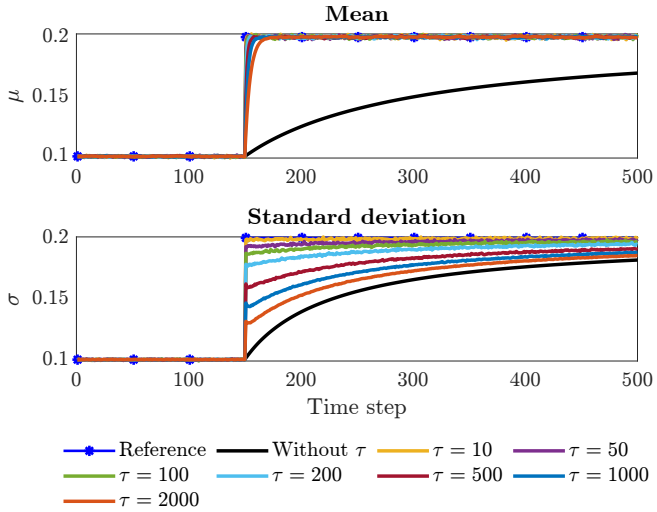

Figure 2.9: Investigation on the adaptability of the forgetting factor τ.

values such as $\tau \in \{100, 200\}$, the standard deviation adapts to the new value. However, it requires a few time steps. For $\tau \in \{500, 1000, 2000\}$, the standard deviation does not adapt completely to the new value anymore. To summarize, the choice of the forgetting factor τ is a trade-off between responsiveness to changes in the artificial measurement noise and stability. If the value is too low, the noise estimate reacts to every small change, which could also be caused by random, volatile effects. If the value is too high, the noise estimate may no longer adapt adequately to changes. In the following chapters, a forgetting factor of $\tau = 200$ is applied for each experiment.

2.7 Conclusions

This chapter established the essential methodological foundations for the 3D EOT algorithms that will be developed in the following chapters. Key insights were gained concerning the measurement-to-source association problem, handling of state interval constraints in Kalman filtering, and processing measurements with varying unpredictable spatial distributions. The review of the SDM, GAM, and RHM measurement-to-source association methods highlighted the inherent trade-offs: SDMs require potentially unknown prior source distributions, GAMs offer efficiency but can suffer from biases, while RHMs and ERHMs provide flexibility in modeling measurement sources at the cost of increased complexity, often necessitating sampling-based filters such as LRKFs. The suitability of specific association techniques, such as radial or projected associations within the GAM or ERHM frameworks, especially for cylindrical coordinate systems relevant to later chapters, was established as a crucial design choice influencing both accuracy and computational load.

Furthermore, two significant practical challenges were addressed. Firstly, the presented transformation technique enabling state interval constraints in the estimation procedure offers a computationally efficient and easy-to-implement method to enforce constraints on estimated parameters. For example, positive extent estimates ensuring physically plausible results without altering the core Kalman filtering equations can be guaranteed with this method. Secondly, and perhaps most critically for handling realistic 3D sensor data, the proposed RAMN estimation procedure provides a novel solution for dealing with mixed sets of boundary and interior measurements. Initial experiments demonstrated that the RAMN approach allows simpler boundary-focused models such as the GAM and simultaneously achieves a robust performance

by adaptively compensating for interior measurements, mitigating the estimation bias towards the object's center often observed when such measurements are ignored or incorrectly modeled. This approach avoids strong assumptions about the spatial distribution of interior measurements required by some alternative methods. In summary, these findings on measurement-to-source association techniques, constraint handling, and particularly the RAMN approach, provide a robust and adaptable toolkit for developing the specific 3D EOT measurement models developed and investigated in the remainder of this thesis.

CHAPTER 3

Parametric Shapes: Object-Specific Shapes

Contents

3.1 Motivation and Contributions . . . 36
3.2 Related Work . . . 37
3.3 Elliptic Cylinders for Motor Boats . . . 38
3.3.1 Elliptic Cylinder 3D GAM . . . 39
3.3.2 Elliptic Cylinder ERHM . . . 40
3.3.3 Recursive Artificial Measurement Noise for the Elliptic Cylinder . . . 41
3.4 Elliptic Cones for Sailing Boats . . . 42
3.4.1 Elliptic Cone 3D GAM . . . 43
3.4.2 Elliptic Cone ERHM . . . 44
3.4.3 Recursive Artificial Measurement Noise for the Elliptic Cone . . . 44
3.5 Implementation Details . . . 45
3.5.1 Elliptic Cylinder Implementation Details . . . 45
3.5.2 Elliptic Cone Implementation Details . . . 47
3.6 Experiments . . . 49
3.6.1 Elliptic Cylinder Experiments . . . 50
3.6.2 Elliptic Cone Experiments . . . 51
3.7 Conclusions . . . 55

3.1 Motivation and Contributions

In this chapter, two measurement models are presented that utilize parametric shapes for the representation of motor and sailing boats. As a shape representation for motor boats, an elliptic cylinder is used. For sailing boats, elliptic cones are applied in the measurement model. Fig. 3.1 shows why these shape approximations are a valid choice as a first approximation. The elliptic cylinder and the elliptic cone represent the characteristic shape features of both object classes sufficiently well. The light detection and ranging (Lidar) measurements, which can be seen as red dots in both figures, were calibrated to the images so that the measurements and figures could be superimposed. Both measurement sets and figures were recorded on Lake Constance by the *Solgenia*, shown in Fig. 1.1.

Object-specific extended object tracking (EOT) measurement models can be used, for example, when a camera system is employed in combination with a point cloud sensor such as a Lidar, which is used to classify the individual dynamic objects in the surveillance area. The detected object classes can then be used to select the appropriate measurement model. Since motor and sailing boats represent the most common object classes in the maritime sector, several

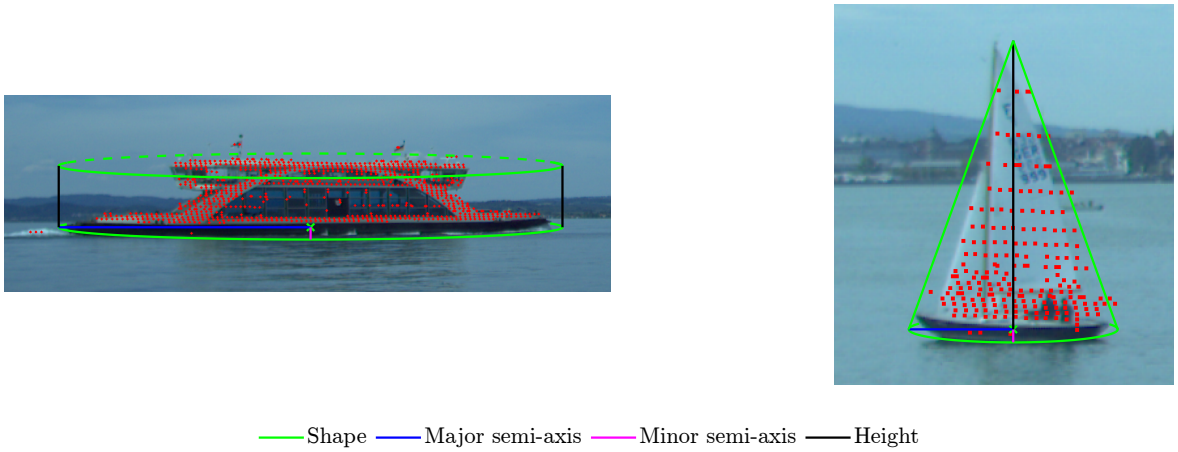

Figure 3.1: Parametric object-specific shapes for maritime traffic participants.

possibilities for measurement processing for the shape approximations of these two classes are presented in this chapter. As an extension of an ellipse, an ellipsoid would also be suitable as a shape approximation for a motorboat. An ellipsoidal measurement model can, for example, be found in [C4]. However, although the results in [C4] were promising, it was shown in [O6] that measurement models that employ shape representations in spherical coordinates can have difficulties in estimating the object's extent in the maritime sector. If measurements from the top and bottom surfaces are missing, which is often the case in maritime object tracking, extent estimates can be error-prone. Since parts of the objects are usually underwater, measurements are mainly taken from an object's lateral surface, which provides insufficient information for estimating the extent in spherical coordinates. Shape representations in cylindrical coordinates naturally solve this problem.

Contributions In this chapter, several contributions are made. First of all, several approaches applying a 3D greedy association model (GAM) and an extrusion random hypersurface model (ERHM) are presented for estimating the extent of motor and sailing boats using elliptic cylinders in Sec. 3.3 and elliptic cones in Sec. 3.4, respectively. Also, radial and projected measurement source associations at specific height sections are presented for both shapes. Furthermore, the recursive artificial measurement noise (RAMN) estimation procedure is added to each measurement model to be able to process measurement sets containing both boundary and interior measurements. In addition to the procedure presented in Sec. 2.6, implicit functions generating the "inside-outside" information for the elliptic cylinder and cone are needed, which are presented in this chapter. In addition to the derivation of the measurement models, pseudo-code that can be used to implement the presented approaches is given in Sec. 3.5. Following this, the different versions of each measurement model are compared using a simulated static scenario in Sec. 3.6. A static simulated scenario can be considered the most basic scenario for 3D EOT. It can therefore be applied to investigate the viability of the presented approaches in a first step before deploying the measurement models to Lidar measurements in Ch. 6.

3.2 Related Work

EOT in 3D space using parametric shapes in maritime domains is still rare in the literature. Nevertheless, an example of further approaches for tracking maritime objects in 3D space using

parametric shape representations can be found in [C4]. In this paper, virtual measurement models and an adaptation loop are applied for generating artificial measurements of the assumed shape and adapting the estimate of the random matrix (RM) approach [40, 83] until it fits the statistics of the measurement set. Further 3D parametric shape models, which were used as inspiration for the measurement models in this chapter, can be found in [33, 38]. These papers propose a cylindrical and a conical model with circular base shapes, which are extended to elliptical versions in this chapter. Furthermore, in both papers, the concept of ERHMs is applied for the measurement-to-source association problem [148], which is based on the random hypersurface model (RHM) [15, 16] and can be implemented using an smart sampling Kalman filter (S2KF) [116, 118, 119]. Further information on the GAM, which is also applied for solving the measurement-to-source association problem for each shape description, can be found in [32, 35]. If applicable, the measurement models applying the ERHM are extended using symmetry assumptions [36] in this chapter. The EOT filter can then be implemented using an unscented Kalman filter (UKF) [76, 77, 130]. Symmetry assumptions can be used to increase the efficiency of the measurement model. Furthermore, the quadratic extension [14] is no longer needed in the measurement model. The RAMN estimation procedure is inspired by [80] and extended in this work for adaptively estimating an artificial measurement noise for the elliptic cylinder and elliptic cone measurement models.

3.3 Elliptic Cylinders for Motor Boats

As mentioned in Sec. 1.2, ellipses provide an appropriate shape approximation for motor boats using 2D measurements. However, shape approximations in spherical coordinates are error-prone for objects in maritime environments since measurements from the bottom side of the object are normally missing. Thus, this section presents an elliptic cylinder as a 3D shape approximation for motor boats as the first measurement model for maritime traffic participants. A parametric representation for an elliptic cylinder in local coordinates can be given as

$$\underline{z}(\theta, s) = [a \cdot \cos(\theta), b \cdot \sin(\theta), s \cdot h]^\top. \tag{3.1}$$

using the semi-axes $a, b > 0$, the height $h > 0$, and the parameters $\theta \in [0, 2\pi)$, and $s \in [0, 1]$. Then, the system state required to estimate an elliptic cylinder out of a recorded measurement set can be given as

$$\underline{x}_{\mathrm{kin}_k} = \left[\underline{m}_k^\top, \phi_k, \underline{x}_{\mathrm{vel}_k}^\top\right]^\top, \tag{3.2a}$$

$$\underline{x}_{\mathrm{ext}_k} = [a_k, b_k, h_k]^\top. \tag{3.2b}$$

The kinematic system state comprises the 3D position $\underline{m}_k$, the yaw angle ϕ_k, and the dynamics $\underline{x}_{\mathrm{vel}_k}$ representing variables such as the velocity, yaw rate, or acceleration of the object. The yaw angle ϕ_k is modeled to be aligned with the direction of movement. Furthermore, roll and pitch angles are assumed to be negligible. However, the model can easily be extended to include these using quaternions [85] or a 3D orientation represented by Euler angles. The position $\underline{m}_k$ and the yaw angle ϕ_k describe a local coordinate system in which the shape is defined.

In the following, two measurement models are presented and later on compared in a simulation study in Sec. 3.6.1. The first measurement model to be presented is a 3D GAM, as it is the most efficient model that can be implemented among the considered options. However, the GAM is known to possibly produce biased height estimates [34] due to a missing penalization for overestimated heights. Thus, to generate an unbiased height estimate, an ERHM for the elliptic cylinder is presented as a measurement model afterwards. Additionally, symmetry assumptions

as given in Sec. 2.4.3 can be included as a further simplification in the measurement model to be able to estimate the system state using an UKF without quadratic extension instead of using an S2KF with quadratic extension. In the ERHM, the shape is assumed to be represented using two parameters, as is the case for the elliptic cylinder. The measurement source association is then constructed using an spatial distribution model (SDM) for the extrusion factor $s_{k,l}$ that defines the height section of the shape, and a 2D GAM for the angular parameter $\hat{\theta}_{k,l}$. This 2D GAM association problem can be solved using a radial or a projected association.

A radial association for solving the 2D GAM in the ERHM and the 3D GAM is presented in this section. The projected association for solving the 2D GAM can be implemented using the description in Sec. 2.4.3. Both association procedures are interchangeable in the elliptic cylinder measurement models and are compared in Sec. 3.6.1. Additionally, a procedure for estimating a RAMN for the elliptic cylinder, as proposed in Sec. 2.6, is presented. The measurement models, therefore, initially assume the measurements to be generated exclusively from the object's boundary.

Remark 3.1. *The initial idea for the elliptic cylinder measurement model for 3D EOT of motor boats is published in [O4]. In this chapter, further improvements to this measurement model are made and compared.*

3.3.1 Elliptic Cylinder 3D GAM

For the 3D GAM, both parameters of the elliptic cylinder are greedily associated with the boundary. Therefore, the measurement must first be transformed to a local coordinate system given as

$$\underline{\tilde{y}}_{k,l} = \mathbf{R}\left(\phi_{k|k-1}\right)^{-1} \cdot \left(\underline{y}_{k,l} - \underline{m}_{k|k-1}\right), \tag{3.3a}$$

$$\mathbf{R}(\phi) = \begin{pmatrix} \cos(\phi) & -\sin(\phi) & 0 \\ \sin(\phi) & \cos(\phi) & 0 \\ 0 & 0 & 1 \end{pmatrix} \tag{3.3b}$$

using the rotation matrix $\mathbf{R}(\phi)$. Afterwards, the greedy parameter estimates for each measurement can be calculated. For the extrusion factor $s_{k,l}$, it is assumed that the measurement sources are located on the same height section as the measurement. Therefore, the extrusion factor can be calculated as

$$\hat{s}_{k,l} = \min\left(\max\left(\frac{\tilde{y}_{k,l}^{(z)}}{h_{k|k-1}}, 0\right), 1\right) \tag{3.4}$$

limiting the estimated values to the interval $[0, 1]$. The greedy association of a point on a specific height section defined by $\hat{s}_{k,l}$ can be generated using either a radial or a projected association. For the radial association, the estimate of the angular parameter $\hat{\theta}_{k,l}$ can be generated as

$$\frac{b_{k|k-1} \cdot \sin(\hat{\theta}_{k,l})}{a_{k|k-1} \cdot \cos(\hat{\theta}_{k,l})} = \frac{\tilde{y}_{k,l}^{(y)}}{\tilde{y}_{k,l}^{(x)}} \tag{3.5a}$$

$$\tan(\hat{\theta}_{k,l}) = \frac{a_{k|k-1} \cdot \tilde{y}_{k,l}^{(y)}}{b_{k|k-1} \cdot \tilde{y}_{k,l}^{(x)}} \tag{3.5b}$$

$$\hat{\theta}_{k,l} = \operatorname{atan2}\left(a_{k|k-1} \cdot \tilde{y}_{k,l}^{(y)}, b_{k|k-1} \cdot \tilde{y}_{k,l}^{(x)}\right) \tag{3.5c}$$

considering the eccentricity of the ellipse. Given the greedy estimates for the elliptic cylinder parameters and the parametric equation for the cylinder (3.1), a measurement source in local coordinates with a radial association can be calculated as

$$\tilde{\underline{z}}_{\text{rad}}\left(\hat{\underline{x}}_{k|k-1}, \tilde{\underline{y}}_{k,l}\right) = \left[\tilde{\underline{z}}_{\text{rad}}^{(xy)}\left(\hat{\underline{x}}_{k|k-1}, \tilde{\underline{y}}_{k,l}\right)^{\top}, \hat{s}_{k,l} \cdot h_{k|k-1}\right]^{\top} \tag{3.6a}$$

$$= \left[a_{k|k-1} \cdot \cos\left(\hat{\theta}_{k,l}\right), b_{k|k-1} \cdot \sin\left(\hat{\theta}_{k,l}\right), \hat{s}_{k,l} \cdot h_{k|k-1}\right]^{\top}. \tag{3.6b}$$

A projected association $\tilde{\underline{z}}_{\text{proj}}^{(xy)}\left(\underline{x}_{k|k-1}, \tilde{\underline{y}}_{k,l}\right)$ in local coordinates computing the closest point on the approximated boundary on a specific height section can be calculated using the procedure presented in Sec. 2.4.3, the predicted ellipse semi-axes $a_{k|k-1}$, and, $b_{k|k-1}$, and the measurement in local coordinates (3.3). The different measurement source association techniques at a specific height section are visualized in a 2D top-down view in Fig. 3.2. Finally, a measurement equation in local coordinates for the elliptic cylinder 3D GAM can be formulated as

$$\hat{\underline{y}}_{k,l} = \begin{bmatrix}\tilde{\underline{z}}^{(xy)}\left(\hat{\underline{x}}_{k|k-1}, \tilde{\underline{y}}_{k,l}\right) \\ \hat{s}_{k,l} \cdot h_{k|k-1}\end{bmatrix} - \tilde{\underline{y}}_{k,l} + \underline{v}_{k,l} \tag{3.7a}$$

$$= \tilde{\underline{z}}_{\text{GAM}}\left(\hat{\underline{x}}_{k|k-1}, \tilde{\underline{y}}_{k,l}\right) + \underline{v}_{k,l} \tag{3.7b}$$

where both the radial and the projected measurement source association procedure can be applied for the greedy association at a specific height section. In the measurement update of the nonlinear Kalman filter, the predicted measurement $\hat{\underline{y}}_{k,l}$ can then be associated with the pseudo-measurement $\underline{0}_3$ in (2.16b). Implementation details for the elliptic cylinder 3D GAM are given in Sec. 3.5.1.

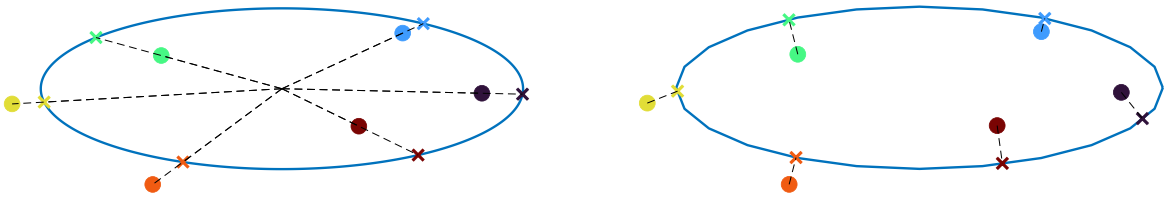

(a) Radial measurement source association.

(b) Projected measurement source association.

Figure 3.2: Elliptical measurement source association. Measurements as balls, and measurement sources as crosses. Related items are displayed in the same color.

3.3.2 Elliptic Cylinder ERHM

When implementing an elliptic cylinder ERHM, the greedy association on a specific height section can be calculated using the radial or projected association and the measurement in local coordinates (3.3) as presented before in Sec. 3.3.1 for the elliptic cylinder 3D GAM. However, in contrast to the 3D GAM, the extrusion factor $s_{k,l}$ is modeled as an SDM in the ERHM. The distribution of the extrusion factor should then resemble a uniform distribution on the surface of the elliptic cylinder due to the lack of prior knowledge of the actual distribution. In the z direction, the probability density function (PDF) of measurements associated with the surface then scales linearly with the shape's perimeter at each height section. For the elliptic cylinder, the perimeter is constant in the z direction. Therefore, a uniform distribution $s_{k,l} \sim \mathcal{U}(0,1)$ in the interval $[0,1]$ is assumed for the extrusion factor for the elliptic cylinder ERHM.

Due to the uniform distribution of the extrusion factor, symmetry assumptions for the ERHM as presented in Sec. 2.4.3 can be included in the measurement equation. The measurement equation for the symmetrical elliptic cylinder ERHM can finally be given as

$$\hat{\underline{y}}_{k,l} = \begin{bmatrix} \tilde{\underline{z}}^{(xy)}\left(\hat{\underline{x}}_{k|k-1}, \tilde{\underline{y}}_{k,l}\right) \\ s_{k,l} \cdot \frac{h_{k|k-1}}{2} \end{bmatrix} - \begin{bmatrix} \tilde{\underline{y}}_{k,l}^{(xy)} \\ |\tilde{y}_{k,l}^{(z)}| \end{bmatrix} + \underline{v}_{k,l} \tag{3.8a}$$

$$= \tilde{\underline{z}}_{\mathrm{ERHM}}\left(\hat{\underline{x}}_{k|k-1}, \tilde{\underline{y}}_{k,l}\right) + \underline{v}_{k,l} \tag{3.8b}$$

where the extrusion factor $s_{k,l}$ is subject to sampling. In this measurement equation, the origin of the local coordinate system is located in the middle of the shape, in contrast to the 3D GAM where the origin is located in the base ellipse. Due to the factor $\frac{h_{k|k-1}}{2}$ in the z coordinate of the measurement function, the full height is still estimated in this approach. In the measurement update step of the nonlinear Kalman filter, the predicted measurement $\hat{\underline{y}}_{k,l}$ can then again be associated with the pseudo-measurement $\underline{0}_3$ in (2.16b). Implementation details for the elliptic cylinder ERHM are given in Sec. 3.5.1.

3.3.3 Recursive Artificial Measurement Noise for the Elliptic Cylinder

In both the elliptic cylinder 3D GAM and the elliptic cylinder ERHM, measurements are initially assumed to be generated from the object's boundary. However, due to several reasons, measurements may also be generated from the object's interior. For the elliptic cylinder measurement models, measurements from the interior of the object could be processed with an additional RHM for each height section as was presented in [15, 16]. However, it was seen in Sec. 2.6 that the estimate of the extent using an RHM can be biased if the wrong distribution of the scaling factor is assumed. Also, in addition to the extrusion factor that is needed for the ERHM, an additional factor would be needed and would also be subject to sampling if an additional RHM were used to process measurements from the interior of the object.

Therefore, a RAMN estimation procedure for processing measurements from the interior of the elliptic cylinder is presented in this section. The basic equations for the recursive parameter estimation of the artificial measurement noise are given in Sec. 2.6. Since the elliptic cylinder is defined in cylindrical coordinates, an estimation of the artificial measurement noise only in x and y coordinates is sufficient. Also, the extent of the ellipses does not change in the z direction, so the problem of calculating the "inside-outside" information for each measurement can be reduced to calculating the value for the 2D ellipse defined by the extent parameters $a_{k|k-1}$ and $b_{k|k-1}$.

In addition to calculating whether measurements are inside the boundary, the information about measurements being outside the $3\sigma_{\underline{v}}$ border must be calculated. An implicit equation for the ellipse that can be used to calculate this information is given by

$$\mathcal{I}(\tilde{\underline{y}}_{k,l}, \hat{\underline{x}}_{k|k-1}) = \frac{\tilde{y}_{k,l}^{(x)^2}}{(a_{k|k-1} - 3 \cdot \sigma_{\underline{v}})^2} + \frac{\tilde{y}_{k,l}^{(y)^2}}{(b_{k|k-1} - 3 \cdot \sigma_{\underline{v}})^2} - 1 \begin{cases} > 0: & \text{outside} \\ = 0: & 3\sigma_{\underline{v}} \text{ boundary} \\ < 0: & \text{inside} \end{cases} \tag{3.9}$$

using the predicted system state $\hat{\underline{x}}_{k|k-1}$, and the measurement in local coordinates $\tilde{\underline{y}}_{k,l}$, which can be calculated using (3.3). A visualization of the measurement separation for the RAMN estimation can be seen in Fig. 3.3. The blue measurements in the figure are then applied for the recursive estimation of the artificial measurement noise parameters. The Euclidean distances needed for the calculation are directly given by the measurement sources as

$$d_{k,l}^{(i,\eta)} = \left| \tilde{z}^{(i,\eta)}\left(\hat{\underline{x}}_{k|k-1}, \tilde{\underline{y}}_{k,l}\right) \right|. \tag{3.10}$$

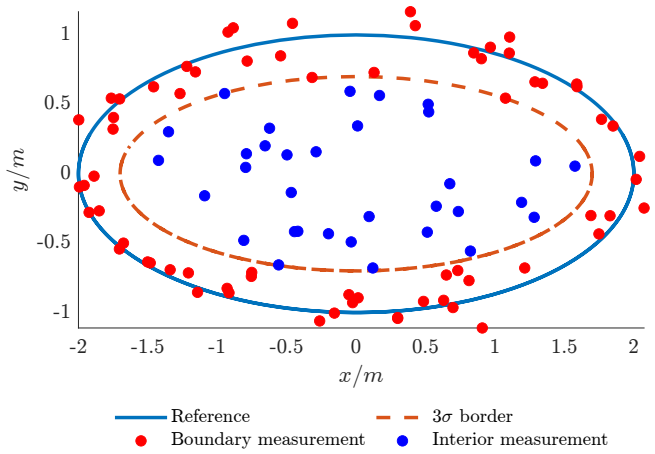

Figure 3.3: Visualization of the measurement separation for the RAMN estimation of an ellipse.

Both the radial and the projected associations can be applied to calculate the artificial measurement noise. Also, both the measurement sources of the elliptic cylinder 3D GAM and ERHM can be directly applied for calculating the Euclidean distances. After calculating the RAMN parameters using a forgetting factor of $\tau = 200$, the measurement noise parameters can be generated as

$$\hat{\underline{\mu}}_{\underline{v}_{k,l}} = \begin{cases} \left[\hat{\mu}_k^{(i,x)}, \hat{\mu}_k^{(i,y)}, 0\right]^\top & \text{if inside} \\ [0,0,0]^\top & \text{else} \end{cases} \tag{3.11a}$$

$$\underline{\mathbf{\Sigma}}_{\underline{v}_{k,l}} = \begin{cases} \operatorname{diag}\left(\hat{\mathrm{v}}_k^{(i,x)}, \hat{\mathrm{v}}_k^{(i,y)}, \sigma_{\underline{v}}^2\right) & \text{if inside} \\ \operatorname{diag}(\sigma_{\underline{v}}^2, \sigma_{\underline{v}}^2, \sigma_{\underline{v}}^2) & \text{else} \end{cases} \tag{3.11b}$$

for each measurement individually. The stacked measurement noise covariance matrix ${}^s\underline{\mathbf{\Sigma}}_{\underline{v}}$ can then be generated using (2.19). The artificial measurement noise mean is added to each predicted measurement. Details on the implementation can also be found in Sec. 3.5.1.

3.4 Elliptic Cones for Sailing Boats

The last section presented an elliptic cylinder as a shape approximation for motor boats in 3D EOT. However, although an elliptic base shape is also an appropriate shape approximation for sailing boats in 2D, the elliptic cylinder assumption can be further improved for 3D EOT of sailing boats. Therefore, this section presents an elliptic cone 3D shape approximation as a further measurement model for a second class of maritime traffic participants. A parametric representation for an elliptic cone in local coordinates can be given as

$$\underline{z}(\theta, s) = [(1-s)\cdot a \cdot \cos(\theta), (1-s)\cdot b \cdot \sin(\theta), s \cdot h]^\top. \tag{3.12}$$

using the semi-axes $a, b > 0$, the height $h > 0$, and the parameters $\theta \in [0, 2\pi)$, and $s \in [0, 1]$. Then, the system state required to estimate an elliptic cone is the same as for the elliptic cylinder and is given as

$$\underline{x}_{\mathrm{kin}_k} = \left[\underline{m}_k^\top, \phi_k, \underline{x}_{\mathrm{vel}_k}^\top\right]^\top, \tag{3.13a}$$

$$\underline{x}_{\mathrm{ext}_k} = [a_k, b_k, h_k]^\top. \tag{3.13b}$$

Again, the yaw angle ϕ_k is modeled to be aligned with the direction of movement, and roll and pitch angles are assumed to be negligible.

In the following sections, again two measurement models for estimating an elliptic cone, a 3D GAM and an ERHM, are presented and compared in a simulation study in Sec. 3.6.2. However, as will be seen, symmetry assumptions as given in Sec. 2.4.3 cannot be included in the elliptic cone ERHM. Thus, a quadratic extension in combination with an S2KF must be applied for estimating the parameters of the elliptic cone when using an ERHM. Furthermore, for the 2D association of the measurement source on a specific height section, again, a radial and a projected association can be applied. Finally, also for the elliptic cone measurement models, a procedure for estimating a RAMN for processing measurements from the interior of the shape is presented and investigated in Sec. 3.6.2.

Remark 3.2. *The initial idea for the elliptic cone measurement model for 3D EOT of sailing boats is published in [O5]. In this chapter, further improvements to this measurement model are made and compared.*

3.4.1 Elliptic Cone 3D GAM

For the elliptic cone 3D GAM, both parameters are greedily associated with the boundary. When using a radial association, the equations for greedy associations are given by (3.4) for the extrusion factor $\hat{s}_{k,l}$, and by (3.5) for the angular parameter $\hat{\theta}_{k,l}$ using the measurement in local coordinates given by (3.3). Given the greedy estimates for the elliptic cone parameters, and the parametric equation for the elliptic cone (3.12), a measurement source in local coordinates with a radial association can be calculated as

$$\underline{\tilde{z}}_{\mathrm{rad}}\left(\underline{\hat{x}}_{k|k-1}, \underline{\tilde{y}}_{k,l}\right) = \begin{bmatrix} \underline{\tilde{z}}^{(xy)}_{\mathrm{rad}}\left(\underline{\hat{x}}_{k|k-1}, \underline{\tilde{y}}_{k,l}\right) \\ \hat{s}_{k,l} \cdot h_{k|k-1} \end{bmatrix} \tag{3.14a}$$

$$= \begin{bmatrix} (1-\hat{s}_{k,l}) \cdot a_{k|k-1} \cdot \cos\left(\hat{\theta}_{k,l}\right) \\ (1-\hat{s}_{k,l}) \cdot b_{k|k-1} \cdot \sin\left(\hat{\theta}_{k,l}\right) \\ \hat{s}_{k,l} \cdot h_{k|k-1} \end{bmatrix}. \tag{3.14b}$$

A projected association $\underline{\tilde{z}}^{(xy)}_{\mathrm{proj}}\left(\underline{\hat{x}}_{k|k-1}, \underline{\tilde{y}}_{k,l}\right)$ in local coordinates computing the closest point on the approximated boundary on a specific height section can be calculated using the procedure presented in Sec. 2.4.3. Therefore, the semi-axes must be scaled using the predicted extrusion factor $\hat{s}_{k,l}$ as $(1-\hat{s}_{k,l}) \cdot a_{k|k-1}$ for the major semi-axis and $(1-\hat{s}_{k,l}) \cdot b_{k|k-1}$ for the minor semi-axis. Using this scaled ellipse at a specific height section and the measurement in local coordinates (3.3), a projected association can be calculated. Finally, a measurement equation in local coordinates for the elliptic cone 3D GAM can be formulated as

$$\underline{\hat{y}}_{k,l} = \begin{bmatrix} \underline{\tilde{z}}^{(xy)}\left(\underline{\hat{x}}_{k|k-1}, \underline{\tilde{y}}_{k,l}\right) \\ \hat{s}_{k,l} \cdot h_{k|k-1} \end{bmatrix} - \underline{\tilde{y}}_{k,l} + \underline{v}_{k,l} \tag{3.15a}$$

$$= \underline{\tilde{z}}_{\mathrm{GAM}}\left(\underline{\hat{x}}_{k|k-1}, \underline{\tilde{y}}_{k,l}\right) + \underline{v}_{k,l} \tag{3.15b}$$

where both the radial and the projected measurement source association procedure can be applied for the greedy association at a specific height section. In the measurement update of the nonlinear Kalman filter, the predicted measurement $\underline{\hat{y}}_{k,l}$ can be associated with the pseudo-measurement $\underline{0}_3$ in (2.16b). Implementation details for the elliptic cone 3D GAM are given in Sec. 3.5.2.

3.4.2 Elliptic Cone ERHM

When implementing an elliptic cone ERHM, the greedy association on a specific height section can be calculated using the radial or projected association presented in the sections before. In contrast to the elliptic cylinder ERHM presented in Sec. 3.3.2, measurements are not assumed to be uniformly distributed in the z direction for the elliptic cone. Since the PDF of measurements in the z direction scales linearly with the perimeter of the shape at each height section, if the extrusion factor is chosen to resemble a uniform distribution of measurements on the surface of the elliptic cone, the extrusion factor can be modeled using a triangular distribution. It is then distributed as $s_{k,l} \sim \mathcal{T}(0,1,0)$ where $\mathcal{T}(a,b,c)$ describes a triangular distribution with lower limit a, upper limit b, and mode c [38].

Due to the triangular distribution, symmetry assumptions in the z direction cannot be included in the elliptic cone ERHM. Thus, a quadratic extension in combination with an S2KF must be applied to estimate the height. The measurement equation in global coordinates without applying the quadratic extension is then given as

$$\hat{\underline{y}}_{k,l} = \underline{m}_{k|k-1} + \mathbf{R}\left(\phi_{k|k-1}\right) \cdot \begin{bmatrix} \underline{\tilde{z}}^{(xy)}\left(\hat{\underline{x}}_{k|k-1}, \tilde{\underline{y}}_{k,l}\right) \\ s_{k,l} \cdot h_{k|k-1} \end{bmatrix} - \underline{y}_{k,l} + \underline{v}_{k,l} \tag{3.16a}$$

$$= \underline{z}_{\mathrm{ERHM}}\left(\hat{\underline{x}}_{k|k-1}, \tilde{\underline{y}}_{k,l}\right) + \underline{v}_{k,l}. \tag{3.16b}$$

The quadratic extension can then be added for an unbiased height estimation using the measurement equation for the z direction as

$$\begin{bmatrix} \hat{\underline{y}}_{k,l} \\ \hat{y}_{k,l}^{(z)^2} \end{bmatrix} = \begin{bmatrix} \underline{z}_{\mathrm{ERHM}}\left(\hat{\underline{x}}_{k|k-1}, \tilde{\underline{y}}_{k,l}\right) + \underline{v}_{k,l} \\ \left(m_{k|k-1}^{(z)} + s_{k,l} \cdot h_{k|k-1} + v_{k,l}^{(z)}\right)^2 - y_{k,l}^{(z)^2} \end{bmatrix} \tag{3.17a}$$

When using the quadratic extension for estimating the height of the shape, the measurement equation must be formulated in global coordinates rather than in local coordinates as compared to the elliptic cylinder ERHM. Also, due to the quadratic extension, not only is the extrusion factor subject to sampling, but also the measurement noise of the z coordinate. After the quadratic extension, the extended predicted measurement $\left[\hat{\underline{y}}_{k,l}^{\top}, \hat{y}_{k,l}^{(z)^2}\right]^{\top}$ can be associated with the pseudo-measurement $\underline{0}_4$ in (2.16b) in the update step of the nonlinear Kalman filter. Implementation details can be found in Sec. 3.5.2.

3.4.3 Recursive Artificial Measurement Noise for the Elliptic Cone

Also, in the measurement models of the elliptic cone, measurements are initially assumed to be generated from the object's boundary. Therefore, a RAMN can again be added to the measurement model for processing measurements from the object's interior. The basic equations for the parameter estimation of the artificial measurement noise are given in Sec. 2.6. For the elliptic cone, the artificial parameters can again be calculated for x and y coordinates to be able to process measurements from the interior of the object.

However, in contrast to the elliptic cylinder, the extent parameters at each height section vary for the elliptic cone, which needs to be considered in the "inside-outside" equation. Hence, first, a greedy estimate for the extrusion factor of each measurement must be calculated using (3.4) and the measurement in local coordinates (3.3). Then, the information for each measurement

being inside the boundary of the elliptic cone and outside the $3\sigma_{\underline{v}}$ border can be calculated using the implicit equation

$$\mathcal{I}(\tilde{\underline{y}}_{k,l}, x_{k|k-1}) = \frac{\tilde{y}_{k,l}^{(x)^2}}{\left((1-\hat{s}_{k,l})\cdot(a_{k|k-1}-3\cdot\sigma_{\underline{v}})\right)^2} + \frac{\tilde{y}_{k,l}^{(y)^2}}{\left((1-\hat{s}_{k,l})\cdot(b_{k|k-1}-3\cdot\sigma_{\underline{v}})\right)^2} - 1 \quad (3.18)$$

$$\begin{cases} > 0: & \text{outside} \\ = 0: & 3\sigma_{\underline{v}} \text{ boundary} . \\ < 0: & \text{inside} \end{cases}$$

Using this "inside-outside" function, the procedure described in Sec. 3.3.3 can be applied for calculating the parameters of the artificial recursive measurement noise. Implementation details can be found in Sec. 3.5.2.

3.5 Implementation Details

In this section, details on implementing the presented algorithms are given. In particular, pseudo-code for the elliptic cylinder and the elliptic cone EOT algorithms is presented. Also, details on implementing the calculation to estimate the artificial measurement noise parameters for processing interior measurements are given. However, the theoretical sections exclusively focus on the measurement update step in the Kalman filter. Thus, the procedures given in this section also only constitute the measurement updates using the respective nonlinear Kalman filters. Details on the prediction steps can be found in the respective literature, such as [19, 27, 66]. The implementation details of the algorithms described in the following chapters can then be built based on the information provided in this section.

Remark 3.3. *In addition to the pseudo-code given in this section, an implementation of the elliptic cylinder measurement models can be found at [R2] and for the elliptic cone at [R1].*

3.5.1 Elliptic Cylinder Implementation Details

This section presents the details of the implementation of the elliptic cylinder measurement models. Although the elliptic cylinder GAM could be implemented using an extended Kalman filter (EKF), every elliptic cylinder 3D EOT filter is implemented using an UKF to ensure better comparability among all the presented versions. Due to the symmetry assumptions in the elliptic cylinder ERHM, an UKF is the least complex algorithm among the ones applied in this thesis that can be used for state estimation in the elliptic cylinder ERHM. The algorithm for a sequential batch linear regression Kalman filter (LRKF) measurement update, which is the same procedure for the UKF and the S2KF, can be found in Alg. 3.1. The deterministic sample calculation in line 3 can then either be solved using the sigma point generation of the UKF or the sample generation of the S2KF. The artificial measurement noise mean and covariance matrix in line 11 for the elliptic cylinder can be generated using the "inside-outside" function (3.9) and the procedure described in Sec. 3.3.3. The main difference among the filters presented in this thesis, which are implemented using an LRKF, can be traced back to lines 3–5 in Alg. 3.1, which differ for each shape description and measurement source association procedure. The following lines in the loop from lines 6–15 are the same for every EOT filter, which is implemented using an LRKF. For the elliptic cylinder measurement model, the pseudo-code for implementing lines 3–5 in Alg. 3.1 can be found in Alg. 3.2. In this algorithm, implementations of the elliptic

Algorithm 3.1 Sequential batch LRKF measurement update

Require:

predicted state $\hat{\underline{x}}_{k|k-1}$, predicted state covariance $\mathbf{P}_{k|k-1}$, measurements $\mathcal{Y}_k$, single update measurement number n_u

1: set $\hat{\underline{x}}_1 = \hat{\underline{x}}_{k|k-1}$, $\mathbf{P}_1 = \mathbf{P}_{k|k-1}$
2: **for** $n \leftarrow 1$ **to** $\lfloor n_k/n_u \rfloor$ **do**
3: Gaussian samples $\left\{\underline{x}_{n,j}, w_{n,j}\right\}_{j=1}^{n_s}$ using [130] or [116, 118]
4: get $\left\{\underline{y}_{n,l}\right\}_{l=1}^{n_u}$ from $\mathcal{Y}_k$ using next n_u measurements
5: predicted measurements $\left\{\left\{\hat{\underline{y}}_{n,j,l}\right\}_{l=1}^{n_u}\right\}_{j=1}^{n_s}$ for each measurement and sample
6: **for** $l \leftarrow 1$ **to** n_u **do**
7: predicted measurements $\hat{\underline{y}}_{n,l} = \sum_{j=1}^{n_s} w_{n,j} \cdot \hat{\underline{y}}_{n,j,l}$
8: **end for**
9: stack predicted measurement samples $\left\{{}^{s}\hat{\underline{y}}_{n,j} = \left[\hat{\underline{y}}_{n,j,1}^{\top}, \ldots, \hat{\underline{y}}_{n,j,n_u}^{\top}\right]^{\top}\right\}_{j=1}^{n_s}$
10: RAMN parameters $\hat{\mu}_n^{(i,\eta)}$, $\hat{\mathrm{v}}_n^{(i,\eta)}$ using Sec. 2.6.1 and "inside-outside" function
11: measurement noise parameters $\hat{\underline{\mu}}_{\underline{v}_{n,l}}$, $\mathbf{\Sigma}_{\underline{v}_{n,l}}$ using (3.11a) and (3.11b)
12: stack predicted measurements ${}^{s}\hat{\underline{y}}_n = \left[\left(\hat{\underline{y}}_{n,1} + \hat{\underline{\mu}}_{\underline{v}_{n,1}}\right)^{\top}, \ldots, \left(\hat{\underline{y}}_{n,n_u} + \hat{\underline{\mu}}_{\underline{v}_{n,n_u}}\right)^{\top}\right]^{\top}$
13: stack measurement noise covariance matrices ${}^{s}\mathbf{\Sigma}_{\underline{v}_n}$ using (2.19)
14: innovation covariance matrix $\mathbf{S}_n = \sum_{j=1}^{n_s} w_{n,j} \cdot \left({}^{s}\hat{\underline{y}}_{n,j} - {}^{s}\hat{\underline{y}}_n\right) \cdot \left({}^{s}\hat{\underline{y}}_{n,j} - {}^{s}\hat{\underline{y}}_n\right)^{\top} + {}^{s}\mathbf{\Sigma}_{\underline{v}_n}$
15: cross covariance matrix $\mathbf{\Psi}_n = \sum_{j=1}^{n_s} w_{n,j} \cdot \left(\underline{x}_{n,j} - \hat{\underline{x}}_n\right) \cdot \left({}^{s}\hat{\underline{y}}_{n,j} - {}^{s}\hat{\underline{y}}_n\right)^{\top}$
16: updated state mean vector $\hat{\underline{x}}_{n+1} = \hat{\underline{x}}_n + \mathbf{\Psi}_n \cdot \mathbf{S}_n^{-1} \cdot \left(\underline{0} - {}^{s}\hat{\underline{y}}_n\right)$
17: updated state covariance matrix $\mathbf{P}_{n+1} = \mathbf{P}_n - \mathbf{\Psi}_n \cdot \mathbf{S}_n^{-1} \cdot \mathbf{\Psi}_n^{\top}$
18: **end for**
19: set $\hat{\underline{x}}_k = \hat{\underline{x}}_{n+1}$, $\mathbf{P}_k = \mathbf{P}_{n+1}$

cylinder measurement model where the measurement source association is solved using a 3D GAM or an ERHM are described in detail. A main difference in both association procedures can be found in lines 1–5, where the sigma point generation of the predicted system state distribution can be found. For the 3D GAM, only samples from the system state parameters must be generated. On the other hand, when implementing an elliptic cylinder ERHM, the extrusion factors must be sampled for each of the n_u measurements individually. Since the extrusion factor is assumed to be distributed uniformly as $s_{k,l} \sim \mathcal{U}(0,1)$, one possibility would be to approximate the uniform distribution as a Gaussian distribution with $\mu_s = \frac{1}{2}$ and $\sigma_s^2 = \frac{1}{12}$ and sample the extrusion factors from this approximated distribution. However, when doing so, an approximation error can be introduced as extrusion factors will also be sampled outside the interval $[0,1]$. Therefore, an idea presented in [117] can be applied if uniformly distributed samples are to be generated. When generating samples from the standard Gaussian distribution with $\mu_s = 0$ and $\sigma_s^2 = 1$ and transforming the samples through the cumulative distribution function (CDF)

$$\Phi(s_{k,l}) = \tilde{s}_{k,l} = \frac{1}{2}\left(1 + \operatorname{erf}\left(\frac{s_{k,l}}{\sqrt{2}}\right)\right) \tag{3.19}$$

of the standard Gaussian distribution, the transformed samples $\tilde{s}_{k,l}$ will be uniformly distributed as $\tilde{s}_{k,l} \sim \mathcal{U}(0,1)$ [102]. Therefore, the system state distribution can be extended with the parameters of a standard Gaussian distribution for each of the n_u measurements in line 4 to be able to sample uniformly distributed sigma points in lines 6 and 18. Another difference between the 3D GAM and the ERHM is in the calculation of the predicted measurement, which can be found in lines 16 and 19. For the ERHM, the symmetry assumption in the z direction is applied to compensate for the missing quadratic extension and enable the application of an UKF instead of requiring an S2KF. Finally, for the elliptic cylinder, the extent state is subject to constraints. Therefore, the transformation function (2.38) with a lower bound of 0 to prevent negative values is applied for the full extent state in line 10.

Algorithm 3.2 Elliptic cylinder UKF measurement prediction

1: **if** 3D GAM measurement source association **then**
2: distribution parameters $\underline{x}_u = \underline{\hat{x}}_n$, $\mathbf{P}_u = \mathbf{P}_n$
3: **else if** ERHM measurement source association **then**
4: extended distribution parameters $\underline{x}_u = \left[\underline{\hat{x}}_n^\top, \underline{0}_{n_u}^\top\right]^\top$, $\mathbf{P}_u = \mathrm{blkdiag}\left(\mathbf{P}_n, \mathbf{I}_{n_u}\right)$
5: **end if**
6: sigma points $\left\{\underline{\boldsymbol{x}}_{n,j}, \boldsymbol{w}_{n,j}\right\}_{j=1}^{n_s}$ using [130] and $\underline{x}_u$, $\mathbf{P}_u$
7: get $\left\{\underline{y}_{n,l}\right\}_{l=1}^{n_u}$ from $\mathcal{Y}_k$ using next n_u measurements
8: **for** $j \leftarrow 1$ **to** n_s **do**
9: extract $\underline{\boldsymbol{x}}_{\mathrm{kin}_{n,j}}$ from $\underline{\boldsymbol{x}}_{n,j}$
10: extract constrained $\underline{\tilde{\boldsymbol{x}}}_{\mathrm{ext}_{n,j}} = c_1(\underline{\boldsymbol{x}}_{\mathrm{ext}_{n,j}}, 0)$ with lower bound from $\underline{\boldsymbol{x}}_{n,j}$ using (2.38)
11: **for** $l \leftarrow 1$ **to** n_u **do**
12: measurement in local coordinates $\underline{\tilde{\boldsymbol{y}}}_{n,j,l}$ using (3.3), and $\underline{\boldsymbol{x}}_{\mathrm{kin}_{n,j}}$
13: measurement source $\underline{\tilde{\boldsymbol{z}}}_{n,j,l}^{(xy)}\left(\underline{\tilde{\boldsymbol{x}}}_{\mathrm{ext}_{n,j}}, \underline{\tilde{\boldsymbol{y}}}_{n,j,l}\right)$ using (3.6) or projected association
14: **if** 3D GAM measurement source association **then**
15: extrusion factor $\hat{\jmath}_{n,j,l}$ using (3.4), $\tilde{\boldsymbol{y}}_{n,j,l}^{(z)}$, and constrained height sample $\tilde{\hbar}_{n,j}$
16: predicted measurement $\underline{\hat{\boldsymbol{y}}}_{n,j,l} = \left[\underline{\tilde{\boldsymbol{z}}}_{n,j,l}^{(xy)\top}, \hat{\jmath}_{n,j,l} \cdot \tilde{\hbar}_{n,j}\right]^\top - \underline{\tilde{\boldsymbol{y}}}_{n,j,l}$
17: **else if** ERHM measurement source association **then**
18: extract extrusion factor sample $\tilde{\jmath}_{n,j,l} = \frac{1}{2}\left(1 + \mathrm{erf}\left(\frac{\jmath_{n,j,l}}{\sqrt{2}}\right)\right)$ from $\underline{\boldsymbol{x}}_{n,j}$
19: predicted measurement $\underline{\hat{\boldsymbol{y}}}_{n,j,l} = \left[\underline{\tilde{\boldsymbol{z}}}_{n,j,l}^{(xy)\top}, \tilde{\jmath}_{n,j,l} \cdot \frac{\tilde{\hbar}_{n,j}}{2}\right]^\top - \left[\underline{\tilde{\boldsymbol{y}}}_{n,j,l}^{(xy)\top}, |\tilde{\boldsymbol{y}}_{n,j,l}^{(z)}|\right]^\top$
20: **end if**
21: **end for**
22: **end for**

3.5.2 Elliptic Cone Implementation Details

This section presents the details of the implementation of the elliptic cone measurement models. Also, for the elliptic cone, an EKF could be applied for the 3D GAM. However, due to the quadratic extension in the ERHM, an S2KF [116, 118] must be used for this filter and is then also used for the 3D GAM for better comparability among the elliptic cone measurement models. The implementation of the elliptic cone measurement models is again built on the sequential batch LRKF measurement update in Alg. 3.1. In this algorithm, the measurement noise covariance matrix in line 12 for the elliptic cone can be calculated using the "inside-outside" function (3.18) and the procedure described in Sec. 3.4.3. The implementation of lines 3–5 in

Alg. 3.1 can be found in Alg. 3.3. In this algorithm, the implementation of the elliptic cone measurement model with the measurement source association solved using a 3D GAM or an ERHM can be found. For the 3D GAM, the implementation is similar to the elliptic cylinder, with the difference that the measurement source model (3.14) is used in line 13.

Algorithm 3.3 Elliptic cone S2KF measurement prediction

1: **if** 3D GAM measurement source association **then**
2: distribution parameters $\underline{x}_u = \underline{\hat{x}}_n$, $\mathbf{P}_u = \mathbf{P}_n$
3: **else if** ERHM measurement source association **then**
4: extended distribution parameters $\underline{x}_u = \left[\underline{\hat{x}}_n^\top, \underline{0}_{2n_u}^\top\right]^\top$, $\mathbf{P}_u = \text{blkdiag}\left(\mathbf{P}_n, \mathbf{I}_{n_u}, \sigma_{\underline{v}}^2 \cdot \mathbf{I}_{n_u}\right)$
5: **end if**
6: Gaussian samples $\left\{\underline{\boldsymbol{x}}_{n,j}, \boldsymbol{w}_{n,j}\right\}_{j=1}^{n_s}$ using [116, 118] and $\underline{x}_u$, $\mathbf{P}_u$
7: get $\left\{\underline{y}_{n,l}\right\}_{l=1}^{n_u}$ from $\mathcal{Y}_k$ using next n_u measurements
8: **for** $j \leftarrow 1$ **to** n_s **do**
9: extract $\underline{\boldsymbol{x}}_{\text{kin}_{n,j}}$ from $\underline{\boldsymbol{x}}_{n,j}$
10: extract constrained $\underline{\tilde{\boldsymbol{x}}}_{\text{ext}_{n,j}} = c_1(\underline{\boldsymbol{x}}_{\text{ext}_{n,j}}, 0)$ with lower bound from $\underline{\boldsymbol{x}}_{n,j}$ using (2.38)
11: **for** $l \leftarrow 1$ **to** n_u **do**
12: measurement sample in local coordinates $\underline{\tilde{\boldsymbol{y}}}_{n,j,l}$ using (3.3), and $\underline{\boldsymbol{x}}_{\text{kin}_{n,j}}$
13: measurement source $\underline{\tilde{\boldsymbol{z}}}_{n,j,l}^{(xy)}\left(\underline{\tilde{\boldsymbol{x}}}_{\text{ext}_{n,j}}, \underline{\tilde{\boldsymbol{y}}}_{n,j,l}\right)$ using (3.14) or projected association
14: **if** 3D GAM measurement source association **then**
15: extrusion factor $\hat{\jmath}_{n,j,l}$ using (3.4), $\tilde{\boldsymbol{y}}_{n,j,l}^{(z)}$, and constrained height sample $\tilde{\hbar}_{n,j}$
16: predicted measurement $\underline{\hat{\boldsymbol{y}}}_{n,j,l} = \left[\underline{\tilde{\boldsymbol{z}}}_{n,j,l}^{(xy)\top}, \hat{\jmath}_{n,j,l} \cdot \tilde{\hbar}_{n,j}\right]^\top - \underline{\tilde{\boldsymbol{y}}}_{n,j,l}$
17: **else if** ERHM measurement source association **then**
18: extract extrusion factor sample $\tilde{\jmath}_{n,j,l} = 1 - \sqrt{1 - \Phi(\jmath_{n,j,l})}$
19: extract noise sample $\boldsymbol{v}_{n,j,l}$ from $\underline{\boldsymbol{x}}_{n,j}$
20: measurement source $\underline{\boldsymbol{z}}_{n,j,l} = \underline{\boldsymbol{m}}_{n,j} + \mathbf{R}\left(\phi_{n,j}\right) \cdot \left[\underline{\tilde{\boldsymbol{z}}}_{n,j,l}^{(xy)\top}, \tilde{\jmath}_{n,j,l} \cdot \tilde{\hbar}_{n,j}\right]^\top$
21: predicted measurement
$\underline{\hat{\boldsymbol{y}}}_{n,j,l} = \left[\underline{\boldsymbol{z}}_{n,j,l}^{(xy)\top}, \boldsymbol{z}_{n,j,l}^{(z)} + \boldsymbol{v}_{n,j,l}, (\boldsymbol{z}_{n,j,l}^{(z)} + \boldsymbol{v}_{n,j,l})^2\right]^\top - \left[\underline{y}_{n,l}^\top, y_{n,l}^{(z)^2}\right]^\top$
22: **end if**
23: **end for**
24: **end for**

When implementing an elliptic cone ERHM, the sample generation in line 4 is already different from that in the elliptic cylinder ERHM. The extrusion factors must again be sampled for each of the n_u measurements individually. However, for the elliptic cone, the extrusion factors are assumed to be sampled from the triangular distribution $s_{k,l} \sim \mathcal{T}(0, 1, 0)$. As the sampling procedure in the S2KF only samples Gaussian distributed samples, again, a transformation based on the inverse transform sampling [104] can be performed to generate samples that are distributed according to the triangular distribution. In inverse transform sampling, uniformly distributed samples $s_{k,l} \sim \mathcal{U}(0, 1)$ are transformed using the inverse CDF of the target distribution. Thus, in line 4, standard Gaussian distributed samples are generated, which can be transformed using the Gaussian CDF to result in uniformly distributed samples, which then can be transformed using the inverse of the triangular CDF. The full transformation of the samples can then be given as

$$\tilde{\jmath}_{k,l} = 1 - \sqrt{1 - \Phi(s_{k,l})} \tag{3.20}$$

where $\Phi(s_{k,l})$ is the CDF of the standard Gaussian distribution. The samples $\tilde{\jmath}_{k,l}$ will then be distributed as $\tilde{\jmath}_{k,l} \sim \mathscr{T}(0,1,0)$. The extrusion factor sample transformation can be found in line 18 of Alg. 3.3. Concerning interval constraints, for the elliptic cone, the same transformation function as in the elliptic cylinder measurement models is used to prevent negative values in the extent state in line 10.

In addition to the extrusion factor, the measurement noise in the z direction must also be sampled for the elliptic cone ERHM due to the quadratic extension, where the additive noise is transformed as well. The noise $v^{(z)} \sim \mathcal{N}(0, \sigma_v^2)$ can perfectly be sampled using the S2KF by also extending the state distribution parameters for each of the n_u measurements individually. The measurement function that applies the quadratic extension using the transformed extrusion factor samples and the noise samples can then be found in lines 20–21 of Alg. 3.3. Since the noise in the z direction is also sampled in the elliptic cone ERHM, and the quadratic extension must be applied in the update step, the measurement noise mean and covariance matrix differ from the ones given in (3.11a) and (3.11b). After the calculation of the RAMN parameters, the individual measurement noise means and covariance matrices can be calculated as

$$\hat{\underline{\mu}}_{\underline{v}_{k,l}} = \begin{cases} \left[\hat{\mu}_k^{(i,x)}, \hat{\mu}_k^{(i,y)}, 0, 0\right]^\top & \text{if inside} \\ [0,0,0,0]^\top & \text{else} \end{cases} \tag{3.21}$$

$$\boldsymbol{\Sigma}_{\underline{v}_{k,l}} = \begin{cases} \operatorname{diag}\left(\hat{\mathrm{v}}_k^{(i,x)}, \hat{\mathrm{v}}_k^{(i,y)}, 0, 0\right) & \text{if inside} \\ \operatorname{diag}(\sigma_{\underline{v}}^2, \sigma_{\underline{v}}^2, 0, 0) & \text{else} \end{cases} \tag{3.22}$$

After the calculation of the individual measurement noise covariance matrices, the stacked measurement noise covariance matrix ${}^s\boldsymbol{\Sigma}_{\underline{v}}$ can then again be generated using (2.19).

3.6 Experiments

In this section, the elliptic cylinder and elliptic cone measurement models are investigated and compared in a simulated static scenario. In these simulated scenarios with 100 time steps, measurements are generated from both the boundary of the reference shape and the interior of the object. With a probability of 0.7, measurement sources are generated from the boundary of the objects using the shape functions (3.1) for the elliptic cylinder and (3.12) for the elliptic cone. Uniformly distributed boundary measurement sources can be generated by sampling the shape parameters from the respective distributions. The angular parameter is sampled from the uniform distribution $\theta \sim \mathscr{U}(0, 2\pi)$ for both shapes. The extrusion parameter is sampled from the uniform distribution $s \sim \mathscr{U}(0,1)$ for the elliptic cylinder and from the triangular distribution $s \sim \mathscr{T}(0,1,0)$ for the elliptic cone. In addition, with a probability of 0.3, a scaling factor $t \sim \mathscr{T}(0,1,1)$ is sampled to also generate measurement sources from the object's interior. An interior measurement source can then be generated by scaling the measurement source in the xy plane as $\underline{z}^{(xy)}(\theta, s) = t \cdot \underline{z}^{(xy)}(\theta, s)$. Finally, to generate a measurement, the measurement noise $v \sim \mathcal{N}\left(0, 0.1^2\right)$ is sampled for each dimension and added to the measurement source.

In the simulation, the elliptic cylinder and elliptic cone 3D EOT filters are implemented using a 3D GAM, an ERHM, with a radial and projected measurement source association at a specific height section, and with and without the RAMN estimation. If no RAMN estimation is applied, a standard measurement noise covariance matrix is used, assuming measurements are exclusively generated from the object's boundary. Each filter is initialized using the first measurement set. Details can be found at [R1, R2]. In each time step, 50 measurements are generated, and for the sequential batch update, $n_u = 20$ measurements are used for a single update in each

filter. In the following sections, the quantitative results are presented using the mean root mean square errors (RMSEs) of each system state parameter in a Monte Carlo (MC) simulation with 100 runs.

3.6.1 Elliptic Cylinder Experiments

In this section, the simulation results for the elliptic cylinder 3D EOT filters are presented. The quantitative MC simulation results are depicted in Fig. 3.4. In this figure, the mean values of the RMSEs of the full system state, comprising the position $\underline{m}_k$, the yaw angle ϕ_k, the major semi-axis a_k, the minor semi-axis b_k, and the height h_k, are depicted for the full scenario.

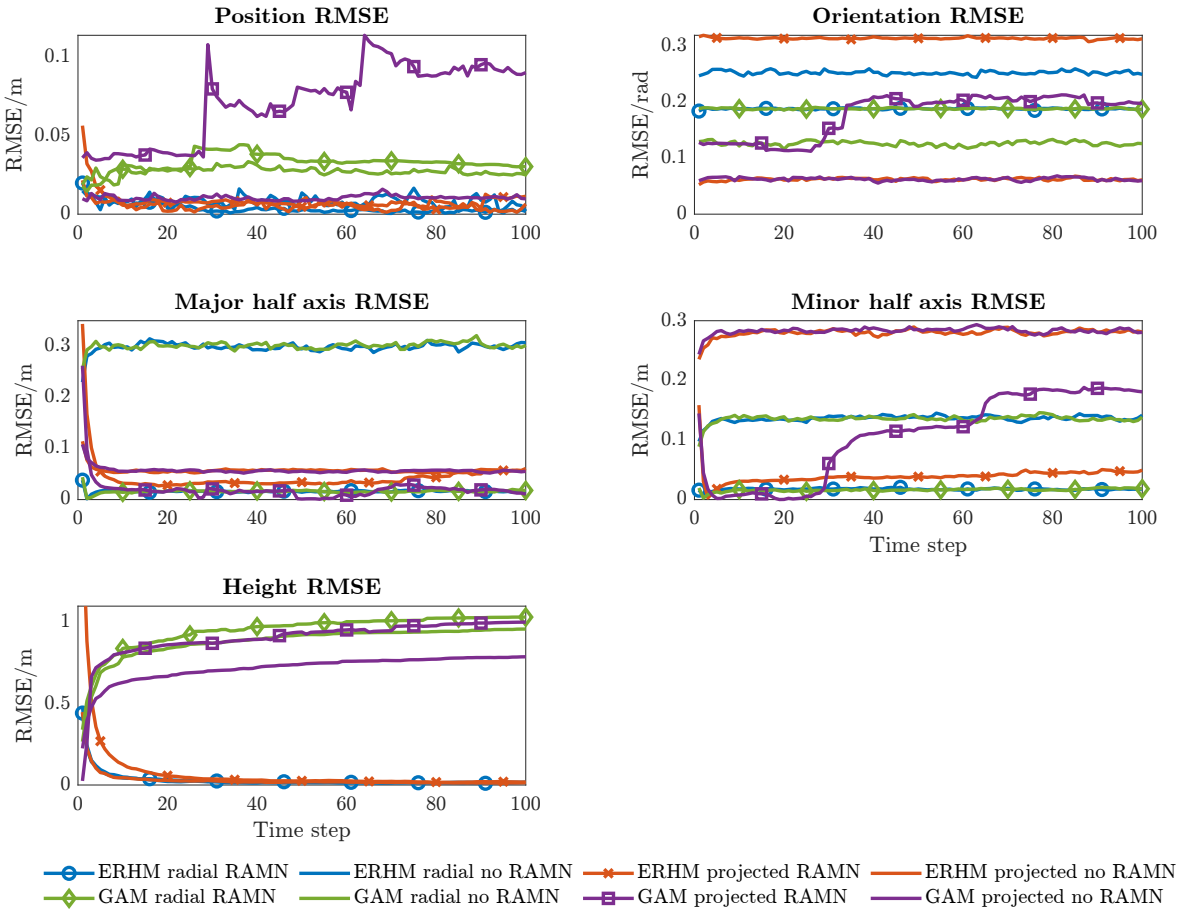

Figure 3.4: MC simulation RMSE estimation results of the static elliptic cylinder simulation experiment.

In the simulation, eight implementations, which were discussed in the previous sections, of the elliptic cylinder 3D EOT filter are compared. In the figure, it can be seen that the ERHM implementations of the elliptic cylinder yield an unbiased height estimate. The 3D GAM implementations typically overestimate the height due to the missing penalization mechanism for overestimated heights in the GAM. In the figure, it can also be seen that the implementations applying the RAMN estimation in the update procedure yield precise estimates of the semi-axes a and b except for the minor semi-axis b when a projected measurement-to-source association at a specific height section is used. Therefore, the implementations exhibiting the best performance are the ERHM implementations applying the RAMN estimation when measurements from the boundary and the interior of the object are present. Due to the overestimated minor semi-axis b when using a projected measurement-to-source association, a radial association already seems

Table 3.1: Mean computation times per measurement for the elliptic cylinder.

Algorithm	Computation time
ERHM radial RAMN	29.06 µs
ERHM radial no RAMN	29.42 µs
ERHM projected RAMN	136.13 µs
ERHM projected no RAMN	148 µs
GAM radial RAMN	14.94 µs
GAM radial no RAMN	15.06 µs
GAM projected RAMN	25.3 µs
GAM projected no RAMN	25.2 µs

beneficial for the elliptic cylinder measurement models after this simulation. The following investigations in Ch. 6 will further confirm this result. The estimates of the yaw angle reveal huge errors, which can be ascribed to the fact that the shapes are symmetric and the angle is a periodic variable, which is why ambiguities in the estimates can occur. However, the orientation RMSE converges in each implementation, which indicates a reliable angle estimation.

In addition to the quantitative estimation results, the mean calculation times per measurement are given in Tab. 3.1. Each calculation is conducted using MATLAB R2023b on an Intel(R) Xeon(R) X5680 CPU with 3.33 GHz. It can be seen that the 3D GAM implementations are the most efficient. However, the ERHM implementations with radial measurement source association at a specific height section are almost as efficient. In comparison, the projected association is distinctly slower in this comparison. However, for the ERHM applying a RAMN estimation with a projected association at a specific height section and $n_u < n_k$, problems with the positive definiteness of the system state covariance matrix $\mathbf{P}_n$ in the UKF were encountered. In future work, therefore, a square root implementation of the UKF [126] should be applied if this combination is to be used.

Finally, in Fig. 3.5, the qualitative estimation results after 50 time steps and 2500 processed measurements for two filter implementations of the elliptic cylinder are depicted. In the left column, the elliptic cylinder is depicted in a 2D top view, and in the right column, in a 3D view. In each figure, the ERHM implementation with a radial measurement source association at a specific height section is applied. In Fig. 3.5a, no RAMN estimation is applied, while in Fig. 3.5b, the RAMN estimation is used in the update step. In the second row of the figure, it can be seen that the extent of the elliptic cylinder can be perfectly estimated, while the shapes in the first row showcase a bias of the extent parameters towards the center of the shape. Furthermore, these results were also obtained for different spatial distributions of interior measurements. Thus, the RAMN estimation is independent of the spatial distribution of interior measurements, and no assumptions need to be made. In contrast to the RHM approach, where the spatial distribution needs to be specified beforehand, this fact represents a major advantage.

3.6.2 Elliptic Cone Experiments

In this section, the simulation results for the elliptic cone 3D EOT filters are presented. The quantitative MC simulation results are depicted in Fig. 3.6. In this figure, again, the mean values of the RMSEs of the full system state for the simulated scenario can be seen. Also, again, the eight filters that were discussed in the sections before are implemented and investigated.

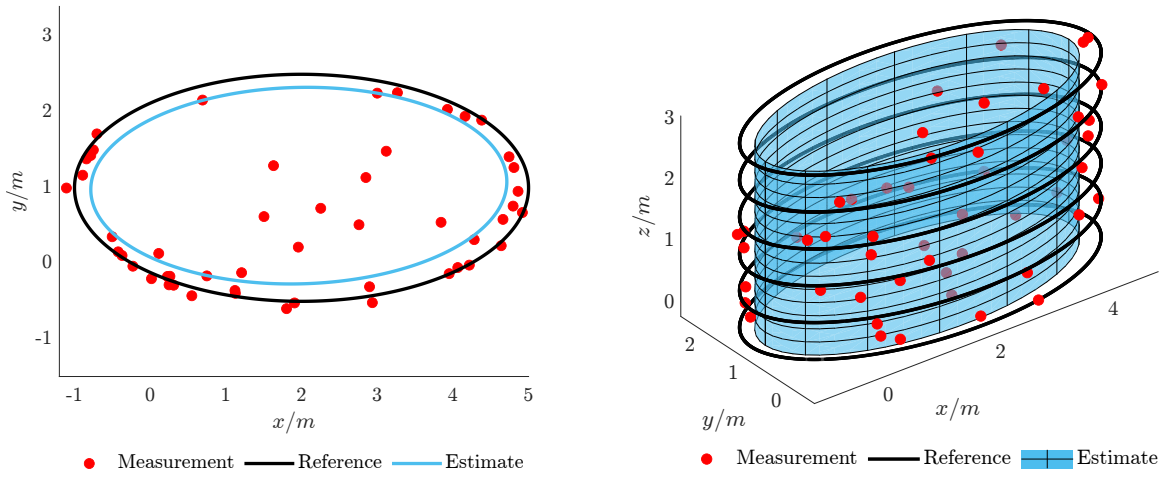

(a) Estimation results of the elliptic cylinder ERHM applying a radial measurement source association without artificial noise estimation.

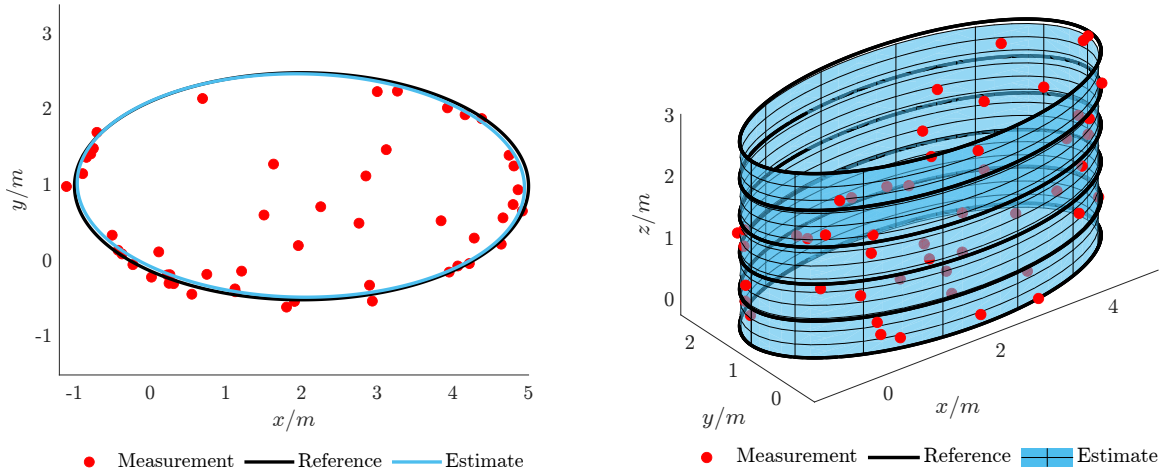

(b) Estimation results of the elliptic cylinder ERHM applying a radial measurement source association with artificial noise estimation.

Figure 3.5: Estimation results of the elliptic cylinder ERHM applying a radial measurement source association with and without artificial noise estimation in 2D and 3D views. Estimates are at the same time step with the same random seed for the measurement generation.

In contrast to the elliptic cylinder, an S2KF is applied for the elliptic cone for each filter instead of an UKF. For the ERHM implementations, the quadratic extension must also be applied. In the figure, it can again be seen that the ERHM implementations yield an unbiased height estimate for the elliptic cone. When using a 3D GAM, the height estimate is biased and overestimated in this scenario. When using the RAMN estimation for the elliptic cone, again, precise estimates of the semi-axes can be obtained. The estimates of the yaw angle again reveal huge errors, however, they converged in each implementation, which indicates a reliable angle estimation. In summary, again, the implementations exhibiting the best performance are the ERHM implementations applying the RAMN estimation for measurements concurrently gathered from the boundary and the interior of the object. A clear difference when using either a radial or a projected association at a specific height section can not be detected.

The mean computation times per measurement for each implementation are given in Tab. 3.2. It can be seen that the computation times for the 3D GAM applying a radial association

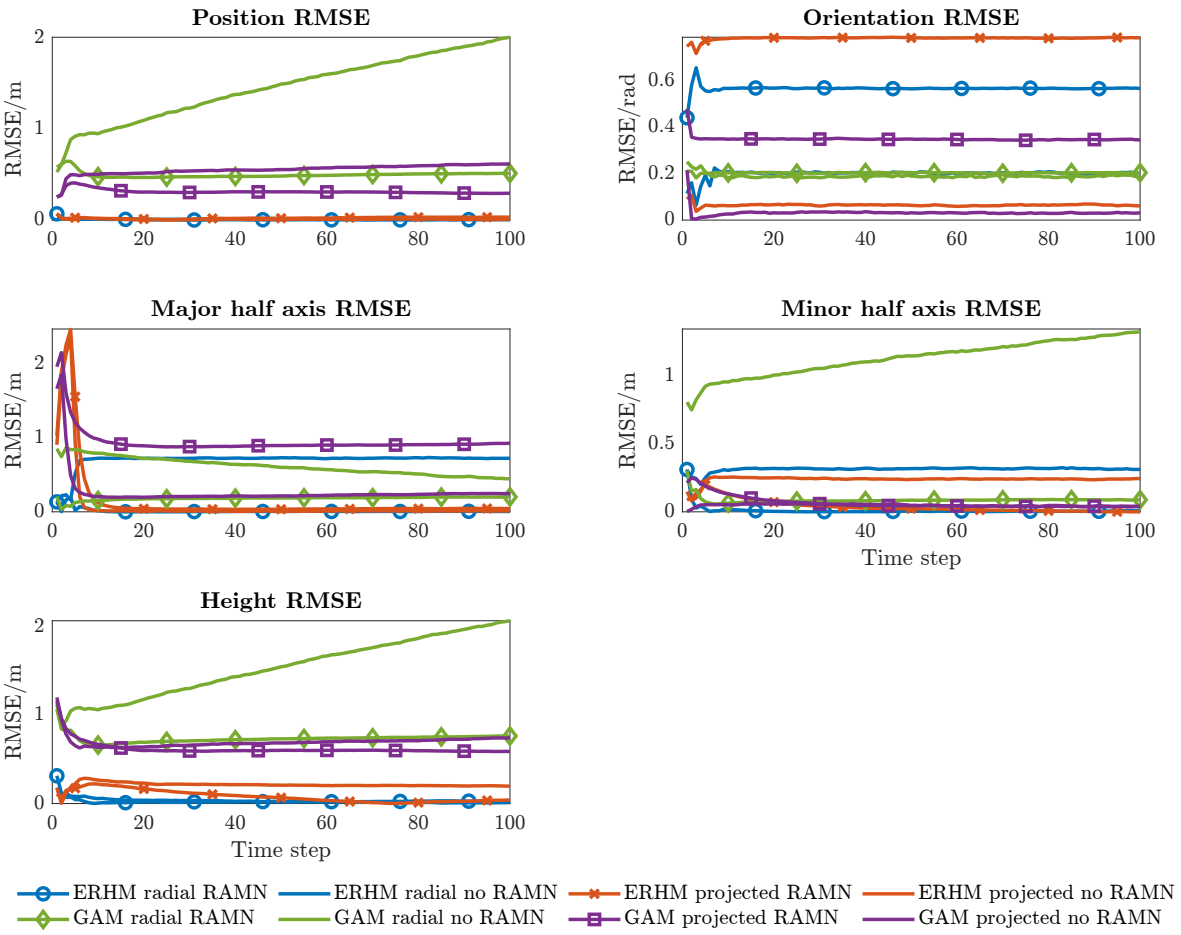

Figure 3.6: MC simulation RMSE estimation results of the static elliptic cone simulation experiment.

at a specific height section are the lowest. For the ERHM implementation applying a radial association, the computation times are comparable to the times of the 3D GAM applying a projected association. The computation times for the ERHM implementation applying a projected association are by far the highest. In contrast to the elliptic cylinder, no problems with the positive definiteness of the system state covariance matrix were encountered for the ERHM applying a RAMN with a projected association and $n_u < n_k$.

Table 3.2: Mean computation times per measurement for the elliptic cone.

Algorithm	Computation time
ERHM radial RAMN	79.39 µs
ERHM radial no RAMN	84.71 µs
ERHM projected RAMN	412.16 µs
ERHM projected no RAMN	411.86 µs
GAM radial RAMN	14.21 µs
GAM radial no RAMN	14.14 µs
GAM projected RAMN	67.55 µs
GAM projected no RAMN	67.32 µs

Qualitative estimation results for the elliptic cone 3D EOT filters after 50 time steps, and 2500 processed measurements for two implementations are finally again depicted in Fig. 3.7. In each figure, an ERHM implementation with a radial measurement source association at a specific height section is applied. In Fig. 3.7a, no RAMN estimation is applied, while in Fig. 3.7b, the RAMN estimation is used in the update step. Also, for the elliptic cone, it can be seen that the application of the RAMN estimation yields precise estimates of the extent parameters of the elliptic cone in this static scenario, while the estimates of the extent parameters when not using the RAMN estimation are biased towards the center of the object. Finally, for the elliptic cone, these results could also be obtained for different spatial distributions of interior measurements, showcasing the independence of the RAMN estimation approach from the present spatial distribution of interior measurements.

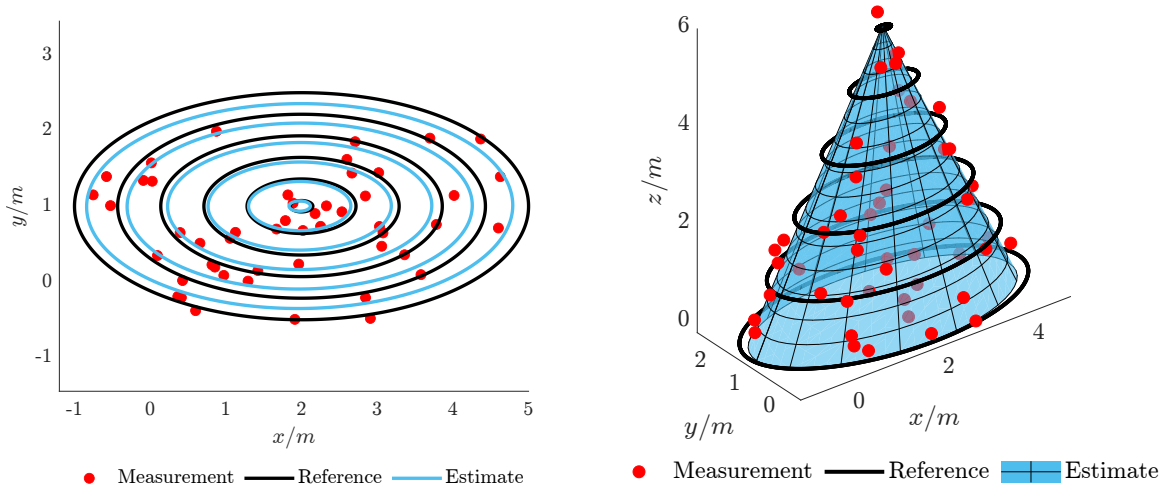

(a) Estimation results of the elliptic cone ERHM applying a radial measurement source association without artificial noise estimation.

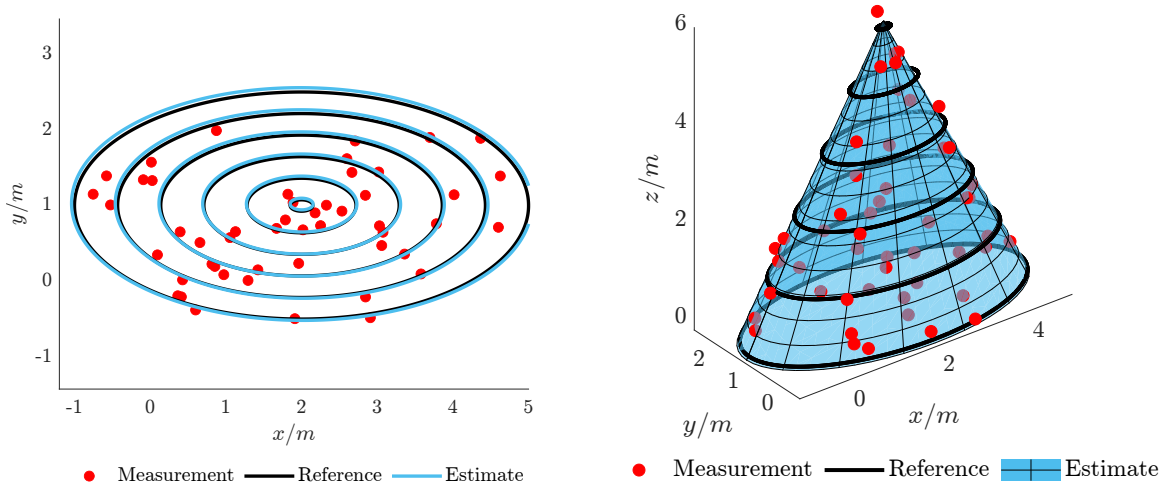

(b) Estimation results of the elliptic cone ERHM applying a radial measurement source association with artificial noise estimation.

Figure 3.7: Estimation results of the elliptic cone ERHM applying a radial measurement source association with and without artificial noise estimation in 2D and 3D views. Estimates are at the same time step with the same random seed for the measurement generation.

In this chapter, both the elliptic cylinder and the elliptic cone measurement models were applied only to static artificial scenarios in a simulation environment. To showcase the effectiveness of the approaches on real-world data in maritime environments, both parametric shape descriptions are applied to real-world Lidar data in Sec. 6.1 with data of a motor boat for the elliptic cylinder and data of a sailing boat for the elliptic cone measurement models. In addition, to examine the generalizability to further environments, the elliptic cylinder measurement models are also applied to real-world automotive data in Sec . 6.2.

3.7 Conclusions

This chapter transitioned from the general EOT framework established previously to the development and initial evaluation of specific 3D parametric measurement models tailored for common maritime object classes, namely motor boats and sailing boats. Recognizing the limitations of spherical coordinate representations in maritime scenarios due to typically missing measurements from top and bottom surfaces, this work focused on shape representations defined in cylindrical coordinates: the elliptic cylinder for motor boats and the elliptic cone for sailing boats. These shapes were motivated by their ability to capture the essential visual characteristics of the respective vessel types while inherently addressing the missing measurement challenge.

Comparative simulation experiments provided important insights into the performance of different strategies for the measurement-to-source association for these parametric shapes. As expected, the ERHM consistently provided unbiased height estimates, overcoming the tendency of the simpler 3D GAM to overestimate the object height due to its missing penalization mechanism. This result favors ERHM-based approaches when accurate 3D extent estimation is critical, even if more complex filters such as the UKF or the S2KF may be required. Furthermore, the experiments demonstrated the successful integration and significant benefits of the RAMN estimation procedure. The RAMN approach significantly improved the accuracy of horizontal extent parameters for both cylinder and cone models by effectively compensating for distortions caused by simulated interior measurements. This confirms the RAMN approach as a promising component for improving the robustness of parametric 3D EOT measurement models when processing mixed boundary and interior measurements. While the differences between radial and projected association techniques were less pronounced in these static tests, the radial measurement-to-source association generally offered higher computational efficiency. These initial results confirmed the suitability of the developed object-specific models, in particular the ERHM variants applying the RAMN procedure, and paved the way for their evaluation in more complex dynamic and real-world scenarios.

CHAPTER 4

Non-Parametric Shapes: Series Expansions

Contents

4.1 Motivation and Contributions 56
4.2 Related Work 57
4.3 Shape Estimation and Tracking in Cylindrical Coordinates 58
4.3.1 Fourier-Chebyshev Double Series as Shape Representation 58
4.3.2 FCDS 3D GAM Measurement Model 62
4.3.3 FCDS quasi-ERHM Measurement Model 63
4.3.4 Recursive Artificial Measurement Noise for FCDS 66
4.4 Implementation Details 67
4.4.1 FCDS 3D GAM Implementation Details 67
4.4.2 FCDS quasi-ERHM Implementation Details 70
4.5 Experiments 73
4.5.1 Comparison to Shape Representations in Spherical Coordinates 74
4.5.2 Investigation of the FCDS Models with Artificial Measurement Noise 77
4.6 Conclusions 78

4.1 Motivation and Contributions

In this chapter, various 3D extended object tracking (EOT) measurement models, which can be applied for maritime object tracking by deploying non-parametric shape descriptions, are presented. Non-parametric shape descriptions are beneficial for two different reasons. First, when using flexible non-parametric shape descriptions within the measurement model, no classification of the object to be tracked is needed. The shape description can be chosen with sufficient flexibility to adapt to the shape of common objects that may appear in the surveillance area. This can be advantageous if there is no camera system available that can be used to classify objects and select a suitable measurement model. Furthermore, the performance of the EOT algorithm can be increased by choosing a flexible non-parametric shape description. The flexible shape description not only allows the shape to be adapted to the object, but the measurement source on the object's surface can also be described more generally. As a result, the remaining system state can also be estimated with greater accuracy [32, 145].

For the shape representation of the flexible non-parametric 3D EOT measurement model, a radial function is used. Similar to [17, 129] in 2D space, this radial function then maps a given input to a radial distance, which ultimately defines the shape of the object. For the definition of this radial function, the known properties of the expected measurement data are to be included. In the maritime domain, for example, it can be assumed that measurements will primarily be

recorded from the lateral surface of the objects and that measurements of the top and bottom surfaces will be rare. Since parts of the object will always be underwater, and a light detection and ranging (Lidar) sensor, for example, cannot see through water, it can be assumed that measurements from the object's bottom surface will never occur. Furthermore, depending on the mounting position and the opening angle of the sensor, only a few measurements can be taken from the top surface of the object, if any. If measurements are missing in these two areas, radial functions defined in spherical coordinates can lead to error-prone estimates in these areas, since no information is available that would enable the shape estimate to converge. In [O6], it was shown that shape representations in cylindrical coordinates can be advantageous in this case. Therefore, a shape representation in cylindrical coordinates will be developed in this chapter.

Contributions The contributions made in this chapter are manifold. First, a double series radial function expansion, using Fourier and Chebyshev series [97], which is then applied as a shape representation in the measurement model, is presented and discussed in Sec. 4.3. In this section, the Fourier-Chebyshev double series (FCDS), which can be applied for expanding a radial function in cylindrical coordinates, is presented at the beginning. A combination of these two basis functions is currently unique in the EOT tracking community. Following this, the FCDS is integrated in two different measurement-to-source association approaches to enable 3D shape estimation and tracking. First, a 3D greedy association model (GAM) is presented in Sec. 4.3.2. Due to known problems of biased height estimates with 3D GAMs, the Fourier-Chebyshev shape representation is then integrated into an extrusion random hypersurface model (ERHM). However, since the ERHM is not suitable for nonlinear mappings of the extrusion parameter, an approach is described in Sec. 4.3.3 which assumes that the height and position in the z direction are statistically independent of the remaining system state. The implications of this assumption are discussed. Since the system states in both approaches can be relatively high-dimensional, an extended Kalman filter (EKF) [27] is used for implementation, as it is the least computationally intensive nonlinear Kalman filter considered suitable. As before, an "inside-outside" function is presented for the FCDS shape representation, which makes it possible to use the recursive artificial measurement noise (RAMN) estimation procedure. As a further contribution of this chapter, details on the implementation, including pseudo-code, can be found in Sec. 4.4. The final contribution of this chapter is the investigation and comparison of the different approaches in static simulated scenarios in Sec. 4.5. In addition to investigating the proposed methods, a comparison to 3D shape estimation and tracking measurement models applying shape representations in spherical coordinates is presented in this section.

4.2 Related Work

The relevant literature on 3D shape estimation and tracking in maritime applications using non-parametric shape models is also limited. In [95], an approach can be found that is based on the FCDS shape representation approach described in this chapter and [O8]. In this paper, a principal component analysis is performed on the horizontal shape representation to reduce the number of shape components while maintaining accuracy. Further 3D non-parametric shape models applying 3D radial functions, which were used as inspiration for the measurement models in this chapter, can be found in [O7, 85, 87]. In these papers, the shape is represented using radial functions in spherical coordinates. In addition to the radial function approach, 3D EOT measurement models deploying flexible non-parametric shape representations using splines can be found in [67, 100]. In both papers, the spline control points are estimated for

flexible shape estimation and tracking in 3D space. The measurement-to-source association of the FCDS shape representation measurement models is solved using a 3D GAM [32, 35] and an ERHM approach. In the ERHM approach, the state of a line object is estimated, which is based on [34] and symmetry assumptions regarding the extrusion factor distribution, proposed in [36]. Information on the EKF, which is applied for inference of the shape state, can be found in common literature such as [10, 11, 19, 27]. The line state in the ERHM approach is estimated using an unscented Kalman filter (UKF) [76, 77, 130]. The RAMN estimation procedure is again inspired by [80].

4.3 Shape Estimation and Tracking in Cylindrical Coordinates

As discussed in the sections before, the shape estimation and tracking problem can be solved using shape representations in spherical coordinates expanded using spherical double Fourier series (SDFS) [O7], spherical harmonics (SH) [87], or a 3D Gaussian process (GP) [30, 84, 85]. When representing the shape to be estimated as a radial function in spherical coordinates, a function $f(\theta, \phi)$ with $\theta \in [0, \pi]$ and $\phi \in [0, 2\pi)$, mapping each angle pair $[\theta, \phi]^T$ to a specific radius, must be estimated. This can be achieved by directly estimating the coefficients of the chosen expansion or the radii when applying a 3D GP. However, if measurements from an object's lateral surface can mainly be expected, as is often the case in maritime scenarios, shape representations in cylindrical coordinates are preferable, as these provide a more natural modeling approach for shape estimation and tracking. If measurements from the top and bottom surfaces are rare or even missing, EOT filters with shape representations in spherical coordinates can be error-prone in these areas, leading to unpredictable estimation results. Therefore, a shape estimation and tracking approach in cylindrical coordinates is presented in this section. When representing the shape to be estimated as a radial function in cylindrical coordinates, a function $f(\theta, z)$ with $\theta \in [0, 2\pi)$ and $z \in [0, h]$, mapping each angle and height section pair $[\theta, z]^T$ to a specific radius, must be estimated. The variable h again represents the height of the object. While such a representation better depicts the expected data, it also has another practical property. A shape representation in spherical coordinates has the property that only star-convex shapes can be displayed. This means that every connecting line drawn from the center to the object's edge is itself completely inside the object. A shape representation in cylindrical coordinates, on the other hand, can represent shapes that only have to be star-convex for each plane curve on a fixed height section. A shape representation in cylindrical coordinates can, therefore, represent a wider range of different shapes.

4.3.1 Fourier-Chebyshev Double Series as Shape Representation

To be able to estimate such a shape $f(\theta, z)$ in cylindrical coordinates, a suitable shape representation must first be defined. The shape should be representable by a series expansion, comparable to [O7] or [87]. The series expansion should be periodic in θ and non-periodic in z. A first approach was presented in [O6] as a solution to a boundary value problem for Laplace's equation in cylindrical coordinates [134]. The solution to this boundary value problem was then a specialized double Fourier series (DFS) for expanding radial functions in cylindrical coordinates. However, when expanding a cylindrical radial function using a DFS, both parameters θ and z of the function are modeled to be periodic. In the definition of the boundary value problem for Laplace's equation in cylindrical coordinates, a boundary condition needed is that the function (and therefore also the radius) is 0 at the top and bottom. This boundary condition then ensured that the shape was periodic in the parameter z. However,

since the shape should be non-periodic in the parameter z to be able to display any general 3D shapes, a non-periodic basis in z is used below.

Chebyshev Polynomials According to [20], either Legendre or Chebyshev polynomials can be applied when expanding non-periodic functions in a specified interval. Both sets of polynomials form an orthogonal basis on the closed interval $[-1, 1]$. Due to the latter one having a slightly better convergence behavior and their close relationship to the well-known Fourier basis [20], Chebyshev polynomials are applied as a basis for the cylindrical shape expansion in the parameter z in this thesis. Chebyshev polynomials of the first kind can be defined by

$$T_n(s) = \cos(n \cdot \theta), \tag{4.1}$$

with $n \in \mathbb{N}$, $\theta \in [0, \pi]$, and $s = \cos(\theta)$ [97], forming a series of orthogonal polynomials on the interval $[-1, 1]$. These polynomials can then be calculated using the recursion

$$T_n(s) = 2 \cdot s \cdot T_{n-1}(s) - T_{n-2}(s) \tag{4.2}$$

with initial conditions $T_0(s) = 1$ and $T_1(s) = s$. Instead of using the recursive formula for the Chebyshev polynomials, explicit formulas also exist for calculating the respective polynomials, which can also be differentiated [20, 97]. However, due to numerical issues when implementing the Chebyshev polynomials using an explicit formula, a hard-coded list is used in the implementation in the further course of this thesis. The first nine polynomials with their respective derivatives are then given as

$$T_0(s) = 1, \qquad T_0'(s) = 0, \tag{4.3a}$$
$$T_1(s) = s, \qquad T_1'(s) = 1, \tag{4.3b}$$
$$T_2(s) = 2s^2 - 1, \qquad T_2'(s) = 4s, \tag{4.3c}$$
$$T_3(s) = 4s^3 - 3s, \qquad T_3'(s) = 12s^2 - 3, \tag{4.3d}$$
$$T_4(s) = 8s^4 - 8s^2 + 1, \qquad T_4'(s) = 32s^3 - 16s, \tag{4.3e}$$
$$T_5(s) = 16s^5 - 20s^3 + 5s, \qquad T_5'(s) = 80s^4 - 60s^2 + 5, \tag{4.3f}$$
$$T_6(s) = 32s^6 - 48s^4 + 18s^2 - 1, \qquad T_6'(s) = 192s^5 - 192s^3 + 36s, \tag{4.3g}$$
$$T_7(s) = 64s^7 - 112s^5 + 56s^3 - 7s, \qquad T_7'(s) = 448s^6 - 560s^4 + 168s^2 - 7, \tag{4.3h}$$
$$T_8(s) = 128s^8 - 256s^6 + 160s^4 - 32s^2 + 1, \qquad T_8'(s) = 1024s^7 - 1536s^5 + 640s^3 - 64s. \tag{4.3i}$$

These nine Chebyshev polynomials are also visualized in Fig. 4.1. Using the Chebyshev polynomials, any non-periodic, piecewise smooth, and continuous function $g(s)$ in the interval $s \in [-1, 1]$ can be expanded using the possibly infinite sum

$$g(s) = \sum_{n=0}^{\infty} a_n \cdot T_n(s) \tag{4.4}$$

with appropriate coefficients a_n. Now, given a non-periodic basis together with the well-known Fourier basis, the final shape representation can be defined in the next paragraph.

Radial Function in Cylindrical Coordinates Using the Chebyshev polynomials and the Fourier basis, a radial function in cylindrical coordinates with a non-periodic behavior in the z direction can now be defined by combining both bases in a single double series. The radial function can be given as

$$f(\theta, s) = \sum_{n=0}^{n_s} \sum_{m=0}^{n_\theta} a_n \cdot T_n(s) \cdot (a_m \cdot \cos(m\theta) + b_m \cdot \sin(m\theta)) \tag{4.5}$$

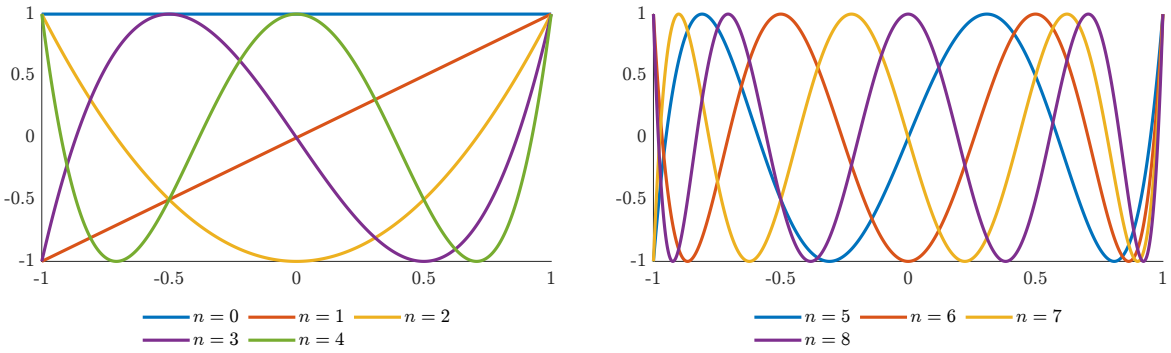

(a) First five Chebyshev polynomials.

(b) Next four Chebyshev polynomials.

Figure 4.1: Visualization of the first nine Chebyshev polynomials.

using the normalized height parameter $s \in [-1, 1]$ and the angular parameter $\theta \in [0, 2\pi)$. When the Chebyshev and Fourier series are multiplied out, the coefficients a_n, a_m, b_m can be redefined as the new coefficients a_{nm}, b_{nm}. After some rearrangements, the new double series can be expressed as

$$f(\theta, s) = \frac{a_{00}}{4} + \frac{1}{2} \cdot \sum_{n=1}^{n_s} a_{n0} \cdot T_n(s) + \frac{1}{2} \cdot \sum_{m=1}^{n_\theta} \Psi_{0m}(\theta) + \sum_{n=1}^{n_s} \sum_{m=1}^{n_\theta} T_n(s) \cdot \Psi_{nm}(\theta). \tag{4.6}$$

The factors $\frac{1}{4}$ and $\frac{1}{2}$ in front of the first three summands are often used to simplify the definition of the coefficients a_{nm}, b_{nm} [122], but are not strictly necessary. Mapping the height parameter s to the respective height section z will be discussed in the measurement models in the following sections. The Fourier series [68, 122] used in the double series (4.6) can be given as

$$\Psi_{nm}(\theta) = a_{nm} \cdot \cos(m\theta) + b_{nm} \cdot \sin(m\theta). \tag{4.7}$$

This shape representation will be termed Fourier-Chebyshev double series (FCDS) in the further course of this thesis and requires $1 + n_s + 2 \cdot n_\theta + 2 \cdot n_s \cdot n_\theta$ coefficients. The respective basis functions that are superimposed in the FCDS are visualized in Fig. 4.2. Since an infinite sum

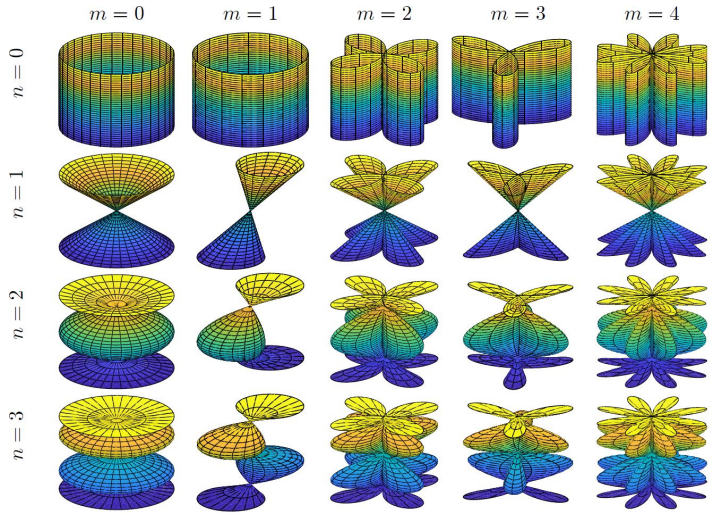

Figure 4.2: Visualization of the FCDS basis functions.

cannot be implemented, both the Fourier and Chebyshev polynomials are truncated at the final summands defined by n_θ and n_s. In the implementation, these values serve as parameters, defining the level of detail that can be reached using the respective shape definition. The higher

n_θ and n_s, the more detailed shapes can be estimated using the FCDS shape representation. However, the higher n_θ and n_s, the more information and thus measurements are needed for the convergence of the filter for shape estimation and tracking defined in the following sections. By choosing different values for n_θ and n_s, different levels of detail can be reached in the shape representation for both parameters. Approximation errors for truncated Fourier and Chebyshev series can be found in [20].

When using the FCDS shape representation in a tracking scenario, mainly measurements from the object's side facing the sensor can be expected. Therefore, modeling the object's unseen backside can be beneficial in many scenarios. An obvious approach that can easily be implemented using the FCDS shape representation is to model the backside using symmetry assumptions. By assuming a vertical plane of symmetry aligned with the orientation of the shape, the backside can be modeled as being identical to the front side. In Fig. 4.3, this modeling approach is visualized using a boat shape, which is only seen from the front side. By modeling the unseen backside using the visualized plane of symmetry, it can be modeled as being symmetrical to the front side. In the FCDS shape representation, this vertical plane of

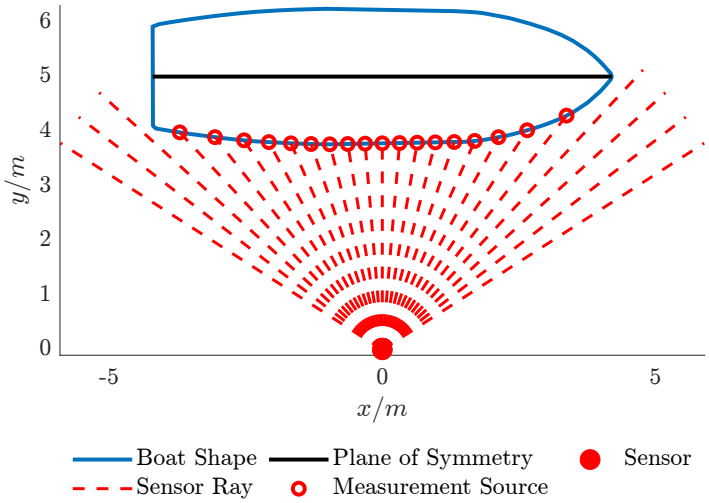

Figure 4.3: Visualization of the vertical plane of symmetry of a boat object in top-down view modeled in the FCDS shape representation.

symmetry can be integrated by forcing the function $f(\theta, s)$ to be even in the angle θ. In the shape function, this can be achieved by discarding the sinusoidal components in the Fourier series [68, 122]. The Fourier series terms $\Psi_{nm}(\theta)$ can then be given as

$$\Psi_{nm}(\theta) = a_{nm} \cdot \cos(m\theta). \tag{4.8}$$

When using this Fourier series, the number of coefficients for the shape representation reduces to a total of $1 + n_s + n_\theta + n_s \cdot n_\theta$. In the further course of this thesis, only the FCDS shape representation containing a vertical plane of symmetry is applied in the measurement models. Finally, a non-parametric 3D shape in cylindrical coordinates can then be given as

$$\underline{z}(\theta, s) = \left[f(\theta, s) \cdot \cos(\theta), f(\theta, s) \cdot \sin(\theta), s \cdot \frac{h}{2} \right]^\top \tag{4.9}$$

using the height $h > 0$ and the FCDS $f(\theta, s)$ with proper coefficients. Here, $s \in [-1, 1]$ is the normalized height parameter, and the shape's origin is located at $z = 0$. In the following sections, the measurement models for shape estimation and tracking using the FCDS shape representation can now be defined. Two measurement models associating the measurement with a measurement source located on the boundary of the FCDS shape are presented. Measurements

located in the interior of the shape can again be processed using a RAMN, presented in Sec. 4.3.4. Due to a projected association being overly computationally expensive to calculate, only a radial association on each height section is presented and investigated for the FCDS measurement models.

Remark 4.1. *The 3D shape definition applying an FCDS and a first measurement model using this shape representation was originally published in [O8]. In this thesis, a further measurement model based on the FCDS as shape representation is presented and investigated.*

4.3.2 FCDS 3D GAM Measurement Model

The first measurement model to be defined using the FCDS shape representation, which was presented in [O8], is a 3D GAM. The system state for shape estimation and tracking to be estimated can then be given as

$$\underline{x}_{\mathrm{kin}_k} = \left[\underline{m}_k^\top, \phi_k, \underline{x}_{\mathrm{vel}_k}^\top\right]^\top, \tag{4.10a}$$

$$\underline{x}_{\mathrm{ext}_k} = \left[h_k, a_{00_k}, a_{10_k}, \ldots, a_{n_s n_{\theta k}}\right]^\top \tag{4.10b}$$

comprising the 3D position $\underline{m}_k$, the yaw angle ϕ_k, and the dynamics $\underline{x}_{\mathrm{vel}_k}$ in the kinematic state $\underline{x}_{\mathrm{kin}_k}$. The extent state $\underline{x}_{\mathrm{ext}_k}$ comprises the height h_k and the FCDS shape coefficients a_{nm}. In this extent state definition, the FCDS shape description comprising a vertical plane of symmetry is used. If the symmetry assumption is to be omitted, the coefficients b_{nm} must also be included in the extent state. The yaw angle ϕ_k is again modeled to be aligned with the velocity, and roll and pitch angles are assumed to be negligible. Due to the Chebyshev polynomials being defined in the interval $s \in [-1, 1]$, the position $\underline{m}_k$ is located in the center of the FCDS shape rather than at the base shape as was the case for the elliptic cylinder 3D GAM.

For the 3D GAM, both parameters are greedily associated with the boundary of the FCDS shape. Therefore, the measurement in local coordinates $\underline{\tilde{y}}_{k,l}$ must first be calculated using (3.3). Then, a greedy estimate for the extrusion factor can be calculated as

$$\hat{s}_{k,l} = \min\left(\max\left(\frac{2 \cdot \tilde{y}_{k,l}^{(z)}}{h_{k|k-1}}, -1\right), 1\right). \tag{4.11}$$

For the greedy association of the angular parameter $\hat{\theta}_{k,l}$, only a radial association is implemented and investigated for the FCDS shape representation. A projected association could also be implemented using the details given in section 2.4.2. However, the shape approximation would have to be calculated individually for each height section, resulting in an overly computationally intensive procedure. The radial association of the angular parameter can be given as

$$\hat{\theta}_{k,l} = \mathrm{atan2}\left(\tilde{y}_{k,l}^{(y)}, \tilde{y}_{k,l}^{(x)}\right). \tag{4.12}$$

Given the greedy estimates for the FCDS shape parameters and the parametric equation for the FCDS shape (4.9), a measurement source in local coordinates using a radial association can be calculated as

$$\tilde{\underline{z}}_{\mathrm{rad}}\left(\underline{\hat{x}}_{k|k-1}, \underline{\tilde{y}}_{k,l}\right) = \left[\tilde{\underline{z}}_{\mathrm{rad}}^{(xy)}\left(\underline{\hat{x}}_{k|k-1}, \underline{\tilde{y}}_{k,l}\right)^\top, \hat{s}_{k,l} \cdot \frac{h_{k|k-1}}{2}\right]^\top \tag{4.13a}$$

$$= \left[f\left(\hat{\theta}_{k,l}, \hat{s}_{k,l}\right) \cdot \cos\left(\hat{\theta}_{k,l}\right), f\left(\hat{\theta}_{k,l}, \hat{s}_{k,l}\right) \cdot \sin\left(\hat{\theta}_{k,l}\right), \hat{s}_{k,l} \cdot \frac{h_{k|k-1}}{2}\right]^\top. \tag{4.13b}$$

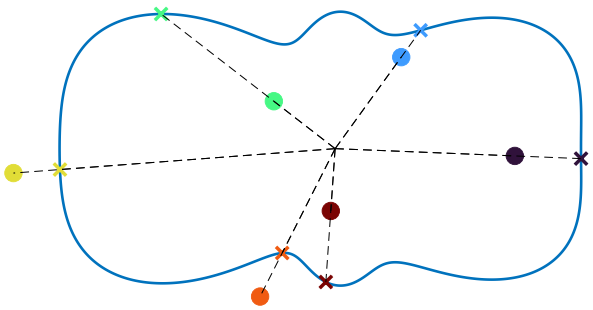

Figure 4.4: FCDS radial measurement source association. Measurements as balls, and measurement sources as crosses. Related items are displayed in the same color.

The FCDS radial measurement source association is visualized in Fig. 4.4. A measurement equation in global coordinates can then finally be formulated as

$$\underline{\hat{y}}_{k,l} = \underline{m}_{k|k-1} + \mathbf{R}(\phi_{k|k-1}) \cdot \begin{bmatrix} \tilde{z}_{\mathrm{rad}}^{(xy)} \left(\underline{\hat{x}}_{k|k-1}, \underline{\tilde{y}}_{k,l} \right) \\ \hat{s}_{k,l} \cdot \frac{h_{k|k-1}}{2} \end{bmatrix} - \underline{y}_{k,l} + \underline{v}_{k,l} \tag{4.14a}$$

$$= \underline{z}_{\mathrm{GAM}} \left(\underline{\hat{x}}_{k|k-1}, \underline{\tilde{y}}_{k,l} \right) + \underline{v}_{k,l} \tag{4.14b}$$

using the 3D rotation matrix $\mathbf{R}(\phi_{k|k-1})$ defined in (3.3). In the measurement update of the nonlinear Kalman filter, the predicted measurement $\underline{\hat{y}}_{k,l}$ can then again be associated with the pseudo-measurement $\underline{0}_3$ in (2.11b). Please note that the measurement equation could also be defined in local coordinates instead of global coordinates, which would not result in any difference in the estimation quality. Implementation details for the FCDS 3D GAM can be found in Sec. 4.4.1.

4.3.3 FCDS quasi-ERHM Measurement Model

Due to the missing penalization for overestimated heights in the 3D GAM [34], an ERHM comparable to the elliptic cylinder model is also desirable for the FCDS measurement model. However, due to the nonlinear nature of the extrusion parameter s in the FCDS shape, which can be interpreted as multiplicative noise [142], the quadratic estimator [49], which was also applied in [14], and also the symmetry assumptions from Sec. 2.4.3 are no longer valid for the ERHM in a straightforward manner. Therefore, it is assumed that the position in z and the height h are statistically independent of the rest of the system state and can be estimated in a separate filter. Both estimates are then used in a second filter for estimating the remainder of the full system state. This procedure enables an unbiased height estimate in combination with a proper shape estimate. However, an estimation error can potentially be introduced by assuming that the position in z and height h are statistically independent of the rest of the system state. A discussion of this can be found in the results in the following sections and Ch. 6. Following this, the full procedure is referred to as quasi-ERHM.

In the first step, the position in z and the height h need to be estimated, as the results are needed in the second filter. The system state for estimating a line segment in the z direction is then given as

$$\underline{x}_{\mathrm{line}_k} = \left[m_k^{(z)}, h_k \right] \tag{4.15}$$

comprising the position $m_k^{(z)}$ in z and the height h_k. A parametric equation representing each point on the line segment can be given as

$$z(s) = s \cdot h \tag{4.16}$$

using the parameter $s \in [0, 1]$. To be able to apply symmetry assumptions in the measurement update of the line estimator, the extrusion factor is assumed to be uniformly distributed as $s_{k,l} \sim \mathcal{U}(0, 1)$ for each measurement. In the measurement update, the z coordinates of the measurements can then be mapped to the non-redundant part of the line object. Details can be found in Sec. 2.4.3. The measurement equation for the line estimator can be given as

$$\hat{y}_{k,l}^{(z)} = s_{k,l} \cdot \frac{h_{k|k-1}}{2} - |y_{k,l}^{(z)} - m_{k|k-1}^{(z)}| + v_{k,l}^{(z)} \tag{4.17}$$

where the extrusion factor $s_{k,l}$ is subject to sampling for each measurement individually. Please note that for the line estimator, the origin of the local coordinate system is also positioned in the middle of the line due to the symmetry assumptions applied in the measurement equation. The line estimator, however, still estimates the full height of the object. In the measurement update of the nonlinear Kalman filter, the predicted measurement can then be associated with the pseudo-measurement 0 in (2.16b), however, using a scalar instead of a vector-valued residual.

Given an unbiased height estimate, the remainder of the full system state can be estimated using a 3D GAM without estimating the height and position in z. The system state to be estimated for this second filter in the quasi-ERHM can then be given as

$$\underline{x}_{\mathrm{kin}_k} = \left[\underline{m}_k^{(xy)^\top}, \phi_k, \underline{x}_{\mathrm{vel}_k}^\top\right]^\top, \tag{4.18a}$$

$$\underline{x}_{\mathrm{ext}_k} = \left[a_{00_k}, a_{10_k}, \ldots, a_{n_s n_{\theta_k}}\right]^\top \tag{4.18b}$$

comprising the 2D position $\underline{m}_k^{(xy)}$, the yaw angle ϕ_k, and the dynamics $\underline{x}_{\mathrm{vel}_k}$ in the kinematic state $\underline{x}_{\mathrm{kin}_k}$. The extent state $\underline{x}_{\mathrm{ext}_k}$ only comprises the FCDS shape coefficients a_{nm}. In this extent state definition again, the FCDS shape description comprising a vertical plane of symmetry is used. If the symmetry assumption is to be omitted, the coefficients b_{nm} must also be included in the extent state. The yaw angle ϕ_k is again modeled to be aligned with the velocity, and roll and pitch angles are assumed to be negligible. Using the estimated line state, the shape parameters θ and s can now greedily be associated with the boundary of the FCDS shape. Therefore, the measurement in local coordinates $\underline{\tilde{y}}_{k,l}$ must be calculated using (3.3). Please note that for calculating the measurement in local coordinates, the estimated position $m_k^{(z)}$ from the line filter must be used in addition to the predicted 2D position $\underline{m}_k^{(xy)}$. The greedy estimate for the normalized height parameter $\hat{s}_{k,l}$ can then be calculated using (4.11). Please note that for calculating the greedy estimate of the extrusion factor, the estimated height h_k of the line estimator must be used. The greedy estimate for the angular parameter $\hat{\theta}_{k,l}$ can then finally be calculated using (4.12). Given both estimates for the FCDS shape parameters and the parametric equation for the FCDS shape (4.9), a measurement source projected onto the xy plane in local coordinates using a radial association can be calculated as

$$\underline{\tilde{z}}_{\mathrm{rad}}\left(\underline{\hat{x}}_{k|k-1}, \underline{\tilde{y}}_{k,l}\right) = \underline{\tilde{z}}_{\mathrm{rad}}^{(xy)}\left(\underline{\hat{x}}_{k|k-1}, \underline{\tilde{y}}_{k,l}\right)^\top \tag{4.19a}$$

$$= \left[f\left(\hat{\theta}_{k,l}, \hat{s}_{k,l}\right) \cdot \cos\left(\hat{\theta}_{k,l}\right), f\left(\hat{\theta}_{k,l}, \hat{s}_{k,l}\right) \cdot \sin\left(\hat{\theta}_{k,l}\right)\right]^\top. \tag{4.19b}$$

Please note that the measurement source is only calculated in xy coordinates, as this is sufficient for estimating the desired system state in this second filter. A measurement equation in global coordinates can then finally be formulated as

$$\underline{\hat{y}}_{k,l} = \underline{m}_{k|k-1}^{(xy)} + \mathbf{R}_{\mathrm{2D}}(\phi_{k|k-1}) \cdot \underline{\tilde{z}}_{\mathrm{rad}}^{(xy)}\left(\underline{\hat{x}}_{k|k-1}, \underline{\tilde{y}}_{k,l}\right) - \underline{y}_{k,l}^{(xy)} + \underline{v}_{k,l} \tag{4.20a}$$

$$= \underline{z}_{\mathrm{ERHM}}\left(\underline{\hat{x}}_{k|k-1}, \underline{\tilde{y}}_{k,l}\right) + \underline{v}_{k,l} \tag{4.20b}$$

using the 2D rotation matrix

$$\mathbf{R}_{2\mathrm{D}}(\phi) = \begin{pmatrix} \cos(\phi) & -\sin(\phi) \\ \sin(\phi) & \cos(\phi) \end{pmatrix}. \tag{4.21}$$

In the measurement update of the nonlinear Kalman filter, the predicted measurement can then be associated with the pseudo-measurement $\underline{0}_2$ in (2.11b). Implementation details for the full quasi-ERHM can be found in Sec. 4.4.2. Fig. 4.5 shows a flowchart of the quasi-ERHM process to illustrate the procedure once again.

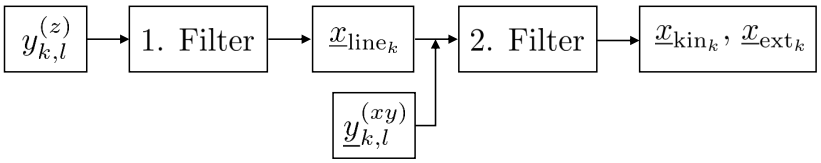

Figure 4.5: Flowchart of the quasi-ERHM estimation procedure.

Extrusion Factor Distribution In the quasi-ERHM presented before, the extrusion factor in the line estimator is assumed to be uniformly distributed. However, as was also discussed for the elliptic cone in Sec. 3.4.2, the probability density function (PDF) of the extrusion factor should ideally scale linearly with the perimeter of the shape at each height section if it is to resemble a uniform distribution of measurements on the full 3D surface of the object. Given the estimated FCDS shape parameters, the perimeters of the shape on each height section can be calculated using the FCDS (4.6). This perimeter function can then be transformed into a distribution for the extrusion factor s, which can be used for sampling in the nonlinear Kalman filter update step of the line estimator. The perimeter of the shape at each height section can be calculated as

$$\rho(s) = \int_{\theta=0}^{2\pi} f(\theta, s)\,\mathrm{d}\,\theta \tag{4.22a}$$

$$= \pi \cdot \left(\frac{a_{00}}{2} + \sum_{n=1}^{n_s} a_{n0} \cdot T_n(s) \right). \tag{4.22b}$$

Please note that the perimeter $\rho(s)$ is only dependent on the shape coefficients a_{00} and a_{n0}. To transform the perimeter function into a distribution, a normalization factor is needed so that the distribution integrates to 1. This normalization factor can be calculated as

$$\xi = \int_{s=-1}^{1} \rho(s)\,\mathrm{d}\,s \tag{4.23a}$$

$$= \pi \cdot \int_{s=-1}^{1} \frac{a_{00}}{2} + \sum_{n=1}^{n_s} a_{n0} \cdot T_n(s)\,\mathrm{d}\,s \tag{4.23b}$$

$$= \pi \cdot \left(a_{00} + \sum_{n\,\mathrm{even}}^{n_s} a_{n0} \cdot \frac{(-1)^n + 1}{1 - n^2} \right). \tag{4.23c}$$

Given the perimeter function $\rho(s)$ and the normalization factor ξ, an extrusion factor distribution, given an estimated shape, can be calculated as

$$p(s|x_{\mathrm{ext}}) = \frac{\rho(s)}{\xi} \tag{4.24a}$$

$$= \frac{1}{\xi} \cdot \left(\frac{a_{00}}{2} + \sum_{n=1}^{n_s} a_{n0} \cdot T_n(s) \right). \tag{4.24b}$$

In the quasi-ERHM, this extrusion factor distribution could now be used for sampling the extrusion factor for each measurement in the line estimator. However, neither the UKF nor the smart sampling Kalman filter (S2KF) sampling procedures are capable of sampling from an arbitrary distribution directly. Also, the inverse transform sampling technique [104] applied for the elliptic cone ERHM cannot be applied for sampling since no closed-form expression for the inverse of the extrusion factor cumulative distribution function (CDF) is available. Thus, the extrusion factor distribution would need to be approximated as a Gaussian distribution to sample from the approximated distribution. Calculating the mean and variance of the approximated Gaussian distribution is possible in closed form and can be performed using a symbolic math toolbox.

However, using the approximated Gaussian extrusion factor distribution for sampling in the measurement update of the nonlinear Kalman filter has some disadvantages. Due to the extrusion factor not being uniformly distributed anymore, symmetry assumptions as applied in the measurement equation of the line estimator (4.17) cannot be included anymore. As a consequence, a quadratic extension as described in Sec. 2.4.3 must be introduced to the measurement equation (4.17), and an S2KF rather than an UKF must be applied for inference. Furthermore, initial experiments have shown that the influence of an incorrectly assumed distribution for the extrusion factor might be low. Therefore, in the further course of this thesis, a uniformly distributed extrusion factor is applied in the FCDS quasi-ERHM, and the investigation on applying the calculated extrusion factor distribution $p(s|x_{\text{ext}})$ in the measurement update is left for future work.

4.3.4 Recursive Artificial Measurement Noise for FCDS

Also in the measurement models applying an FCDS shape description, measurements are initially assumed to be generated from the object's boundary. However, if measurements are also gathered from the object's interior, an estimation bias towards the object's center can be introduced. Therefore, a RAMN can be added to the measurement update for processing measurements from the interior of the object. The equations for the parameter estimation of the RAMN can be found in Sec. 2.6.1. For the FCDS shape representation, it is sufficient to calculate the RAMN parameters only for xy coordinates and to use the measurement noise induced by the sensor for the z coordinate.

Since the shape of the FCDS varies at each height section, a greedy estimate for the extrusion factor $\hat{s}_{k,l}$ must be calculated using (4.11), the measurement in local coordinates (3.3), and the predicted system state, to be able to calculate the "inside-outside" information. Furthermore, a greedy estimate for the angular parameter $\hat{\theta}_{k,l}$ must be calculated for each measurement using (4.12). The information for each measurement being inside the boundary of the FCDS shape and outside the $3\sigma_{\underline{v}}$ surrounding of the boundary can then be calculated using the implicit equation

$$\mathcal{I}(\underline{\tilde{y}}_{k,l}, \underline{\hat{x}}_{k|k-1}) = \|\underline{\tilde{y}}_{k,l}\| - (f(\hat{\theta}_{k,l}, \hat{s}_{k,l}) - 3 \cdot \sigma_{\underline{v}}) = \begin{cases} > 0: & \text{outside} \\ = 0: & 3\sigma_{\underline{v}} \text{ boundary} \\ < 0: & \text{inside} \end{cases} \tag{4.25}$$

using the predicted system state $\underline{\hat{x}}_{k|k-1}$ and the measurement in local coordinates $\underline{\tilde{y}}_{k,l}$. A visualization of the measurement separation needed for calculating the RAMN parameters for the FCDS measurement models can be seen in Fig. 4.6. The Euclidean distances needed for the calculation are then directly given using the respective measurement source and (3.10). The final

measurement noise covariance can be generated using (3.11b). The artificial measurement noise mean (3.11a) can be added to the predicted measurement. Further details on the implementation can be found in Sec. 4.4.

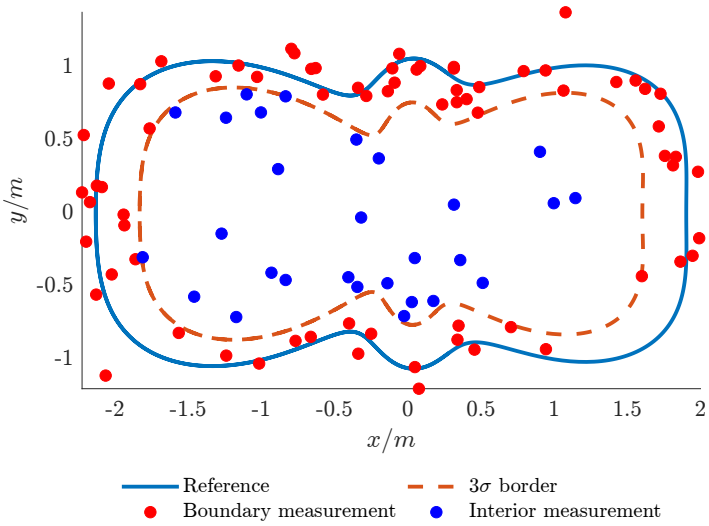

Figure 4.6: Visualization of the measurement separation for the RAMN estimation of the FCDS shape representation at a single height section.

4.4 Implementation Details

After presenting the FCDS measurement models, implementation details on both procedures are given in this section. In particular, pseudo-code for the FCDS 3D GAM and the FCDS quasi-ERHM EOT algorithms is given. The implementation details again focus only on the update step in the respective Kalman filters. Further details on the prediction step can be found in the respective literature, such as [19, 27, 66]. For both measurement association procedures applying an FCDS shape representation, the measurement update can be performed using an EKF, as this filter is the least complex one applicable to both measurement models. Furthermore, the EKF can be considered the most efficient filter among the nonlinear Kalman filters applied in this thesis. The line estimator in the quasi-ERHM is instead implemented using an UKF since the extrusion factor in the respective measurement model is subject to sampling for an update. Details are given in the following sections.

Remark 4.2. *In addition to the pseudo-code given in this section, an implementation of the FCDS measurement models can be found at [R3].*

4.4.1 FCDS 3D GAM Implementation Details

In this section, the implementation details for the FCDS 3D GAM are given. In the first step, details for the sequential batch EKF measurement update are discussed. The pseudo-code can be found in Alg. 4.1. The difference between both filters for the FCDS measurement models in the sequential batch EKF update can then only be found in line 4, where the predicted measurements and measurement matrices are calculated. The following lines 5–13 in the loop are the same for both measurement models. The artificial measurement noise mean and covariance matrix in line 6 for the FCDS shape description can be generated using the ”inside-outside“ function (4.25) and the procedure described in Sec. 4.3.4.

Algorithm 4.1 Sequential batch EKF measurement update

Require:

predicted state $\underline{\hat{x}}_{k|k-1}$, predicted state covariance $\mathbf{P}_{k|k-1}$, measurements $\mathcal{Y}_k$, single update measurement number n_u

1: set $\underline{\hat{x}}_1 = \underline{\hat{x}}_{k|k-1}$, $\mathbf{P}_1 = \mathbf{P}_{k|k-1}$
2: **for** $n \leftarrow 1$ **to** $\lfloor n_k/n_u \rfloor$ **do**
3: get $\left\{\underline{y}_{n,l}\right\}_{l=1}^{n_u}$ from $\mathcal{Y}_k$ using next n_u measurements
4: predicted measurements $\left\{\underline{\hat{y}}_{n,l}\right\}_{l=1}^{n_u}$ and measurement matrices $\{\mathbf{H}_{n,l}\}_{l=1}^{n_u}$
5: RAMN parameters $\hat{\mu}_n^{(i,\eta)}$, $\hat{\mathrm{v}}_n^{(i,\eta)}$ using Sec. 2.6.1 and "inside-outside" function
6: measurement noise parameters $\underline{\hat{\mu}}_{\underline{v}_{n,l}}$, $\mathbf{\Sigma}_{\underline{v}_{n,l}}$ using (3.11a) and (3.11b)
7: stack predicted measurements ${}^{s}\underline{\hat{y}}_n = \left[\left(\underline{\hat{y}}_{n,1} + \underline{\hat{\mu}}_{\underline{v}_{n,1}}\right)^{\top}, \ldots, \left(\underline{\hat{y}}_{n,n_u} + \underline{\hat{\mu}}_{\underline{v}_{n,n_u}}\right)^{\top}\right]^{\top}$
8: stack measurement noise covariance matrices ${}^{s}\mathbf{\Sigma}_{\underline{v}_n}$ using (2.19)
9: stack measurement matrices ${}^{s}\mathbf{H}_n$ using (2.17)
10: innovation covariance matrix $\mathbf{S}_n = {}^{s}\mathbf{H}_n \cdot \mathbf{P}_n \cdot {}^{s}\mathbf{H}_n{}^{\top} + {}^{s}\mathbf{\Sigma}_{\underline{v}_n}$
11: Kalman Gain $\mathbf{K}_n = \mathbf{P}_n \cdot {}^{s}\mathbf{H}_n{}^{\top} \cdot \mathbf{S}_n^{-1}$
12: updated state mean vector $\underline{\hat{x}}_{n+1} = \underline{\hat{x}}_n + \mathbf{K}_n \cdot \left(\underline{0} - {}^{s}\underline{\hat{y}}_n\right)$
13: updated state covariance matrix $\mathbf{P}_{n+1} = \mathbf{P}_n - \mathbf{K}_n \cdot {}^{s}\mathbf{H}_n \cdot \mathbf{P}_n$
14: **end for**
15: set $\underline{\hat{x}}_k = \underline{\hat{x}}_{n+1}$, $\mathbf{P}_k = \mathbf{P}_{n+1}$

The pseudo-code for implementing line 4 in Alg. 4.1 for the FCDS 3D GAM can be found in Alg. 4.2. Within this algorithm, the measurement prediction is completely described in Sec. 4.3.2 and can be directly used for the implementation. A transformation function for one-sided constraints (2.38) is only applied to the height in this algorithm, to prevent the height from becoming negative.

The equations still missing are the ones for the Jacobi matrix needed for the measurement update in the EKF [27] and are given in this section. In the following derivation, the Jacobi matrix for a single measurement is presented. The stacked full measurement matrix can then be generated using the structure shown in (2.17). The final Jacobi matrix can be given as

$$\mathbf{H}_{k,l} = \left.\frac{\partial\, \underline{y}_{k,l}}{\partial\, \underline{x}}\right|_{\underline{x}=\underline{x}_{k|k-1}} = \left[\frac{\partial\, \underline{y}_{k,l}}{\partial\, \underline{m}}, \frac{\partial\, \underline{y}_{k,l}}{\partial\, \phi}, \frac{\partial\, \underline{y}_{k,l}}{\partial\, \underline{x}_{\mathrm{vel}}}, \frac{\partial\, \underline{y}_{k,l}}{\partial\, h}, \frac{\partial\, \underline{y}_{k,l}}{\partial\, \underline{a}_{nm}}\right] \in \mathbb{R}^{3\times n_x}, \tag{4.26}$$

where $\frac{\partial\, \underline{y}_{k,l}}{\partial\, \underline{x}_{\mathrm{vel}}} = \mathbf{0}$ and $\frac{\partial\, \underline{y}_{k,l}}{\partial\, \underline{a}_{nm}}$ represents the derivative with respect to every shape coefficient in the FCDS. In the following derivation, the time index k and measurement index l are omitted.

Position Derivatives: In the first step, the derivatives with respect to the position $\underline{m}$ can be calculated. The full derivative is given as

$$\frac{\partial\, \underline{y}}{\partial\, \underline{m}} = I_3 + \mathbf{R}(\phi) \cdot \begin{bmatrix} \frac{\partial\, f(\hat{\theta},\hat{s})}{\partial\, \underline{m}} \cdot \cos(\hat{\theta}) + f(\hat{\theta},\hat{s}) \cdot \frac{\partial\, cos(\hat{\theta})}{\partial\, \underline{m}} \\ \frac{\partial\, f(\hat{\theta},\hat{s})}{\partial\, \underline{m}} \cdot \sin(\hat{\theta}) + f(\hat{\theta},\hat{s}) \cdot \frac{\partial\, sin(\hat{\theta})}{\partial\, \underline{m}} \\ \frac{\partial\, \hat{s}}{\partial\, \underline{m}} \cdot \frac{\tilde{h}}{2} \end{bmatrix} \in \mathbb{R}^{3\times 3}, \tag{4.27}$$

Algorithm 4.2 FCDS 3D GAM measurement prediction

1: extract $\underline{x}_{\text{kin}_n}$ from $\hat{\underline{x}}_n$
2: extract shape parameters $\underline{x}_{\text{ext}_n}$ from $\hat{\underline{x}}_n$
3: extract constrained height $\tilde{h}_n = c_1(h_n, 0)$ with lower bound from $\underline{x}_{\text{ext}_n}$ using (2.38)
4: **for** $l \leftarrow 1$ **to** n_u **do**
5: measurement in local coordinates $\tilde{\underline{y}}_{n,l}$ using (3.3), and $\underline{\boldsymbol{x}}_{\text{kin}_n}$
6: measurement source $\tilde{\underline{z}}_{n,l}\left(\underline{x}_{\text{ext}_n}, \tilde{h}_n, \tilde{\underline{y}}_{n,l}\right)$ using (4.13)
7: measurement matrix $\mathbf{H}_{n,l}\left(\hat{\underline{x}}_n, \underline{y}_{n,l}\right)$ using (4.26)
8: predicted measurement $\hat{\underline{y}}_{n,l} = \underline{m}_{k|k-1} + \mathbf{R}(\phi_{k|k-1}) \cdot \tilde{\underline{z}}_{n,l} - \underline{y}_{n,l}$
9: **end for**

with the expressions

$$\frac{\partial f(\hat{\theta}, \hat{s})}{\partial \underline{m}} = \left[\frac{\partial f(\hat{\theta}, \hat{s})}{\partial \hat{\theta}}, \frac{\partial f(\hat{\theta}, \hat{s})}{\partial \hat{s}}\right] \cdot \left[\frac{\partial \hat{\theta}}{\partial \underline{m}}, \frac{\partial \hat{s}}{\partial \underline{m}}\right]^\top, \tag{4.28}$$

$$\frac{\partial f(\hat{\theta}, \hat{s})}{\partial \hat{\theta}} = \frac{1}{2} \cdot \sum_{m=1}^{n_\theta} \frac{\partial \Psi_{0m}(\hat{\theta})}{\partial \hat{\theta}} + \sum_{n=1}^{n_s} \sum_{m=1}^{n_\theta} T_n(\hat{s}) \cdot \frac{\partial \Psi_{nm}(\hat{\theta})}{\partial \hat{\theta}}, \tag{4.29}$$

$$\frac{\partial \Psi_{nm}(\hat{\theta})}{\partial \hat{\theta}} = -m \cdot a_{nm} \cdot \sin(m\hat{\theta}), \tag{4.30}$$

$$\frac{\partial f(\hat{\theta}, \hat{s})}{\partial \hat{s}} = \frac{1}{2} \cdot \sum_{n=1}^{n_s} a_{n0} \cdot T_n'(\hat{s}) + \sum_{n=1}^{n_s} \sum_{m=1}^{n_\theta} T_n'(\hat{s}) \Psi_{nm}(\hat{\theta}), \tag{4.31}$$

for the radial function $f(\theta, s)$. Please note that the derivatives for the first nine Chebyshev polynomials are given in (4.3). Also, for the derivative of the Fourier series $\frac{\partial \Psi_{nm}(\hat{\theta})}{\partial \hat{\theta}}$, the series comprising a vertical plane of symmetry is assumed. The derivative of the full Fourier series can be calculated straightforwardly. Furthermore, the derivatives

$$\frac{\partial \hat{\theta}}{\partial \underline{m}} = \frac{\partial \hat{\theta}}{\partial \tilde{\underline{y}}} \cdot \frac{\partial \tilde{\underline{y}}}{\partial \underline{m}}, \qquad \frac{\partial \hat{s}}{\partial \underline{m}} = \frac{\partial \hat{s}}{\partial \tilde{\underline{y}}} \cdot \frac{\partial \tilde{\underline{y}}}{\partial \underline{m}}, \qquad \frac{\partial \tilde{\underline{y}}}{\partial \underline{m}} = -\mathbf{R}(\phi)^{-1}, \tag{4.32}$$

$$\frac{\partial \hat{\theta}}{\partial \tilde{\underline{y}}} = \left[-\frac{\tilde{y}^{(y)}}{\tilde{y}^{(x)^2} + \tilde{y}^{(y)^2}}, \frac{\tilde{y}^{(x)}}{\tilde{y}^{(x)^2} + \tilde{y}^{(y)^2}}, 0\right], \qquad \frac{\partial \hat{s}}{\partial \tilde{\underline{y}}} = \left[0, 0, \begin{cases} 0 & -\frac{\tilde{h}}{2} > \tilde{y}^{(z)} > \frac{\tilde{h}}{2} \\ \frac{2}{\tilde{h}} & \text{else} \end{cases}\right], \tag{4.33}$$

$$\frac{\partial \cos(\hat{\theta})}{\partial \underline{m}} = -\sin(\hat{\theta}) \cdot \frac{\partial \hat{\theta}}{\partial \underline{m}}, \qquad \frac{\partial \sin(\hat{\theta})}{\partial \underline{m}} = \cos(\hat{\theta}) \cdot \frac{\partial \hat{\theta}}{\partial \underline{m}} \tag{4.34}$$

are needed for the position derivatives with $\tilde{\underline{y}}$ being the measurement in local coordinates, which can be calculated using (3.3).

Orientation Derivatives: In the next step, the derivatives with respect to the orientation ϕ can be calculated. The full derivative is given as

$$\frac{\partial \underline{y}}{\partial \phi} = \frac{\partial \mathbf{R}(\phi)}{\partial \phi} \cdot \begin{bmatrix} f(\hat{\theta}, \hat{s}) \cdot \cos(\hat{\theta}) \\ f(\hat{\theta}, \hat{s}) \cdot \sin(\hat{\theta}) \\ \hat{s} \cdot \frac{\tilde{h}}{2} \end{bmatrix} + \mathbf{R}(\phi) \cdot \begin{bmatrix} \frac{\partial f(\hat{\theta}, \hat{s})}{\partial \phi} \cdot \cos(\hat{\theta}) + f(\hat{\theta}, \hat{s}) \cdot \frac{\partial \cos(\hat{\theta})}{\partial \phi} \\ \frac{\partial f(\hat{\theta}, \hat{s})}{\partial \phi} \cdot \sin(\hat{\theta}) + f(\hat{\theta}, \hat{s}) \cdot \frac{\partial \sin(\hat{\theta})}{\partial \phi} \\ \frac{\partial \hat{s}}{\partial \phi} \cdot \frac{\tilde{h}}{2} \end{bmatrix} \in \mathbb{R}^3, \tag{4.35}$$

using the expressions

$$\frac{\partial f(\hat{\theta}, \hat{s})}{\partial \phi} = \left[\frac{\partial f(\hat{\theta}, \hat{s})}{\partial \hat{\theta}}, \frac{\partial f(\hat{\theta}, \hat{s})}{\partial \hat{s}}\right] \cdot \left[\frac{\partial \hat{\theta}}{\partial \phi}, \frac{\partial \hat{s}}{\partial \phi}\right]^\top, \tag{4.36}$$

$$\frac{\partial\,\hat{\theta}}{\partial\,\phi} = \frac{\partial\,\hat{\theta}}{\partial\,\underline{\tilde{y}}} \cdot \frac{\partial\,\underline{\tilde{y}}}{\partial\,\phi}, \qquad \frac{\partial\,\hat{s}}{\partial\,\phi} = \frac{\partial\,\hat{s}}{\partial\,\underline{\tilde{y}}} \cdot \frac{\partial\,\underline{\tilde{y}}}{\partial\,\phi}, \qquad \frac{\partial\,\underline{\tilde{y}}}{\partial\,\phi} = -\frac{\partial\,\mathbf{R}(\phi)^{-1}}{\partial\,\phi} \cdot (\underline{y} - \underline{m}), \tag{4.37}$$

$$\frac{\partial\,\cos(\hat{\theta})}{\partial\,\phi} = -\sin(\hat{\theta}) \cdot \frac{\partial\,\hat{\theta}}{\partial\,\phi}, \qquad \frac{\partial\,\sin(\hat{\theta})}{\partial\,\phi} = \cos(\hat{\theta}) \cdot \frac{\partial\,\hat{\theta}}{\partial\,\phi}. \tag{4.38}$$

The differentiation of the inverse rotation matrix $\frac{\partial\,\mathbf{R}(\phi)^{-1}}{\partial\,\phi}$ can be performed element-wise.

Height Derivatives: Now, the derivatives with respect to the height h can be calculated. The full derivative can be given as

$$\frac{\partial\,\underline{y}}{\partial\,h} = \mathbf{R}(\phi) \cdot \begin{bmatrix} \frac{\partial\,f(\hat{\theta},\hat{s})}{\partial\,h} \cdot \cos(\hat{\theta}) \\ \frac{\partial\,f(\hat{\theta},\hat{s})}{\partial\,h} \cdot \sin(\hat{\theta}) \\ \frac{\partial\,\hat{s}}{\partial\,h} \cdot \frac{\tilde{h}}{2} + \frac{\hat{s}}{2} \cdot \frac{\partial\,c_1(h,0)}{\partial\,h} \end{bmatrix} \in \mathbb{R}^3, \tag{4.39}$$

where $c_1(h,0)$ is the constraining function (2.38) with a lower bound 0. Furthermore, the equations

$$\frac{\partial\,f(\hat{\theta},\hat{s})}{\partial\,h} = \frac{\partial\,f(\hat{\theta},\hat{s})}{\partial\,\hat{s}} \cdot \frac{\partial\,\hat{s}}{\partial\,h}, \qquad \frac{\partial\,c_1(h,0)}{\partial\,h} = \frac{\exp(h)}{\exp(h)+1} \tag{4.40}$$

$$\frac{\partial\,\hat{s}}{\partial\,h} = \begin{cases} 0 & -\frac{\tilde{h}}{2} > \tilde{y}^{(z)} > \frac{\tilde{h}}{2} \\ -\frac{\exp(h)\cdot\tilde{y}^{(z)}}{(\exp(h)+1)\cdot\log^2(\exp(h)+1)} & \text{else} \end{cases} \tag{4.41}$$

are needed for the height derivatives.

Shape Derivatives: Finally, the derivatives with respect to the shape parameters $\underline{a}_{nm}$ can be calculated. The full derivative can be given as

$$\frac{\partial\,\underline{y}}{\partial\,\underline{a}_{nm}} = \mathbf{R}(\phi) \begin{bmatrix} \frac{\partial\,f(\hat{\theta},\hat{s})}{\partial\,\underline{a}_{nm}} \cdot \cos(\hat{\theta}) \\ \frac{\partial\,f(\hat{\theta},\hat{s})}{\partial\,\underline{a}_{nm}} \cdot \sin(\hat{\theta}) \\ 0 \end{bmatrix} \in \mathbb{R}^{3\times(1+n_s+n_\theta+n_s\cdot n_\theta)}, \tag{4.42}$$

using the derivatives of the radial function with respect to the shape coefficients

$$\frac{\partial\,f(\hat{\theta},\hat{s})}{\partial\,\underline{a}_{nm}} = \left[\frac{1}{4}, \frac{1}{2} \cdot T_1(\hat{s}), \ldots, \frac{1}{2} \cdot \cos(\hat{\theta}), \ldots, T_1(\hat{s}) \cdot \cos(\hat{\theta}), \ldots\right]. \tag{4.43}$$

Please note that the derivatives with respect to the shape coefficients also represent the derivatives assuming a Fourier series comprising a vertical plane of symmetry. The derivatives of the full Fourier series can again be calculated straightforwardly.

4.4.2 FCDS quasi-ERHM Implementation Details

In this section, implementation details for the FCDS quasi-ERHM are given. As described in Sec. 4.3.3, the state estimation is split into two filters for the FCDS quasi-ERHM. In the first step, the line state $\underline{x}_{\text{line}}$ must be updated. Due to the line estimator being implemented as a symmetrical ERHM, according to Sec. 2.4.3, an UKF can be applied for state estimation. The pseudo-code for the sequential batch linear regression Kalman filter (LRKF), which is a generalization of the UKF, can be found in Alg. 3.1. In this algorithm, lines 3–5 must now only be specified for the line estimator applied in the FCDS quasi-ERHM. The pseudo-code for implementing these three lines can be found in Alg. 4.3. For the line estimator, measurement sources are assumed to be uniformly distributed in normalized height $s \sim \mathcal{U}(0,1)$ to associate

the measurements to the non-redundant part of the line object. To sample from this uniform distribution in the UKF, the same procedure as described for the elliptic cylinder ERHM in Sec. 3.5.1 is also applied for the line estimator. By extending the system state with the parameters of a standard Gaussian distribution $\mu_s = 0$ and $\sigma_s^2 = 1$ and transforming the samples through the CDF of the standard Gaussian distribution $\Phi(s)$, as depicted in line 8, uniformly distributed extrusion factor samples in the interval $[0, 1]$ can be generated. For the line estimator, the transformation function for one-sided constraints (2.38) is applied to the height to prevent the height from becoming negative.

Algorithm 4.3 Line UKF measurement prediction

1: extended distribution parameters $\underline{x}_u = \left[\hat{\underline{x}}_n^\top, \underline{0}_{n_u}^\top\right]^\top$, $\mathbf{P}_u = \text{blkdiag}\left(\mathbf{P}_n, \mathbf{I}_{n_u}\right)$
2: sigma points $\left\{\underline{\boldsymbol{x}}_{n,j}, \boldsymbol{w}_{n,j}\right\}_{j=1}^{n_s}$ using [130] and $\underline{x}_u$, $\mathbf{P}_u$
3: get $\left\{\underline{y}_{n,l}\right\}_{l=1}^{n_u}$ from $\mathcal{Y}_k$ using next n_u measurements
4: **for** $j \leftarrow 1$ **to** n_s **do**
5: extract $m_{n,j}^{(z)}$ from $\underline{\boldsymbol{x}}_{n,j}$
6: extract constrained $\tilde{\hbar}_{n,j} = c_1(\hbar_{n,j}, 0)$ with lower bound from $\underline{\boldsymbol{x}}_{n,j}$ using (2.38)
7: **for** $l \leftarrow 1$ **to** n_u **do**
8: extract extrusion factor sample $\tilde{\jmath}_{n,j,l} = \frac{1}{2}\left(1 + \text{erf}\left(\frac{\jmath_{n,j,l}}{\sqrt{2}}\right)\right)$ from $\underline{\boldsymbol{x}}_{n,j}$
9: predicted measurement $\hat{\underline{\boldsymbol{y}}}_{n,j,l} = \tilde{\jmath}_{n,j,l} \cdot \frac{\tilde{\hbar}_{n,j}}{2} - |y_{n,l}^{(z)} - m_{n,j}^{(z)}|$
10: **end for**
11: **end for**

After having updated the line state, the remaining system state for shape estimation and tracking using an FCDS shape representation can be updated. The remaining system state can then again be updated using an EKF as before for the FCDS 3D GAM. The pseudo-code for the sequential batch EKF can be found in Alg. 4.1. In this filter, the measurement prediction and the generation of the measurement noise parameters are left to be specified for the FCDS quasi-ERHM. The pseudo-code for the measurement prediction can be found in Alg. 4.4. Please note that the constraints for the height are already ensured in the line estimator, and no further constraints are needed in this second filter stage. Within this algorithm, again, the procedure is adequately described using the pseudo-code and Sec. 4.3.3 except for the Jacobian of the measurement equation needed as the measurement matrix in the EKF.

Algorithm 4.4 FCDS quasi-ERHM measurement prediction

1: extract $\underline{x}_{\text{kin}_n}$ from $\hat{\underline{x}}_n$
2: extract shape parameters $\underline{x}_{\text{ext}_n}$ from $\hat{\underline{x}}_n$
3: extract height $\tilde{h}_k = c_1(h_k, 0)$ with lower bound from $\underline{x}_{\text{line}_k}$ using (2.38)
4: **for** $l \leftarrow 1$ **to** n_u **do**
5: measurement in local coordinates $\tilde{\underline{y}}_{n,l}$ using (3.3), $\underline{\boldsymbol{x}}_{\text{kin}_n}$, and $\underline{x}_{\text{line}_k}$
6: measurement source $\tilde{\underline{z}}_{n,l}\left(\underline{x}_{\text{ext}_n}, \tilde{h}_k, \tilde{\underline{y}}_{n,l}\right)$ using (4.19)
7: measurement matrix $\mathbf{H}_{n,l}\left(\hat{\underline{x}}_n, \underline{y}_{n,l}\right)$ using (4.44)
8: predicted measurement $\hat{\underline{y}}_{n,l} = \underline{m}_{k|k-1}^{(xy)} + \mathbf{R}_{\text{2D}}(\phi_{k|k-1}) \cdot \tilde{\underline{z}}_{n,l} - \underline{y}_{n,l}^{(xy)}$
9: **end for**

The derivation of the Jacobian for the FCDS quasi-ERHM is given in this section. The final Jacobi matrix can be given as

$$\mathbf{H}_{k,l} = \left.\frac{\partial\, \underline{y}_{k,l}^{(xy)}}{\partial\, \underline{x}}\right|_{\underline{x}=\underline{x}_{k|k-1}} = \left[\frac{\partial\, \underline{y}_{k,l}^{(xy)}}{\partial\, \underline{m}^{(xy)}}, \frac{\partial\, \underline{y}_{k,l}^{(xy)}}{\partial\, \phi}, \frac{\partial\, \underline{y}_{k,l}^{(xy)}}{\partial\, \underline{x}_{\mathrm{vel}}}, \frac{\partial\, \underline{y}_{k,l}^{(xy)}}{\partial\, \underline{a}_{nm}}\right] \in \mathbb{R}^{2\times n_x}, \tag{4.44}$$

where $\frac{\partial\, \underline{y}_{k,l}^{(xy)}}{\partial\, \underline{x}_{\mathrm{vel}}} = \mathbf{0}$ and $\frac{\partial\, \underline{y}_{k,l}^{(xy)}}{\partial\, \underline{a}_{nm}}$ again represents the derivative with respect to every shape coefficient in the FCDS. In the following derivation, the time index k and measurement index l are omitted. Please note that the full measurement matrix has lower dimensionality in the FCDS quasi-ERHM compared to the 3D GAM since the measurement equation is only defined in the xy plane. In the following derivation, only the derivatives that vary from the measurement matrix derivatives of the 3D GAM are given. Missing equations can be found in Sec. 4.4.1.

Position Derivatives: In the first step, the derivatives with respect to the 2D position $\underline{m}^{(xy)}$ can be calculated. The full derivative is given as

$$\frac{\partial\, \underline{y}^{(xy)}}{\partial\, \underline{m}^{(xy)}} = I_2 + \mathbf{R}_{2\mathrm{D}}(\phi) \cdot \begin{bmatrix} \frac{\partial\, f(\hat{\theta},\hat{s})}{\partial\, \underline{m}^{(xy)}} \cdot \cos(\hat{\theta}) + f(\hat{\theta},\hat{s}) \cdot \frac{\partial\, cos(\hat{\theta})}{\partial\, \underline{m}^{(xy)}} \\ \frac{\partial\, f(\hat{\theta},\hat{s})}{\partial\, \underline{m}^{(xy)}} \cdot \sin(\hat{\theta}) + f(\hat{\theta},\hat{s}) \cdot \frac{\partial\, sin(\hat{\theta})}{\partial\, \underline{m}^{(xy)}} \end{bmatrix} \in \mathbb{R}^{2\times 2}, \tag{4.45}$$

using the expression

$$\frac{\partial\, f(\hat{\theta},\hat{s})}{\partial\, \underline{m}^{(xy)}} = \frac{\partial\, f(\hat{\theta},\hat{s})}{\partial\, \hat{\theta}} \cdot \frac{\partial\, \hat{\theta}}{\partial\, \underline{m}^{(xy)}}, \tag{4.46}$$

for the radial function $f(\theta, s)$. Please note that the derivative of the FCDS with respect to the 2D position is not dependent on the extrusion factor $\hat{s}$ anymore, as it was for the FCDS 3D GAM. Also, again, for the derivative of the Fourier series, the series comprising a vertical plane of symmetry is assumed. Furthermore, the derivatives

$$\frac{\partial\, \hat{\theta}}{\partial\, \underline{m}^{(xy)}} = \frac{\partial\, \hat{\theta}}{\partial\, \underline{\tilde{y}}^{(xy)}} \cdot \frac{\partial\, \underline{\tilde{y}}^{(xy)}}{\partial\, \underline{m}^{(xy)}}, \qquad \frac{\partial\, \underline{\tilde{y}}^{(xy)}}{\partial\, \underline{m}^{(xy)}} = -\mathbf{R}_{2\mathrm{D}}(\phi)^{-1}, \tag{4.47}$$

$$\frac{\partial\, \hat{\theta}}{\partial\, \underline{\tilde{y}}^{(xy)}} = \left[-\frac{\tilde{y}^{(y)}}{\tilde{y}^{(x)^2} + \tilde{y}^{(y)^2}}, \frac{\tilde{y}^{(x)}}{\tilde{y}^{(x)^2} + \tilde{y}^{(y)^2}}\right] \tag{4.48}$$

are needed for the position derivatives with $\underline{\tilde{y}}^{(xy)}$ being the xy coordinates of the measurement in local coordinates, which can be calculated using (3.3).

Orientation Derivatives: In the next step, the derivatives with respect to the orientation ϕ can be calculated. The full derivative is given as

$$\begin{aligned}\frac{\partial\, \underline{y}^{(xy)}}{\partial\, \phi} = \frac{\partial\, \mathbf{R}_{2\mathrm{D}}(\phi)}{\partial\, \phi} \cdot \begin{bmatrix} f(\hat{\theta},\hat{s}) \cdot \cos(\hat{\theta}) \\ f(\hat{\theta},\hat{s}) \cdot \sin(\hat{\theta}) \end{bmatrix} \\ + \mathbf{R}_{2\mathrm{D}}(\phi) \cdot \begin{bmatrix} \frac{\partial\, f(\hat{\theta},\hat{s})}{\partial\, \phi} \cdot \cos(\hat{\theta}) + f(\hat{\theta},\hat{s}) \cdot \frac{\partial\, \cos(\hat{\theta})}{\partial\, \phi} \\ \frac{\partial\, f(\hat{\theta},\hat{s})}{\partial\, \phi} \cdot \sin(\hat{\theta}) + f(\hat{\theta},\hat{s}) \cdot \frac{\partial\, \sin(\hat{\theta})}{\partial\, \phi} \end{bmatrix} \in \mathbb{R}^2,\end{aligned} \tag{4.49}$$

using the expressions

$$\frac{\partial\, f(\hat{\theta},\hat{s})}{\partial\, \phi} = \frac{\partial\, f(\hat{\theta},\hat{s})}{\partial\, \hat{\theta}} \cdot \frac{\partial\, \hat{\theta}}{\partial\, \phi}, \tag{4.50}$$

$$\frac{\partial\, \hat{\theta}}{\partial\, \phi} = \frac{\partial\, \hat{\theta}}{\partial\, \underline{\tilde{y}}^{(xy)}} \cdot \frac{\partial\, \underline{\tilde{y}}^{(xy)}}{\partial\, \phi}, \qquad \frac{\partial\, \underline{\tilde{y}}^{(xy)}}{\partial\, \phi} = -\frac{\partial\, \mathbf{R}_{2\mathrm{D}}(\phi)^{-1}}{\partial\, \phi} \cdot (\underline{y}^{(xy)} - \underline{m}^{(xy)}). \tag{4.51}$$

The differentiation of the inverse 2D rotation matrix $\frac{\partial \mathbf{R}_{2\mathrm{D}}(\phi)^{-1}}{\partial \phi}$ can be performed element-wise.

Shape Derivatives: Finally, the derivatives with respect to the shape parameters $\underline{a}_{nm}$ can be calculated. The full derivative can be given as

$$\frac{\partial \underline{y}^{(xy)}}{\partial \underline{a}_{nm}} = \mathbf{R}_{2\mathrm{D}}(\phi) \begin{bmatrix} \frac{\partial f(\hat{\theta},\hat{s})}{\partial \underline{a}_{nm}} \cdot \cos(\hat{\theta}) \\ \frac{\partial f(\hat{\theta},\hat{s})}{\partial \underline{a}_{nm}} \cdot \sin(\hat{\theta}) \end{bmatrix} \in \mathbb{R}^{2\times(1+n_s+n_\theta+n_s\cdot n_\theta)}, \tag{4.52}$$

Please note that the derivatives with respect to the shape coefficients also represent the derivatives assuming a Fourier series comprising a vertical plane of symmetry.

For the measurement noise parameters in the FCDS quasi-ERHM, the RAMN parameters can be calculated using the measurement source (4.19), the "inside-outside" function (4.25), and the procedure described in Sec. 2.6.1. The measurement noise parameters can then be generated as

$$\hat{\underline{\mu}}_{\underline{v}_{k,l}} = \begin{cases} \left[\hat{\mu}_k^{(i,x)}, \hat{\mu}_k^{(i,y)}\right]^\top & \text{if inside} \\ [0,0]^\top & \text{else} \end{cases} \tag{4.53a}$$

$$\mathbf{\Sigma}_{\underline{v}_{k,l}} = \begin{cases} \mathrm{diag}\left(\hat{\mathrm{v}}_k^{(i,x)}, \hat{\mathrm{v}}_k^{(i,y)}\right) & \text{if inside} \\ \mathrm{diag}(\sigma_{\underline{v}}^2, \sigma_{\underline{v}}^2) & \text{else} \end{cases} \tag{4.53b}$$

since the measurement equation of the FCDS quasi-ERHM is only defined in the xy plane. Having provided the implementation details for both FCDS measurement models, the algorithms can be evaluated and compared in the following section.

4.5 Experiments

In this section, the FCDS measurement models are evaluated and compared in a simulation study. In the first scenario, the FCDS measurement models are compared to shape estimation and tracking approaches where the shape is represented as a radial function in spherical coordinates. In the second simulation study, the RAMN for the FCDS shape estimation procedure is investigated in a simulated scenario. Both investigations are conducted for a static scenario, as the most basic challenge for shape estimation and tracking. Also, in both investigations, measurements are gathered from a static cuboid. Details on the simulation environments are given in the respective sections.

In every scenario, the estimation results are evaluated using the orientation and height root mean square errors (RMSEs) as was done in Sec. 3.6. However, for the FCDS shape description, no shape parameters can be applied for an evaluation of the shape estimation quality in an RMSE. Therefore, the shape estimation performance of the FCDS measurement models is measured using the intersection over union (IoU) [93]. The IoU can be calculated as

$$\mathrm{IoU} = \frac{\mathrm{area}(S_r \cap S_e)}{\mathrm{area}(S_r \cup S_e)} \tag{4.54}$$

with S_r being the reference shape and S_e the estimated one. However, a general IoU in 3D space is not easy to calculate since the intersection and union of two arbitrary shapes need to be calculated. Therefore, when calculating the IoU in 3D space in this thesis, the reference and estimated shapes are discretized in 20 height sections from bottom to top. For each height section, the 2D IoU is calculated. Using shape approximations as a polygonal chain, the intersection and union of both shapes can easily be calculated. The final 3D IoU is then

taken as the mean value over all 2D IoUs. The IoU is a measure that incorporates the position, orientation, height, and shape estimate into a single value. The orientation and height RMSEs are reported as well due to their specific interest.

In addition to the RMSE and IoU measures, the calculation time divided by the number of measurements at each time step is reported for each method evaluated in the following sections. Each calculation is conducted using MATLAB R2023b on an Intel(R) Xeon(R) X5680 CPU with 3.33 GHz. For a better comparability regarding the computation time, the sequential batch measurement update procedure presented in Sec. 2.3.3 is applied for each measurement model used in the following investigation.

4.5.1 Comparison to Shape Representations in Spherical Coordinates

In the first experiment, the FCDS shape measurement models are compared to shape estimation and tracking approaches applying shape representations in spherical coordinates. For the comparison, three different shape representations in spherical coordinates are applied:

- spherical double Fourier series (SDFS): The SDFS shape representation [21] is a specialized DFS for shape representations in spherical coordinates applied for 3D EOT in [O7]. Since shape representations in cylindrical coordinates have proven to be superior in maritime applications, the SDFS shape representation is only used as a comparison method and not further described in this thesis. The filter is implemented using an UKF as proposed in [O7], but can also be implemented using an EKF. For the SDFS shape representation, 13 shape coefficients are estimated by the filter in this investigation.
- spherical harmonics (SH): The SH basis functions are specialized functions on a sphere that result from solving Laplace's equation in the spherical domain [6]. In [87], the SH basis is applied for expanding radial functions in the spherical domain. The resulting filter can be implemented using an UKF. For the SH shape representation, 49 shape coefficients are estimated by the filter in this investigation.
- 3D Gaussian process (GP): The 3D GP shape representation presented in [30, 84, 85] can be seen as a generalization of [129] where a GP is applied for representing a 2D radial function. For the 3D generalization, azimuth and elevation angle pairs are mapped to the respective radius in the 3D GP for representing the 3D shape. The filter can be implemented using an EKF as proposed by [85]. For the 3D GP shape representation, the radii of 401 equidistantly placed angle pairs on the unit sphere are estimated by the filter in this investigation. An arbitrary number of equidistantly placed points on a unit sphere can be generated using Fibonacci lattices [56].

A different number of coefficients is used in the estimation for each shape representation. These are chosen so that the methods examined can estimate a similar level of detail in the shape representation. For the FCDS shape representation, 24 shape coefficients are estimated by the respective filter in this investigation.

In the first experiment presented in this section, the shape representations in spherical coordinates are compared to the FCDS 3D GAM and quasi-ERHM algorithms presented before. Therefore, a simulated scenario with 100 time steps is generated where measurements are only taken from the lateral surface of a static cuboid. This experiment is intended to illustrate the effects on shape representations in spherical coordinates compared to a shape representation in cylindrical coordinates when measurements from the top and bottom surfaces are missing. The measurement source generation process is similar to the simulated scenarios presented before. The z coordinates of the measurements are sampled uniformly distributed using the

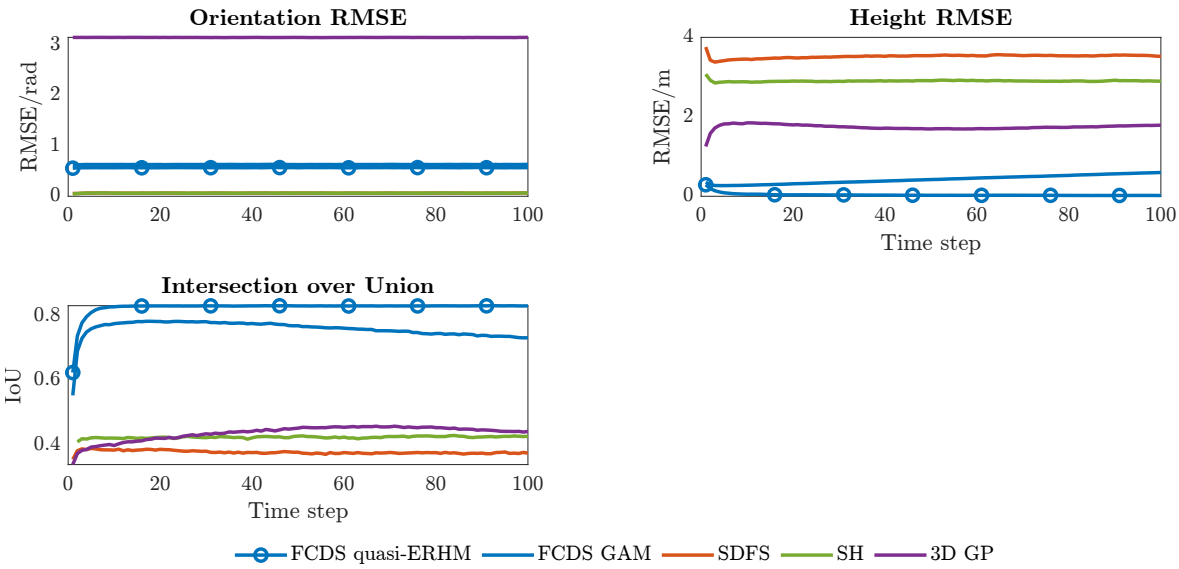

Figure 4.7: Monte Carlo (MC) simulation RMSE and IoU estimation results of the static simulation experiment comparing the FCDS shape representation to spherical shape representations.

Table 4.1: Mean computation times per measurement for the FCDS measurement model and the comparison methods.

Algorithm	Computation time
FCDS ERHM with RAMN	23.44 µs
FCDS ERHM without RAMN	19.22 µs
FCDS 3D GAM with RAMN	16.77 µs
FCDS 3D GAM without RAMN	14.34 µs
SDFS	58.43 µs
SH	298.45 µs
3D GP	2.98 ms

normalized height parameter $s \sim \mathcal{U}(0,1)$ and then multiplied by the reference height of the simulated cuboid. Sampling the angular parameter at a specific height section can also be realized by sampling from the uniform distribution $\theta \sim \mathcal{U}(0, 2\pi)$ and passing the sampled parameter through a rectangular radial function, which can be defined as a piecewise function. An implementation can be found at [R3]. The measurement noise, sampled from the Gaussian distribution $v \sim \mathcal{N}(0, 0.1^2)$ for each dimension, can then be added to the measurement source. In each time step, 50 measurements are generated and processed in a sequential batch update with $n_u = 20$ measurements for each method. The filters are initialized using the first measurement set. Details can be found at [R3]. Due to no measurements being generated from the interior of the object, the RAMN estimation procedure for the FCDS shape measurement models is omitted in this scenario.

The mean values of the orientation and height RMSEs and the mean IoUs after an MC simulation with 100 runs are depicted in Fig. 4.7. Especially for the height RMSE and the IoU, it can be seen that the FCDS shape representation is superior to the spherical shape representations in this scenario. Due to the missing measurements and, therefore, the missing information at the top and bottom surfaces of the cuboid, the spherical shapes are estimated

to be much higher than the reference. In the spherical shape representations, the height is not estimated explicitly but can be extracted using the estimated shape parameters. The IoU of each shape representation in spherical coordinates is worse than that of the FCDS shape representation due to the overestimated heights. On the other hand, in the FCDS shape representation, the height is estimated explicitly. In addition, the shape representation itself is a more natural representation of the present measurement distribution.

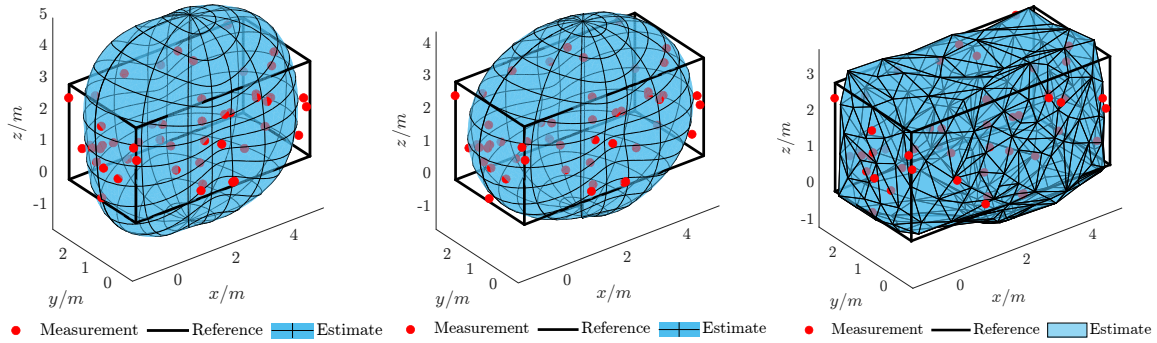

(a) Estimation results of the first experiment for the spherical shape representations. SDFS on the left, SH in the middle, and a 3D GP on the right.

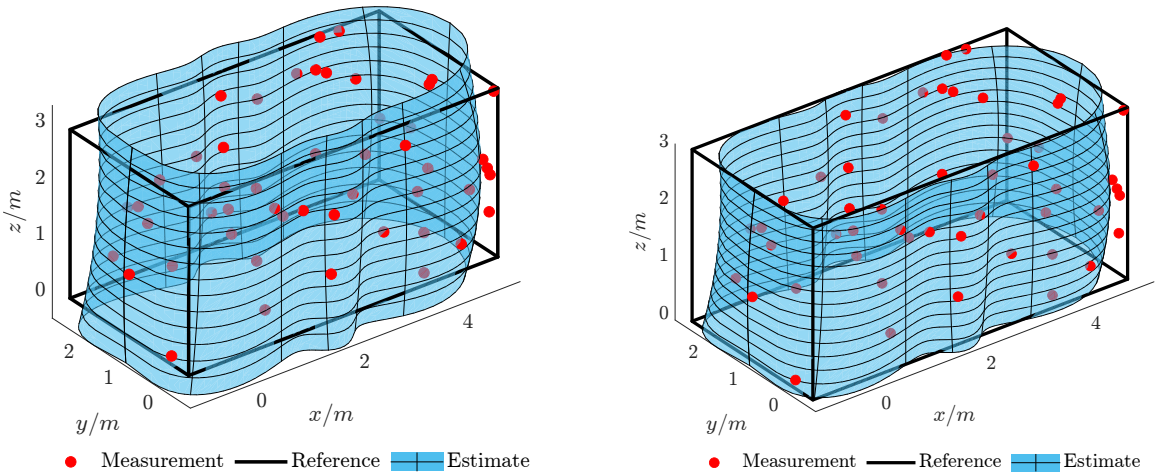

(b) Estimation results of the first experiment for the FCDS shape representations. A 3D GAM on the left and a quasi-ERHM on the right.

Figure 4.8: Estimation results of the first experiment comparing the FCDS shape representation measurement model to spherical shape representation measurement models. Estimates are at the same time step with the same random seed for the measurement generation.

Comparing the 3D GAM and quasi-ERHM FCDS algorithms, it can be seen that the 3D GAM has problems with height estimation, which is why the IoU also drops within the scenario. Due to the missing penalization for overestimated heights, as was also seen for the elliptic cylinder 3D GAM in Sec. 3.6.1, the height estimates keep growing within the entire scenario. On the other hand, the height estimates of the FCDS quasi-ERHM converge to a static unbiased value and exhibit the highest IoU measure among all compared algorithms. Handling the line state and the remaining system state statistically independent in two different filters for the FCDS quasi-ERHM generates promising results in this scenario. However, since the scenario shows no dynamics in the reference object, further investigations must be carried out. These can be found in Ch. 6. The estimates of the yaw angle reveal huge errors, which can be ascribed

to the fact that the shapes are symmetric and the angle is a periodic variable, which is why ambiguities in the estimates can occur. However, the orientation RMSEs converge in each implementation, which indicates a reliable angle estimation. In future work, either a specialized transformation function comparable to the procedure presented in Sec. 2.5 or results based on directional statistics [54, 88] could be applied to resolve these ambiguities.

In addition to the quantitative estimation results, the mean computation times per measurement for each method are depicted in Tab. 4.1. For a better comparability among all methods, the FCDS measurement models with the RAMN estimation procedure, investigated in the following experiment, are also contained in this table. It can be seen that the FCDS measurement models exhibit the lowest computation time among all methods compared in this section. Furthermore, no drastic difference in the computation time between the 3D GAM and the quasi-ERHM without RAMN can be seen. The computation times of the FCDS measurement models with the RAMN estimation procedure are discussed in the following scenario.

Finally, the qualitative estimation results for each method after 50 time steps and 2500 processed measurements are visualized in Fig. 4.8. In the figure, the estimated shapes of the comparison methods in spherical coordinates are depicted in the first row in Fig. 4.8a. The estimation results of the FCDS measurement models can be seen in the second row in Fig. 4.8b. For the shape estimates in spherical coordinates, it can be seen that each shape is estimated to be higher than the actual reference due to the missing measurements at the top and bottom surfaces. In the areas where measurements are present, the methods in spherical coordinates converge. These results again illustrate the disadvantages of spherical shape EOT methods if mainly measurements from the lateral surface of an object can be expected. On the other hand, both FCDS measurement models exhibit a better performance than the spherical methods. However, the 3D GAM overestimates the height of the object as expected, whereas the quasi-ERHM provides an unbiased height estimate and produces the best overall results in this scenario.

4.5.2 Investigation of the FCDS Models with Artificial Measurement Noise

In the second scenario, the FCDS measurement models in combination with the RAMN estimation procedure are investigated in another simulated static scenario. Therefore, the simulation environment applied in the first scenario is modified so that measurements are sampled from the boundary with a probability of 0.7 and from the interior with a probability of 0.3, as was presented in the previous chapter in Sec. 3.6. The measurement set in each time step is then given as a mixture of boundary and interior measurements. The remaining simulation environment and the initialization process of the FCDS methods are left unchanged. This scenario is intended to investigate the RAMN estimation procedure presented in Sec. 4.3.4 in combination with both FCDS measurement models.

The mean orientation and height RMSEs and the mean IoUs of a MC simulation with 100 runs for this scenario are depicted in Fig. 4.9. Also, in this scenario, it can be seen that the height estimates of the 3D GAM increase over the whole scenario. At the same time, the IoU measurement drops over the entire scenario. Due to the missing penalization for overestimated heights within the 3D GAM, the filter has no chance to converge. On the other hand, both FCDS quasi-ERHM methods converge for the height and IoU measures. Comparing the implementations with and without applying the RAMN estimation procedure, it can be seen that the artificial noise can provide a clear advantage in the FCDS measurement models if a mixture of boundary and interior measurements is present in the measurement set. For both methods, the IoU is higher when the RAMN is applied than when only boundary measurements

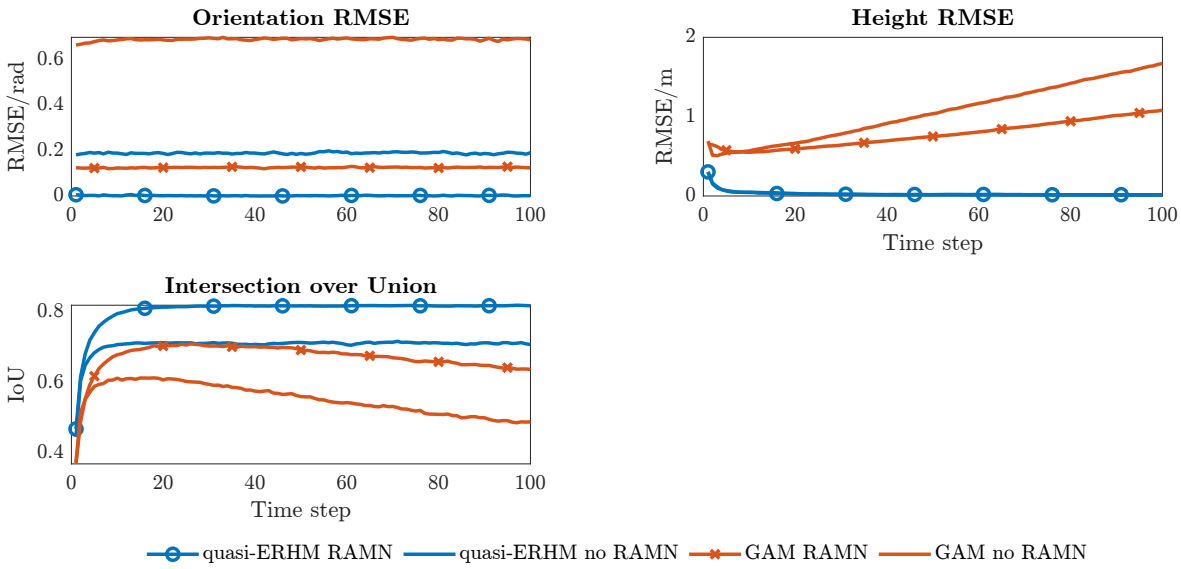

Figure 4.9: MC simulation RMSE and IoU estimation results of the static simulation experiment investigating the RAMN estimation procedure for the FCDS shape representation.

are assumed in the measurement model. The orientation estimates again show ambiguities that the filter cannot resolve in this static scenario. However, the estimates converge for each FCDS measurement model. The calculation times per measurement for each FCDS measurement source association procedure with and without applying the RAMN are given in Tab. 4.1. It can be seen that while the 3D GAM methods are the most efficient, the quasi-ERHM methods are not significantly less efficient. It is also clear that the RAMN estimation method is hardly significant in terms of computation time.

Finally, in addition to the quantitative results, the qualitative results after 50 time steps and 2500 processed measurements for this scenario are visualized in Fig. 4.10. The estimation results applying the 3D GAM are depicted in the first row in Fig. 4.10a, while the quasi-ERHM results can be seen in the second row in Fig. 4.10b. In the first column, the RAMN estimation procedure is omitted and utilized in the second column. These figures clearly show how the FCDS 3D GAM can overestimate the reference height. For both implemented versions, the shape is estimated well in the areas where measurements are simulated, however, it is highly error-prone in the height estimate and also in the shape estimates where no measurements are gathered. On the other hand, the FCDS quasi-ERHM results both exhibit an unbiased height estimate in combination with well-estimated shape information. For both measurement source association procedures, the shape estimates are biased towards the center of the object when the RAMN is omitted. The best overall performance is provided by the FCDS quasi-ERHM applying the RAMN estimation procedure.

4.6 Conclusions

This chapter addressed the need for flexible shape representations within the 3D EOT framework presented in Ch. 2, especially for scenarios where object classes are unknown a priori or parametric models do not provide sufficient accuracy. Building on the proven advantages of shape representations in cylindrical coordinates for maritime environment perception, a novel non-parametric shape representation based on an FCDS has been introduced. This

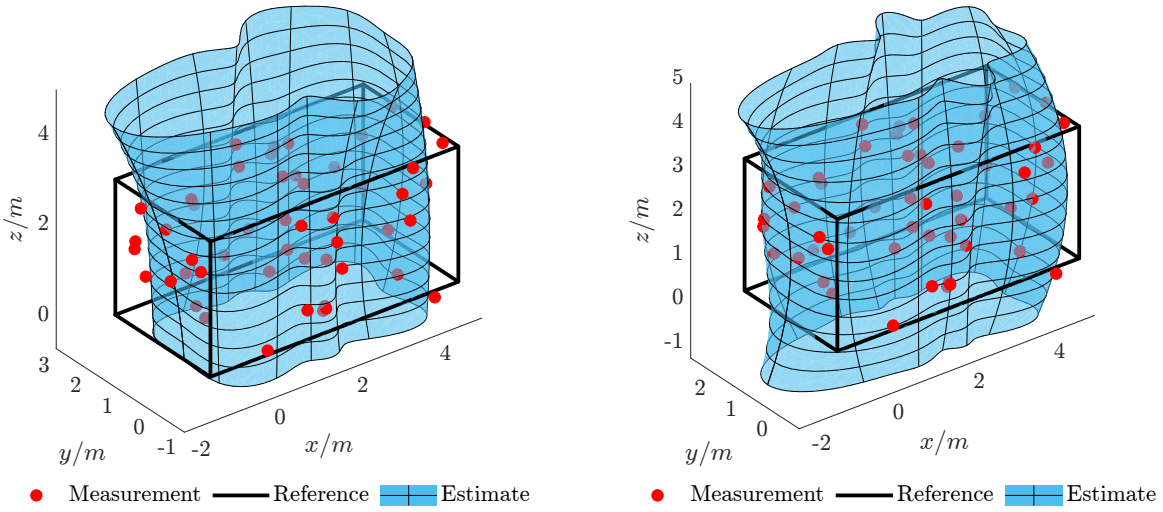

(a) Estimation results of the second experiment investigating the RAMN estimation procedure for the FCDS shape representation in a 3D GAM.

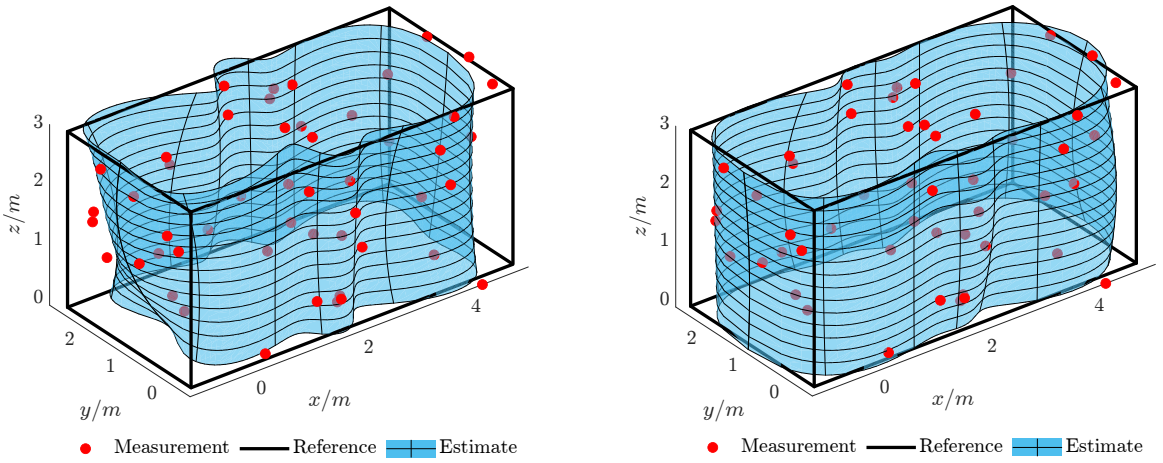

(b) Estimation results of the second experiment investigating the RAMN estimation procedure for the FCDS shape representation in a quasi-ERHM.

Figure 4.10: Estimation results of the second experiment investigating the RAMN estimation procedure for the FCDS shape representation. Estimates are at the same time step with the same random seed for the measurement generation.

representation uniquely combines periodic Fourier series for the angular dimension with non-periodic Chebyshev polynomials for the height dimension, allowing for flexible modeling of shapes that are star-convex only within horizontal slices, a potentially less restrictive constraint than global star-convexity required by shape representations in spherical coordinates. The most important finding from the comparative experiments is the clear advantage of the FCDS shape representation in cylindrical coordinates over established shape representations in spherical coordinates when processing measurement data characteristic of maritime scenarios where lateral surface measurements are predominant and measurements from the top and bottom surfaces are often missing.

In addition, the comparison between the two proposed FCDS measurement models revealed important findings. The developed quasi-ERHM FCDS approach, which decouples the estimation of the height and z position using a line estimator from the remaining system state, proved effective in overcoming the height estimation errors inherent in the simpler 3D GAM approach.

This confirms the system state decoupling strategy as a practical method for achieving unbiased height estimates using the FCDS shape representation in a 3D EOT measurement model. Finally, the integration of the RAMN estimation approach also proved beneficial for this non-parametric shape representation integrated into a 3D EOT measurement model. In simulations with mixed boundary and interior measurements, the RAMN approach improved the shape estimation accuracy for both the 3D GAM and the quasi-ERHM FCDS measurement models compared to the assumption of pure boundary measurements. Combining the quasi-ERHM FCDS and RAMN approach provided the most accurate and robust results in these initial static tests. Therefore, this chapter's findings validate the FCDS shape representation as a promising approach for flexible 3D EOT. The quasi-ERHM method enhanced by the RAMN approach proved particularly effective in these initial tests and warrants further evaluation in dynamic and real-world scenarios.

CHAPTER 5

Flexible Parametric Shapes: Superellipses

Contents

5.1 Motivation and Contributions 81
5.2 Related Work 82
5.3 Superellipses as Shape Representation 83
5.4 Superellipse measurement models 84
5.4.1 2D Measurement Model 85
5.4.2 3D Measurement Models 86
5.4.3 Recursive Artificial Measurement Noise for the Superellipse Shape 88
5.5 Implementation Details 89
5.6 Experiments 91
5.7 Conclusions 94

5.1 Motivation and Contributions

In the previous chapter, a non-parametric shape description applying a Fourier-Chebyshev double series (FCDS) expansion of a radial function in cylindrical coordinates was presented as a flexible shape representation in cases where no information about the object class to be tracked is available. However, the double series shape representation also has drawbacks compared to applying parametric shape representations in the extended object tracking (EOT) measurement model. The shape coefficients in the FCDS shape representation have no direct relation to the physical shape or extent, which makes it difficult to decide how many shape coefficients to use. Furthermore, the number of measurements gathered from the object can determine the level of detail in the shape that can be estimated. This level of detail ultimately also determines the maximum number of shape coefficients that should be chosen. However, this information is either unknown, can change for each object, or over time for a single object, since the number of measurements depends on the distance of the object to the sensor. If the number of shape coefficients is chosen too high, the shape estimate can diverge since the level of information gathered in the measurements is too low. In summary, choosing the appropriate number of shape coefficients in the FCDS shape representation can be challenging.

In addition to the problem of choosing an appropriate number of shape coefficients for a shape function expansion, parametric shapes such as ellipses or rectangles are often sufficient for a multitude of different objects. Choosing parametric shapes in the EOT measurement model can have advantages such as low-dimensionality and efficiency if the state estimates do not need to be highly accurate. However, if the class of the object to be tracked is unknown, a multiple measurement model approach such as [60, 72] might be required to ensure proper

extent estimates. These multiple measurement model approaches can, however, be more computationally expensive than employing a single measurement model approach. To overcome the issues mentioned above, extruded deformable superellipses [29, 105] are chosen as a 3D shape representation in this chapter. These provide a flexible and compact representation of a wide range of parametric shapes, which can then be estimated in a single measurement model. By using superellipses as the shape representation, choosing an appropriate number of shape coefficients is no longer needed, and various parametric shapes can be estimated using a single measurement model rather than relying on a multiple measurement model approach.

Contributions Also in this chapter, several contributions are made. First, the superellipse, which is a compact representation of deformations of the elliptical shape, is presented and discussed as a possibility for shape representations in EOT in Sec. 5.3. In addition to shape deformations related to the ellipse, a tapering deformation is also introduced [115], to be able to taper the superellipse in each coordinate direction. These deformations allow a compact representation of parametric 2D shapes such as ellipses, rectangles, triangles, rhombuses, trapezoids, and various shapes in between, using only up to 5 parameters. Subsequently, the superellipse shape is used to derive several measurement models for EOT in Sec. 5.4. First, a 2D measurement model using the superellipse shape with a radial and projected measurement-to-source association is presented. This measurement model is then extended to a 3D measurement model using an extrusion random hypersurface model (ERHM) approach with a superellipse base shape. To be able to apply the recursive artificial measurement noise (RAMN) estimation procedure for the superellipse measurement models, an implicit function generating the ”inside-outside“ information is finally presented in this section. Further contributions of this chapter are the presentation of pseudo-code for the implementation in Sec. 5.5 and an evaluation of the 3D measurement models in a static simulated scenario in Sec. 5.6. In the evaluation, two different reference shapes are used to generate the measurements to examine the shape adaptability of the extruded superellipse measurement models.

5.2 Related Work

In the context of 3D EOT in a maritime area using flexible parametric shapes, no other reference could be found in the literature so far. However, applying superellipses as shape representation in 2D EOT is also proposed in [46, 50, 144]. In [50], an optimization-based geometric curve fitting algorithm for 2D EOT applying bent superellipses is proposed. The papers [46, 144] both deploy a particle filter for state estimation. In [46], an explicit measurement equation is presented, whereas [144] uses an implicit measurement equation. In comparison, the following chapter proposes an explicit measurement equation using deformable extruded superellipses, which can be implemented with an unscented Kalman filter (UKF) [76, 77]. An extruded superellipse measurement model, instead of using superquadratics, which are the natural 3D extension of superellipses, is used since measurement models in cylindrical coordinates have proven to be superior to measurement models in spherical coordinates in maritime domains [O6]. A 3D EOT measurement model using superquadratics as shape representation has been proposed in [47]. The measurement-to-source association problem for the extruded superellipse measurement models is again solved using a 3D greedy association model (GAM) [32, 35] and an ERHM [36]. In the ERHM, symmetry assumptions [36] can again be applied since the extrusion factor can be assumed to be uniformly distributed. By using symmetry assumptions in the extrusion, the quadratic extension proposed in [14] can be omitted again, and the inference can be performed using an UKF. The RAMN estimation procedure is again inspired by [80].

5.3 Superellipses as Shape Representation

Superellipses, also known as Lamé curves, are a special class of 2D curves that give a compact representation of basic parametric 2D shapes [29, 105]. Implicitly, a superellipse can be given as the set

$$\mathcal{S}(\underline{p}, a, b, \varepsilon) = \left\{ \underline{p} \in \mathbb{R}^2 \,\middle|\, F(\underline{p}, a, b, \varepsilon) = \left|\frac{p^{(x)}}{a}\right|^{\varepsilon} + \left|\frac{p^{(y)}}{b}\right|^{\varepsilon} - 1 = 0 \right\} \tag{5.1}$$

with $\underline{p} = \left[p^{(x)}, p^{(y)}\right]^\top$, and $a, b > 0$ being the major and minor semi-axes defining the extent of the superellipse, and the squareness parameter ε defining the shape. This implicit representation (5.1) describes the closed curve centered at the origin and aligned with the coordinate axes. The squareness parameter $\varepsilon \geq 0$ defines the shape of the curve. With $\varepsilon \in (0, 1)$, the superellipse describes concave, star-like shapes with a cross at the limit case of $\varepsilon \to 0$. At $\varepsilon = 1$, the shape results in a rhombus. At $\varepsilon = 2$, an ellipse can be represented using the superellipse shape representation. With $\varepsilon \in (2, \infty)$, the superellipse shape gives shapes between an ellipse and a rectangle, approaching a rectangle as $\varepsilon \to \infty$. An illustration of the superellipse shape concerning the squareness parameter ε can be seen in Fig. 5.1a.

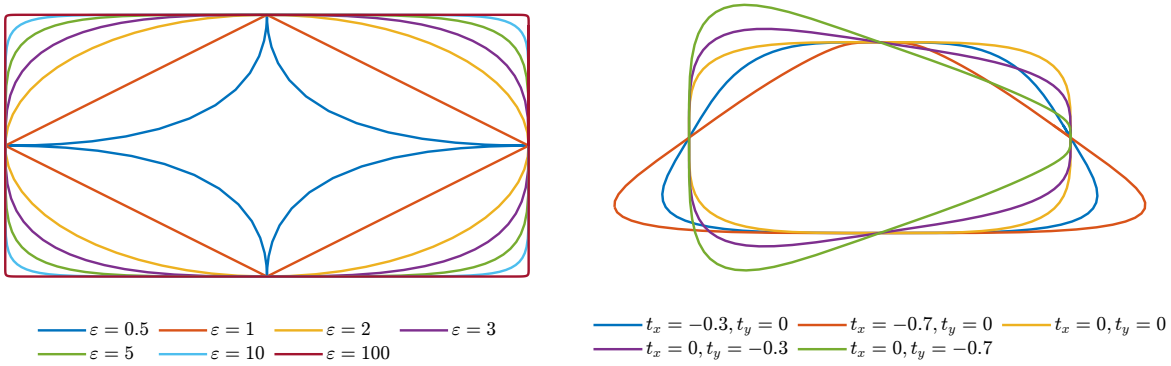

(a) Illustration of superellipses with different squareness parameters.

(b) Illustration of superellipses with different tapering parameters.

Figure 5.1: Visualization of superelliptical shape representations.

Another representation of the superellipse shape can be given explicitly using the parameter $\theta \in [0, 2\pi)$ as

$$\underline{z}(\theta) = \left[a \operatorname{sign}\big(\cos(\theta)\big) \left|\cos(\theta)\right|^{\frac{2}{\varepsilon}}, b \operatorname{sign}\big(\sin(\theta)\big) \left|\sin(\theta)\right|^{\frac{2}{\varepsilon}} \right]^\top \tag{5.2}$$

where sign() represents the sign function [29]. The explicit representation can be used to plot the superellipse.

In addition to the squareness transformation, a tapering transformation [115] for each axis can be introduced to be able to taper the shape in each direction. In doing so, shapes such as triangles and trapezoids can also be represented using superellipses. A tapering transformation $T(\underline{p})$ can be given as

$$T(\underline{p}) = \left[\left(t^{(x)} \frac{p^{(y)}}{b} + 1 \right) p^{(x)}, \left(t^{(y)} \frac{p^{(x)}}{a} + 1 \right) p^{(y)} \right]^\top \tag{5.3}$$

using the tapering coefficients $t^{(x)}, t^{(y)} \in [-1, 1]$. An inverse tapering transformation will be denoted as T^{-1} in the following. An illustration of tapered superellipses can be seen in Fig. 5.1b.

5.4 Superellipse measurement models

In this section, different measurement models for tracking objects with a superellipse shape are presented. Since the superellipse shape is less common in the EOT literature compared to ellipses or rectangles, a measurement model processing measurements in 2D space is presented first. In the next step, this measurement model is then extended as an ERHM to be able to process measurements in 3D space in an extruded superellipse shape EOT filter. The measurement models assume measurements originate from the object boundary, as measurements from the interior are processed using the RAMN estimation, which is presented in Sec. 5.4.3.

Preliminary considerations Before deriving the measurement models for the superellipse EOT filters, the system state to be estimated must be defined. The first measurement model to be derived is the model for processing 2D measurements. Thus, the system state is defined in 2D space at first. Changes to the system state for processing measurements in 3D space are given in Sec. 5.4.2. The kinematic state to be estimated is modeled as

$$\underline{x}_{\mathrm{kin}_k} = \left[\underline{m}_k^{(xy)^\top}, \phi_k, \underline{x}_{\mathrm{vel}_k}^\top\right]^\top \tag{5.4}$$

comprising the 2D position $\underline{m}_k^{(xy)}$, the orientation ϕ_k, and the dynamics $\underline{x}_{\mathrm{vel}_k}$ representing variables such as the velocity, yaw rate, or acceleration of the object. The orientation ϕ_k is modeled to be aligned with the direction of movement. The extent state can be defined individually depending on the desired flexibility of the model. More and more parameters can be added to achieve an increasingly flexible model. In the following, three possibilities for defining the extent state are given:

- $\underline{x}_{\mathrm{ext}_k} = [a_k, b_k]^\top$: The least flexible model in 2D space estimates only the extent of a specific superellipse with a fixed squareness parameter ε. However, it must be highlighted that this option can be very powerful as well if prior knowledge of the class of the object shape is available. With $t^{(x)} = t^{(y)} = 0$, which is equal to no tapering transformation, and $\varepsilon = 10$ for example, a rectangle with rounded corners similar to [O1, 79] can be described.
- $\underline{x}_{\mathrm{ext}_k} = [a_k, b_k, \varepsilon_k]^\top$: By adding the squareness parameter ε_k to the extent state, scaled versions of the shapes from Fig. 5.1a can be estimated.
- $\underline{x}_{\mathrm{ext}_k} = \left[a_k, b_k, \varepsilon_k, t_k^{(x)}, t_k^{(y)}\right]^\top$: By also adding the tapering coefficients $t_k^{(x)}, t_k^{(y)}$ to the extent state, tapering deformations, as can be seen in Fig. 5.1b, of the superellipse shape can be estimated.

In the following investigations of this thesis, the extent state comprises the semi-axes $a_k, b_k > 0$ and the squareness coefficient ε_k together with the tapering coefficient $t_k^{(y)} \in [-1, 1]$ to allow tapering deformations in the y-axis. The tapering coefficient $t_k^{(x)}$ is omitted to integrate the prior knowledge that many shapes in various tracking scenarios entail a line of symmetry in the x direction. The squareness parameter ε produces concave shapes for $\varepsilon < 1$ and convex shapes for the opposite interval. Concave shapes are generally not preferable for EOT. Therefore, the squareness parameter will be restricted as $\varepsilon_k \geq 1$.

In this thesis, the boundary of the superellipse shape in local coordinates is described by the set (5.1). Ideally, this implicit representation could be used in a measurement equation similar to [147]. However, investigations have already shown that the nonlinear nature of the squareness parameter ε makes parameter estimation very difficult [105]. Therefore, radial and projected measurement source association techniques are presented and investigated in the following sections.

5.4.1 2D Measurement Model

To derive an explicit measurement equation, the measurement source model (2.22) can be applied. However, the unknown measurement source has to be approximated. This section presents a radial measurement source association in 2D space, which can also be used for the 3D measurement model afterwards. A projected measurement source association can be calculated using the procedure presented in Sec. 2.4.2 and the explicit superellipse equation (5.2). In the following, the calculations are explicitly presented using xy coordinates, since measurements in 3D space could also be projected onto the 2D horizontal plane to apply the following measurement model.

The radial measurement source association approximates the measurement source as the intersection of the boundary and the connecting line between the center of the superellipse and the inverse tapered measurement. This approach enables an efficient analytical calculation of the measurement source. To be able to predict the measurement source, the first step is to transform the measurement to local coordinates

$$\underline{\tilde{y}}_{k,l}^{(xy)} = \mathbf{R}_{\mathrm{2D}}\left(\phi_{k|k-1}\right)^{-1} \cdot \left(\underline{y}_{k,l}^{(xy)} - \underline{m}_{k|k-1}^{(xy)}\right) \tag{5.5}$$

using the rotation matrix $\mathbf{R}_{\mathrm{2D}}(\phi)$ (4.21). If a tapering transformation is applied, the next step is to inversely taper the measurement in local coordinates $\underline{\tilde{y}}_{k,l}$. The inverse tapered measurement in local coordinates can then be given as

$${}^{t}\underline{\tilde{y}}_{k,l}^{(xy)} = T\left(\underline{\tilde{y}}_{k,l}^{(xy)}\right)^{-1} = \left[\frac{\tilde{y}_{k,l}^{(x)}}{t_{k|k-1}^{(x)} \cdot \frac{\tilde{y}_{k,l}^{(y)}}{b_{k|k-1}} + 1}, \frac{\tilde{y}_{k,l}^{(y)}}{t_{k|k-1}^{(y)} \cdot \frac{\tilde{y}_{k,l}^{(x)}}{a_{k|k-1}} + 1}\right]^{\top}. \tag{5.6}$$

If no tapering transformation is applied, the measurement in local coordinates (5.5) can be directly used in the following calculations. Given the inverse tapered measurement in local coordinates ${}^{t}\underline{\tilde{y}}_{k,l}^{(xy)}$, the intersection point for the radial association in local coordinates $\underline{\tilde{z}}_{k,l}^{(xy)}$ can analytically be calculated using

$$\left|\frac{z_{k,l}^{(x)}}{a_{k|k-1}}\right|^{\varepsilon_{k|k-1}} + \left|\frac{z_{k,l}^{(x)} \cdot {}^{t}\tilde{y}_{k,l}^{(y)}}{b_{k|k-1} \cdot {}^{t}\tilde{y}_{k,l}^{(x)}}\right|^{\varepsilon_{k|k-1}} = 1. \tag{5.7}$$

by plugging in the intersection line equation into the implicit superellipse representation (5.1) [106]. Then, the equation can be reshaped as

$$1 = \left|z_{k,l}^{(x)}\right|^{\varepsilon_{k|k-1}} \cdot \left(\left|\frac{1}{a_{k|k-1}}\right|^{\varepsilon_{k|k-1}} + \left|\frac{{}^{t}\tilde{y}_{k,l}^{(y)}}{b_{k|k-1} \cdot {}^{t}\tilde{y}_{k,l}^{(x)}}\right|^{\varepsilon_{k|k-1}}\right) \tag{5.8a}$$

$$\left|z_{k,l}^{(x)}\right| = \left(\left|a_{k|k-1}\right|^{-\varepsilon_{k|k-1}} + \left|\frac{{}^{t}\tilde{y}_{k,l}^{(y)}}{b_{k|k-1} \cdot {}^{t}\tilde{y}_{k,l}^{(x)}}\right|^{\varepsilon_{k|k-1}}\right)^{-\frac{1}{\varepsilon_{k|k-1}}}. \tag{5.8b}$$

The absolute value of the measurement source $z_{k,l}^{(x)}$ in the x coordinate can finally be resolved by knowing that the x coordinate of the inverse tapered measurement in local coordinates ${}^{t}\tilde{y}_{k,l}^{(x)}$ has the same sign in the radial association scheme. The measurement source in local coordinates can then finally be calculated as

$$\tilde{z}_{\mathrm{rad}}^{(x)}\left(\underline{\hat{x}}_{k|k-1}, {}^{t}\underline{\tilde{y}}_{k,l}^{(xy)}\right) = \operatorname{sign}\left({}^{t}\tilde{y}_{k,l}^{(x)}\right) \cdot \left(\left|a_{k|k-1}\right|^{-\varepsilon_{k|k-1}} + \left|\frac{{}^{t}\tilde{y}_{k,l}^{(y)}}{b_{k|k-1} \cdot {}^{t}\tilde{y}_{k,l}^{(x)}}\right|^{\varepsilon_{k|k-1}}\right)^{-\frac{1}{\varepsilon_{k|k-1}}} \tag{5.9a}$$

$$\tilde{z}_{\mathrm{rad}}^{(y)}\left(\underline{\hat{x}}_{k|k-1}, {}^{t}\tilde{\underline{y}}_{k,l}^{(xy)}\right) = \tilde{z}_{\mathrm{rad}}^{(x)}\left(\underline{\hat{x}}_{k|k-1}, {}^{t}\tilde{\underline{y}}_{k,l}^{(xy)}\right) \cdot \frac{{}^{t}\tilde{y}_{k,l}^{(y)}}{{}^{t}\tilde{y}_{k,l}^{(x)}} \tag{5.9b}$$

and will be abbreviated as $\tilde{\underline{z}}_{\mathrm{rad}}^{(xy)}\left(\underline{\hat{x}}_{k|k-1}, {}^{t}\tilde{\underline{y}}_{k,l}^{(xy)}\right)$ for the radial measurement source association. A projected measurement source association $\tilde{\underline{z}}_{\mathrm{proj}}^{(xy)}\left(\underline{\hat{x}}_{k|k-1}, {}^{t}\tilde{\underline{y}}_{k,l}^{(xy)}\right)$ can be calculated using the procedure presented in Sec. 2.4.2, the inverse tapered measurement in local coordinates ${}^{t}\tilde{\underline{y}}_{k,l}^{(xy)}$, the predicted system state $\underline{\hat{x}}_{k|k-1}$, and the explicit superellipse equations (5.2). An illustration of the radial and projected measurement source association, including the inverse tapering transformation, can be found in Fig. 5.2. Given a predicted measurement source, the measurement equation can be stated as

$$\underline{\hat{y}}_{k,l}^{(xy)} = \underline{\tilde{z}}^{(xy)}\left(\underline{\hat{x}}_{k|k-1}, {}^{t}\tilde{\underline{y}}_{k,l}^{(xy)}\right) - {}^{t}\tilde{\underline{y}}_{k,l}^{(xy)} + \underline{v}_{k,l} \tag{5.10a}$$

$$= \tilde{\underline{z}}_{\mathrm{GAM}}^{(xy)}\left(\underline{\hat{x}}_{k|k-1}, {}^{t}\tilde{\underline{y}}_{k,l}^{(xy)}\right) + \underline{v}_{k,l}. \tag{5.10b}$$

In the nonlinear Kalman filter update step, the predicted measurement $\underline{\hat{y}}_{k,l}^{(xy)}$ can then be associated with the pseudo-measurement $\underline{0}_2$ in (2.16b). In the measurement equation (5.10), both association procedures, the radial and the projected, can be included.

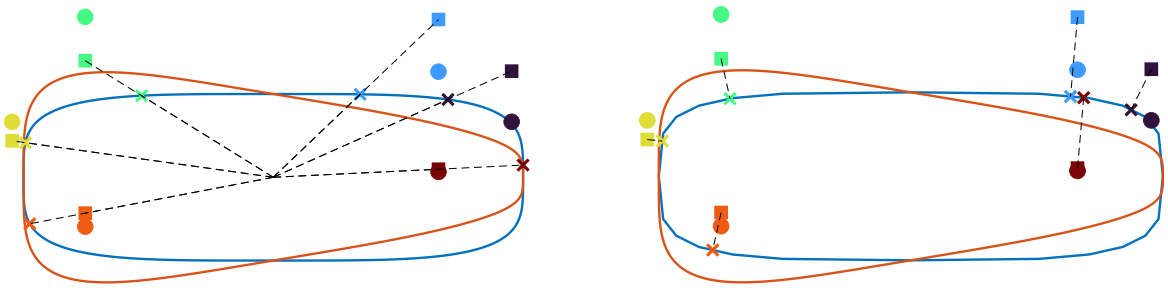

(a) Radial measurement source association.

(b) Projected measurement source association.

Figure 5.2: Tapered superellipse and measurement source association. Squareness parameter $\varepsilon = 4$. Tapering parameter $t^{(y)} = -0.5$. Measurements as circles, inverse tapered measurements as squares, and measurement sources on non-tapered shapes as crosses. Related items are displayed in the same color.

Remark 5.1. *The 2D measurement equation applying superellipses as shape representation was originally published in [O3].*

5.4.2 3D Measurement Models

As was seen in Ch. 4, a shape representation in cylindrical coordinates can be beneficial compared to spherical representations if measurements from the top and bottom surfaces of the object are missing. Thus, extruded superellipse shape representations are applied for deriving the 3D measurement models in this section instead of applying superquadratics [47] as a 3D shape representation and extension of the superellipse measurement model presented before. A parametric representation for the extruded superellipse shape in local coordinates can be given as

$$\underline{z}(\theta, s) = \left[a\,\mathrm{sign}\big(\cos(\theta)\big)\,|\cos(\theta)|^{\frac{2}{\varepsilon}}, b\,\mathrm{sign}\big(\sin(\theta)\big)\,|\sin(\theta)|^{\frac{2}{\varepsilon}}, s \cdot h\right]^{\top} \tag{5.11}$$

using the parameter $s \in [0, 1]$ in addition and the height $h > 0$. As before in Sec. 3.3, a 3D GAM and an ERHM are presented as measurement models for the 3D extruded superellipse shape representation. For both measurement models, the kinematic state is modeled as

$$\underline{x}_{\mathrm{kin}_k} = \left[\underline{m}_k^\top, \phi_k, \underline{x}_{\mathrm{vel}_k}^\top\right]^\top \tag{5.12}$$

comprising the 3D position $\underline{m}_k$, the yaw angle ϕ_k, and the dynamics $\underline{x}_{\mathrm{vel}_k}$ representing variables such as the velocity, yaw rate, or acceleration of the object. The yaw angle ϕ_k is modeled to be aligned with the direction of movement. Roll and pitch angles are again assumed to be negligible, but can easily be integrated into the estimation procedure if required. The extent state can again be defined individually depending on the desired flexibility. However, the height h_k must be added to the extent state and will be estimated in both measurement models. The extent state, which is applied in the following investigations, can then be given as

$$\underline{x}_{\mathrm{ext}_k} = \left[a_k, b_k, h_k, \varepsilon_k, t_k^{(y)}\right]^\top \tag{5.13}$$

comprising the semi-axes $a_k, b_k > 0$, the squareness parameter $\varepsilon_k \geq 1$, the tapering coefficient $t_k^{(y)} \in [-1, 1]$, and the height $h_k > 0$. The tapering coefficient $t_k^{(x)}$ is omitted to integrate the prior knowledge that many shapes in various tracking scenarios entail a line of symmetry in the x-direction.

Extruded Superellipse 3D GAM For the extruded superellipse 3D GAM, the extrusion parameter s in (5.11) and the 2D source point corresponding to the angular parameter θ are greedily associated with the boundary of the explicit extruded superellipse shape. The angular parameter θ in (5.11) is not directly calculated. The z coordinate of the measurement in local coordinates $\tilde{y}_{k,l}^{(z)}$ can be calculated using an inverse translation. The greedy association of the extrusion parameter $\hat{s}_{k,l}$ can then be solved using (3.4), while the greedy association of the measurement source at a specific height section can be solved using the procedures presented in Sec. 5.4.1. The measurement equation for the extruded superellipse 3D GAM can then be given as

$$\begin{aligned}
\underline{\hat{y}}_{k,l} &= \begin{bmatrix} \tilde{\underline{z}}^{(xy)}\left(\hat{\underline{x}}_{k|k-1}, {}^t\tilde{\underline{y}}_{k,l}^{(xy)}\right) - {}^t\tilde{\underline{y}}_{k,l}^{(xy)} \\ \hat{s}_{k,l} \cdot h_{k|k-1} - \tilde{y}_{k,l}^{(z)} \end{bmatrix} + \underline{v}_{k,l} && \text{(5.14a)} \\
&= \begin{bmatrix} \tilde{\underline{z}}_{\mathrm{GAM}}^{(xy)}\left(\hat{\underline{x}}_{k|k-1}, {}^t\tilde{\underline{y}}_{k,l}^{(xy)}\right) \\ \hat{s}_{k,l} \cdot h_{k|k-1} - \tilde{y}_{k,l}^{(z)} \end{bmatrix} + \underline{v}_{k,l} && \text{(5.14b)} \\
&= \tilde{\underline{z}}_{\mathrm{GAM}}\left(\hat{\underline{x}}_{k|k-1}, {}^t\tilde{\underline{y}}_{k,l}\right) + \underline{v}_{k,l}. && \text{(5.14c)}
\end{aligned}$$

The predicted measurement $\underline{\hat{y}}_{k,l}$ can then be associated with the pseudo-measurement $\underline{0}_3$ in (2.16b) in the nonlinear Kalman filter update. In this measurement equation, the center of the extruded superellipse local coordinate system is located at the bottom surface. Details on the implementation of the extruded superellipse 3D GAM can be found in Sec. 5.5.

Extruded Superellipse ERHM For the extruded superellipse ERHM, a uniformly distributed extrusion factor $s_{k,l} \sim \mathcal{U}(0, 1)$ can be applied since the perimeter of the extruded superellipse does not change in the z direction, and a uniformly distributed scaling factor, therefore, resembles a uniform distribution of measurements on the entire surface of the extruded superellipse. Due to the uniform distribution of the extrusion factor, symmetry assumptions for the ERHM as presented in Sec. 2.4.3 can be applied for the extruded superellipse ERHM measurement

equation. The greedy association of the measurement source at a specific height section can be solved using the procedures presented for the 2D superellipse measurement model of Sec. 5.4.1. The measurement equation for the extruded superellipse ERHM can then be given as

$$\hat{\underline{y}}_{k,l} = \begin{bmatrix} \tilde{\underline{z}}^{(xy)} \left(\hat{\underline{x}}_{k|k-1}, {}^{t}\tilde{\underline{y}}_{k,l}^{(xy)} \right) - {}^{t}\tilde{\underline{y}}_{k,l}^{(xy)} \\ s_{k,l} \cdot \frac{h_{k|k-1}}{2} - \left| \tilde{y}_{k,l}^{(z)} \right| \end{bmatrix} + \underline{v}_{k,l} \tag{5.15a}$$

$$= \begin{bmatrix} \tilde{\underline{z}}_{\mathrm{GAM}}^{(xy)} \left(\hat{\underline{x}}_{k|k-1}, {}^{t}\tilde{\underline{y}}_{k,l}^{(xy)} \right) \\ s_{k,l} \cdot \frac{h_{k|k-1}}{2} - \left| \tilde{y}_{k,l}^{(z)} \right| \end{bmatrix} + \underline{v}_{k,l} \tag{5.15b}$$

$$= \tilde{\underline{z}}_{\mathrm{ERHM}} \left(\hat{\underline{x}}_{k|k-1}, {}^{t}\tilde{\underline{y}}_{k,l} \right) + \underline{v}_{k,l} \tag{5.15c}$$

where the predicted measurement $\hat{\underline{y}}_{k,l}$ can then be associated with the pseudo-measurement $\underline{0}_3$ in (2.16b) in the nonlinear Kalman filter update. In this measurement equation, the center of the extruded superellipse local coordinate system is located in the middle of the shape, and the full height is estimated in the extent state. Also, in this measurement equation, inverse tapering and rotation transformations are only applied to x and y coordinates. For the z coordinate of the measurement in local coordinates $\tilde{y}_{k,l}^{(z)}$, only an inverse translation transformation must be performed. Details on the implementation of the extruded superellipse ERHM can be found in Sec. 5.5.

Remark 5.2. *The 3D measurement equation applying extruded superellipses in an ERHM as shape representation and an extension of the 2D measurement equation was originally proposed in [O2].*

5.4.3 Recursive Artificial Measurement Noise for the Superellipse Shape

Also, in the measurement models for the extruded superellipse shape, measurements are initially assumed to be generated from the object's boundary. Therefore, a RAMN estimation procedure using the equations given in Sec. 2.6.1 is presented in this section. Since the perimeter of the extruded superellipse shape does not change in the z direction, estimating the RAMN parameters in the x, y plane is sufficient for this shape. Furthermore, the "inside-outside" information can also be calculated using the measurements projected to the horizontal x, y plane.

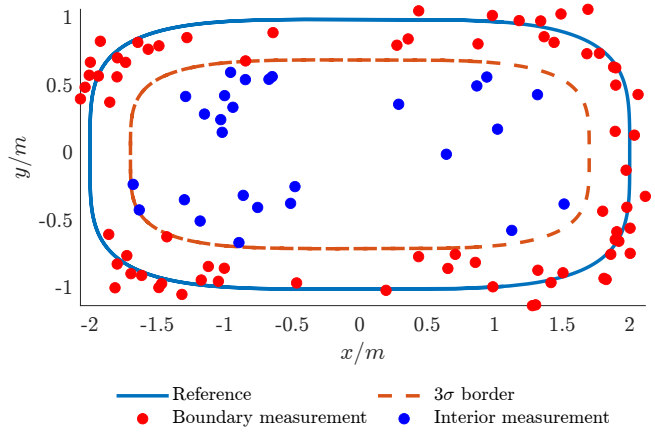

Figure 5.3: Visualization of the measurement separation for the RAMN estimation of a superellipse.

As was seen in Sec. 2.6.1, the $3\sigma_{\underline{v}}$ border must also be taken into account for a better convergence behavior, as measurements inside this region might also originate from the boundary of the

object. Due to the additive measurement noise, measurements can also be located inside the boundary of the object, which is attempted to be regulated by adding the $3\sigma_{\underline{v}}$ border to the "inside-outside" information generation. An implicit equation for the superellipse to calculate this information is given by (5.1) and can be modified as

$$\mathcal{I}({}^{t}\tilde{\underline{y}}_{k,l}, \hat{\underline{x}}_{k|k-1}) = \left| \frac{{}^{t}\tilde{y}^{(x)}_{k,l}}{a_{k|k-1} - 3 \cdot \sigma_{\underline{v}}} \right|^{\varepsilon_{k|k-1}} + \left| \frac{{}^{t}\tilde{y}^{(y)}_{k,l}}{b_{k|k-1} - 3 \cdot \sigma_{\underline{v}}} \right|^{\varepsilon_{k|k-1}} - 1 \tag{5.16}$$

$$= \begin{cases} > 0: & \text{outside} \\ = 0: & 3\sigma_{\underline{v}}\text{boundary} \\ < 0: & \text{inside} \end{cases} \tag{5.17}$$

using the inverse tapered measurement in local coordinates ${}^{t}\tilde{\underline{y}}_{k,l}$ as input. A visualization of the measurement separation for the RAMN estimation of the superellipse shape can be seen in Fig. 5.3. The blue measurements in the figure are used for the parameter estimation of the RAMN. The measurement sources associated with these interior points directly give the Euclidean distances needed for the calculation as

$$d^{(i,\eta)}_{k,l} = \left| \tilde{z}^{(i,\eta)} \left(\hat{\underline{x}}_{k|k-1}, {}^{t}\tilde{\underline{y}}^{(xy)}_{k,l} \right) \right| \tag{5.18}$$

where the superscript i again indicates measurements inside the boundary and outside the $3\sigma_{\underline{v}}$ border. After calculating the parameters of the RAMN, the measurement noise mean and covariance matrix are given by (3.11a) and (3.11b). The artificial measurement noise mean value can again be added to the predicted measurements $\hat{\underline{y}}^{(xy)}_{k,l}$ before they are used in the update equations of the Kalman filter.

5.5 Implementation Details

In this section, details on the implementation of the presented extruded superellipse EOT filters are given. In particular, pseudo-code is given for the 3D extruded superellipse measurement models. The 2D superellipse measurement model can be implemented by omitting the extrusion part of the 3D models. Details are not given in this thesis but can be found in [O2, O3]. The extruded superellipse 3D GAM and ERHM, including symmetry assumptions in the z direction, can be implemented using an UKF. The pseudo-code for the sequential batch linear regression Kalman filter (LRKF) can be found in Alg. 3.1, and the UKF is one version of the LRKF. In this algorithm, lines 3–5 must be specified for the extruded superellipse measurement models. The RAMN estimation and the artificial measurement noise mean and covariance matrix for the extruded superellipse in line 11 can be generated using the "inside-outside" function (5.16) and the procedure described in Sec. 5.4.3.

The pseudo-code for implementing the extruded superellipse 3D GAM and ERHM replacing lines 3–5 in Alg. 3.1 can be found in Alg. 5.1. In the first six lines of this algorithm, the sigma point calculation of the UKF is depicted. Comparable to the elliptic cylinder ERHM, and also for the extruded superellipse ERHM, the extrusion factors must be sampled for each of the n_u measurements individually. As these extrusion factors for the extruded superellipse ERHM are also assumed to be uniformly distributed as $s_{k,l} \sim \mathcal{U}(0,1)$, the procedure presented in Sec. 3.5.1 for generating these samples can be applied. In lines 4 and 6, the extrusion samples are generated being distributed as $s_{k,l} \sim \mathcal{N}(0,1)$ and then transformed in line 22 using the cumulative distribution function (CDF) $\Phi(s_{k,l})$ of the standard Gaussian distribution. Afterwards, these transformed extrusion samples are uniformly distributed as required. The

extruded superellipse 3D GAM can be implemented straightforwardly, similar to the elliptic cylinder 3D GAM implementation in Sec. 3.5.1.

Algorithm 5.1 Extruded superellipse UKF measurement prediction

1: **if** 3D GAM measurement source association **then**
2: distribution parameters $\underline{x}_u = \hat{\underline{x}}_n$, $\mathbf{P}_u = \mathbf{P}_n$
3: **else if** ERHM measurement source association **then**
4: extended distribution parameters $\underline{x}_u = \left[\hat{\underline{x}}_n^\top, \underline{0}_{n_u}^\top\right]^\top$, $\mathbf{P}_u = \mathrm{blkdiag}\left(\mathbf{P}_n, \mathbf{I}_{n_u}\right)$
5: **end if**
6: sigma points $\left\{\underline{\boldsymbol{x}}_{n,j}, \boldsymbol{w}_{n,j}\right\}_{j=1}^{n_s}$ using [130] and $\underline{x}_u$, $\mathbf{P}_u$
7: get $\left\{\underline{y}_{n,l}\right\}_{l=1}^{n_u}$ from $\mathcal{Y}_k$ using next n_u measurements
8: **for** $j \leftarrow 1$ **to** n_s **do**
9: extract $\underline{\boldsymbol{x}}_{\mathrm{kin}_{n,j}}$ from $\underline{\boldsymbol{x}}_{n,j}$
10: extract constrained $[\tilde{\boldsymbol{a}}_{n,j}, \tilde{\boldsymbol{b}}_{n,j}, \tilde{\boldsymbol{h}}_{n,j}]^\top = c_1([\boldsymbol{a}_{n,j}, \boldsymbol{b}_{n,j}, \boldsymbol{h}_{n,j}]^\top, 0)$ with lower bound from $\underline{\boldsymbol{x}}_{n,j}$ using (2.38)
11: extract constrained $\tilde{\varepsilon}_{n,j} = c_1(\varepsilon_{n,j}, 1)$ with lower bound from $\underline{\boldsymbol{x}}_{n,j}$ using (2.38)
12: extract constrained $\tilde{t}_{n,j}^{(y)} = c_2(\tilde{t}_{n,j}^{(y)}, -1, 1)$ from $\underline{\boldsymbol{x}}_{n,j}$ using (2.39)
13: **for** $l \leftarrow 1$ **to** n_u **do**
14: measurement in local coordinates $\underline{\tilde{\boldsymbol{y}}}_{n,j,l}^{(xy)}$ using (5.5), and $\underline{\boldsymbol{x}}_{\mathrm{kin}_{n,j}}$
15: inverse tapered measurement in local coordinates ${}^t\underline{\tilde{\boldsymbol{y}}}_{n,j,l}^{(xy)}$ using (5.6), and $\tilde{t}_{n,j}^{(y)}$
16: measurement source $\underline{\tilde{\boldsymbol{z}}}_{n,j,l}^{(xy)}\left(\underline{\tilde{\boldsymbol{x}}}_{\mathrm{ext}_{n,j}}, {}^t\underline{\tilde{\boldsymbol{y}}}_{n,j,l}^{(xy)}\right)$ using (5.9) or projected association
17: measurement in local coordinates $\tilde{\boldsymbol{y}}_{n,j,l}^{(z)} = y_{n,l}^{(z)} - \boldsymbol{m}_{n,j}^{(z)}$
18: **if** 3D GAM measurement source association **then**
19: extrusion factor $\hat{\imath}_{n,j,l}$ using (3.4), $\tilde{\boldsymbol{y}}_{n,j,l}^{(z)}$, and constrained height sample $\tilde{\boldsymbol{h}}_{n,j}$
20: predicted measurement $\hat{\underline{\boldsymbol{y}}}_{n,j,l} = \left[\underline{\tilde{\boldsymbol{z}}}_{n,j,l}^{(xy)\top}, \hat{\imath}_{n,j,l} \cdot \tilde{\boldsymbol{h}}_{n,j}\right]^\top - \underline{\tilde{\boldsymbol{y}}}_{n,j,l}$
21: **else if** ERHM measurement source association **then**
22: extract extrusion factor sample $\tilde{\imath}_{n,j,l} = \frac{1}{2}\left(1 + \mathrm{erf}\left(\frac{\imath_{n,j,l}}{\sqrt{2}}\right)\right)$ from $\underline{\boldsymbol{x}}_{n,j}$
23: predicted measurement $\hat{\underline{\boldsymbol{y}}}_{n,j,l} = \left[\underline{\tilde{\boldsymbol{z}}}_{n,j,l}^{(xy)\top}, \tilde{\imath}_{n,j,l} \cdot \frac{\tilde{\boldsymbol{h}}_{n,j}}{2}\right]^\top - \left[{}^t\underline{\tilde{\boldsymbol{y}}}_{n,j,l}^{(xy)\top}, |\tilde{\boldsymbol{y}}_{n,j,l}^{(z)}|\right]^\top$
24: **end if**
25: **end for**
26: **end for**

Another specialty of the extruded superellipse measurement models can be found in lines 10–12. In these lines, the constrained state samples are extracted from the state samples $\underline{\boldsymbol{x}}_{n,j}$. The semi-axes and the height of the extruded superellipse are prevented from becoming negative by transforming them through the transformation function (2.38) with 0 as a lower bound. Furthermore, the squareness parameter is prevented from becoming smaller than 1 by also transforming it through the transformation function (2.38), however, with 1 as a lower bound. Finally, the tapering coefficient is forced to be in the interval $[-1, 1]$ by transforming it through the transformation function (2.39) with respective bounds to prevent the tapering coefficient from being higher or lower, as these values would produce loops in the shape which are not preferable. The final details of the extruded superellipse measurement models can be found in lines 20 and 23, where the measurement equations are depicted, including contained symmetry assumptions in the z direction for the extruded superellipse ERHM.

Remark 5.3. *In addition to the pseudo-code given in this section, an implementation of the 2D and 3D superellipse measurement models can be found at [R5].*

5.6 Experiments

In this section, the extruded superellipse measurement models are investigated and compared in two simulated static scenarios. In these scenarios with 100 time steps, measurements are again generated from the boundary of the reference shape and the object's interior to investigate the RAMN estimation in the extruded superellipse measurement models. To also investigate the basic parametric shape estimation capabilities of the superellipse, two scenarios with a cuboid and an elliptic cylinder reference shape are simulated, described, and evaluated in this section. The measurement generation process is comparable to the simulated scenarios

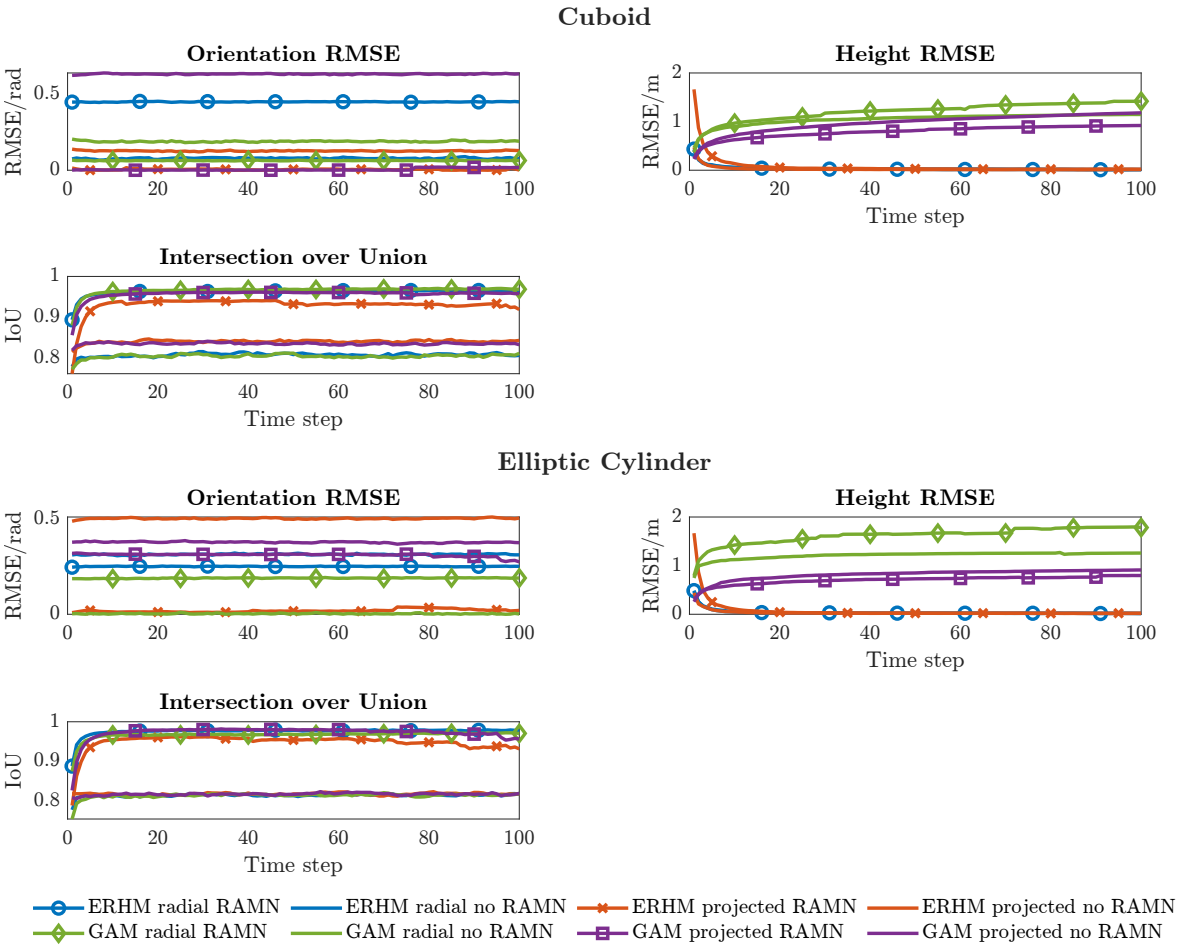

Figure 5.4: Monte Carlo (MC) simulation root mean square error (RMSE) and intersection over union (IoU) estimation results of the static superellipse simulation experiment.

presented before. The z coordinates of the measurements are sampled uniformly distributed using the normalized height parameter $s \sim \mathcal{U}(0,1)$ and then multiplied by the reference height of the simulated shape. This procedure can be applied to both reference shapes. Sampling the angular parameter of the elliptic cylinder for the measurement generation is described in Sec. 3.6.1. The measurement source generation of the cuboid at a specific height section can also be realized by sampling an angular parameter from the uniform distribution $\theta \sim \mathcal{U}(0, 2\pi)$

and passing the sampled parameter through a rectangular radial function, which can be defined as a piecewise function. An implementation can be found at [R5]. With a probability of 0.3, after calculating the measurement sources from the boundary, a scaling factor $t \sim \mathscr{T}(0, 1, 1)$ is selected to multiply the measurement source in the xy plane and generate measurements from the object's interior. With a probability of 0.7, measurements are sampled from the object's boundary. The measurement set is then given as a mixture of boundary and interior measurements. Finally, the measurement noise is sampled from the Gaussian distribution $v \sim \mathcal{N}(0, 0.1^2)$ for each dimension and added to the measurement source.

In the simulation, the extruded superellipse 3D EOT filters are implemented using a 3D GAM and an ERHM, with a radial and a projected measurement source association at a specific height section, and with and without the RAMN estimation procedure. The filter is initialized using the first measurement set. Details can be found at [R5]. In each time step, 50 measurements are generated and processed in a sequential batch update with $n_u = 20$ measurements for a single update. The quantitative results are presented using the mean IoUs for evaluating the shape estimation capabilities of the extruded superellipse shape measurement models. The IoU is specified in Sec. 4.5. However, for the extruded superellipse shape, only the 2D top-down view IoU is calculated at each time step, as this is sufficient for the evaluation of the shape estimation performance in this scenario. For the 2D top-down view IoU, the convex hulls of the estimated and reference shapes in top-down view are utilized for calculating the intersection and union areas throughout this thesis. In addition, the mean RMSEs for the yaw angle and height estimates are calculated. Results are presented as mean values of a MC simulation with 100 runs.

Table 5.1: Mean computation times per measurement for the superellipse.

Algorithm	**Computation time**
ERHM radial RAMN	43.66 µs
ERHM radial no RAMN	41.92 µs
ERHM projected RAMN	155.55 µs
ERHM projected no RAMN	73.91 µs
GAM radial RAMN	27.4 µs
GAM radial no RAMN	26.81 µs
GAM projected RAMN	36.96 µs
GAM projected no RAMN	36.99 µs

The mean values after the MC simulation are depicted in Fig. 5.4. In the first half of the figure, the results with a cuboid as a reference shape can be seen. In the second half, the results with an elliptic cylinder as a reference shape are depicted. The measurement models applied to estimate the parameters of the extended object are the same for both reference shapes. For both simulations, it can be seen that the 2D IoU for the measurement models applying the RAMN estimation converges to a static value close to 1, meaning that the 2D reference shape in the top-down view is almost perfectly estimated. When not applying the RAMN estimation procedure in the measurement update, the 2D IoU is substantially lower since the shape estimate is biased towards the interior of the object. Also, in the results, no major difference between using a radial or projected measurement source association at a specific height section can be detected. Only the IoU of the ERHM with projected measurement source association applying the RAMN estimation procedure is slightly lower than the remaining implementations applying the RAMN procedure. The radial association can, therefore, be

assumed to be the more reliable measurement source association for the extruded superellipse shape in this scenario. Also, for the superellipse measurement models, the estimates of the yaw angle reveal huge errors, which can again be ascribed to the fact that the shapes are symmetric and the angle is a periodic variable, which is why ambiguities in the estimates can occur. However, the orientation RMSEs also converge in this scenario in each implementation, which indicates a reliable angle estimation. In contrast to the ERHM implementations, the height estimates of the 3D GAM implementations diverge in this scenario due to the lack of a penalty for overestimated heights in the 3D GAM.

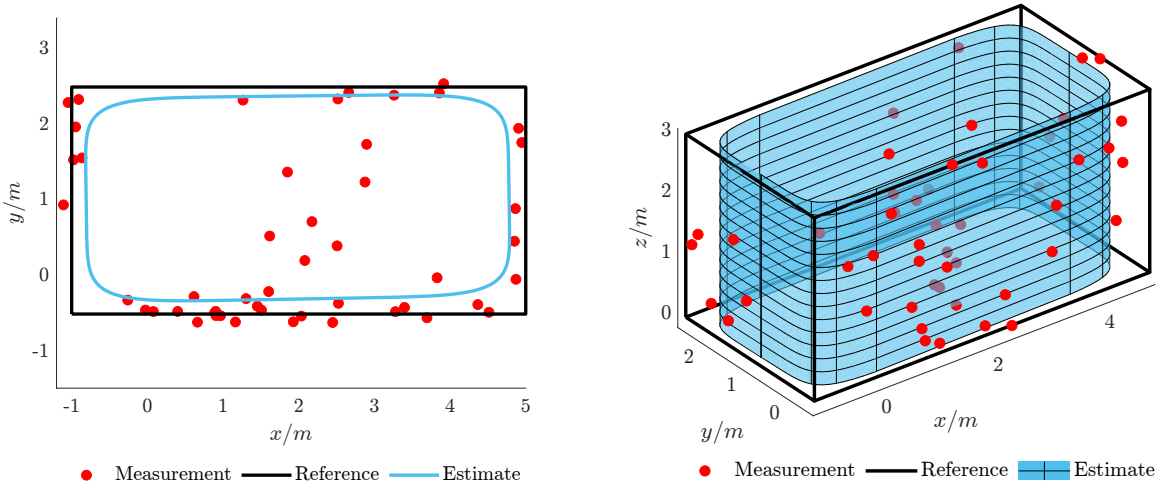

(a) Estimation results of the superellipse ERHM applying a radial measurement source association without RAMN estimation.

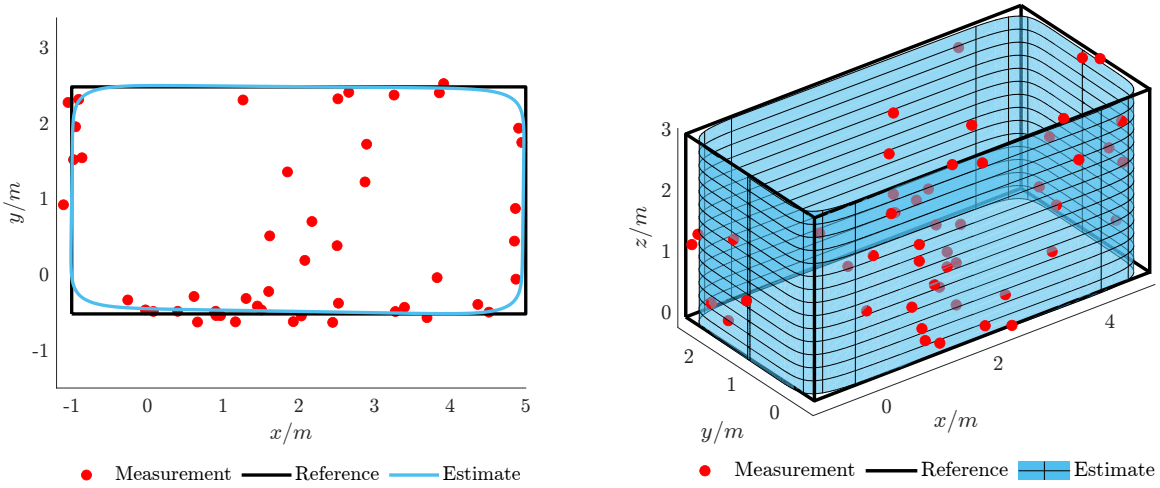

(b) Estimation results of the superellipse ERHM applying a radial measurement source association with RAMN estimation.

Figure 5.5: Estimation results of the superellipse ERHM applying a radial measurement source association with and without RAMN estimation in 2D and 3D view for the cuboid reference. Estimates are at the same time step with the same random seed for the measurement generation.

In addition to the quantitative estimation results, the mean computation times per measurement for each version of the superellipse measurement models are reported in Tab. 5.1. Each calculation is conducted using MATLAB R2023b on an Intel(R) Xeon(R) X5680 CPU with 3.33 GHz. In the table, it can be seen that the implementations applying a radial measurement source association at a specific height section are slightly faster than the projected measurement source association. It can also be seen that the RAMN estimation procedure can be calculated

very efficiently in this implementation and has only a little impact on the computation time. In combination with the quantitative estimation results from Fig. 5.4, the RAMN estimation procedure can be considered a promising approach for processing a mixture of boundary and interior measurements in EOT.

Finally, qualitative estimation results of the extruded superellipse ERHM are visualized in Fig. 5.5. In each figure, estimation results after 50 time steps and 2500 processed measurements for the cuboid reference, applying a radial measurement source association at a specific height section, are depicted. In the top row, results without applying the RAMN estimation procedure in 2D top-view and 3D view can be seen. In the bottom row, the same figures are shown, however, when applying the RAMN estimation procedure. The qualitative results for the elliptic cylinder reference are not included as they are comparable to the visualization in Fig. 3.5. It can be seen that when applying the RAMN estimation procedure, the extent and also the shape can almost perfectly be estimated. Also, the shape of the elliptic cylinder is very well matched using the extruded superellipse shape representation. These results make the superellipse shape representation a very competitive alternative to flexible non-parametric shape representations and also a multiple model approach, as discussed in Sec. 5.1. The application of the superellipse shape representation to real-world measurements is presented and discussed in Ch. 6.

5.7 Conclusions

This chapter introduced and investigated extruded superellipses as a novel shape representation for 3D EOT, aiming to provide a balance between the simplicity of basic parametric shapes presented in Ch. 3 and the high flexibility of non-parametric series expansions presented in Ch. 4. The motivation stemmed from the need for a single, compact model capable of representing a variety of common parametric object shapes, such as ellipses or rectangles, without requiring prior classification or facing the complexities of high-dimensional shape coefficient spaces. Superellipses, defined by semi-axes and the squareness and optional tapering shape parameters, offer this flexibility. The extruded variant was chosen over 3D superquadrics to maintain the advantages of shape representations in cylindrical coordinates for maritime environment perception. An important finding from the initial static simulation experiments is the successful demonstration of the adaptability of the extruded superellipse model. Using its squareness and optional tapering shape parameters, it accurately captured the geometries of both cuboid and elliptic cylinder reference objects within a single measurement model. This validates the potential of extruded superellipses to handle common object shapes without requiring multiple specialized models.

Consistent with the results for simpler parametric shapes, the comparative evaluation in this chapter confirmed the superiority of the ERHM approach over the 3D GAM in achieving unbiased height estimates. Furthermore, the experiments highlight the importance of the RAMN approach for this measurement model. The integration of the RAMN significantly improved the accuracy of the horizontal shape and extent estimates for both reference objects by effectively mitigating estimation errors caused by interior measurements. Combining the ERHM with the RAMN approach delivered the most robust and accurate results in these static tests. These results validate the extruded superellipse, in particular the ERHM with the RAMN approach, as a promising approach for 3D EOT that offers an effective mix of shape flexibility and efficiency.

CHAPTER 6

Evaluation

Contents

6.1 Evaluation in a Maritime Environment 95
6.1.1 Simulated Motor Boat Scenario Results 96
6.1.2 Real-World Motor Boat Scenario Results 103
6.1.3 Real-World Sailing Boat Scenario Results 107
6.2 Generalization to an Automotive Environment 109
6.3 Discussion 113
6.4 Conclusions 114

In this chapter, the measurement models presented before are further investigated and evaluated in simulated and real-world dynamic scenarios. In the first part of this chapter, simulated and real-world maritime scenarios are applied to each presented measurement model from the previous chapters. In doing so, further insights are gained on the complexity needed in the measurement models for a proper 3D extended object tracking (EOT) filter. Furthermore, the recursive artificial measurement noise (RAMN) estimation procedure is investigated in real-world scenarios and compared to state-of-the-art EOT methods, which can be found in the literature, and not using the approach at all. In the second half of the chapter, the developed 3D EOT measurement models are investigated in an automotive domain. In doing so, the generalization capabilities of the approaches are examined. The dataset applied for the investigation in the second half of the chapter is the famous KITTI data set [48]. The raw data set contains roughly 1200 objects annotated in consecutive time steps, which can be used for the study. By using a well-known and extensive automotive dataset to evaluate the developed 3D EOT measurement models, a versatile result can be achieved that helps to further evaluate and classify the approaches. Comparable data sets in the maritime sector with high-resolution light detection and ranging (Lidar) sensors and corresponding evaluation options do not yet exist.

6.1 Evaluation in a Maritime Environment

In this section, the developed 3D EOT measurement models are examined in a maritime environment. Therefore, three different scenarios are presented and investigated. First, a simulated scenario using a computer-aided design (CAD) model of the *Solgenia* research vessel [C6] from HTWG Konstanz as the tracking object is presented in Sec. 6.1.1. When using the CAD model of the *Solgenia* in the simulation environment, realistic 3D Lidar measurements can be generated for an in-depth investigation. In the second scenario, a real-world maritime scenario, also with the *Solgenia* as a tracking object, is presented in Sec. 6.1.2. In this scenario, the CAD model can be applied as a detailed 3D shape reference, which is unique in the maritime

tracking community. In the simulated and real-world scenarios using the *Solgenia* as a tracking object, every measurement model except for the elliptic cone measurement models, presented in Sec. 3.4, is applied for 3D EOT. The elliptical cone measurement models are examined in a separate real-world scenario in section 6.1.3, in which measurements were recorded from a sailing boat participating in a regatta on Lake Constance.

6.1.1 Simulated Motor Boat Scenario Results

In this section, the simulated scenario with *Solgenia* as a tracking object is presented and evaluated for the elliptical cylinder, Fourier-Chebyshev double series (FCDS), and extruded superellipse measurement models. For the evaluation, a single reference trajectory with 300 time steps and a sampling rate of 0.1 seconds is generated using a coordinated turn (CT) model in polar coordinates [108] with standard deviations $\sigma_{\text{la}} = 3\text{m}\,\text{s}^{-2}$ in the linear acceleration and $\sigma_{\text{ra}} = 5^\circ\,\text{s}^{-2}$ in the rotational acceleration. The CT model with the same parameters is then also employed in the prediction step for each implemented method in the following. The extent and shape parameters are modeled as constant in the prediction step. To prevent the estimation of local minima in the extent state and to allow small changes in the extent and shape estimates over time, a random walk prediction with a standard deviation of $\sigma_{\text{ext}} = 1\text{e}{-5}$ is used for each extent and shape parameter. The *Solgenia* CAD is then simulated to move along this reference trajectory. Using the point cloud generator [75] in Matlab, simulated Lidar measurements can be generated from the *Solgenia*. The simulated Lidar sensor has a resolution of 0.5° in the azimuth and 1.25° in the elevation. In the first step, the measurements are generated without any measurement noise. For the following Monte Carlo (MC) simulation, however, the measurement noise is resampled with a standard deviation of $v \sim \mathcal{N}(0, 0.1^2)$ in each direction for each run. This means that the scenario and the measurement sources in the MC simulation remain unchanged, and only the additive measurement noise varies. The initialization for each EOT filter is carried out with the first measurement data set, as was done in the simulation studies in the previous chapters. The simulated scenario with the *Solgenia* and the respective measurement set at specific time steps is visualized in Fig. 6.1.

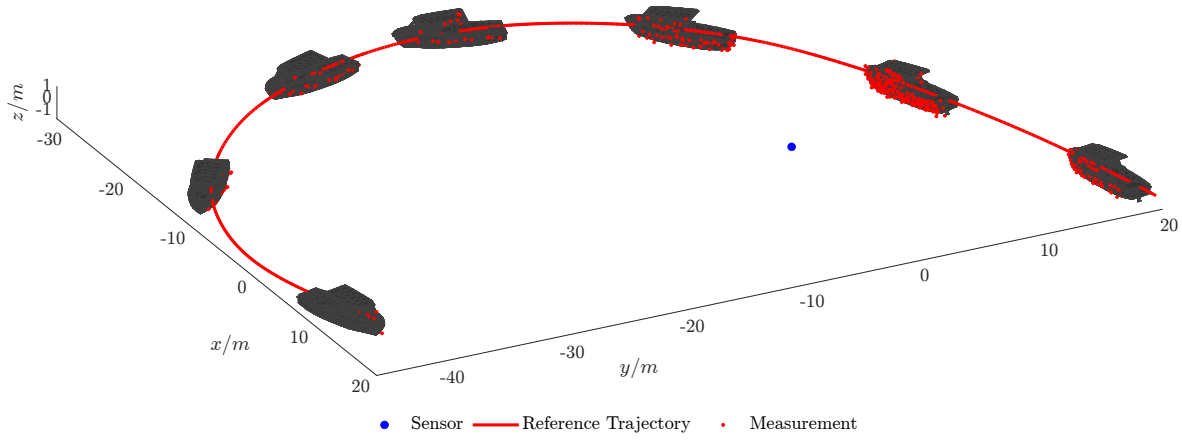

Figure 6.1: Simulated scenario with *Solgenia* CAD in black as tracking object.

The number of simulated measurements during the entire scenario is visualized in Fig. 6.2. Due to the low resolution of the simulated Lidar sensor, the number of simulated measurements for

the entire scenario is also rather low compared to high-resolution sensors available on the market [1]. By using such a low resolution for the sensor, the ability of the 3D EOT measurement models to track the extent and shape of an object using a sparse point cloud is examined.

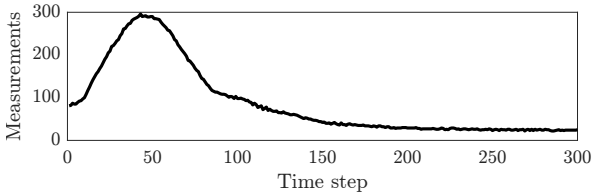

Figure 6.2: Number of simulated measurements per scan during the entire scenario.

To be able to compare the estimation results between the individual 3D EOT measurement models applied, the same evaluation measures are used for each model. First, the orientation and height root mean square errors (RMSEs) are calculated for each time step and averaged after the MC simulation. In addition, the 2D top-down view intersection over union (IoU), described in Sec. 4.5 and Sec. 5.6, is calculated for each model and averaged after the MC simulation. As a reference shape for the calculation, the convex hull of the *Solgenia* CAD model in 2D top-down view is applied. The 2D IoU can then be calculated by approximating the estimated and reference shapes using a polygonal chain. In combination with the height RMSE, the 2D top-down view IoU gives a good overall measure of the shape fitting and estimation ability of the different approaches. Especially for the elliptic cylinder and extruded superellipse measurement models, a 3D IoU measure would not be meaningful, as the presented approaches are not able to fit the varying reference shape at different height sections. On the other hand, for the FCDS measurement models, the approximated 3D IoU as described in Sec. 4.5 can be calculated and averaged after the MC simulation. The 2D top-down view IoU of the FCDS measurement models serves as a comparison measure to the remaining approaches. Finally, the results are compared to the spherical double Fourier series (SDFS) [O7], spherical harmonics (SH) [87], and 3D Gaussian process (GP) [30, 84, 85] approaches. The authors of the 3D GP EOT algorithm [85] have published an implementation. For the comparison methods, also the 2D top-down view and 3D IoUs are calculated and averaged after the MC simulation.

Remark 6.1. *The simulated scenario with Solgenia as the tracking object has previously been applied to evaluate the approaches presented in [O2–O4, O8]. In this section, additional evaluations of each measurement model developed in this thesis are presented in detail.*

Elliptical Cylinder Results This paragraph presents and discusses the simulation results using the elliptic cylinder measurement models presented in Ch. 3 in the simulated *Solgenia* scenario. The mean values for the orientation and height RMSEs and the 2D top-down view IoU measures after the MC simulation are visualized in Fig. 6.3. In the simulated scenario, the elliptic cylinder measurement model is implemented using a 3D greedy association model (GAM) and an extrusion random hypersurface model (ERHM), each with a radial and projected measurement source association at a specific height section, and with and without applying the RAMN estimation procedure. The evaluation of each combination results in eight different approaches.

In the figure, it can be seen that the 3D GAM and the ERHM with radial measurement source association and applying the RAMN estimation procedure exhibit the best performance. Both approaches show the highest and similar 2D top-down view IoU measures with a slightly better performance of the ERHM approach. Interestingly, the height RMSE of both approaches is also similar, however, again with a slightly better performance of the ERHM approach. These results suggest that the 3D GAM approach can also be a promising approach if guarantees can

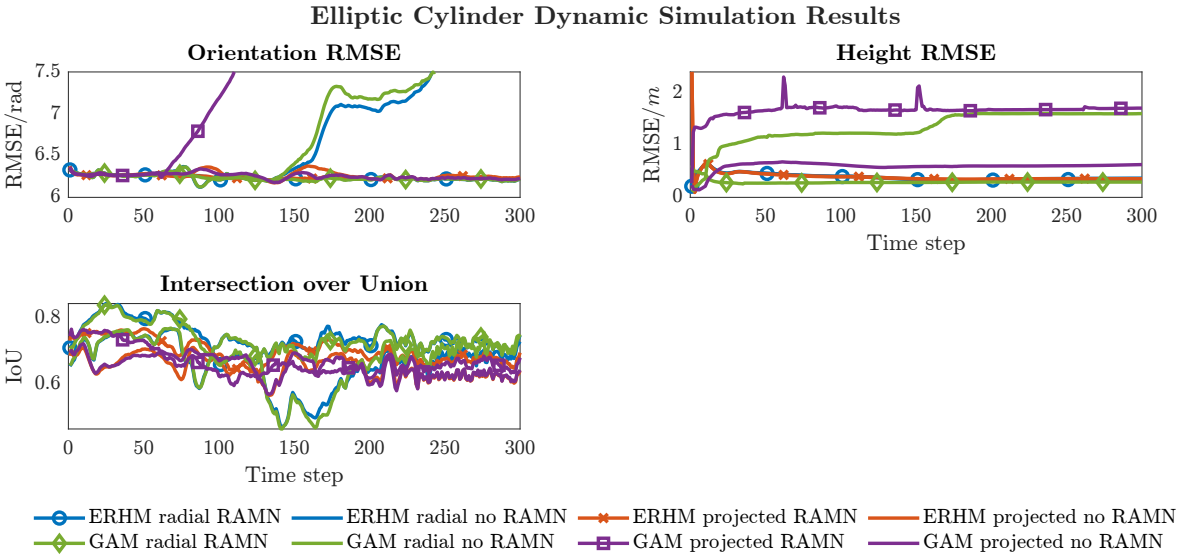

Figure 6.3: MC simulation RMSE and IoU estimation results of the dynamic *Solgenia* scenario for the elliptic cylinder measurement models.

be implemented that the height estimate converges. This could be achieved by regularization, as was done in [147], for example. As seen in Sec. 3.6.1, the approach can also diverge in the height estimation. In the orientation estimates, both approaches have an offset to the reference. However, they converge, in contrast to the 3D GAM with projected measurement source association and RAMN estimation procedure. In summary, applying the RAMN estimation approach in the measurement model improves the performance in the 2D top-down view IoU of each approach in this scenario. Interestingly, the RAMN estimation approach also has a significant impact on the height estimation in the 3D GAM implementations in this scenario, although the approach does not affect the measurement source in the z direction. A deeper investigation is left for future work. Regarding the measurement source association at a specific height section, the radial association exhibits the best performance in the 2D top-down view IoU.

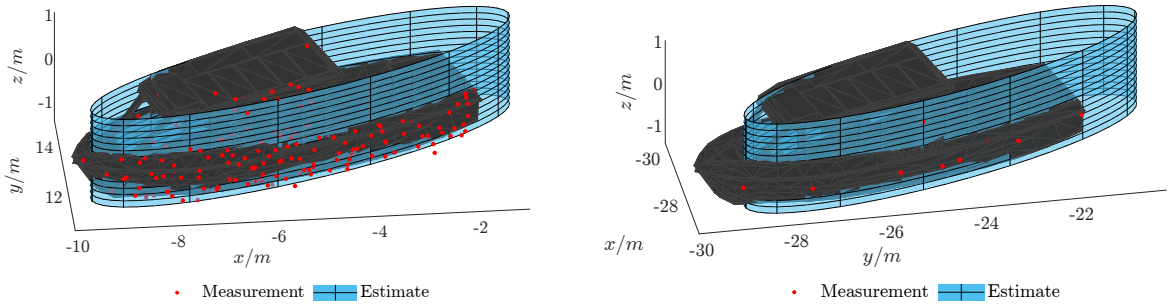

(a) Time step $k = 50$.

(b) Time step $k = 200$.

Figure 6.4: Estimation results of the simulated dynamic *Solgenia* scenario for the elliptic cylinder ERHM with a radial measurement source association applying the RAMN approach at time steps $k = 50, 200$. The *Solgenia* shape reference is depicted as the black surface.

In addition to the quantitative results, qualitative estimation results of the elliptic cylinder measurement model are visualized in Fig. 6.4. In the figure, the estimation results in the simulated *Solgenia* scenario for the ERHM with radial measurement source association applying

the RAMN estimation procedure are depicted at time steps 50 and 200. The variant of the elliptical cylinder measurement model was chosen as it provided the most promising results in the quantitative investigation. At time step 50, considerably more measurements are gathered from the object, leading to a better estimation result than in time step 200. However, even with a low number of measurements at time step 200, the approach can track the object reliably.

FCDS Results This paragraph presents and discusses the simulation results using the FCDS measurement models presented in Ch. 4 in the simulated *Solgenia* scenario. In this investigation, the FCDS measurement models are implemented using 48 shape coefficients. The mean values for the orientation and height RMSEs and the 2D top-down view IoU measures after the MC simulation are visualized in Fig. 6.5. In addition to the 2D top-down view IoU, the approximated 3D IoU as described in Sec. 4.5 is also reported for the FCDS measurement models in this figure. The approximated 3D IoU gives a good overall measure of the shape estimation capabilities of the FCDS measurement models. For the FCDS shape description, only the 3D GAM and quasi-ERHM with radial measurement source association with and without applying the RAMN estimation procedure are implemented since the projected association would result in an unnecessarily high computational effort for the FCDS shape. The evaluation of each combination then results in four different implemented approaches.

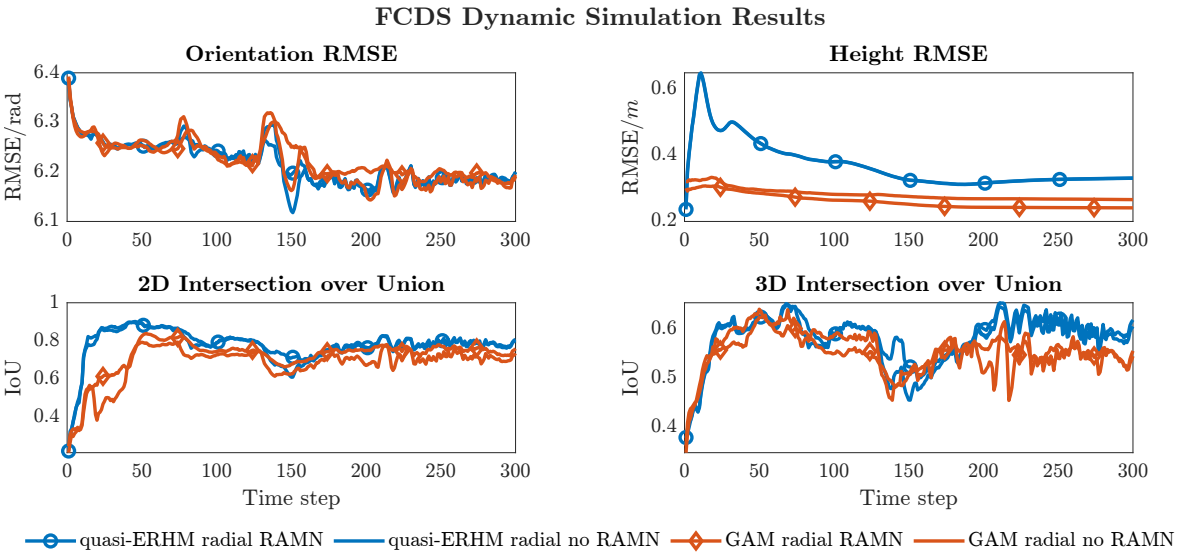

Figure 6.5: MC simulation RMSE and IoU estimation results of the dynamic *Solgenia* scenario for the FCDS measurement models.

In Fig. 6.5, it can be seen that the quasi-ERHM with and without applying the RAMN estimation procedure exhibits a better performance in terms of the 2D top-down view and 3D IoUs compared to the 3D GAM implementations in this scenario. On the other hand, the height RMSE reveals a slightly better performance of the 3D GAM approaches compared to the quasi-ERHM implementations. The orientation estimates converge for each of the implemented methods. In the 2D top-down view IoU, it can be seen that both approaches take some time at the beginning of the scenario to converge. After convergence, most of the implemented approaches show a similar performance, except for the 3D GAM without applying the RAMN estimation procedure, which is slightly worse. Interestingly, the RAMN estimation procedure has no crucial impact on the performance of the FCDS measurement models. Only in certain time steps does the application of RAMN bring a few advantages. The flexibility

of the FCDS approach as a shape representation seems to be sufficient to compensate for the incorrect assumption in the measurement data distribution. The 3D IoU finally reveals the performance of the quasi-ERHM being slightly better than the 3D GAM. In summary, this dynamic scenario also shows that the assumption of the line state and the remaining system state being statistically independent in the FCDS quasi-ERHM, as presented in Sec. 4.3.3, leads to promising estimation results in this scenario. The following experiments further investigate this approach.

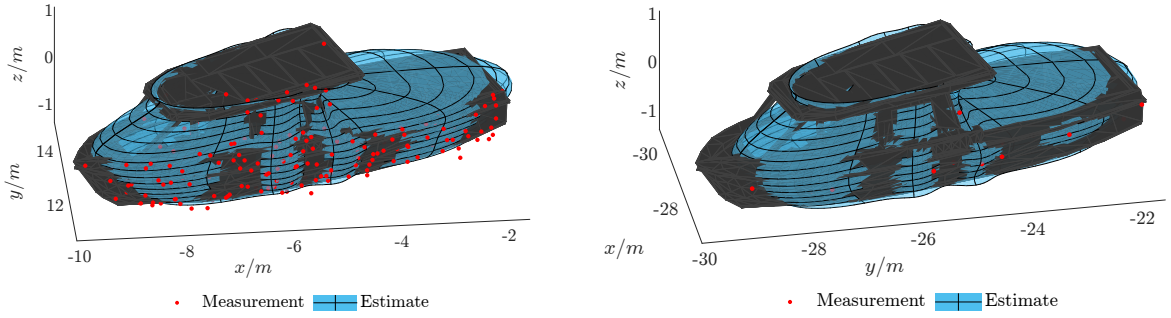

(a) Time step $k = 50$.

(b) Time step $k = 200$.

Figure 6.6: Estimation results of the simulated dynamic *Solgenia* scenario for the FCDS quasi-ERHM with a radial measurement source association and applying the RAMN approach at time steps $k = 50, 200$. The *Solgenia* shape reference is depicted as the black surface.

In addition to the quantitative results before, qualitative estimation results for the FCDS measurement models are given in Fig. 6.6 for the same time steps and random seed as before for the elliptic cylinder qualitative results in Fig. 6.3. The figure shows the estimation results of the quasi-ERHM using the RAMN estimation method, as this approach showed the best overall performance in the previous quantitative study. At time step 50, it can be seen that the estimate fits the shape of the *Solgenia* precisely. With fewer measurements at time step 200, the shape estimate gets worse, but still reliably approximates the shape of the *Solgenia*. Also, even with fewer measurements, the approach can track the object throughout the entire scenario.

Extruded Superellipse Results This paragraph presents and discusses the simulation results for the extruded superellipse measurement models presented in Ch. 5 in the simulated *Solgenia* scenario. Like before, the mean values for the orientation and height RMSEs and the 2D top-down view IoU measures after the MC simulation are reported in Fig. 6.8. For the extruded superellipse measurement models, the 3D IoU is not calculated since the approach is not able to fit the reference shape at different height sections. In this examination, the eight different approaches comprising the 3D GAM and ERHM approaches, each with a radial and projected measurement source association and with and without applying the RAMN estimation procedure, are evaluated.

In Fig. 6.7, it can be seen that the 3D GAM and ERHM with radial measurement source association applying the RAMN estimation procedure have the highest 2D top-down view IoU in this scenario. The implementations with radial measurement source association without applying the RAMN estimation procedure exhibit worse results. Since some measurements are also taken from the interior of the object, the estimates show a bias towards the center of the object if these measurements are not explicitly processed. A closer look at the 2D top-down view IoU also reveals that the models with projected measurement source association all perform

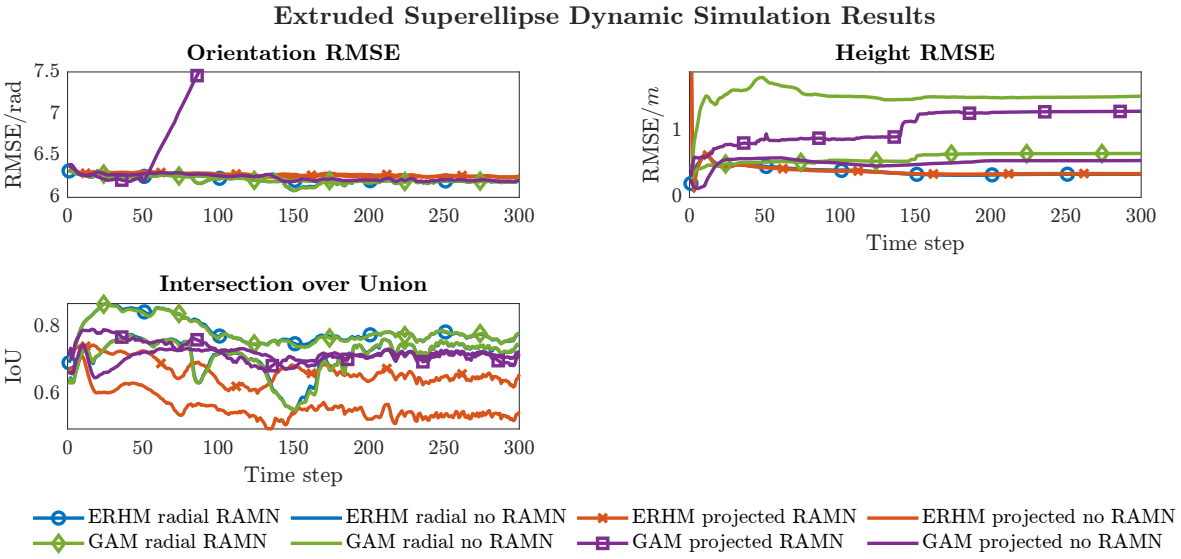

Figure 6.7: MC simulation RMSE and IoU estimation results of the dynamic *Solgenia* scenario for the superellipse measurement models.

worse. In the RMSE of the height estimate, every ERHM implementation exhibits the same performance and attains a better outcome than the 3D GAM implementations. The orientation RMSEs converges with an exception for the 3D GAM with projected measurement source association and applying the RAMN estimate. To summarize, the ERHM implementation with radial measurement source association and RAMN estimation procedure exhibits the best performance in this scenario.

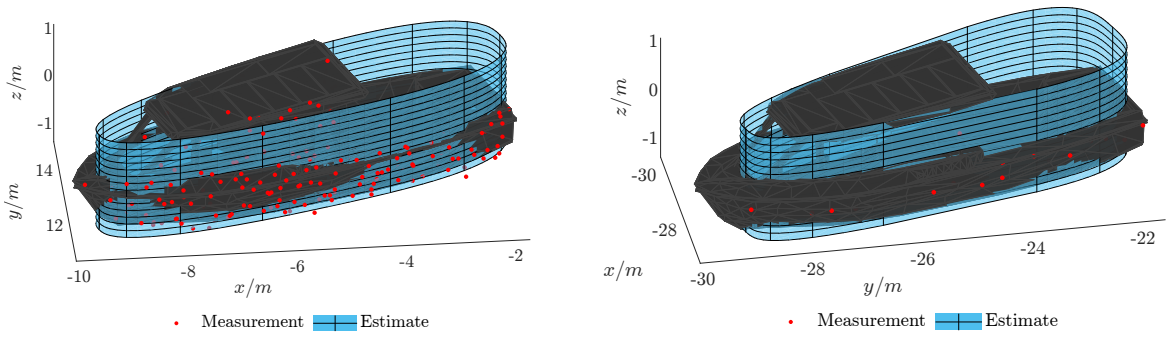

(a) Time step $k = 50$.

(b) Time step $k = 200$.

Figure 6.8: Estimation results of the simulated dynamic *Solgenia* scenario for the superellipse ERHM with RAMN at time steps $k = 50, 200$. The *Solgenia* shape reference is depicted as the black surface.

In addition to the quantitative results shown before, some qualitative estimation results at the same time steps and with the same random seed as before in the elliptic cylinder and FCDS paragraphs are visualized in Fig. 6.8. It can be seen that the extruded superellipse ERHM with radial measurement source association applying the RAMN estimation procedure can track the extent and position of the *Solgenia* CAD properly in the entire scenario. Furthermore, especially at time step $k = 200$ in Fig. 6.8b, it can be seen that the tapering deformation for the extruded superellipse shape is a promising shape deformation parameter for adapting to different shapes with few state parameters and a low computational effort.

Comparison This section compares the results presented before. Since the 3D GAM and the ERHM implementations with radial measurement source association applying the RAMN estimation procedure exhibited the best results among the presented shape descriptions, these implementations are compared in the following investigation. In addition to comparing the methods that have been developed in this thesis, a comparison to state-of-the-art measurement models from the literature is also performed in this paragraph. As before in Sec. 4.5.1, the results are compared with the measurement models applying SDFSs [O7], SHs [87], and a 3D GP [85] as shape representation in spherical coordinates. In the investigation, 31 shape coefficients for the SDFS shape representation, 121 shape coefficients for the SH shape representation, and 401 equidistantly distributed angle pairs for the 3D GP shape representation are estimated. Equidistantly distributed angle pairs on the unit sphere can be sampled using Fibonacci lattices [56]. The different number of shape coefficients results from the aim of achieving a similar approximation quality among the different approaches.

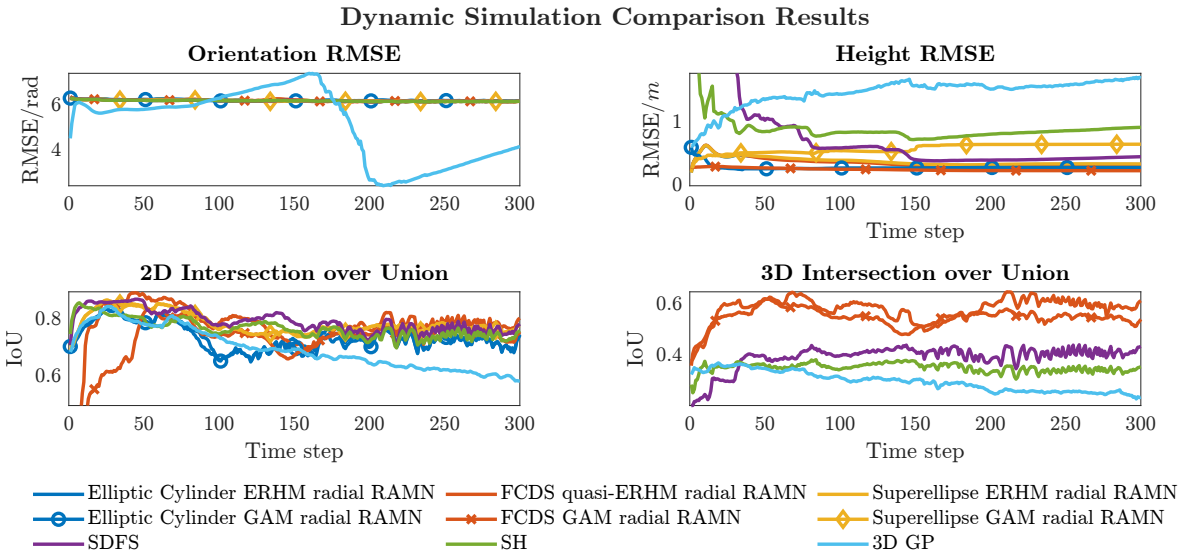

Figure 6.9: Comparison of MC simulation RMSE and IoU estimation results of the dynamic simulated *Solgenia* scenario.

The results of the comparison are visualized in Fig. 6.9. In the figure, the orientation and height RMSEs, as well as the 2D top-down view IoU, are given for each measurement model to provide a comparison among all the investigated methods. In addition, the approximated 3D IoU as presented in Sec. 4.5 is given for the state-of-the-art comparison methods and the FCDS measurement models. For these four shape descriptions, a 3D IoU measure is appropriate as these approaches can provide varying shape estimates at different height sections. Unfortunately, the figure directly reveals that the 3D GP approach [85] as implemented by the authors diverges in this scenario. The orientation estimate of the 3D GP measurement model is the only orientation estimate that does not converge to a static value. The remaining measurement models converge in the orientation estimates with an offset of 2π, which can be explained by the periodicity of the orientation angle. In the height RMSEs, the 3D GP and the SH models diverge. The SDFS shape description exhibits a better performance, however, it also diverges in the height estimate in the second half of the scenario. In the 2D top-down view IoU, the state-of-the-art comparison methods, except for the 3D GP model, show a comparable performance to the methods developed in this thesis. In combination with the poorer height estimates, it becomes clear that the state-of-the-art comparison methods converge in the area of the lateral surfaces, where a sufficient number of measurements are available, however, they

diverge in the area of the top and bottom surfaces, where measurements are missing. The approximated 3D IoUs also confirms this result since the FCDS results are considerably higher, and the FCDS shape description naturally solves the problem of missing measurements in the area of the top and bottom surfaces.

Comparing the height estimates of the approaches developed in this thesis, it can be seen that every approach except for the extruded superellipse 3D GAM converges to a low value. In this investigation, also the elliptic cylinder and FCDS 3D GAMs converge to a low value, although the 3D GAM is naturally missing a penalization for overestimated heights. The extruded superellipse 3D GAM demonstrates this problem in this MC simulation. The 2D top-down view IoU reveals a slight superiority of the more flexible shape descriptions when comparing the elliptic cylinder measurement models to the extruded superellipse and FCDS measurement models. However, an elliptic cylinder as the shape description with the lowest dimensionality is already appropriate for approximating the boat's shape in this scenario. Comparing the extruded superellipse and FCDS measurement models, it becomes clear that the flexibility of the FCDS measurement models is not superior in approximating the top-down view convex hull reference of the boat compared to the squareness and tapering parameters in the extruded superellipse measurement models, which can deform the ellipse shape.

6.1.2 Real-World Motor Boat Scenario Results

In this section, a real-world scenario, also with the *Solgenia* as a tracking object, is presented and evaluated again for the elliptical cylinder, FCDS, and extruded superellipse measurement models. For the evaluation, a single scenario with 300 time steps and a sampling rate of 0.1 seconds has been recorded with a 3D Lidar sensor [1]. The Lidar sensor has a vertical resolution of 0.11° with 128 stacked channels and a measurement range of 245 meters, producing up to 4.8 million measurements per second. The measurement noise is set to $v \sim \mathcal{N}(0, 0.025^2)$ in each Cartesian coordinate direction for each measurement model. In the recorded scenario, the *Solgenia* drives on the Rhine River through the field of view of the Lidar sensor. A picture of the *Solgenia* taken during the scenario can be seen in Fig. 6.10. The sensor is statically placed

Figure 6.10: Picture of the *Solgenia* tracking object at a single time step in the real-world scenario.

on the shore of the Rhine River, recording the *Solgenia*. Attached to the sensor assembly at the shore is also an real-time kinematic (RTK) global positioning system (GPS) and an inertial measurement unit (IMU) for a global position and orientation reference of the measurement setup. On the roof of the *Solgenia*, also two GPS antennas with RTK positioning solution are attached. By using two antennas, which provide a high-precision position measurement, the orientation of the boat can be measured with the GPS system in addition to the position. In combination with the CAD model of the *Solgenia*, the sensor setup on the roof of the *Solgenia*, and the static setup at the shore, a high-precision reference in position, orientation,

and shape of the tracking object is enabled. So far, this combination is unique in the maritime tracking community. The reference trajectory, in addition to the CAD reference and gathered measurements at specific time steps of the *Solgenia*, is visualized in Fig. 6.11.

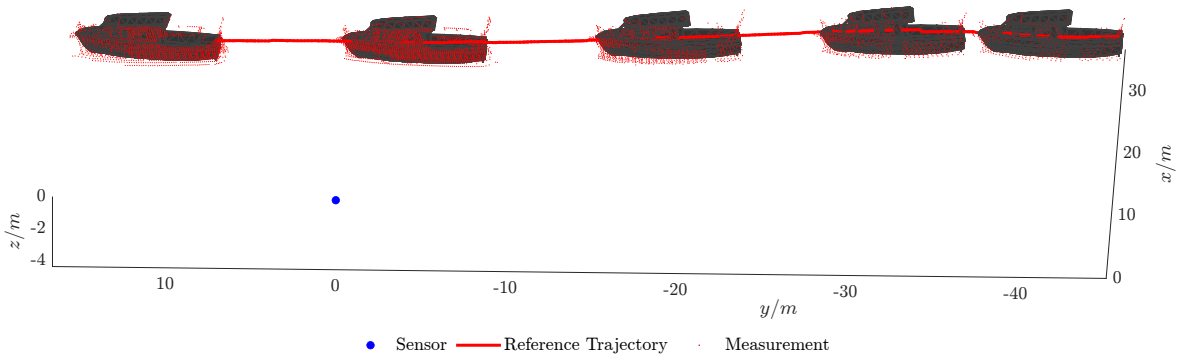

Figure 6.11: Measurements and reference of the real-world scenario with the *Solgenia* as tracking object.

In contrast to the number of measurements processed in the simulated scenario in the previous section, the number of measurements in this scenario is distinctly higher. The number of measurements throughout the entire scenario is visualized in Fig. 6.12. It can be seen that the number of measurements starts at a lower number of 500 measurements and then rises to almost 2000 measurements at the end of the scenario.

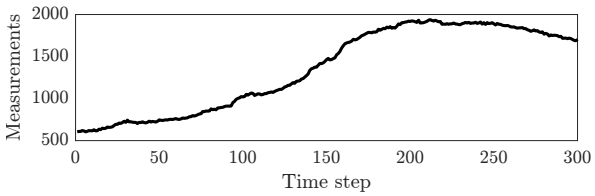

Figure 6.12: Number of measurements per scan in the entire real-world scenario.

Remark 6.2. *The real-world scenario with Solgenia as a tracking object has previously already been applied for the evaluation of the approaches presented in [O2–O4, O8]. In this section, additional evaluations are presented for each measurement model developed in this thesis.*

Remark 6.3. *The real-world data set with Solgenia as a tracking object and the complete evaluation presented in this section can be found at [R4].*

Due to the results in the previous sections, a separate investigation of the different variants for each of the shape descriptions presented in this thesis is omitted for the evaluation in the real-world motor boat scenario. Instead, the comparative study that was also carried out for the simulated scenario is presented directly in this section. In this comparison, the 3D GAM and ERHM implementations for each shape description with a radial measurement source association applying the RAMN estimation procedure are applied for tracking the *Solgenia* in the real-world scenario. In addition, again, the SDFS [O7], SH [87], and 3D GP [85] shape descriptions in spherical coordinates are applied as state-of-the-art comparison methods from the literature. The number of shape coefficients for each state-of-the-art comparison method is identical to the settings used before in the simulated *Solgenia* scenario. For the FCDS measurement models, again, 48 shape coefficients are employed. In the prediction step, the CT model [108] with standard deviations $\sigma_{\mathrm{la}} = 3\mathrm{m\,s^{-2}}$ in the linear acceleration and $\sigma_{\mathrm{ra}} = 5^\circ\,\mathrm{s^{-2}}$

in the rotational acceleration is employed. For the extent parameters, again, a random walk prediction with a standard deviation of $\sigma_{\text{ext}} = 1\text{e}{-5}$ is used to prevent local minima and to allow minor changes in the extent and shape estimates over time. The initialization step is again carried out using the first measurement set. As a position and orientation reference, the measurements from the GPS with RTK positioning solution can be taken. The height and shape reference can be calculated from the CAD model of the *Solgenia* as before in the simulated scenario in Sec. 6.1.1. For the evaluation, again, the orientation and height RMSEs as well as the 2D top-view IoU are calculated for each method throughout the entire scenario to be able to compare the different shape descriptions and measurement models. Furthermore, the approximated 3D IoU is calculated for the FCDS measurement models and the state-of-the-art comparison methods since these can estimate varying shapes at different height sections.

The quantitative results of the real-world motor boat scenario are visualized in Fig. 6.20. Unfortunately, also in the real-world motor boat scenario, it can be directly recognized that the 3D GP measurement model, as implemented by the authors of [85], diverges in this scenario. The orientation RMSE of the 3D GP approach is the only measurement model that cannot converge in this scenario. The remaining approaches converge with an offset of π, which can be explained by the periodicity of the orientation. In the height RMSE, the 2D top-down view, and approximated 3D IoU, the 3D GP approach completely diverges in this scenario. Comparing the SDFS and SH approaches, it becomes clear that the shape representations in spherical coordinates have major drawbacks in maritime scenarios. Although the 2D top-down view IoU of both approaches is comparable to the approaches developed in this thesis, the height estimates are distinctly worse. Both shape representations in spherical coordinates produce large errors, caused by missing measurements from the top and bottom surfaces. The worse performance is also depicted in the approximated 3D IoU, where the FCDS approaches exhibit a distinctly better performance compared to the shape representations in spherical coordinates.

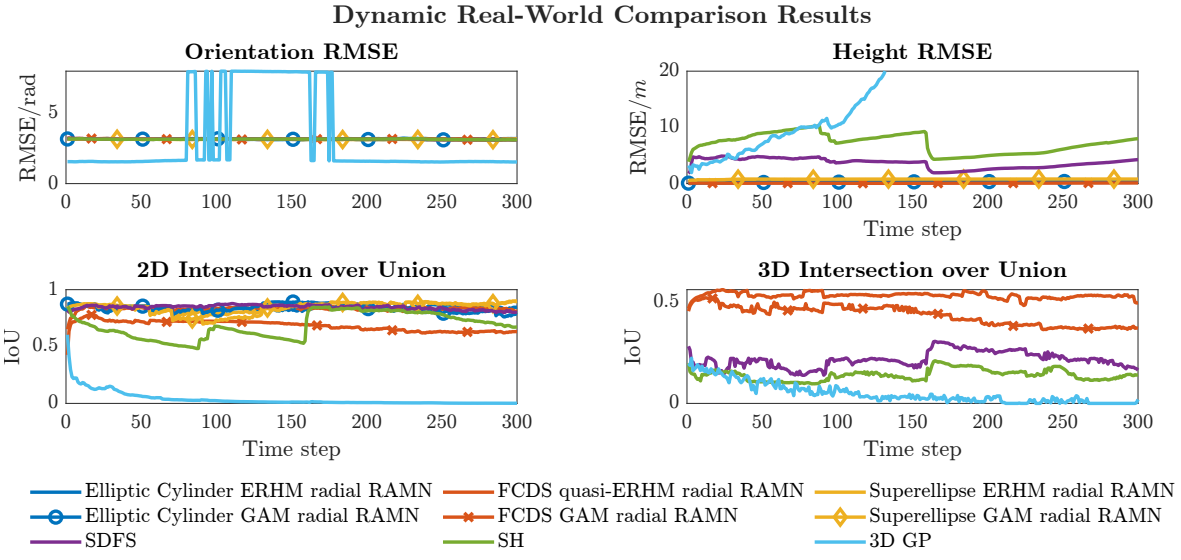

Figure 6.13: Comparison of RMSE and IoU estimation results of the dynamic real-world *Solgenia* scenario.

Comparing the approaches presented in this thesis, it can be seen that each method converges in the height and orientation RMSEs. In the 2D top-down view IoU, the approaches exhibit a comparable performance, except for the FCDS 3D GAM that shows a slightly worse result than the remaining approaches. These results illustrate again that the elliptic cylinder shape representation, with its low dimensionality, is already a decent shape approximation for the

boat's shape. The FCDS and extruded superellipse shape representation cannot provide major advantages in the shape approximation capabilities as measured by 2D top-down view IoU in this scenario. Comparing the 3D GAM and quasi-ERHM FCDS measurement models in this scenario, once again, the assumption that the line and remaining system state can be assumed to be statistically independent in the quasi-ERHM implementation is supported. The quasi-ERHM results, both in the 2D top-down view and approximated 3D IoU, exhibit a better performance than the 3D GAM results.

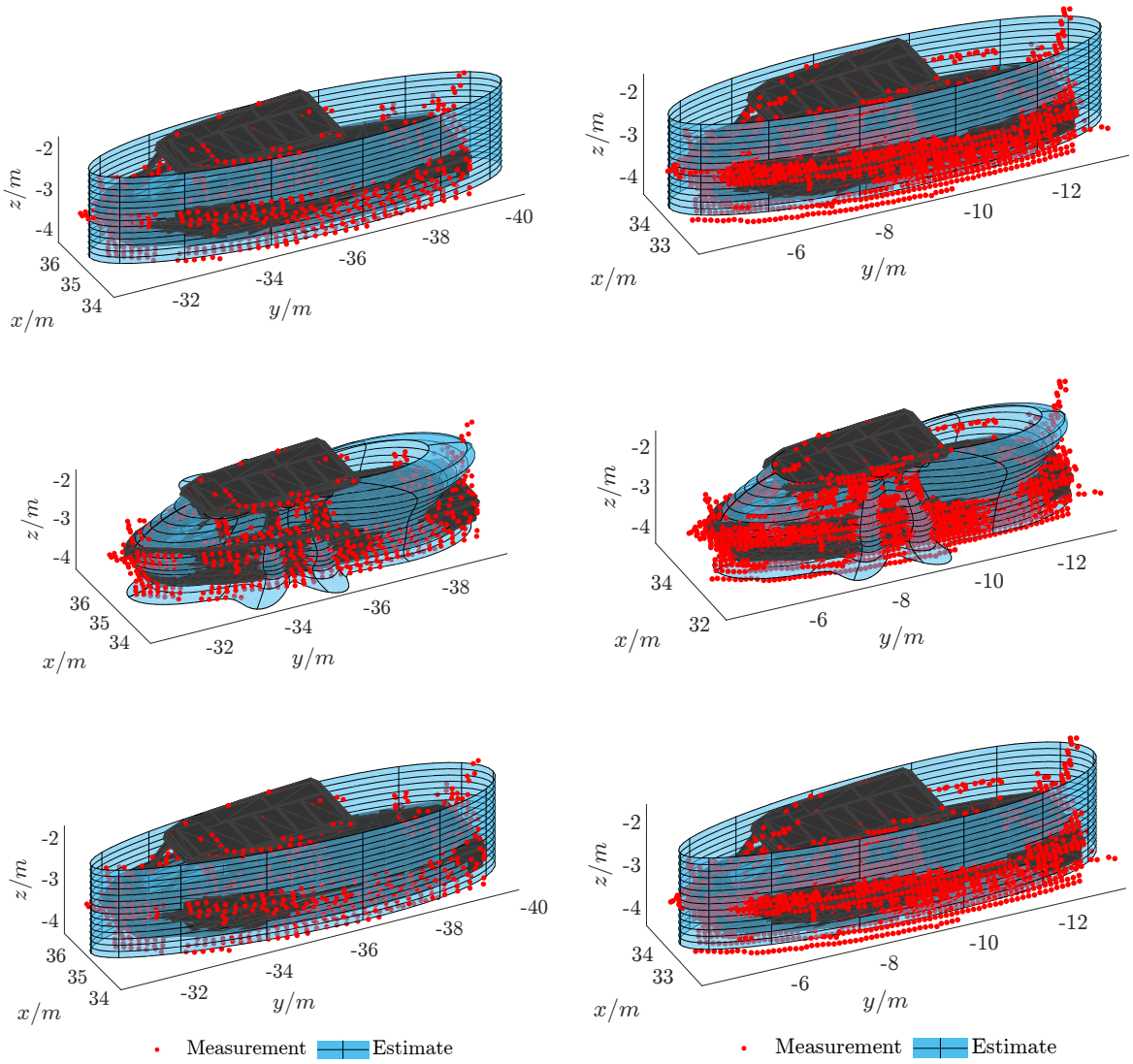

(a) Time step $k = 50$.

(b) Time step $k = 200$.

Figure 6.14: Estimation results of the real-world dynamic *Solgenia* scenario for the ERHMs with a radial measurement source association and applying the RAMN approach at time steps $k = 50, 200$. The *Solgenia* shape reference is depicted as the black surface. The elliptic cylinder in the first, FCDS in the second, and extruded superellipse results in the third row.

In addition to the quantitative results of the real-world scenario, qualitative estimation results for each shape description at the same time step are visualized in Fig. 6.14. For each method, estimates at time steps $k = 50$ and $k = 200$ are depicted. In the first row of Fig. 6.14, the elliptic cylinder results, in the second row the FCDS results, and in the third row the extruded superellipse results are depicted. In comparison to the FCDS estimates of the simulated *Solgenia*

scenario in Fig. 6.6, the FCDS shape estimate of the real-world scenario shows a bulge in the upper rear part of the ship. This can be attributed to the flagpole, which can be seen in Fig. 6.10, but is not included in the CAD model, however, it still generates a significant number of measurements. The shape estimate then naturally also processes the measurements of the flagpole. Comparing the elliptic cylinder and the extruded superellipse estimation results, it becomes clear that the elliptical shape is already a suitable shape description for a motor boat. However, the tapering parameter still offers an advantage to the extruded superellipse. This makes it possible to extract the flatter rear side compared to the more pointed front side in the shape of the boat. The height estimates and tracking performance are decent for every measurement model in this scenario.

6.1.3 Real-World Sailing Boat Scenario Results

In this section, the specialized elliptical cone measurement model, presented in Sec. 3.4, is evaluated in a real-world scenario with measurements from a sailing boat. For the evaluation, a single scenario with 200 time steps and a sampling rate of 0.1 seconds has been recorded with the same Lidar sensor [1] as before in Sec. 6.1.2. The measurement noise is therefore again set to $v \sim \mathcal{N}(0, 0.025^2)$ in each Cartesian coordinate direction for each investigated measurement model. The sailing boat scenario was recorded with the catamaran ferry as a test vehicle, which commutes between Constance and Friedrichshafen on Lake Constance. This catamaran was equipped with the same sensor setup that previously recorded the Solgenia in Sec. 6.1.2. An illustration of the sensor setup on the catamaran can be seen in Fig. 6.15a.

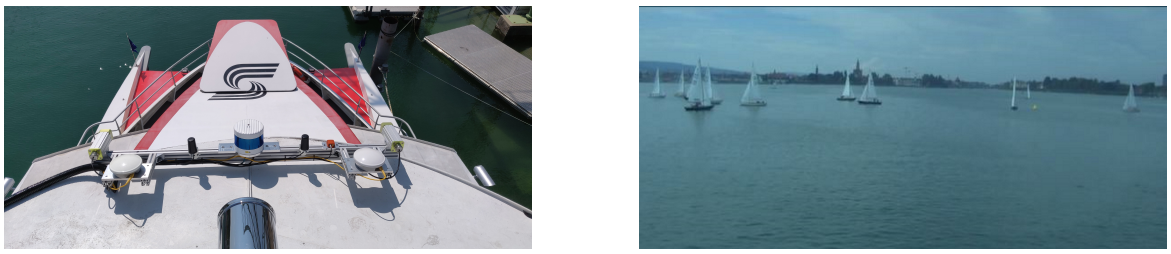

(a) Sensor mounting on the catamaran.

(b) Camera image of the sailing boats [C4].

Figure 6.15: Figure of the sensor setup on the catamaran and the sailing boats in a regatta, which were recorded by the sensor setup.

For the evaluation, a scenario is used in which the catamaran has to pass through a regatta of folk boats. An image of this trip, taken by the camera system on the sensor setup, can be seen in Fig. 6.15b. Within this scenario, the measurements of a single sailing boat are extracted and utilized for the evaluation. Since the regatta was contested by standardized sailing boats of the folk boat class [103], a reference is available for the object's extent parameters. Hence, the reference used for the major semi-axis is 3.84 meters, for the minor semi-axis 1.10 meters, and the height, subtracting the draft, is 9.80 meters. However, there is no absolute certainty about the correctness of this reference, since the boats could not be measured. They therefore serve as a rough guideline in the following analysis.

The number of measurements processed in this scenario is visualized in Fig. 6.16. The figure shows that the number of measurements at the beginning of the scenario, when the sailing boat enters the sensor's surveillance area, is rather low. Subsequently, the number of measurements increases permanently the closer the sailing boat gets to the sensor. At the end of the scenario, a large part of the sailing boat is partially occluded by the catamaran. Due to the mounting

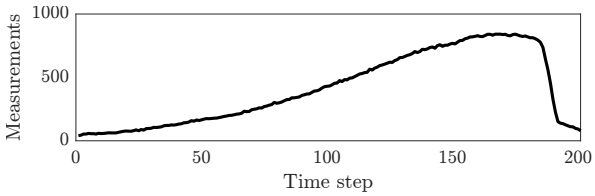

Figure 6.16: Number of measurements per scan in the entire real-world sailing boat scenario.

position of the sensor, a blind angle occurs in which the sensor can only record the catamaran itself. The number of measurements, therefore, drops very quickly towards the end of the scenario before the sailing boat leaves the sensor's surveillance area.

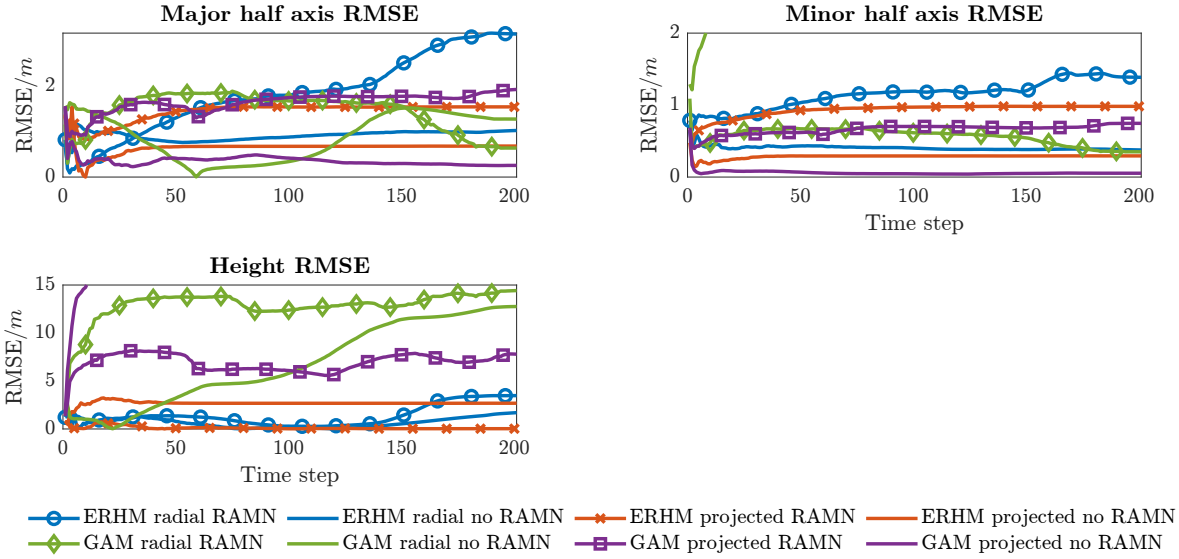

Figure 6.17: RMSE estimation results of the dynamic real-world sailing boat scenario.

The real-world sailing boat scenario is now analyzed using the algorithms described in Sec. 3.4. This involves evaluating both the 3D GAM and the ERHM, each with the radial and projected measurement-to-source association and with and without the RAMN estimation procedure. Each combination results in an analysis of eight different algorithms. The only difference between the evaluation and the algorithms described in Sec. 3.4 lies in the assumed distribution of the extrusion parameter $s_{k,l}$. In the measurements, it was seen that the distribution does not entirely follow a triangular distribution. Also, the extent estimates were extremely sensitive to variations in the extrusion parameter distribution. Therefore, the statistically determined mean and variance of the measurements in the z direction are determined and used in the evaluation. The extrusion parameter is then sampled using an approximated Gaussian distribution derived from the measurements, specifically $s_{k,l} \sim \mathcal{N}(0.2902, 0.0434)$. The RMSEs using the folk boat extent parameters as a reference for each of the eight algorithms can be seen in Fig. 6.17. In the figure, it can be seen directly that the algorithms perform very differently in this scenario. The 3D GAM approaches all diverge in the height estimate due to the missing penalization for overestimated heights. Unfortunately, the ERHM with radial association applying the RAMN estimation procedure also had problems converging in this scenario. The remaining ERHMs, however, converged to mostly static values in the RMSEs.

In addition to the quantitative results, qualitative results of the real-world sailing boat scenario are visualized in Fig. 6.18 and 6.19. In Fig. 6.18, 3D estimation results are depicted at the time steps given in the captions of the figures. Fig. 6.19 gives the respective 2D top-down view

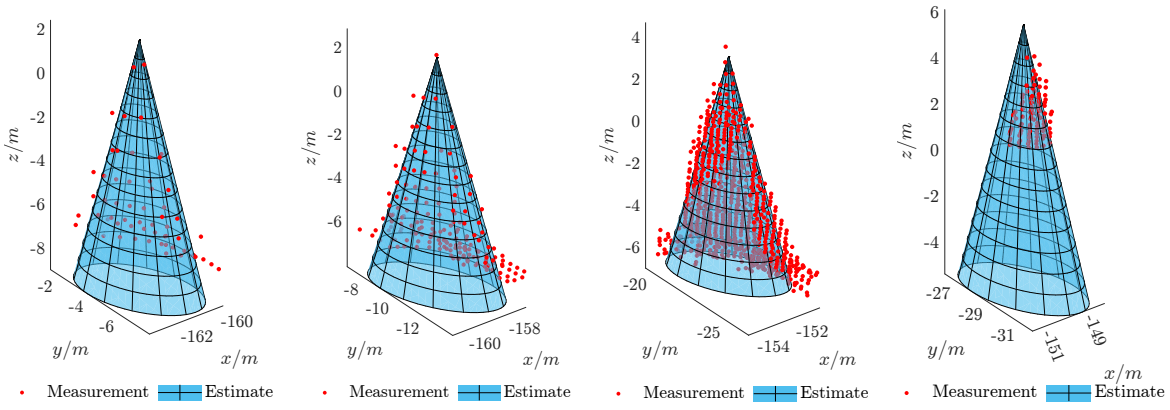

(a) $k = 5$. **(b)** $k = 50$. **(c)** $k = 150$. **(d)** $k = 200$.

Figure 6.18: 3D estimation results of the real-world sailing boat scenario.

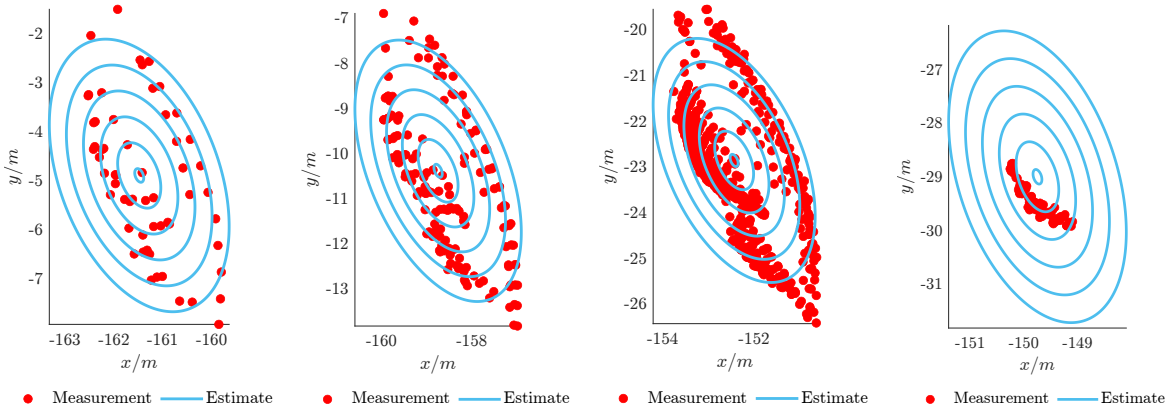

(a) $k = 5$. **(b)** $k = 50$. **(c)** $k = 150$. **(d)** $k = 200$.

Figure 6.19: 2D estimation results of the real-world sailing boat scenario.

estimation results. Due to the quantitative results discussed before, the estimation results for the ERHM with radial measurement source association without applying the RAMN estimation procedure are shown. In both figures, it can be seen that the elliptic cone measurement model is capable of tracking a sailing boat and estimating its extent. Particularly, the estimates at time step $k = 200$ are interesting due to the partial occlusion of the sailing boat by the catamaran. Due to the convergence in the estimates of the previous time steps, the approach can still estimate a decent extent of the sailing boat. In total, however, the elliptic cone measurement models can be significantly improved in future work. First, a rolling motion should be included in the kinematic system state and the motion model, since this is characteristic of sailing boats, depending on their orientation to the wind and its speed. Furthermore, a shear mapping [41] could be incorporated to model the displacement of the mast towards the center of the sailing boat. Preliminary investigations have already shown promising results, but are left to future work.

6.2 Generalization to an Automotive Environment

In the previous section, the developed algorithms were applied to tracking maritime objects. In this section, a generalization of the presented algorithms to the automotive domain is

investigated. Therefore, the famous KITTI data set [48] is applied. Depending on the sensor position on the ego-vehicle, measurements can often mainly be expected from the lateral surface of an object in the automotive environment, where shape descriptions defined in cylindrical coordinates can be superior to shape descriptions defined in spherical coordinates. In the KITTI data set, measurements are taken with 2 grayscale cameras, 2 color cameras, an IMU, a GPS, and a Lidar sensor. The Lidar sensor generates measurements with a sampling rate of 0.1 seconds, an angular resolution of 0.09° with 64 stacked channels, and a measurement range of 120 meters, producing up to 1.3 million measurements per second. In the following investigation, the Lidar measurements for specific objects are extracted to evaluate the developed algorithms on a large-scale data set. The measurement noise for the Lidar measurements is set to $v \sim \mathcal{N}(0, 0.025^2)$ in each Cartesian coordinate direction for each measurement model. In the data set, scenarios were recorded and annotated in city and residential areas and on the roadside. In the raw data set [48], a varying number of objects are annotated over consecutive time steps in each scenario. These annotated objects are called tracklets in the following. In total, 932 cars, 98 vans, 22 trucks, 84 pedestrians, 16 sitters, 43 cyclists, 9 trams, and 33 remaining categories, such as trailers or segways, resulting in 1237 tracklets, are annotated in the raw data set. The annotations are directly given in the Lidar frame. Using the annotated bounding boxes, measurements inside the bounding box can be extracted and directly employed for the developed EOT algorithms. To take into account incorrect annotations and minor inaccuracies in the calibration between the sensors, the dimensions of the bounding boxes are artificially enlarged by 10 centimeters for the extraction of the measurements.

For the evaluation, the elliptic cylinder, the FCDS, and the extruded superellipse shape descriptions are employed. Due to the elliptic cone measurement models being defined specifically for sailing boats, these are omitted in this investigation. As state-of-the-art comparison methods, again the SDFS [O7], the SH [87], and the 3D GP [85] are used. As shape references, the bounding boxes are taken for the cars, vans, trucks, sitters, trams, and the remaining categories. For the pedestrians and cyclists, an elliptic cylinder is employed as a shape reference. Since these shape references have a lower level of detail compared to the *Solgenia* reference CAD model in the scenarios before, the measurement models utilized to process the measurements are also adapted to estimate fewer details in the shape estimates. The elliptic cylinder measurement models are left unchanged, as they already produce low-dimensional extent estimates. The number of shape coefficients for the FCDS measurement models is reduced to 24. For the extruded superellipse measurement models, the tapering deformation is completely omitted. In doing so, the shape deformation using the squareness parameter of the superellipse shape can be examined in more detail. In the high number of scenarios in the KITTI data set, extruded ellipse and extruded rectangle reference shapes are present, where the squareness deformation can provide an advantage over the pure elliptic cylinder measurement model. For the state-of-the-art comparison methods, the dimensionality is also reduced. For the SDFS measurement model, 21 shape coefficients, for the SH measurement model, 49 shape coefficients, and for the 3D GP measurement model, 201 equidistantly distributed angle pairs on the unit sphere are applied.

In the prediction steps, the CT model [108] with standard deviations $\sigma_{\mathrm{la}} = 3\,\mathrm{m\,s^{-2}}$ in the linear acceleration and $\sigma_{\mathrm{ra}} = 5\,\mathrm{rad\,s^{-2}}$ in the rotational acceleration is employed. Each filter is initialized using the first measurement set for each tracklet. As before in the real-world motor boat scenario, a comparison of the eight different versions for the elliptic cylinder and extruded superellipse, and four different versions of the FCDS measurement models is omitted for the investigation in the automotive environment. Instead, the 3D GAM and ERHM implementations with radial measurement source association both with and without applying

the RAMN estimation procedures are directly compared to the state-of-the-art comparison methods, as the radial measurement source association exhibited the best performances in the investigations before. For the evaluation, the orientation and height RMSEs and the 2D top-down view IoUs are calculated for each time step and tracklet. Afterwards, the mean values for each evaluation measure and tracklet are calculated for the consecutive time steps. By evaluating the RAMN estimation procedure on the large-scale KITTI raw data set, the approach is extensively tested again for each measurement model. Since visualizing the mean values directly in a single figure would produce highly confusing illustrations, the mean values are used to generate a box plot for each implemented algorithm. These box plots then visualize the main statistical parameters for each method. However, outliers are cropped in the y direction since these are often far apart from the whiskers, which would greatly compress the box representing the important statistical parameters.

The box plots for the orientation and height RMSEs and 2D top-down view IoUs can be seen in Fig. 6.20. In this figure, the statistical values of the mean orientation estimate RMSEs calculated from each of the 1237 tracklets can be seen in the first row. For this evaluation, the orientation estimates and references are mapped to the interval $[0, 2\pi]$ to handle potential ambiguities and improve comparability among the measurement models. It can be seen that the whiskers of the mean orientation RMSEs for each model, except the 3D GP, span from 0 to almost 2π, meaning that the orientation estimates differ obviously from the reference in some cases. However, they also often converge reasonably well. For most of the models, the median is around 2 degrees, while for the 3D GP it is slightly lower. The orientation estimates of the 3D GP differ from the remaining models since the authors of [85] used a different motion model in their implementation than the CT model [108].

In the mean values of the height estimates in the second row of Fig. 6.20, it can be seen directly that the elliptical cylinder and extruded superellipse ERHM, as well as the FCDS quasi-ERHM, exhibit the best performance. Although a lot of outliers can also be seen for these models, the median, mean values, and the whiskers are close to 0, which illustrates the persuasive performances. Interestingly, the mean height estimates of the FCDS 3D GAM show a similar performance compared to the FCDS quasi-ERHM implementation. The elliptic cylinder and extruded superellipse 3D GAMs often overestimate the height of the objects. The state-of-the-art comparison methods also often overestimated the height of the objects. These results again illustrate the improvement of describing the shape representation in the measurement model in cylindrical rather than in spherical coordinates. Also in the automotive domain, measurements are often mainly gathered from the lateral surface, leading to error-prone estimates at the top and bottom surfaces if measurements are missing in these regions.

In the mean values of the 2D top-down view IoUs in the third row of Fig. 6.20, it can be seen that the estimates for most of the models applying the RAMN estimation procedure are higher compared to the respective models not applying the RAMN. Only for the FCDS measurement models, applying the RAMN approach exhibits similar or worse results compared to the FCDS models not applying the RAMN. The FCDS shape representation seems to be flexible enough to overcome the mismatch in the modeling of the measurement source association to the actual measurement source distribution. For the remaining measurement models, the RAMN approach shows a clear advantage compared to not applying the RAMN estimation. Overall, the extruded superellipse ERHM with the RAMN estimation procedure exhibits the best performance in the 2D top-down view IoU. In combination with the low height RMSEs of the approach, the results seem very promising. The extruded superellipse shape representation gives a good compromise between flexibility and efficiency. The state-of-the-art comparison methods also exhibit high 2D top-down view IoUs. However, in combination with the worse height estimates compared to

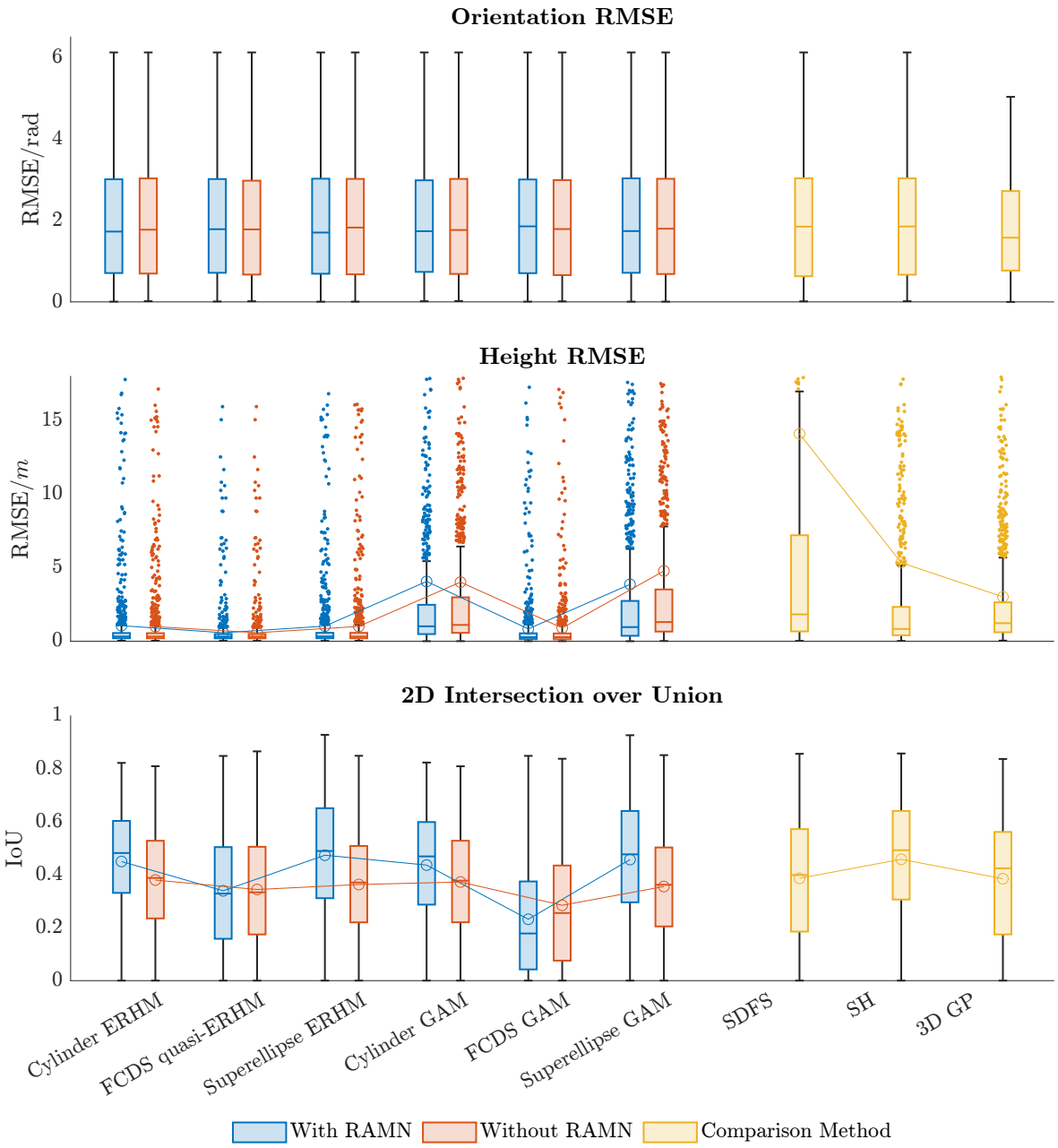

Figure 6.20: Box plot of the RMSEs and IoU mean estimation results for each tracklet in the KITTI raw data set. The radial measurement source association is applied for the elliptic cylinder, FCDS, and extruded superellipse measurement models. Outliers are scattered and cropped in the vertical direction. Mean values for the height RMSEs and IoUs are visualized as curves in the respective color.

the shape representations in cylindrical coordinates, the approaches show a worse performance compared to the methods proposed in this thesis. In many cases, the shape representations in spherical coordinates converge at the lateral surface where enough measurements are present, however, they have large outbursts at the top and bottom surfaces where measurements are often missing.

In addition to the quantitative results presented and discussed before, qualitative results for various methods and objects are visualized in Fig. 6.21. In this figure, estimation results using the ERHMs with radial measurement source association applying the RAMN approach are

visualized. In the first row, results for the elliptic cylinder, in the second row for the FCDS, and in the third row for the extruded superellipse measurement models can be seen. In the first column, a car, in the second column a cyclist, and in the third column a pedestrian tracklet are depicted at a single time step. In the figure, it can be seen that the elliptic cylinder is perfectly capable of estimating the extent of the cyclist and pedestrian, however, it is not directly suitable for the car. The extruded superellipse shape representation, on the other hand, is capable of adapting its shape to better fit the rectangular shape of the car and can also represent the shapes of the cyclist and pedestrian. The FCDS shape estimates are also suitable and show promising results.

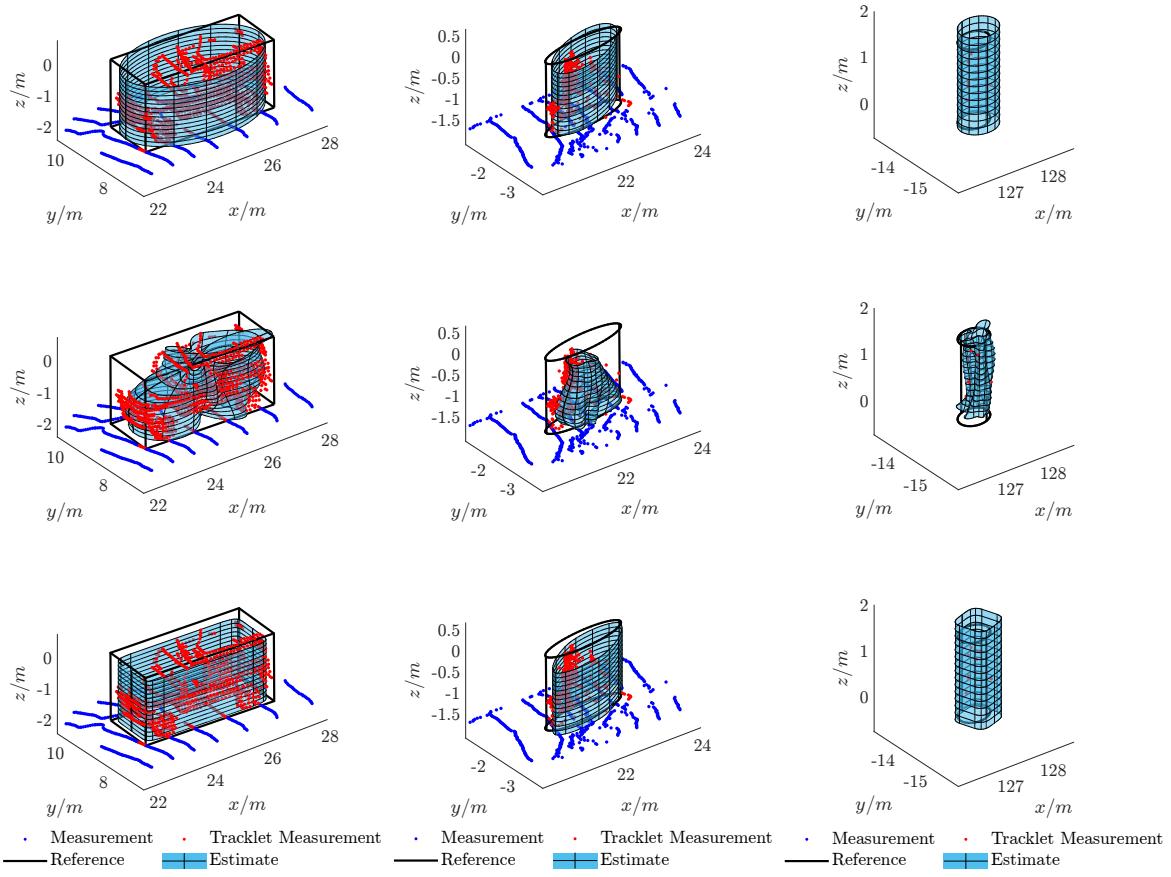

(a) EOT estimates of a car. **(b)** EOT estimates of a cyclist. **(c)** EOT estimates of a pedestrian.

Figure 6.21: Estimation results of the KITTI raw data set for different object categories and the ERHMs with a radial measurement source association applying the RAMN approach. The elliptic cylinder in the first, FCDS in the second, and extruded superellipse results in the third row.

6.3 Discussion

The experimental evaluation based on simulated, real-world maritime, and automotive data sets provides important insights into the performance of the proposed 3D EOT measurement models. While the results were presented in detail in the previous sections, a more in-depth discussion is necessary to interpret some of the underlying reasons for the observed performance differences.

One striking finding is the poor performance in height estimation using state-of-the-art methods such as the SH, SDFS, and 3D GP. As already mentioned, this can be attributed to the fact that these models expect measurements on the top and bottom surfaces of the object, which are often sparse or completely missing. When using shape descriptions in cylindrical coordinates, no measurements are expected in the areas of the top and bottom surfaces. Only the lateral surface is described in the measurement model, which explains the better performance in height estimation. A particularly interesting observation is the significantly poorer performance of the 3D GP model compared to the SDFS and SH approaches. This is likely due to the implementation of the 3D GP model used, which estimates the roll and pitch angles in addition to the yaw angle. While the SDFS and SH models and all models developed in this work only estimate the yaw angle, the additional degrees of freedom in the state space of the 3D-GP model can potentially lead to filter divergence. If there is an insufficient number of measurements to estimate the additional angles, the filter may converge to an incorrect state that cannot be corrected later in the tracking process, leading to a complete divergence of the tracking results.

Furthermore, the difference in performance between the radial and projected measurement-to-source association deserves a more detailed discussion. In all models tested, the radial association consistently performed better than the projected association. The main reason for this superiority may lie in the calculation of the projected measurement-to-source association. The radial association can be described by a closed-form analytical solution, making it both highly efficient and numerically stable. Conversely, the projected association lacks a closed-form solution for the shape representations shown. To perform the association, the boundary of the shape must be approximated by a polygonal chain. This approximation leads to a change in the actual shape, which in turn might harm the performance of the filter. Preliminary studies have confirmed that increasing the number of control points in the polygonal chain can improve the performance again, but this requires a significant amount of computing power per measurement, making it less suitable for real-time applications.

Finally, the impact of the RAMN estimation method deserves closer consideration. The evaluation confirmed its considerable usefulness for elliptical cylinder and extruded superellipse models, particularly in improving the 2D top-down view IoU. The RAMN approach explicitly models the measurements inside the shape, which is crucial for these less flexible shape descriptions. In contrast, the highly flexible FCDS with RAMN model showed little or no improvement over the FCDS without RAMN method in the automotive scenarios. This suggests that the FCDS shape representation is flexible enough to implicitly compensate for the measurements from the interior by simply adjusting its shape coefficients, making explicit modeling by RAMN less necessary. Interestingly, the RAMN approach also led to an improvement in height estimates for some of the measurement models. This is a surprising result, as the RAMN method was developed specifically for handling measurement data in the horizontal plane and, in theory, should have no direct influence on height estimation. To fully understand this phenomenon, more detailed investigations are needed in future work.

6.4 Conclusions

This chapter contains a comprehensive experimental evaluation of the 3D EOT measurement models developed in this thesis, assessing their performance both in the targeted maritime environments and in a generalization to the automotive domain. The evaluations were based on a combination of simulated scenarios, unique real-world maritime data sets with high-precision reference data, and the extensive public KITTI data set. The results provide several important

insights. First, the advantage of using shape representations in cylindrical coordinates over spherical coordinates was consistently confirmed across different data sets and sensor types. Models based on cylindrical coordinates, such as the elliptic cylinder and cone, the FCDS, and the extruded superellipse, demonstrated superior robustness and accuracy in height estimation, especially for sparse measurements at the object's top and bottom surfaces, which is typical for Lidar sensors in the maritime and automotive sectors.

In addition, the evaluations confirmed the results previously achieved in regard of the measurement-to-source association. The ERHM and quasi-ERHM approaches consistently outperformed their 3D GAM counterparts in providing unbiased 3D extent estimates, especially for height estimates. Furthermore, the practical value of the RAMN estimation approach was confirmed. Its application significantly improved the extent and shape estimation accuracy for parametric elliptic cylinder and cone, and flexible parametric extruded superellipse models when processing real-world data with mixed boundary and interior measurements. The results also pointed to an interaction between the flexibility of the model and the influence of the RAMN approach, as its advantage was less pronounced in the highly flexible FCDS models in the automotive tests. Finally, the comparative analysis across models and domains showed that the extruded superellipse ERHM with RAMN is a particularly promising approach that offers a good balance between shape adaptability and low-dimensionality, while also demonstrating robust performance and generalizability. Overall, the comprehensive evaluations presented in this chapter confirmed the effectiveness and practical relevance of the proposed 3D EOT measurement models for further developments of future environment perception systems.

CHAPTER 7

Final Conclusions and Future Work

Contents

7.1 Summary 116
7.2 Future Work 117

7.1 Summary

Within this dissertation, the need for robust 3D extended object tracking (EOT) techniques capable of handling the complexity of maritime environment perception for automated surface vessels is addressed. The central challenge in this research field is to accurately estimate both the kinematic state and the detailed physical extent and shape of surrounding objects using modern high-resolution sensors such as light detection and ranging (Lidar). These often provide incomplete data in maritime environments due to water occlusions and sensor limitations in the field of view and capture measurements from different, potentially unknown object classes with complex shapes. Motivated by the increasing importance of automation in shipping for enhancing safety, efficiency, and availability, conventional point-based tracking approaches have proven insufficient, leading to the necessity of developing advanced EOT methods.

A key finding of this work is the distinct advantage of using shape representations in cylindrical coordinates over shape representations in spherical coordinates for maritime EOT. Extensive evaluations using simulated and real-world measurements consistently showed that shape representations in cylindrical coordinates naturally solve the problem of sparse measurements at the top and bottom surfaces, which is common in maritime sensing but also in other domains such as the automotive environment. By only representing the lateral surface in the cylindrical shape representation, missing measurements do not lead to error-prone estimates in these areas. This was particularly evident in the comparative experiments on height estimation in all studies, in which cylindrical representations achieved significantly better results than the currently most advanced spherical shape representations. This confirms the fundamental choice of shape representations in cylindrical coordinates for the models developed here.

Furthermore, this work has demonstrated the importance of suitable measurement-to-source association techniques for accurate 3D extent estimation. While simpler 3D greedy association models (GAMs) have shown to be computationally more efficient, the extrusion random hypersurface model (ERHM) and the quasi-ERHM, which has been proposed related to the novel non-parametric Fourier-Chebyshev double series (FCDS) model, consistently proved superior in delivering unbiased height estimates. This finding underscores the need to use such advanced association techniques, which may take symmetry assumptions into account to increase efficiency, when reliable 3D extent estimates are required.

Perhaps the most significant practical contribution is the development and investigation of the recursive artificial measurement noise (RAMN) estimation method. This technique provides an effective and computationally feasible solution to the widespread problem of mixed boundary and interior sensor measurements, often prevalent in real-world data. Experiments with all developed parametric, non-parametric, and flexible parametric measurement models confirmed that the RAMN approach improves the accuracy and robustness of extent and shape estimates by reducing distortions caused by interior points. The biggest advantage of this approach is its flexibility, as it does not require the spatial distribution of the measurements to be defined in advance. Instead, this distribution is estimated by a recursive calculation within the approach based on the recorded measurements.

Finally, this dissertation has successfully developed and validated a series of 3D EOT models with varying requirements and degrees of flexibility. While specialized parametric elliptic cylinder and cone measurement models are efficient for known object classes, the novel non-parametric FCDS shape representation offers high accuracy for complex or unknown shapes. Particularly, the extruded superellipse measurement model has proven to be an effective compromise, demonstrating adaptability in representing different object geometries such as boats, cars, and pedestrians within a compact parametric framework and achieving highly accurate performance, especially in an ERHM implementation applying the RAMN estimation procedure. The successful application of these methods not only to unique real-world maritime measurements with high-precision reference data, but also their generalization to the automotive KITTI benchmark, underscores the relevance and effectiveness of the algorithms developed in this dissertation for advancing the state-of-the-art in 3D EOT.

7.2 Future Work

Although this work has made progress in the field of 3D EOT, particularly for maritime applications using shape representations in cylindrical coordinates and robust handling of varying spatial measurement distributions, several possibilities for future research remain open. First, further refinements for the developed measurement models are possible. The elliptical cone measurement model for sailing boats could be improved by integrating roll dynamics into the kinematic state and motion model and possibly by adding shear mappings to the shape to better model the mast position. For the non-parametric FCDS measurement model, investigating alternative basis functions in the vertical direction or adaptive methods for selecting the optimal number of shape coefficients based on the measurement density or object complexity could improve the performance of the approach. The quasi-ERHM approach developed in conjunction with the FCDS shape representation is based on an independence assumption and a fixed extrusion factor distribution for the line estimator. Future work could investigate methods to relax the independence assumption or to estimate the extrusion factor distribution online recursively based on the estimated shape coefficients, which could further improve the accuracy of the approach.

Furthermore, algorithmic improvements could be investigated. The observed ambiguities in orientation estimation, especially for symmetrical shapes, could be addressed using techniques from directional statistics or by developing specialized transformation functions, as was done for state interval constraints in this thesis. In addition, optimizing the computational performance of the developed algorithms, possibly through parallelization strategies or advanced numerical techniques, remains important for real-time applications.

From a system perspective, integrating the developed 3D EOT measurement models for single object tracking into a multiple EOT framework is an important research direction. This involves addressing the complex data association problem in the context of multiple extended objects, possibly generating a vast amount of measurements per time step. Also, the separation of measurements gathered from static objects from dynamic object measurements is an important step in developing a full 3D multiple EOT framework. Fusion with other sensor modalities, such as cameras for classification, is another important area. Object classification could influence the selection of the EOT measurement model, which would lead to a more adaptable perception system.

Finally, the application of the detailed extent and shape estimates generated by these 3D EOT methods to downstream tasks such as collision avoidance, path planning, and risk assessment could be investigated. Quantifying the benefits of using accurate extent and shape information compared to point-based tracking in these applications would demonstrate the practical value of this research. In addition, testing and validation with increasingly diverse and challenging real-world data sets, from the maritime domain and other domains such as an automotive environment, is crucial for further investigation of the developed algorithms' robustness.

Directories

List of Figures

1.1 *Solgenia* picture and computer-aided design (CAD) model with the old and new sensor mounting. The description of sensors and actuators is given in the CAD model. 2

2.1 Visualization of the spatial distribution model. Measurement noise distribution in blue and measurement source distribution in red. Measurements as white crosses. 18

2.2 Visualization of the greedy association model. Measurement noise distribution in blue and measurement sources as red balls. Measurements as white crosses. 20

2.3 Visualization of 3D greedy association models for shape representations in spherical and cylindrical coordinates. Measurements as blue crosses, and measurement sources as red balls. Center as black cross, and shape as grey surface. Measurement sources are located on the surface. 22

2.4 Visualization of the random hypersurface model and the scaling factor distribution. Measurement noise distribution in blue, measurement sources as red balls, and scaled ellipse boundaries as elliptic curves. Measurements as white crosses. 24

2.5 Visualization of the 3D random hypersurface model and the scaling factor distribution. Measurements as blue crosses, measurement sources as red balls, height sections as red curves, and cylinder surface in grey. 26

2.6 Visualization of the 3D symmetrical random hypersurface model. Measurements as blue crosses, measurement sources as red balls, and height sections as red curves. The non-redundant part is the green surface, and the redundant part is the blue surface. 27

2.7 Visualization of the measurement separation for the RAMN estimation. 29

2.8 Qualitative and quantitative results of circular EOT investigating the RAMN estimation procedure. 33

2.9 Investigation on the adaptability of the forgetting factor τ. 34

3.1 Parametric object-specific shapes for maritime traffic participants. 37

3.2 Elliptical measurement source association. Measurements as balls, and measurement sources as crosses. Related items are displayed in the same color. 40

3.3 Visualization of the measurement separation for the RAMN estimation of an ellipse. 42

3.4 Monte Carlo (MC) simulation root mean square error (RMSE) estimation results of the static elliptic cylinder simulation experiment. 50

3.5 Estimation results of the elliptic cylinder ERHM applying a radial measurement source association with and without artificial noise estimation in 2D and 3D views. Estimates are at the same time step with the same random seed for the measurement generation. 52

3.6 MC simulation RMSE estimation results of the static elliptic cone simulation experiment. 53

3.7 Estimation results of the elliptic cone ERHM applying a radial measurement source association with and without artificial noise estimation in 2D and 3D views. Estimates are at the same time step with the same random seed for the measurement generation. 54

4.1 Visualization of the first nine Chebyshev polynomials. 60

4.2 Visualization of the FCDS basis functions. 60

4.3 Visualization of the vertical plane of symmetry of a boat object in top-down view modeled in the FCDS shape representation. 61

4.4 FCDS radial measurement source association. Measurements as balls, and measurement sources as crosses. Related items are displayed in the same color. 63

4.5 Flowchart of the quasi-ERHM estimation procedure. 65

4.6 Visualization of the measurement separation for the RAMN estimation of the FCDS shape representation at a single height section. 67

4.7 MC simulation RMSE and intersection over union (IoU) estimation results of the static simulation experiment comparing the FCDS shape representation to spherical shape representations. 75

4.8 Estimation results of the first experiment comparing the FCDS shape representation measurement model to spherical shape representation measurement models. Estimates are at the same time step with the same random seed for the measurement generation. 76

4.9 MC simulation RMSE and IoU estimation results of the static simulation experiment investigating the RAMN estimation procedure for the FCDS shape representation. 78

4.10 Estimation results of the second experiment investigating the RAMN estimation procedure for the FCDS shape representation. Estimates are at the same time step with the same random seed for the measurement generation. 79

5.1 Visualization of superelliptical shape representations. 83

5.2 Tapered superellipse and measurement source association. Squareness parameter $\varepsilon = 4$. Tapering parameter $t^{(y)} = -0.5$. Measurements as circles, inverse tapered measurements as squares, and measurement sources on non-tapered shapes as crosses. Related items are displayed in the same color. 86

5.3 Visualization of the measurement separation for the RAMN estimation of a superellipse. 88

5.4 MC simulation RMSE and IoU estimation results of the static superellipse simulation experiment. 91

5.5 Estimation results of the superellipse ERHM applying a radial measurement source association with and without RAMN estimation in 2D and 3D view for the cuboid reference. Estimates are at the same time step with the same random seed for the measurement generation. 93

6.1 Simulated scenario with *Solgenia* CAD in black as tracking object. 96

6.2 Number of simulated measurements per scan during the entire scenario. 97

6.3 MC simulation RMSE and IoU estimation results of the dynamic *Solgenia* scenario for the elliptic cylinder measurement models. 98

6.4 Estimation results of the simulated dynamic *Solgenia* scenario for the elliptic cylinder ERHM with a radial measurement source association applying the RAMN approach at time steps $k = 50, 200$. The *Solgenia* shape reference is depicted as the black surface. 98

6.5 MC simulation RMSE and IoU estimation results of the dynamic *Solgenia* scenario for the FCDS measurement models. 99

6.6 Estimation results of the simulated dynamic *Solgenia* scenario for the FCDS quasi-ERHM with a radial measurement source association and applying the RAMN approach at time steps $k = 50, 200$. The *Solgenia* shape reference is depicted as the black surface. 100

6.7 MC simulation RMSE and IoU estimation results of the dynamic *Solgenia* scenario for the superellipse measurement models. 101

6.8 Estimation results of the simulated dynamic *Solgenia* scenario for the superellipse ERHM with RAMN at time steps $k = 50, 200$. The *Solgenia* shape reference is depicted as the black surface. 101

6.9 Comparison of MC simulation RMSE and IoU estimation results of the dynamic simulated *Solgenia* scenario. 102

6.10 Picture of the *Solgenia* tracking object at a single time step in the real-world scenario. 103

6.11 Measurements and reference of the real-world scenario with the *Solgenia* as tracking object. 104

6.12 Number of measurements per scan in the entire real-world scenario. 104

6.13 Comparison of RMSE and IoU estimation results of the dynamic real-world *Solgenia* scenario. 105

6.14 Estimation results of the real-world dynamic *Solgenia* scenario for the ERHMs with a radial measurement source association and applying the RAMN approach at time steps $k = 50, 200$. The *Solgenia* shape reference is depicted as the black surface. The elliptic cylinder in the first, FCDS in the second, and extruded superellipse results in the third row. 106

6.15 Figure of the sensor setup on the catamaran and the sailing boats in a regatta, which were recorded by the sensor setup. 107

6.16 Number of measurements per scan in the entire real-world sailing boat scenario. 108

6.17 RMSE estimation results of the dynamic real-world sailing boat scenario. . . . 108

6.18 3D estimation results of the real-world sailing boat scenario. 109

6.19 2D estimation results of the real-world sailing boat scenario. 109

6.20 Box plot of the RMSEs and IoU mean estimation results for each tracklet in the KITTI raw data set. The radial measurement source association is applied for the elliptic cylinder, FCDS, and extruded superellipse measurement models. Outliers are scattered and cropped in the vertical direction. Mean values for the height RMSEs and IoUs are visualized as curves in the respective color. 112

6.21 Estimation results of the KITTI raw data set for different object categories and the ERHMs with a radial measurement source association applying the RAMN approach. The elliptic cylinder in the first, FCDS in the second, and extruded superellipse results in the third row. 113

List of Tables

3.1 Mean computation times per measurement for the elliptic cylinder. 51

3.2 Mean computation times per measurement for the elliptic cone. 53

4.1 Mean computation times per measurement for the FCDS measurement model and the comparison methods. 75

5.1 Mean computation times per measurement for the superellipse. 92

List of Algorithms

2.1 Extended Kalman Filter 13

2.2 Linear Regression Kalman Filter 15

3.1 Sequential batch linear regression Kalman filter (LRKF) measurement update 46

3.2 Elliptic cylinder unscented Kalman filter (UKF) measurement prediction . . . 47

3.3 Elliptic cone smart sampling Kalman filter (S2KF) measurement prediction . . 48

4.1 Sequential batch extended Kalman filter (EKF) measurement update 68

4.2 FCDS 3D GAM measurement prediction 69

4.3 Line UKF measurement prediction 71

4.4 FCDS quasi-ERHM measurement prediction 71

5.1 Extruded superellipse UKF measurement prediction 90

Bibliography

[1] *Alpha Prime Powering Safe Autonomy*. 63-9679. Rev. 1. Velodyne Lidar. 2019 (cit. on pp. 97, 103, 107).

[2] Hosam Alqaderi, Felix Govaers, and Wolfgang Koch. "Bayesian Wishart filter for random shape tracking". In: *IEEE Transactions on Aerospace and Electronic Systems* 58.3 (2022), pp. 1941–1952. DOI: 10.1109/TAES.2021.3131965 (cit. on p. 4).

[3] Ole Andreas Alsos, Mina Saghafian, Erik Veitch, Felix-Marcel Petermann, Taufik Akbar Sitompul, Jooyoung Park, Eleftherios Papachristos, Egil Eide, Morten Breivik, and Øyvind Smogeli. "Lessons learned from the trial operation of an autonomous urban passenger ferry". In: *Transportation Research Interdisciplinary Perspectives* 26 (2024), p. 101142. DOI: https://doi.org/10.1016/j.trip.2024.101142 (cit. on pp. 2, 3).

[4] *Annual overview of marine casualties and incidents 2024*. Tech. rep. Lisbon, Portugal: European Maritime Safety Agency, 2024 (cit. on p. 1).

[5] Michael Athans, Richard Wishner, and Anthony Bertolini. "Suboptimal state estimation for continuous-time nonlinear systems from discrete noisy measurements". In: *IEEE Transactions on Automatic Control* 13.5 (1968), pp. 504–514. DOI: 10.1109/TAC.1968.1098986 (cit. on p. 14).

[6] Sheldon Axler, Paul Bourdon, and Ramey Wade. *Harmonic Function Theory*. Vol. 137. Springer Science & Business Media, 2013 (cit. on p. 74).

[7] Martin Baerveldt, Audun Gullikstad Hem, and Edmund Førland Brekke. "Comparing multiple extended object tracking with point based multi object tracking for lidar in a maritime context". In: *Journal of Physics: Conference Series*. Vol. 2618. 1. IOP Publishing. 2023, p. 012011. DOI: 10.1088/1742-6596/2618/1/012011 (cit. on p. 3).

[8] Martin Baerveldt, Michael Ernesto López, and Edmund Førland Brekke. "A multiple extended object tracker with the Gaussian process model utilizing negative information". In: *Journal of Advances in Information Fusion* 19.2 (2024), p. 88 (cit. on p. 3).

[9] Martin Baerveldt, Michael Ernesto López, and Edmund Førland Brekke. "Extended target PMBM tracker with a Gaussian process target model on lidar data". In: *2023 26th International Conference on Information Fusion (FUSION)*. 2023, pp. 1–8. DOI: 10.23919/FUSION52260.2023.10224156 (cit. on p. 4).

[10] Yaakov Bar-Shalom. *Tracking and Data Association*. USA: Academic Press Professional, Inc., 1987. ISBN: 0120797607 (cit. on pp. 2, 9, 12, 58).

[11] Yaakov Bar-Shalom, X. Rong Li, and Thiagalingam Kirubarajan. *Estimation with Applications to Tracking and Navigation: Theory Algorithms and Software*. John Wiley & Sons, 2004 (cit. on pp. 2, 12, 58).

[12] Julio Barreiro, Sonia Zaragoza, and Vicente Diaz-Casas. "Review of ship energy efficiency". In: *Ocean Engineering* 257 (2022), p. 111594. DOI: https://doi.org/10.1016/j.oceaneng.2022.111594 (cit. on p. 1).

[13] Marcus Baum. “Simultaneous Tracking and Shape Estimation of Extended Objects”. Dissertation. Karlsruhe Institute of Technology (KIT), Intelligent Sensor-Actuator-Systems Laboratory (ISAS), Referent: U. D. Hanebeck, Korreferent: P. Willett, Karlsruhe Series on Intelligent Sensor-Actuator-Systems 13, 2013 (cit. on p. 23).

[14] Marcus Baum, Florian Faion, and Uwe D. Hanebeck. “Modeling the target extent with multiplicative noise”. In: *Proceedings of the 15th International Conference on Information Fusion (Fusion 2012)*. Singapore, July 2012 (cit. on pp. 4, 25, 38, 63, 82).

[15] Marcus Baum and Uwe D. Hanebeck. “Extended object tracking with random hypersurface models”. In: *IEEE Transactions on Aerospace and Electronic Systems* 50 (Jan. 2014), pp. 149–159. DOI: 10.1109/TAES.2013.120107 (cit. on pp. 3–5, 23, 24, 38, 41).

[16] Marcus Baum and Uwe D. Hanebeck. “Random hypersurface models for extended object tracking”. In: *Proceedings of the 9th IEEE International Symposium on Signal Processing and Information Technology (ISSPIT 2009)*. Ajman, United Arab Emirates, Dec. 2009. DOI: 10.1109/ISSPIT.2009.5407526 (cit. on pp. 3–5, 11, 23, 38, 41).

[17] Marcus Baum and Uwe D. Hanebeck. “Shape tracking of extended objects and group targets with star-convex RHMs”. In: *Proceedings of the 14th International Conference on Information Fusion (Fusion 2011)*. Chicago, Illinois, USA, July 2011 (cit. on pp. 4, 29, 56).

[18] Marcus Baum, Benjamin Noack, and Uwe D. Hanebeck. “Extended object and group tracking with elliptic random hypersurface models”. In: *Proceedings of the 13th International Conference on Information Fusion (Fusion 2010)*. Edinburgh, United Kingdom, July 2010. DOI: 10.1109/icif.2010.5711854 (cit. on pp. 19, 23, 29).

[19] Samuel S. Blackman and Robert Popoli. *Design and Analysis of Modern Tracking Systems*. Artech House, 1999 (cit. on pp. 2, 9, 45, 58, 67).

[20] John P. Boyd. *Chebyshev and Fourier Spectral Methods*. Dover Books on Mathematics. Dover Publications, 2001 (cit. on pp. 59, 61).

[21] John P. Boyd. “The choice of spectral functions on a sphere for boundary and eigenvalue problems: A comparison of Chebyshev, Fourier and associated Legendre expansions”. In: *Monthly Weather Review* 106.8 (1978), pp. 1184–1191 (cit. on p. 74).

[22] Andreas von Brandis, Daniel Menges, and Adil Rasheed. “Multi-target tracking for autonomous surface vessels using lidar and AIS data integration”. In: *Applied Ocean Research* 154 (2025), p. 104348. DOI: https://doi.org/10.1016/j.apor.2024.104348 (cit. on p. 3).

[23] Edmund Førland Brekke, Egil Eide, Bjørn-Olav H. Eriksen, Erik F. Wilthil, Morten Breivik, Even Skjellaug, Øystein K. Helgesen, Anastasios M. Lekkas, Andreas B. Martinsen, Emil H. Thyri, et al. “Milliampere: An autonomous ferry prototype”. In: *Journal of Physics: Conference Series*. Vol. 2311. 1. IOP Publishing. 2022, p. 012029. DOI: 10.1088/1742-6596/2311/1/012029 (cit. on pp. 2, 3).

[24] Edmund Førland Brekke, Erik Falmar Wilthil, Bjørn-Olav H. Eriksen, D. Kwame Minde Kufoalor, Øystein K. Helgesen, Inger Berge Hagen, Morten Breivik, and Tor Arne Johansen. “The Autosea project: Developing closed-loop target tracking and collision avoidance systems”. In: *Journal of Physics: Conference Series* 1357.1 (Oct. 2019), p. 012020. DOI: 10.1088/1742-6596/1357/1/012020 (cit. on p. 10).

[25] Peter Broßeit, Bharanidhar Duraisamy, and Jürgen Dickmann. "The volcanormal density for radar-based extended target tracking". In: *2017 IEEE 20th International Conference on Intelligent Transportation Systems (ITSC)*. 2017, pp. 1–6. DOI: 10.1109/ITSC.2017.8317736 (cit. on p. 4).

[26] Peter Broßeit, Matthias Rapp, Nils Appenrodt, and Jürgen Dickmann. "Probabilistic rectangular-shape estimation for extended object tracking". In: *IEEE Intelligent Vehicles Symposium (IV)*. 2016, pp. 279–285. DOI: 10.1109/IVS.2016.7535398 (cit. on p. 4).

[27] Subhash Challa, Mark R. Morelande, Darko Mušicki, and Robin J. Evans. *Fundamentals of Object Tracking*. Cambridge University Press, 2011. DOI: 10.1017/CBO9780511975837 (cit. on pp. 9, 11–13, 45, 57, 58, 67, 68).

[28] Charles Dugas, Yoshua Bengio, François Bélisle, Claude Nadeau, and René Garcia. "Incorporating second-order functional knowledge for better option pricing". In: *Advances in Neural Information Processing Systems*. Ed. by T. Leen, T. Dietterich, and V. Tresp. Vol. 13. MIT Press, 2000 (cit. on p. 28).

[29] Esther Dura, Judith Bell, and Dave Lane. "Superellipse fitting for the recovery and classification of mine-like shapes in sidescan sonar images". In: *IEEE Journal of Oceanic Engineering* 33.4 (2008), pp. 434–444. DOI: 10.1109/JOE.2008.2002962 (cit. on pp. 7, 82, 83).

[30] Felix Ebert and Hans-Joachim Wuensche. "Dynamic object tracking and 3D surface estimation using Gaussian processes and extended Kalman filter". In: *IEEE Intelligent Transportation Systems Conference (ITSC)*. 2019, pp. 1122–1127. DOI: 10.1109/ITSC.2019.8916891 (cit. on pp. 4–6, 58, 74, 97).

[31] Bjørn-Olav H. Eriksen, Erik F. Wilthil, Andreas L. Flåten, Edmund Førland Brekke, and Morten Breivik. "Radar-based maritime collision avoidance using dynamic window". In: *2018 IEEE Aerospace Conference*. 2018, pp. 1–9. DOI: 10.1109/AERO.2018.8396666 (cit. on p. 10).

[32] Florian Faion. "Tracking Extended Objects in Noisy Point Clouds with Application in Telepresence Systems". Dissertation. Karlsruhe Institute of Technology (KIT), Intelligent Sensor-Actuator-Systems Laboratory (ISAS), Referent: U. D. Hanebeck, Korreferent: W. Koch, Karlsruhe Series on Intelligent Sensor-Actuator-Systems 19, 2015 (cit. on pp. 6, 11, 12, 17, 19, 23–26, 38, 56, 58, 82).

[33] Florian Faion, Marcus Baum, and Uwe D. Hanebeck. "Tracking 3D shapes in noisy point clouds with random hypersurface models". In: *Proceedings of the 15th International Conference on Information Fusion (Fusion 2012)*. Singapore, July 2012 (cit. on pp. 4, 6, 16, 25, 38).

[34] Florian Faion, Antonio Zea, Marcus Baum, and Uwe D. Hanebeck. "Bayesian estimation of line segments". In: *Proceedings of the IEEE ISIF Workshop on Sensor Data Fusion: Trends, Solutions, Applications (SDF 2014)*. Bonn, Germany, Oct. 2014. DOI: 10.1109/SDF.2014.6954710 (cit. on pp. 25, 38, 58, 63).

[35] Florian Faion, Antonio Zea, Marcus Baum, and Uwe D. Hanebeck. "Partial likelihood for unbiased extended object tracking". In: *Proceedings of the 18th International Conference on Information Fusion (Fusion 2015)*. Washington D.C., USA, July 2015 (cit. on pp. 18, 38, 58, 82).

[36] Florian Faion, Antonio Zea, Marcus Baum, and Uwe D. Hanebeck. "Symmetries in Bayesian extended object tracking". In: *Journal of Advances in Information Fusion* 10.1 (June 2015), pp. 13–30 (cit. on pp. 26, 27, 38, 58, 82).

[37] Florian Faion, Antonio Zea, and Uwe D. Hanebeck. "Reducing bias in Bayesian shape estimation". In: *Proceedings of the 17th International Conference on Information Fusion (Fusion 2014)*. Salamanca, Spain, July 2014 (cit. on p. 19).

[38] Florian Faion, Antonio Zea, Jannik Steinbring, Marcus Baum, and Uwe D. Hanebeck. "Recursive Bayesian pose and shape estimation of 3D objects using transformed plane curves". In: *Proceedings of the IEEE ISIF Workshop on Sensor Data Fusion: Trends, Solutions, Applications (SDF 2015)*. Bonn, Germany, Oct. 2015. DOI: 10.1109/SDF.2015.7347698 (cit. on pp. 4, 6, 25, 38, 44).

[39] Ghassan Al-Falouji, Lukas Haschke, Dirk Nowotka, and Sven Tomforde. "Self-explanation as a basis for self-integration-the autonomous passenger ferry scenario". In: *2023 IEEE International Conference on Autonomic Computing and Self-Organizing Systems Companion (ACSOS-C)*. IEEE. 2023, pp. 65–70. DOI: 10.1109/ACSOS-C58168.2023.00038 (cit. on p. 2).

[40] Michael Feldmann, Dietrich Fränken, and Wolfgang Koch. "Tracking of extended objects and group targets using random matrices". In: *IEEE Transactions on Signal Processing* 59.4 (2011), pp. 1409–1420. DOI: 10.1109/TSP.2010.2101064 (cit. on pp. 3–5, 11, 18, 29, 38).

[41] James D Foley. *Computer Graphics: Principles and Practice*. Vol. 12110. Addison-Wesley Professional, 1996 (cit. on p. 109).

[42] Jaya Shradha Fowdur, Marcus Baum, and Frank Heymann. "An elliptical principal axes-based model for extended target tracking with marine radar data". In: *2021 IEEE 24th International Conference on Information Fusion (FUSION)*. IEEE. 2021, pp. 1–8. DOI: 10.23919/FUSION49465.2021.9627039 (cit. on p. 3).

[43] Jaya Shradha Fowdur, Marcus Baum, and Frank Heymann. "Tracking targets with known spatial extent using experimental marine radar data". In: *2019 22th International Conference on Information Fusion (FUSION)*. IEEE. 2019, pp. 1–8. DOI: 10.23919/FUSION43075.2019.9011244 (cit. on p. 3).

[44] Daniel Frisch and Uwe D. Hanebeck. "Deterministic Gaussian sampling with generalized Fibonacci grids". In: *Proceedings of the 24th International Conference on Information Fusion (Fusion 2021)*. Sun City, South Africa, Nov. 2021. DOI: 10.23919/FUSION49465.2021.9626975 (cit. on p. 14).

[45] Daniel Frisch and Uwe D. Hanebeck. "The generalized Fibonacci grid as low-discrepancy point set for optimal deterministic Gaussian sampling". In: *Journal of Advances in Information Fusion* 18.1 (June 2023), pp. 16–34. ISSN: 1557-6418 (cit. on p. 14).

[46] Lin Gao, Giorgio Battistelli, and Luigi Chisci. "Extended object tracking based on superellipses". In: *2024 27th International Conference on Information Fusion (FUSION)*. 2024, pp. 1–8. DOI: 10.23919/FUSION59988.2024.10706410 (cit. on p. 82).

[47] Lin Gao, Giorgio Battistelli, Luigi Chisci, and Matteo Tesori. "Superquadric-based 3D extended object tracking". In: *Authorea Preprints* (2023) (cit. on pp. 82, 86).

[48] Andreas Geiger, Philip Lenz, Christoph Stiller, and Raquel Urtasun. "Vision meets robotics: The KITTI dataset". In: *International Journal of Robotics Research (IJRR)* 32.11 (2013), pp. 1231–1237. DOI: 10.1177/0278364913491297 (cit. on pp. 3, 7, 95, 110).

[49] Alfredo Germani, Costanzo Manes, and Pasquale Palumbo. "Polynomial extended Kalman filter". In: *IEEE Transactions on Automatic Control* 50.12 (2005), pp. 2059–2064. DOI: 10.1109/TAC.2005.860256 (cit. on pp. 25, 63).

[50] Lino Antoni Giefer and Joachim Clemens. "State estimation of articulated vehicles using deformed superellipses". In: *2021 IEEE 24th International Conference on Information Fusion (FUSION)*. 2021, pp. 1–8. DOI: 10.23919/FUSION49465.2021.9626881 (cit. on p. 82).

[51] Kevin Gilholm, Simon Godsill, Simon Maskell, and David Salmond. "Poisson models for extended target and group tracking". In: *Signal and Data Processing of Small Targets 2005*. Vol. 5913. SPIE. 2005, pp. 230–241 (cit. on pp. 3, 18).

[52] Kevin Gilholm and David Salmond. "Spatial distribution model for tracking extended objects". In: *IEE Proceedings - Radar, Sonar and Navigation* 152 (Nov. 2005), pp. 364–371. DOI: 10.1049/ip-rsn:20045114 (cit. on pp. 3, 18).

[53] Igor Gilitschenski and Uwe D. Hanebeck. "Efficient deterministic Dirac mixture approximation of Gaussian distributions". In: *Proceedings of the 2013 American Control Conference (ACC 2013)*. Washington D.C., USA, June 2013. DOI: 10.1109/acc.2013.6580197 (cit. on p. 14).

[54] Igor Gilitschenski, Gerhard Kurz, Simon J. Julier, and Uwe D. Hanebeck. "A new probability distribution for simultaneous representation of uncertain position and orientation". In: *Proceedings of the 17th International Conference on Information Fusion (Fusion 2014)*. Salamanca, Spain, July 2014 (cit. on p. 77).

[55] Gene H. Golub and Charles F. Van Loan. *Matrix Computations*. JHU press, 2013 (cit. on p. 16).

[56] Álvaro González. "Measurement of areas on a sphere using Fibonacci and latitude–longitude lattices". In: *Mathematical geosciences* 42 (2010), pp. 49–64. DOI: 10.1007/s11004-009-9257-x (cit. on pp. 74, 102).

[57] Felix Govaers. "On independent axes estimation for extended target tracking". In: *2019 Sensor Data Fusion: Trends, Solutions, Applications (SDF)*. 2019, pp. 1–6. DOI: 10.1109/SDF.2019.8916660 (cit. on p. 4).

[58] Karl Granström and Marcus Baum. "A tutorial on multiple extended object tracking". In: *TechRxiv Preprint: https://doi.org/10.36227/techrxiv.19115858.v1* (2022) (cit. on pp. 2, 5, 9, 11, 17, 18).

[59] Karl Granström, Marcus Baum, and Stephan Reuter. "Extended object tracking: Introduction, overview, and applications". In: *Journal of Advances in Information Fusion* 12 (Dec. 2017) (cit. on pp. 2, 9, 11, 17, 18).

[60] Karl Granström and Christian Lundquist. "On the use of multiple measurement models for extended target tracking". In: *Proceedings of the 16th International Conference on Information Fusion*. 2013, pp. 1534–1541 (cit. on p. 81).

[61] Karl Granström, Christian Lundquist, and Umut Orguner. "Tracking rectangular and elliptical extended targets using laser measurements". In: *14th International Conference on Information Fusion (FUSION)*. 2011 (cit. on pp. 4, 18).

[62] Karl Granström and Umut Orguner. "A PHD filter for tracking multiple extended targets using random matrices". In: *IEEE Transactions on Signal Processing* 60.11 (2012), pp. 5657–5671. DOI: 10.1109/TSP.2012.2212888 (cit. on pp. 3, 5).

[63] Karl Granström, Lennart Svensson, Stephan Reuter, Yuxuan Xia, and Maryam Fatemi. "Likelihood-based data association for extended object tracking using sampling methods". In: *IEEE Transactions on Intelligent Vehicles* 3.1 (2018), pp. 30–45. DOI: 10.1109/TIV.2017.2788184 (cit. on p. 5).

[64] Dennis Griesser, Matthias O. Franz, and Georg Umlauf. "Enhancing inland water safety: The Lake Constance obstacle detection benchmark". In: *2024 IEEE International Conference on Robotics and Automation (ICRA)*. IEEE. 2024, pp. 14808–14814. DOI: 10.1109/ICRA57147.2024.10610600 (cit. on p. 2).

[65] Yewen Gu and Stein W. Wallace. "Operational benefits of autonomous vessels in logistics—A case of autonomous water-taxis in Bergen". In: *Transportation Research Part E: Logistics and Transportation Review* 154 (2021), p. 102456. DOI: https://doi.org/10.1016/j.tre.2021.102456 (cit. on p. 1).

[66] Fredrik Gustafsson. *Statistical Sensor Fusion*. Studentlitteratur, 2010 (cit. on pp. 12, 45, 67).

[67] Longfei Han, Klaus Kefferpütz, and Jürgen Beyerer. *3D extended object tracking based on extruded B-spline side view profiles*. 2025. arXiv: 2503.10730 [cs.CV] (cit. on pp. 4, 57).

[68] J. Ray Hanna and John H. Rowland. *Fourier Series, Transforms, and Boundary Value Problems: Second Edition*. Dover Books on Mathematics. Dover Publications, 2008. ISBN: 9780486466736 (cit. on pp. 60, 61).

[69] Jindřich Havlík and Ondřej Straka. "Performance evaluation of iterated extended Kalman filter with variable step-length". In: *Journal of Physics: Conference Series* 659.1 (Nov. 2015), p. 012022. DOI: 10.1088/1742-6596/659/1/012022 (cit. on p. 14).

[70] Tobias Hirscher, Alexander Scheel, Stephan Reuter, and Klaus Dietmayer. "Multiple extended object tracking using Gaussian processes". In: *19th International Conference on Information Fusion (FUSION)*. 2016, pp. 868–875 (cit. on p. 5).

[71] Hanna W. Hjelmeland, Bjørn-Olav H. Eriksen, Ole J. Mengshoel, and Anastasios M. Lekkas. "Identification of failure modes in the collision avoidance system of an autonomous ferry using adaptive stress testing". In: *IFAC-PapersOnLine* 55.31 (2022), pp. 470–477. DOI: https://doi.org/10.1016/j.ifacol.2022.10.472 (cit. on p. 2).

[72] Patrick Hoher, Johannes Reuter, Felix Govaers, and Wolfgang Koch. "Extended object tracking and shape classification using random matrices and virtual measurement models". In: *2023 IEEE Symposium Sensor Data Fusion and International Conference on Multisensor Fusion and Integration (SDF-MFI)*. 2023, pp. 1–8. DOI: 10.1109/SDF-MFI59545.2023.10361348 (cit. on pp. 18, 29, 81).

[73] Hannes Homburger, Stefan Wirtensohn, and Johannes Reuter. "Docking control of a fully-actuated autonomous vessel using model predictive path integral control". In: *2022 European Control Conference (ECC)*. 2022, pp. 755–760. DOI: 10.23919/ECC55457.2022.9838090 (cit. on pp. 2, 10).

[74] Jens Honer and Hauke Kaulbersch. "Bayesian extended target tracking with automotive radar using learned spatial distribution models". In: *2020 IEEE International Conference on Multisensor Fusion and Integration for Intelligent Systems (MFI)*. 2020, pp. 316–322. DOI: 10.1109/MFI49285.2020.9235255 (cit. on p. 4).

[75] The MathWorks Inc. *Uavlidarpointcloudgenerator*. Natick, Massachusetts, United States, 2023 (cit. on p. 96).

[76] Simon J. Julier and Jeffrey K. Uhlmann. "New extension of the Kalman filter to nonlinear systems". In: *Signal processing, sensor fusion, and target recognition VI*. Vol. 3068. Spie. 1997, pp. 182–193 (cit. on pp. 14, 38, 58, 82).

[77] Simon J. Julier and Jeffrey K. Uhlmann. "Unscented filtering and nonlinear estimation". In: *Proceedings of the IEEE* 92.3 (2004), pp. 401–422. DOI: 10.1109/JPROC.2003.823141 (cit. on pp. 14, 15, 28, 38, 58, 82).

[78] Rudolph Emil Kalman. "A new approach to linear filtering and prediction problems". In: *Transactions of the ASME–Journal of Basic Engineering* 82.Series D (1960), pp. 35–45. DOI: 10.1115/1.3662552 (cit. on p. 12).

[79] Hauke Kaulbersch, Jens Honer, and Marcus Baum. "A Cartesian B-spline vehicle model for extended object tracking". In: *21st International Conference on Information Fusion (FUSION)*. 2018. DOI: 10.23919/ICIF.2018.8455717 (cit. on pp. 4, 11, 20, 29, 84).

[80] Hauke Kaulbersch, Jens Honer, and Marcus Baum. "Assymetric noise tailoring for vehicle lidar data in extended object tracking". In: *2020 IEEE International Conference on Multisensor Fusion and Integration for Intelligent Systems (MFI)*. 2020, pp. 191–196. DOI: 10.1109/MFI49285.2020.9235253 (cit. on pp. 11, 23, 29, 33, 38, 58, 82).

[81] Hauke Kaulbersch, Jens Honer, and Marcus Baum. "EM-based extended target tracking with automotive radar using learned spatial distribution models". In: *2019 22th International Conference on Information Fusion (FUSION)*. 2019, pp. 1–8. DOI: 10.23919/FUSION43075.2019.9011179 (cit. on p. 4).

[82] Christina Knill, Alexander Scheel, and Klaus Dietmayer. "A direct scattering model for tracking vehicles with high-resolution radars". In: *IEEE Intelligent Vehicles Symposium (IV)*. 2016, pp. 298–303. DOI: 10.1109/IVS.2016.7535401 (cit. on p. 4).

[83] Wolfgang Koch. "Bayesian approach to extended object and cluster tracking using random matrices". In: *IEEE Transactions on Aerospace and Electronic Systems* 44 (July 2008), pp. 1042–1059. DOI: 10.1109/TAES.2008.4655362 (cit. on pp. 3–5, 18, 38).

[84] Murat Kumru and Emre Özkan. "3D extended object tracking using recursive Gaussian processes". In: *21st International Conference on Information Fusion (FUSION)*. 2018. DOI: 10.23919/ICIF.2018.8455480 (cit. on pp. 4–6, 58, 74, 97).

[85] Murat Kumru and Emre Özkan. "Three-dimensional extended object tracking and shape learning using Gaussian processes". In: *IEEE Transactions on Aerospace and Electronic Systems* 57.5 (2021), pp. 2795–2814. DOI: 10.1109/TAES.2021.3067668 (cit. on pp. 4–6, 38, 57, 58, 74, 97, 102, 104, 105, 110, 111).

[86] Murat Kumru and Emre Özkan. "Tracking arbitrarily shaped extended objects using Gaussian processes". In: *2024 27th International Conference on Information Fusion (FUSION)*. 2024, pp. 1–8. DOI: 10.23919/FUSION59988.2024.10706470 (cit. on p. 4).

[87] Gerhard Kurz, Florian Faion, Florian Pfaff, Antonio Zea, and Uwe D. Hanebeck. "Three-dimensional simultaneous shape and pose estimation for extended objects using spherical harmonics". In: *arXiv preprint arXiv:2012.13580* (Dec. 2020) (cit. on pp. 4–7, 57, 58, 74, 97, 102, 104, 110).

[88] Gerhard Kurz, Igor Gilitschenski, Florian Pfaff, Lukas Drude, Uwe D. Hanebeck, Reinhold Haeb-Umbach, and Roland Y. Siegwart. "Directional Statistics and Filtering Using libDirectional". In: *arXiv preprint: Computation (stat.CO)* (Dec. 2017) (cit. on p. 77).

[89] James J. Laird. "Valuing the quality of strategic ferry services to remote communities". In: *Research in Transportation Business & Management* 4 (2012), pp. 97–103. DOI: https://doi.org/10.1016/j.rtbm.2012.06.013 (cit. on p. 1).

[90] Jian Lan. "Extended object tracking using random matrix with extension-dependent measurement numbers". In: *IEEE Transactions on Aerospace and Electronic Systems* 59.4 (2023), pp. 4464–4477. DOI: 10.1109/TAES.2023.3241888 (cit. on p. 18).

[91] Jian Lan and X. Rong Li. "Extended-object or group-target tracking using random matrix with nonlinear measurements". In: *IEEE Transactions on Signal Processing* 67.19 (2019), pp. 5130–5142. DOI: 10.1109/TSP.2019.2935866 (cit. on p. 18).

[92] Johannes Lederer. *Activation functions in artificial neural networks: A systematic overview*. 2021. arXiv: 2101.09957 [cs.LG] (cit. on p. 28).

[93] Michael Levandowsky and David Winter. "Distance between sets". In: *Nature* 234 (1971), pp. 34–35. DOI: 10.1038/234034a0 (cit. on p. 73).

[94] Michael Ernesto López, Edmund Førland Brekke, Rudolf Mester, and Annette Stahl. "Multiscan shape estimation for extended object tracking". In: *2023 26th International Conference on Information Fusion (FUSION)*. 2023, pp. 1–8. DOI: 10.23919/FUSION52260.2023.10224154 (cit. on pp. 3, 4).

[95] Michael Ernesto López, Kjetil Vasstein, Edmund Førland Brekke, Rudolf Mester, and Annette Stahl. "A general low-parameter 3D ship hull extent model for object tracking". In: *2024 27th International Conference on Information Fusion (FUSION)*. IEEE. 2024, pp. 1–7. DOI: 10.23919/FUSION59988.2024.10706457 (cit. on pp. 3, 57).

[96] Ronald Mahler. "PHD filters for nonstandard targets, I: Extended targets". In: *2009 12th International Conference on Information Fusion*. 2009, pp. 915–921 (cit. on p. 5).

[97] John C. Mason and David C. Handscomb. *Chebyshev Polynomials*. CRC Press, 2002. ISBN: 9781420036114 (cit. on pp. 57, 59).

[98] Lyudmila Mihaylova, Avishy Y. Carmi, François Septier, Amadou Gning, Sze Kim Pang, and Simon Godsill. "Overview of Bayesian sequential Monte Carlo methods for group and extended object tracking". In: *Digital Signal Processing* 25 (2014), pp. 1–16. DOI: https://doi.org/10.1016/j.dsp.2013.11.006 (cit. on pp. 2, 9, 11).

[99] Miguel Mujica Mota and Maurice Van der Meche. "Towards a greener europe: Analysis of the SeaBubble waterline in Rotterdam". In: *18th International Multidisciplinary Modeling & Simulation Multiconference (I3M 2021): 33rd European Modeling & Simulation Symposium*. 2021 (cit. on p. 2).

[100] Benjamin Naujoks, Patrick Burger, and Hans-Joachim Wuensche. "Fast 3D extended target tracking using NURBS surfaces". In: *2019 IEEE Intelligent Transportation Systems Conference (ITSC)*. 2019, pp. 1104–1109. DOI: 10.1109/ITSC.2019.8917384 (cit. on pp. 4, 6, 57).

[101] Andras Palffy, Ewoud Pool, Srimannarayana Baratam, Julian F.P. Kooij, and Dariu M. Gavrila. "Multi-class road user detection with 3+ 1d radar in the view-of-delft dataset". In: *IEEE Robotics and Automation Letters* 7.2 (2022), pp. 4961–4968. DOI: 10.1109/LRA.2022.3147324 (cit. on p. 3).

[102] Athanasios Papoulis and S. Unnikrishna Pillai. *Probability, Random Variables, and Stochastic Processes*. Fourth. Boston: McGraw Hill, 2002 (cit. on p. 47).

[103] *Revision of the Class Regulations and the Class Racing Regulations*. Rev. 2012. Folkboat Assn. Feb. 2012 (cit. on p. 107).

[104] Christian P. Robert and George Casella. *Monte Carlo Statistical Methods*. Springer Verlag, 2004 (cit. on pp. 48, 66).

[105] Paul L. Rosin. "Fitting superellipses". In: *IEEE Transactions on Pattern Analysis and Machine Intelligence* 22.7 (2000), pp. 726–732. DOI: 10.1109/34.865190 (cit. on pp. 7, 82–84).

[106] Paul L. Rosin and Geoff A.W. West. "Curve segmentation and representation by superellipses". In: *IEE Proceedings-Vision, Image and Signal Processing* 142.5 (1995), pp. 280–288. DOI: 10.1049/ip-vis:19952140 (cit. on p. 85).

[107] Michael Roth and Fredrik Gustafsson. "An efficient implementation of the second order extended Kalman filter". In: *14th International Conference on Information Fusion*. 2011, pp. 1–6 (cit. on p. 14).

[108] Michael Roth, Gustaf Hendeby, and Fredrik Gustafsson. "EKF/UKF maneuvering target tracking using coordinated turn models with polar/Cartesian velocity". In: *17th International Conference on Information Fusion (FUSION)*. 2014 (cit. on pp. 96, 104, 110, 111).

[109] Kristian Amundsen Ruud, Edmund Førland Brekke, and Jo Eidsvik. "Lidar extended object tracking of a maritime vessel using an ellipsoidal contour model". In: *2018 Sensor Data Fusion: Trends, Solutions, Applications (SDF)*. IEEE. 2018, pp. 1–6. DOI: 10.1109/SDF.2018.8547047 (cit. on p. 3).

[110] Ryohei Sawada and Koichi Hirata. "Mapping and localization for autonomous ship using lidar SLAM on the sea". In: *Journal of Marine Science and Technology* 28.2 (2023), pp. 410–421. DOI: 10.1007/s00773-023-00931-y (cit. on p. 3).

[111] Alexander Scheel and Klaus Dietmayer. “Tracking multiple vehicles using a variational radar model”. In: *IEEE Transactions on Intelligent Transportation Systems* 20.10 (2019), pp. 3721–3736. DOI: 10.1109/TITS.2018.2879041 (cit. on p. 4).

[112] Michael Schuster, Johannes Reuter, and Gerd Wanielik. “Multi detection joint integrated probabilistic data association using random matrices with applications to radar-based multi object tracking”. In: *Journal of Advances in Information Fusion* 12.2 (2017), pp. 175–188 (cit. on p. 3).

[113] Dan Simon and Tien Li Chia. “Kalman filtering with state equality constraints”. In: *IEEE transactions on Aerospace and Electronic Systems* 38.1 (2002), pp. 128–136. DOI: 10.1109/7.993234 (cit. on p. 27).

[114] Martin A. Skoglund, Gustaf Hendeby, and Daniel Axehill. “Extended Kalman filter modifications based on an optimization view point”. In: *2015 18th International Conference on Information Fusion (Fusion)*. 2015, pp. 1856–1861 (cit. on p. 14).

[115] Franc Solina and Ruzena Bajcsy. “Recovery of parametric models from range images: The case for superquadrics with global deformations”. In: *IEEE Transactions on Pattern Analysis and Machine Intelligence* 12.2 (1990), pp. 131–147. DOI: 10.1109/34.44401 (cit. on pp. 82, 83).

[116] Jannik Steinbring. *Nonlinear estimation toolbox* (cit. on pp. 14, 38, 46–48).

[117] Jannik Steinbring. “Nonlinear State Estimation Using Optimal Gaussian Sampling with Applications to Tracking”. Dissertation. Karlsruhe Institute of Technology (KIT), Intelligent Sensor-Actuator-Systems Laboratory (ISAS), Referent: U. D. Hanebeck, Korreferent: O. Straka, 2017 (cit. on pp. 24, 46).

[118] Jannik Steinbring and Uwe D. Hanebeck. “LRKF revisited: The smart sampling Kalman filter (S2KF)”. In: *Journal of Advances in Information Fusion* 9.2 (Dec. 2014), pp. 106–123 (cit. on pp. 14, 17, 38, 46–48).

[119] Jannik Steinbring and Uwe D. Hanebeck. “S2KF: The smart sampling Kalman filter”. In: *Proceedings of the 16th International Conference on Information Fusion (Fusion 2013)*. Istanbul, Turkey, July 2013 (cit. on pp. 14, 38).

[120] Bruno O.S. Teixeira, Leonardo A.B. Tôrres, Luis A. Aguirre, and Dennis S. Bernstein. “On unscented Kalman filtering with state interval constraints”. In: *Journal of Process Control* 20.1 (2010), pp. 45–57. ISSN: 0959-1524. DOI: https://doi.org/10.1016/j.jprocont.2009.10.007 (cit. on p. 27).

[121] Kolja Thormann, Shishan Yang, and Marcus Baum. “A comparison of Kalman filter-based approaches for elliptic extended object tracking”. In: *IEEE 23rd International Conference on Information Fusion (FUSION)*. 2020, pp. 1–8. DOI: 10.23919/FUSION45008.2020.9190375 (cit. on p. 4).

[122] Georgi P. Tolstov and Richard A. Silverman. *Fourier Series*. Dover Books on Mathematics. Dover Publications, 1976. ISBN: 9780486633176 (cit. on pp. 60, 61).

[123] Barkin Tuncer, Murat Kumru, Emre Ozkan, and A. Aydin Alatan. “Extended object tracking and shape classification”. In: *2018 21st International Conference on Information Fusion (FUSION)*. IEEE. 2018, pp. 1–5. DOI: 10.23919/ICIF.2018.8455464 (cit. on p. 2).

[124] Barkin Tuncer, Murat Kumru, and Emre Özkan. "Extended target tracking and classification using neural networks". In: *2019 22th International Conference on Information Fusion (FUSION)*. IEEE. 2019, pp. 1–7. DOI: 10.23919/FUSION43075.2019.9011255 (cit. on p. 2).

[125] Barkın Tuncer and Emre Özkan. "Random matrix based extended target tracking with orientation: A new model and inference". In: *IEEE Transactions on Signal Processing* 69 (2021), pp. 1910–1923. DOI: 10.1109/TSP.2021.3065136 (cit. on p. 3).

[126] Rudolph Van Der Merwe and Eric A. Wan. "The square-root unscented Kalman filter for state and parameter-estimation". In: *2001 IEEE International Conference on Acoustics, Speech, and Signal Processing. Proceedings (Cat. No.01CH37221)*. Vol. 6. 2001, 3461–3464 vol.6. DOI: 10.1109/ICASSP.2001.940586 (cit. on p. 51).

[127] Gemine Vivone and Paolo Braca. "Joint probabilistic data association tracker for extended target tracking applied to X-band marine radar data". In: *IEEE Journal of Oceanic Engineering* 41.4 (2016), pp. 1007–1019. DOI: 10.1109/JOE.2015.2503499 (cit. on p. 3).

[128] Gemine Vivone, Paolo Braca, and Borja Errasti-Alcala. "Extended target tracking applied to X-band marine radar data". In: *OCEANS 2015-Genova*. IEEE. 2015, pp. 1–6. DOI: 10.1109/OCEANS-Genova.2015.7271630 (cit. on p. 3).

[129] Niklas Wahlström and Emre Özkan. "Extended target tracking using Gaussian processes". In: *IEEE Transactions on Signal Processing* 63.16 (2015), pp. 4165–4178. DOI: 10.1109/TSP.2015.2424194 (cit. on pp. 4, 56, 74).

[130] Eric A. Wan and Rudolph Van Der Merwe. "The unscented Kalman filter for nonlinear estimation". In: *Proceedings of the IEEE 2000 Adaptive Systems for Signal Processing, Communications, and Control Symposium (Cat. No.00EX373)*. 2000, pp. 153–158. DOI: 10.1109/ASSPCC.2000.882463 (cit. on pp. 14, 28, 38, 46, 47, 58, 71, 90).

[131] Wei Wang, David Fernández-Gutiérrez, Rens Doornbusch, Joshua Jordan, Tixiao Shan, Pietro Leoni, Niklas Hagemann, Jonathan Klein Schiphorst, Fabio Duarte, Carlo Ratti, et al. "Roboat III: An autonomous surface vessel for urban transportation". In: *Journal of Field Robotics* 40.8 (2023), pp. 1996–2009. DOI: https://doi.org/10.1002/rob.22237 (cit. on pp. 2, 3).

[132] Wei Wang, Banti Gheneti, Luis A Mateos, Fabio Duarte, Carlo Ratti, and Daniela Rus. "Roboat: An autonomous surface vehicle for urban waterways". In: *2019 IEEE/RSJ International Conference on Intelligent Robots and Systems (IROS)*. IEEE. 2019, pp. 6340–6347. DOI: 10.1109/IROS40897.2019.8968131 (cit. on pp. 2, 3).

[133] Wei Wang, Tixiao Shan, Pietro Leoni, David Fernández-Gutiérrez, Drew Meyers, Carlo Ratti, and Daniela Rus. "Roboat II: A novel autonomous surface vessel for urban environments". In: *2020 IEEE/RSJ International Conference on Intelligent Robots and Systems (IROS)*. IEEE. 2020, pp. 1740–1747. DOI: 10.1109/IROS45743.2020.9340712 (cit. on pp. 2, 3).

[134] Hans F. Weinberger. *A First Course in Partial Differential Equations with Complex Variables and Transform Methods*. Wiley, 1965. ISBN: 9780471006237 (cit. on p. 58).

[135] Stefan Wirtensohn, Oliver Hamburger, Hannes Homburger, Leticia Mayumi Kinjo, and Johannes Reuter. "Comparison of advanced control strategies for automated docking". In: *IFAC-PapersOnLine* 54.16 (2021). 13th IFAC Conference on Control Applications in Marine Systems, Robotics, and Vehicles CAMS 2021, pp. 295–300. DOI: https://doi.org/10.1016/j.ifacol.2021.10.107 (cit. on pp. 2, 10).

[136] Yuxuan Xia, Karl Granström, Lennart Svensson, Ángel F. García-Fernández, and Jason L. Williams. "Extended target Poisson multi-Bernoulli mixture trackers based on sets of trajectories". In: *2019 22th International Conference on Information Fusion (FUSION)*. 2019, pp. 1–8. DOI: 10.23919/FUSION43075.2019.9011181 (cit. on p. 5).

[137] Yuxuan Xia, Pu Wang, Karl Berntorp, Petros Boufounos, Philip Orlik, Lennart Svensson, and Karl Granström. "Extended object tracking with automotive radar using learned structural measurement model". In: *2020 IEEE Radar Conference (RadarConf20)*. 2020, pp. 1–6. DOI: 10.1109/RadarConf2043947.2020.9266598 (cit. on pp. 23, 29).

[138] Yuxuan Xia, Pu Wang, Karl Berntorp, Toshiaki Koike-Akino, Hassan Mansour, Milutin Pajovic, Petros Boufounos, and Philip V. Orlik. "Extended object tracking using hierarchical truncation measurement model with automotive radar". In: *ICASSP 2020 - 2020 IEEE International Conference on Acoustics, Speech and Signal Processing (ICASSP)*. 2020, pp. 4900–4904. DOI: 10.1109/ICASSP40776.2020.9054614 (cit. on pp. 23, 29).

[139] Yuxuan Xia, Pu Wang, Karl Berntorp, Lennart Svensson, Karl Granström, Hassan Mansour, Petros Boufounos, and Philip V. Orlik. "Learning-based extended object tracking using hierarchical truncation measurement model with automotive radar". In: *IEEE Journal of Selected Topics in Signal Processing* 15.4 (2021), pp. 1013–1029. DOI: 10.1109/JSTSP.2021.3058062 (cit. on pp. 4, 23).

[140] Chun Yang and Erik Blasch. "Kalman filtering with nonlinear state constraints". In: *IEEE Transactions on Aerospace and Electronic Systems* 45.1 (2009), pp. 70–84. DOI: 10.1109/TAES.2009.4805264 (cit. on p. 27).

[141] Shishan Yang and Marcus Baum. "Second-order extended Kalman filter for extended object and group tracking". In: *2016 19th International Conference on Information Fusion (FUSION)*. 2016, pp. 1178–1184 (cit. on p. 4).

[142] Shishan Yang and Marcus Baum. "Tracking the orientation and axes lengths of an elliptical extended object". In: *IEEE Transactions on Signal Processing* 67.18 (2019), pp. 4720–4729. DOI: 10.1109/TSP.2019.2929462 (cit. on pp. 4, 16, 18, 29, 63).

[143] Gang Yao, Pu Wang, Karl Berntorp, Hassan Mansour, Petros Boufounos, and Philip V. Orlik. "Extended object tracking with spatial model adaptation using automotive radar". In: *2021 IEEE 24th International Conference on Information Fusion (FUSION)*. 2021, pp. 1–8. DOI: 10.23919/FUSION49465.2021.9626890 (cit. on p. 23).

[144] Oğul Can Yurdakul, Mehmet Çetinkaya, Enescan Çelebi, and Emre Özkan. "A Rao-Blackwellized particle filter for superelliptical extended target tracking". In: *2024 27th International Conference on Information Fusion (FUSION)*. 2024, pp. 1–8. DOI: 10.23919/FUSION59988.2024.10706504 (cit. on p. 82).

[145] Antonio Zea. "Tracking Extended Objects With Active Models and Negative Information". Dissertation. Karlsruhe Institute of Technology (KIT), Intelligent Sensor-Actuator-Systems Laboratory (ISAS), Referent: U. D. Hanebeck, Korreferent: U. Orguner, Karlsruhe Series on Intelligent Sensor-Actuator-Systems 21, 2018 (cit. on pp. 6, 11, 12, 17, 19, 24, 25, 56).

[146] Antonio Zea, Florian Faion, Marcus Baum, and Uwe D. Hanebeck. "Level-set random hypersurface models for tracking non-convex extended objects". In: *Proceedings of the 16th International Conference on Information Fusion (Fusion 2013)*. Istanbul, Turkey, July 2013 (cit. on p. 20).

[147] Antonio Zea, Florian Faion, Marcus Baum, and Uwe D. Hanebeck. "Level-set random hypersurface models for tracking nonconvex extended objects". In: *IEEE Transactions on Aerospace and Electronic Systems* (2017). DOI: 10.1109/TAES.2016.130704 (cit. on pp. 4, 19, 20, 84, 98).

[148] Antonio Zea, Florian Faion, and Uwe D. Hanebeck. "Tracking extended objects using extrusion random hypersurface models". In: *Proceedings of the IEEE ISIF Workshop on Sensor Data Fusion: Trends, Solutions, Applications (SDF 2014)*. Bonn, Germany, Oct. 2014. DOI: 10.1109/SDF.2014.6954722 (cit. on pp. 4, 25, 38).

[149] Le Zhang and Jian Lan. "Extended object tracking using random matrix with skewness". In: *IEEE Transactions on Signal Processing* 68 (2020), pp. 5107–5121. DOI: 10.1109/TSP.2020.3019182 (cit. on p. 18).

[150] Lianqing Zheng, Zhixiong Ma, Xichan Zhu, Bin Tan, Sen Li, Kai Long, Weiqi Sun, Sihan Chen, Lu Zhang, Mengyue Wan, et al. "TJ4DRadSet: A 4D radar dataset for autonomous driving". In: *2022 IEEE 25th international conference on intelligent transportation systems (ITSC)*. IEEE. 2022, pp. 493–498. DOI: 10.1109/ITSC55140.2022.9922539 (cit. on p. 3).

[151] Yi Zhou, Tian Wang, Ronghua Hu, Hang Su, Yi Liu, Xiaoming Liu, Jidong Suo, and Hichem Snoussi. "Multiple kernelized correlation filters (MKCF) for extended object tracking using X-band marine radar data". In: *IEEE Transactions on Signal Processing* 67.14 (2019), pp. 3676–3688. DOI: 10.1109/TSP.2019.2917812 (cit. on p. 2).

Own Publications

[O1] Tim Baur, Julian Böhler, Stefan Wirtensohn, and Johannes Reuter. "Tracking of spline modeled extended targets using a Gaussian mixture PHD filter". In: *2019 22th International Conference on Information Fusion (FUSION)*. 2019, pp. 1–8. DOI: 10.23919/FUSION43075.2019.9011298 (cit. on pp. 8, 20, 29, 84).

[O2] Tim Baur, Patrick Hoher, Johannes Reuter, and Uwe D. Hanebeck. "Extended object tracking using superellipses". In: *Journal of Advances in Information Fusion*. unpublished, currently under review. 2025 (cit. on pp. 8, 11, 88, 89, 97, 104).

[O3] Tim Baur, Patrick Hoher, Johannes Reuter, and Uwe D. Hanebeck. "Tracking extended objects with basic parametric shapes using deformable superellipses". In: *2024 27th International Conference on Information Fusion (FUSION)*. 2024, pp. 1–8. DOI: 10.23919/FUSION59988.2024.10706433 (cit. on pp. 8, 11, 23, 86, 89, 97, 104).

[O4] Tim Baur, Johannes Reuter, and Uwe D. Hanebeck. "On runtime reduction in 3D extended object tracking by measurement downsampling". In: *2023 IEEE Symposium Sensor Data Fusion and International Conference on Multisensor Fusion and Integration (SDF-MFI)*. 2023, pp. 1–6. DOI: 10.1109/SDF-MFI59545.2023.10361508 (cit. on pp. 8, 39, 97, 104).

[O5] Tim Baur, Johannes Reuter, Antonio Zea, and Uwe D. Hanebeck. "Extent estimation of sailing boats applying elliptic cones to 3D lidar data". In: *2022 25th International Conference on Information Fusion (FUSION)*. 2022, pp. 1–8. DOI: 10.23919/FUSION49751.2022.9841265 (cit. on pp. 8, 43).

[O6] Tim Baur, Johannes Reuter, Antonio Zea, and Uwe D. Hanebeck. "Harmonic functions for three-dimensional shape estimation in cylindrical coordinates". In: *2022 IEEE International Conference on Multisensor Fusion and Integration for Intelligent Systems (MFI)*. 2022, pp. 1–6. DOI: 10.1109/MFI55806.2022.9913858 (cit. on pp. 8, 37, 57, 58, 82).

[O7] Tim Baur, Johannes Reuter, Antonio Zea, and Uwe D. Hanebeck. "Shape estimation and tracking using spherical double Fourier series for three-dimensional range sensors". In: *2021 IEEE International Conference on Multisensor Fusion and Integration for Intelligent Systems (MFI)*. 2021, pp. 1–6. DOI: 10.1109/MFI52462.2021.9591169 (cit. on pp. 7, 8, 57, 58, 74, 97, 102, 104, 110).

[O8] Tim Baur, Johannes Reuter, Antonio Zea, and Uwe D. Hanebeck. "Shape tracking using Fourier-Chebyshev double series for 3D distance measurements". In: *2023 26th International Conference on Information Fusion (FUSION)*. 2023, pp. 1–8. DOI: 10.23919/FUSION52260.2023.10224120 (cit. on pp. 8, 57, 62, 97, 104).

Own Published Code Repositories

[R1] Tim Baur. *Elliptic-Cone-EOT: Elliptic cone 3D extended object tracking*. Version v1.1. Apr. 2025. DOI: 10.5281/zenodo.15295128 (cit. on pp. 7, 45, 49).

[R2] Tim Baur. *Elliptic-Cylinder-EOT: Elliptic cylinder 3D extended object tracking*. Version v1.2. Apr. 2025. DOI: 10.5281/zenodo.15295136 (cit. on pp. 7, 45, 49).

[R3] Tim Baur. *Fourier-Chebyshev-double-series-EOT: Fourier-Chebyshev double series 3D extended object tracking*. Version v1.0. Feb. 2025. DOI: 10.5281/zenodo.14851547 (cit. on pp. 7, 67, 75).

[R4] Tim Baur. *Real-World-Solgenia-Tracking: Extended object tracking using 3D real-world lidar data*. Version v1.0. May 2025. DOI: 10.5281/zenodo.15411606 (cit. on p. 104).

[R5] Tim Baur. *Superellipse-EOT: Extended object tracking using superellipses*. Version v2.0. Nov. 2024. DOI: 10.5281/zenodo.14228879 (cit. on pp. 7, 91, 92).

Co-authored Publications

[C1] Julian Böhler, Tim Baur, Stefan Wirtensohn, and Johannes Reuter. "Stochastic partitioning for extended object probability hypothesis density filters". In: *2019 Sensor Data Fusion: Trends, Solutions, Applications (SDF)*. 2019, pp. 1–6. DOI: 10.1109/SDF.2019.8916656 (cit. on pp. 5, 8).

[C2] Patrick Hoher, Tim Baur, Johannes Reuter, Felix Govaers, and Wolfgang Koch. "A circular detection driven adaptive birth density for multi-object tracking with sets of trajectories". In: *2022 25th International Conference on Information Fusion (FUSION)*. 2022, pp. 1–8. DOI: 10.23919/FUSION49751.2022.9841312 (cit. on pp. 8, 31).

[C3] Patrick Hoher, Tim Baur, Johannes Reuter, Felix Govaers, and Wolfgang Koch. "Circular detection-driven adaptive birth densities". In: *Journal of Advances in Information Fusion* (2025) (cit. on pp. 8, 31).

[C4] Patrick Hoher, Tim Baur, Johannes Reuter, Dennis Griesser, Felix Govaers, and Wolfgang Koch. "3D-extended object tracking and shape classification with a lidar sensor using random matrices and virtual measurement models". In: *2024 27th International Conference on Information Fusion (FUSION)*. 2024, pp. 1–8. DOI: 10.23919/FUSION59988.2024.10706411 (cit. on pp. 8, 18, 37, 38, 107).

[C5] Patrick Hoher, Stefan Wirtensohn, Tim Baur, Johannes Reuter, Felix Govaers, and Wolfgang Koch. "Extended target tracking with a lidar sensor using random matrices and a virtual measurement model". In: *IEEE Transactions on Signal Processing* 70 (2022), pp. 228–239. DOI: 10.1109/TSP.2021.3138006 (cit. on pp. 3, 8, 18).

[C6] Hannes Homburger, Stefan Wirtensohn, Patrick Hoher, Tim Baur, Dennis Griesser, Moritz Diehl, and Johannes Reuter. "Solgenia—A test vessel toward energy-efficient autonomous water taxi applications". In: *Ocean Engineering* 328 (2025), p. 121011. ISSN: 0029-8018. DOI: 10.1016/j.oceaneng.2025.121011 (cit. on pp. 1–3, 5, 6, 8, 95).